Universität Bonn

Physikalisches Institut

Developing and evaluating new micropattern gas detectors

Marco Villa

Micropattern gas detectors (MPGDs) were introduced in the late 1980s in order to overcome the limited rate capability of traditional proportional counters. Thanks to their microscopic electrode structures, MPGDs are faster and more precise than the previous gas detectors and soon gained popularity. Two of the most successful MPGDs are the gas electron multiplier (GEM) and the micro-mesh gaseous structure (Micromegas). In this thesis I present the features of GEMs and Micromegas, some of their current applications and the research and development that I have done on these technologies. My activity covered two main topics: the test and enhancement of single-mask GEMs for large-area applications and the study of spark-tolerant Micromegas for the upgrade of the ATLAS Small Wheels.

Physikalisches Institut der
Universität Bonn
Nussallee 12
D-53115 Bonn

BONN-IR-2014-03
February 2014
ISSN-0172-8741

Developing and evaluating new micropattern gas detectors

Dissertation
zur
Erlangung des Doktorgrades (Dr. rer. nat.)
der
Mathematisch-Naturwissenschaftlichen Fakultät
der
Rheinischen Friedrich-Wilhelms-Universität Bonn

von
Marco Villa
aus
Desio, Italy

Bonn, November 2013

Dieser Forschungsbericht wurde als Dissertation von der Mathematisch-Naturwissenschaftlichen Fakultät der Universität Bonn angenommen und ist auf dem Hochschulschriftenserver der ULB Bonn `http://hss.ulb.uni-bonn.de/diss_online` elektronisch publiziert.

1. Gutachter:	Prof. Dr. Ian Brock
2. Gutachter:	Prof. Dr. Klaus Desch
Tag der Promotion:	14.02.2014
Erscheinungsjahr:	2014

Contents

Introduction

In this thesis I present the work done while I was employed at the European Organization for Nuclear Research (CERN), where I was awarded a fellowship as an Early Stage Researcher (ESR) within the Marie Curie Training Network on Particle Detectors (MC-PAD)[1].

My activity is articulated in two main projects, both involving R&D on micropattern gas detectors. My supervisors are Leszek Ropelewski and Jörg Wotschack, both based at CERN. My Ph.D. advisor is Ian Brock, with whom I had weekly phone meetings.

My first project, described in Chapter 3, focuses on gas electron multipliers (GEMs). Foils manufactured with the traditional double-mask process have maximum dimensions of about $30 \times 30\,\mathrm{cm}^2$, because of the difficulty in the manual alignment of the two photolithographic masks. To overcome such a limitation, in 2007 the single-mask technology was introduced, which is scalable to square metre size.

I took part in the improvement of the novel technique in two ways. On the one side, I performed numerical simulations to study the electrostatic properties of the GEM as a function of the geometry of the holes in the substrate. On the other side, I evaluated the performance of several specimens in terms of robustness against sparks, maximum achievable gain and gain stability. These research activities, carried out in collaboration with the production workshop, enabled the refinement of the procedure.

Single-mask GEMs now offer the same performance as the traditional foils and they are at the base of various experiments and upgrade projects.

The second topic, presented in Chapter 4, regards the exploitation of the micro-mesh gaseous structure (Micromegas) technology for the construction of tracking chambers. The detectors are aimed for the ATLAS new Small Wheels, which will replace the current ones during the second long shutdown of the Large Hadron Collider. The main challenges are the large area coverage and the elevated discharge probability due to the abundance of highly ionizing particles.

In this context, I investigated two different approaches to make Micromegas spark-tolerant. Firstly, I probed the idea of lowering the discharge probability by introducing a GEM above the amplification mesh. I measured the effective gas gain and the spark rate of a small size Micromegas, both in standalone configuration and in combination with the GEM and I compared the results. Later, I got involved in the analysis of test-beam data acquired with a resistive Micromegas. I developed the analysis framework and several software modules and I performed in-depth studies of the detection efficiency and of the space resolution, confronting the extracted figures to those of a non-resistive chamber.

I demonstrate that a double-stage Micromegas can reduce the discharge probability by more than an order of magnitude and that resistive Micromegas exhibit a superior performance in terms of both detection efficiency and space resolution with respect to non-resistive chambers.

[1] European Union Seventh Framework Programme for Research (FP7) grant agreement no. 214 560-2

CHAPTER 1

Radiation interaction in matter and operating principles of gas detectors

The design and operation of a radiation detector are based on the way in which the particles to be observed interact with matter. The detection ultimately relies on the incident radiation transferring a fraction or all of its energy to the atoms or molecules of the detector active volume. A knowledge of the physical processes with which the radiation loses energy in matter is therefore a prerequisite to the understanding of any detector technology.

This chapter sets the physics framework and gives an overview of the theory that is needed to comprehend the research work presented in the thesis. The most relevant radiation interaction processes in matter are presented. Charged particles are considered at first, classified according to their mass in heavy charged particles and electrons. The treatment of neutral particles follows, giving insights on photon interactions and a quick summary of neutron effects. Finally, the last part of the chapter focuses on the operating principles of gas detectors.

1.1 Interaction of heavy charged particles

Heavy charged particles is a very broad category that covers all the radiation carrying a non-zero electric charge, with the only exceptions of electrons and positrons. Ions, hadrons and muons are examples of particles that belong to this class.

Heavy charged particles lose energy mainly through Coulomb interactions with the orbital electrons of the material they traverse. Interactions with atomic nuclei are possible, but rare and not significant for detection purposes. During a collision, an orbital electron feels an impulse whose intensity is a function of the impact parameter. Depending on the impulse size, the atom containing the electron gets excited or ionized, while the heavy charged particle loses a fraction of its kinetic energy. Most collisions have an impact parameter much larger than the atomic radius and, as a consequence, highly energetic electrons are unlikely to be produced. More specifically, the energy loss probability decreases with the square of the transferred energy. The minimum transferable energy in a single interaction depends on the average electron binding energy in the atom and scales approximately with the square of the atomic number. The maximum transferable energy is $4Em_e/M$, where E and M are the kinetic energy and mass of the incident particle, respectively, and m_e the electron mass. Heavy charged particles therefore lose only a small fraction of their energy in each collision, decelerating slowly and continuously.

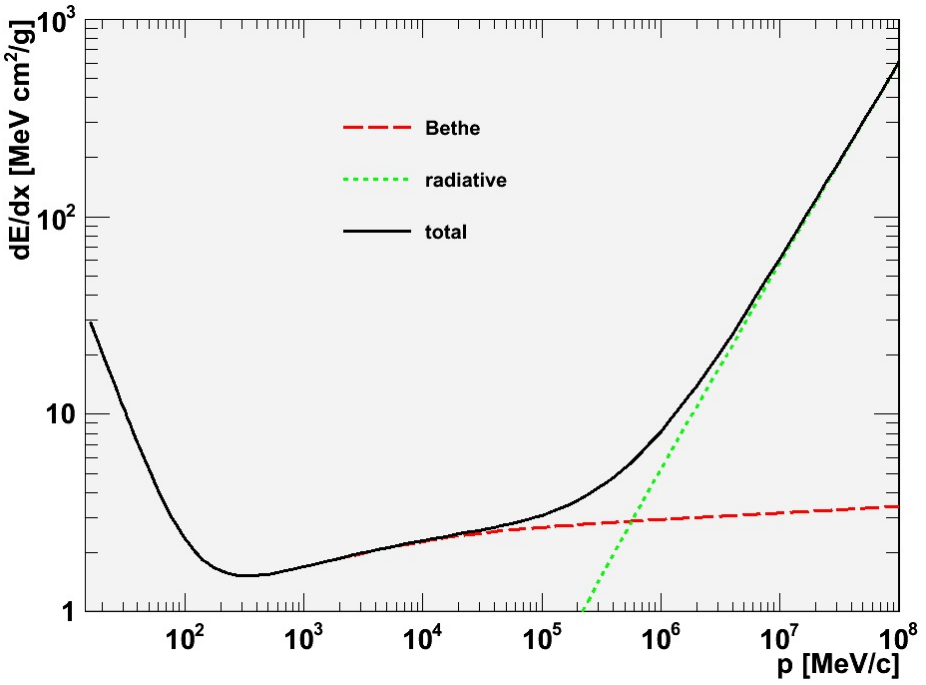

Figure 1.1: Linear energy transfer of muons in argon [1].

The differential energy loss per unit of path length along a particle track is commonly referred to as linear energy transfer or LET. Alternative terminologies include linear stopping power and specific energy loss. Figure 1.1 shows the linear energy transfer for muons in gaseous argon. The LET is conveniently measured in MeV cm^2/g in order to remove the dependence on the material density.

Building on physics considerations similar to the ones above, Bethe produced a model that describes the linear energy transfer with a few percent accuracy [2]. The Bethe equation is valid for heavy charged particles with $0.1 \lesssim \beta\gamma \lesssim 10^3$ traversing media with intermediate atomic number:

$$-\frac{1}{\rho}\left\langle\frac{\mathrm{d}E}{\mathrm{d}x}\right\rangle_{\text{Bethe}} = \frac{N_A e^4}{4\pi\epsilon_0^2 m_\mathrm{e} c^2}\cdot\frac{Z}{A}\cdot\frac{z^2}{\beta^2}\cdot\left[\ln\frac{2m_\mathrm{e}c^2\beta^2\gamma^2}{I\sqrt{1+2\gamma m_\mathrm{e}/M+(m_\mathrm{e}/M)^2}} - \beta^2 - \frac{\delta(\beta\gamma)}{2} - \sum_i \frac{C_i}{Z}\right] \quad (1.1)$$

In the validity region of the Bethe formula, the linear energy transfer does not vary significantly with the material. The dependence is through Z/A and therefore the LET slightly decreases with increasing atomic number. The heavy charged particle mainly contributes with z^2/β^2. The deposited energy decreases as $1/v^2$ and it reaches a minimum where the logarithmic term starts to become important. The position of such minimum drops from $\beta\gamma = 3.5$ to 3 as Z increases from 7 to 100, while the corresponding LET decreases from about 2 to 1 MeV cm^2/g. Particles in this velocity range are called minimum ionizing particles or MIPs.

The logarithmic term takes into account the minimum and maximum transferable energy in a single collision. I is the average electron binding energy in an atom, which roughly corresponds to $10Z$ eV. A dependence on the heavy charged particle mass M is introduced at high velocities through the maximum transferable energy. The logarithmic rise has to be corrected with the density effect term $\delta(\beta\gamma)/2$ to include the medium polarization, that reduces the number of distant collisions, thus suppressing the growth. The remaining relativistic rise comes from the increase of the maximum transferable energy,

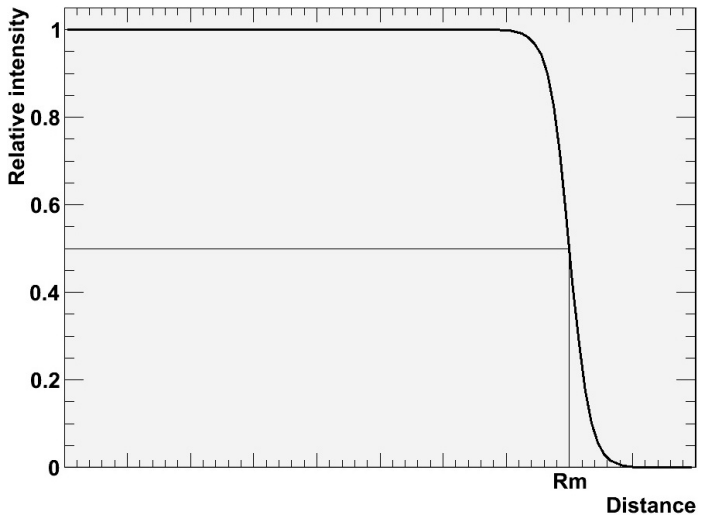

Figure 1.2: Range of heavy charged particles.

which results in the production of rare energetic electrons. Ionization electrons having a kinetic energy much higher than I that can produce secondary ionization are called delta rays.

At low energies, shell corrections C_i/Z describing the material atomic structure become important. This refinement makes the Bethe equation accurate to about 1% down to $\beta\gamma \simeq 0.05$. For $0.01 \lesssim \beta\gamma \lesssim 0.05$, no satisfactory theory exists and phenomenological fits are used. When $\beta\gamma \lesssim 0.01$, that is comparable with the velocity of the outer orbital electrons in the traversed medium, the linear energy transfer is proportional to β. At even lower velocities, non-ionizing nuclear recoils become the dominating mechanism for energy loss.

The upper limit of applicability of the Bethe formula is defined by the onset of radiative effects, which include e^+e^- pair production, bremsstrahlung and photonuclear reactions. The total linear energy transfer is given by Eq. (1.2).

$$-\frac{1}{\rho}\left\langle\frac{\mathrm{d}E}{\mathrm{d}x}\right\rangle_{\text{total}} = -\frac{1}{\rho}\left\langle\frac{\mathrm{d}E}{\mathrm{d}x}\right\rangle_{\text{Bethe}} - \frac{1}{\rho}\left\langle\frac{\mathrm{d}E}{\mathrm{d}x}\right\rangle_{\text{radiative}} = a(E) + b(E)\,E \tag{1.2}$$

$a(E)$ is the Bethe term, which increases logarithmically with the energy of the heavy charged particle. $b(E)$ models the radiative contributions and varies slowly with E, so that the dissipated energy is roughly proportional to E. The condition in which the radiative losses equal the ionization losses is called critical energy and is denoted with E_c.

The radiation penetrating power in matter is conventionally expressed by the range. The range is experimentally determined by placing a particle counter in front of a collimated source of monoenergetic radiation. Absorbers of increasing thickness are interposed between the source and the counter and the corresponding number of detected particles is recorded. Figure 1.2 shows the relative count rate as a function of the traversed distance for heavy charged particles. Small values of the absorber thickness reduce the heavy charged particles' kinetic energy, but, as the paths are almost straight, the beam intensity remains the same. When the thickness reaches the length of the shortest track, the count rate starts to decrease and rapidly drops to zero. The mean range R_m is defined as the distance over which the relative intensity is reduced to one half.

Given the stochastic nature of the energy loss processes, the radiation in an initially monoenergetic beam will show a spread in the path length. This phenomenon is known as range straggling and it is

responsible for the more or less pronounced sharpness of the cutoff in Fig. 1.2. Differentiating this curve leads to a peak whose width is taken as a measure of the range straggling. For heavy charged particles, the effect is not very pronounced and amounts to a few percent of the mean range.

1.2 Interaction of electrons

At low energy, electrons and positrons behave similarly to heavy charged particles, losing energy primarily through excitations and ionizations. However, the mass identity between the incoming radiation and the target atomic electron, and the quantum indistinguishability of the two particles in case of an incident electron, modify the interaction kinematics, thus making the Bethe equation not directly applicable. Moreover, concurrent processes such as Møller scattering, Bhabha scattering and positron annihilation add small corrections to the linear stopping power at low energy.

Fast electrons predominantly lose energy by bremsstrahlung. Bremsstrahlung is a coherent phenomenon involving particle acceleration and deflection on atomic nuclei, in contrast to excitations and ionizations where the momentum is transferred incoherently to the individual orbital electrons. Bremsstrahlung therefore increases as Z^2, rather than linearly with the material atomic number. Energy is irradiated at a rate proportional to the electron energy, which implies an exponential energy decrease along the track, as stated in Eq. (1.3).

$$E(x) = E_0 \exp\left(-\frac{\rho x}{X_0}\right) \tag{1.3}$$

X_0 is called radiation length and it is measured in g/cm^2. It represents the distance that electrons and positrons have to travel to see their energy decreased by a factor e. For $Z > 4$, the radiation length is accurately modeled by Eq. (1.4), where α is the fine structure constant and r_e the classical electron radius [3–5].

$$\frac{1}{X_0} = \frac{4N_A\alpha r_\mathrm{e}^2}{A}\left\{Z^2\left[\ln\frac{184.15}{Z^{1/3}} - \alpha^2Z^2\left(\frac{1}{1+\alpha^2Z^2} + 0.202\,06 - 0.0369\alpha^2Z^2\right)\right] + Z\ln\frac{1194}{Z^{2/3}}\right\} \tag{1.4}$$

Equation (1.5) provides an approximation with a data agreement better than 2.5%.

$$X_0 = \frac{716.4\ \mathrm{g/cm^2}A}{Z(Z+1)\ln\left(287/\sqrt{Z}\right)} \tag{1.5}$$

Since electrons and positrons have the same mass as the orbital electrons, a large fraction of their energy can be lost in a single encounter and large deviations in their trajectories are possible. As a consequence, they show much more tortuous paths then heavy charged particles and their track length can be considerably greater than the penetration distance. This has an impact on the range definition. Figure 1.3 sketches the characteristic intensity trend of a monochromatic electron beam as a function of the traversed material. Even small values of the absorber thickness reduce the count rate, as the electrons can be scattered out of the detector acceptance. The intensity then slowly decreases and levels off to zero, reflecting the amount by which electrons are deviated from their original direction. In these conditions, it is preferable to use the extrapolated range R_e, corresponding to the linear extrapolation of the transmission curve from half intensity to zero. This value corresponds to the absorber thickness that is required to ensure that almost no electrons will pass through.

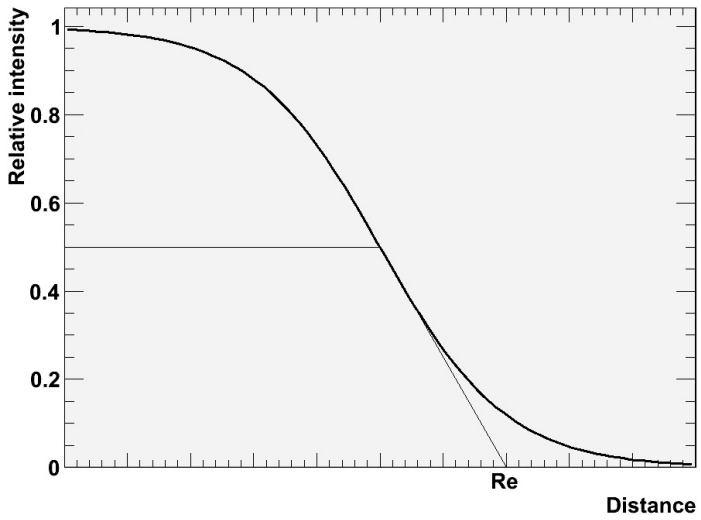

Figure 1.3: Range of electrons and positrons.

1.3 Multiple Coulomb scattering

Besides losing kinetic energy through the mechanisms described in the previous sections, charged particles traversing a medium also have their trajectories modified by many deflections. Although strong interactions play a role for hadronic projectiles, the bulk of the effect is due to Coulomb scattering on atomic nuclei.

Multiple Coulomb scattering is well represented by the theory of Molière [6]. The planar angular distribution is roughly Gaussian at small angles and behaves like Rutherford scattering for wider deflections, with large non-Gaussian tails. In the Gaussian approximation, the central 98% of the projected angular distribution is given by Eq. (1.6).

$$\frac{\mathrm{d}N}{\mathrm{d}\theta} = \frac{1}{\sqrt{2\pi}\theta_{\mathrm{RMS}}} \exp\left(-\frac{\theta^2}{2\theta_{\mathrm{RMS}}^2}\right) \tag{1.6}$$

θ_{RMS} can be obtained from an empirical fit to the Molière distribution, as shown in Eq. (1.7) [7–9]. Here z, βc and p are the charge, velocity and momentum of the incident particles, while x and X_0 are the thickness and radiation length of the traversed material. This formula is valid for media of any atomic number and is accurate to 11% or better in the range $10^{-3} \lesssim x/X_0 \lesssim 100$.

$$\theta_{\mathrm{RMS}} = 13.6\,\mathrm{MeV} \cdot \frac{z}{\beta c p} \cdot \sqrt{\frac{x}{X_0}} \cdot \left(1 + 0.038 \ln \frac{x}{X_0}\right) \tag{1.7}$$

Other useful variables are the RMS linear deviations on the exit plane of the scattering material, along directions perpendicular to the incident beam. These quantities, denoted with y_{RMS} and z_{RMS}, can be expressed in terms of the angular distribution width θ_{RMS}, as indicated in Eq. (1.8).

$$y_{\mathrm{RMS}} = z_{\mathrm{RMS}} = \frac{x\theta_{\mathrm{RMS}}}{\sqrt{3}} \tag{1.8}$$

1.4 Interaction of photons

Photons are neutral radiation and therefore do not experience Coulomb forces. They travel in matter without losing energy until they interact and disappear, emitting secondary particles in the process. This is in sharp contrast with the behaviour of charged radiation, that slowly and continuously loses energy through many simultaneous interactions.

The concept of linear energy transfer used to describe charged particles cannot be applied to photons. Photon interactions are rather defined by their cross section. Given a monoenergetic beam of photons with energy $E = h\nu$ traversing a medium with density ρ and atomic number A, the differential decrease of beam intensity $\mathrm{d}I$ in a material thickness $\mathrm{d}x$ is proportional to the intensity I through the total cross section $\sigma(E)$. This leads to an exponential reduction of the number of photons, according to Eq. (1.9).

$$\frac{\mathrm{d}I}{\mathrm{d}x} = -\frac{N_A \rho \sigma I}{A} \qquad I(x) = I_0 \exp\left(-\frac{N_A \rho \sigma x}{A}\right) \tag{1.9}$$

The above relation is usually expressed in terms of the attenuation coefficient $\mu(E)$, as shown in Eq. (1.10). In order to remove the dependence on the material density, the mass attenuation coefficient μ/ρ is introduced, as shown in Eq. (1.11). The quantity ρx is called absorber mass thickness.

$$\mu = \frac{N_A \rho \sigma}{A} \qquad I(x) = I_0 \exp(-\mu x) \tag{1.10}$$

$$\frac{\mu}{\rho} = \frac{N_A \sigma}{A} \qquad I(\rho x) = I_0 \exp\left(-\frac{\mu}{\rho}\rho x\right) \tag{1.11}$$

An alternative approach makes use of the mean free path $\lambda(E)$. This is defined as the average distance traveled by photons before an interaction takes place and corresponds to $1/\mu$, see Eq. (1.12). Since λ coincides with the material thickness that reduces the beam intensity by a factor e, it is also given the name of attenuation length.

$$\lambda = \frac{A}{N_A \rho \sigma} \qquad I(x) = I_0 \exp\left(-\frac{x}{\lambda}\right) \tag{1.12}$$

Photons interact with matter in several different ways. Each mechanism is characterized by its specific cross section σ_i and the total cross section σ is the sum over all the processes.

The detection of neutral radiation and the measurement of its properties relies on the charged particles emerging from the interactions. Photon interactions give rise to electrons, which then lose energy as described in the first part of this chapter. A photon detector must therefore be designed to favorite the reactions generating the charged secondaries and measure their energy loss.

Section 1.4.1 to 1.4.4 give an overview of the physical processes in which photons interact in matter, focusing on those of higher relevance for particle detection.

1.4.1 Elastic scattering

Elastic scatterings are reactions in which a photon is absorbed and subsequently re-emitted without energy loss. Although the emerging quantum carries the same momentum as the impinging one, its direction changes in the scattering process. The cross section of atomic elastic scattering, such as Rayleigh scattering, is energy-independent for large photon wavelengths and drops above a few keV.

Elastic interactions are of little interest for photon detection and their effects are usually neglected because their cross section is lower than for other mechanisms and their only net effect is a change of the particle direction.

1.4.2 Photoelectric effect

The photoelectric effect is a physical process in which a photon is absorbed by an atom, causing the ejection of an orbital electron. The expelled electron takes the name of photoelectron. In the photoelectric effect the photon interacts with the atom as a whole, not with the single electron. Kinematic considerations forbid the photoelectric effect to happen on a free electron, as a recoiling atom is needed to compensate the photoelectron momentum. For this reason, the interaction is most likely to happen on the most tightly bound electron energetically accessible.

Figures 1.4 and 1.5 show the total cross section as a function of the photon energy in a light material like carbon and in a heavy material like lead. The contributions from different mechanisms are also highlighted, the photoelectric effect being the predominant process at low energy. The shells' influence on the photoelectric cross section in lead is visible as discontinuities called absorption edges, that coincide with the various electron binding energies. The highest-energy discontinuity corresponds to the K shell, the second highest to the L shell and so on. The only absorption edge of carbon lies outside the considered energy range and therefore it is not visible in Fig. 1.4. For energies slightly above an edge, the photon can access an inner shell that has a higher ionization probability and therefore the cross section increases. For energies just below the edge, the reaction is no longer energetically possible and the cross section drops abruptly. Far from absorption edges, the cross section decreases steeply with growing energy because the photon goes off resonance. Although there is no universal analytic expression for the dependence on the photon energy E and the material atomic number Z, an empirical scaling law is given by Eq. (1.13), where n is a function of E and ranges from 4 to 5 [10].

$$\sigma_{\text{photoelectric}} \propto \frac{Z^n}{E^3} \tag{1.13}$$

The emerging photoelectron carries a kinetic energy, E_e, equal to the photon energy, $h\nu$, minus the binding energy, E_b, minus the atom recoil energy, E_a. Although the atom is necessary to compensate the photoelectron momentum, its kinetic energy is negligible due to its high mass. E_e is therefore effectively given by Eq. (1.14).

$$E_\text{e} = h\nu - E_b \tag{1.14}$$

Photoelectrons are not all produced in the same direction nor are they emitted isotropically. To a first approximation, at low energy the process is due to the photon electric field that oscillates perpendicularly to the wave propagation vector, thus generating a bipolar angular probability distribution for the ejected photoelectron. As the energy increases, the electron gains a Lorentz boost and the two lobes of the angular distribution get squeezed in the forward direction.

The photoelectric effect leaves an ionized atom, that presents a vacancy in the shell from where the photoelectron was expelled. This vacancy is quickly filled through the rearrangement of the atomic electrons or the capture of a free electron from the medium and the consequent production of a characteristic X-ray photon or Auger electron. In most cases either particle can emerge and the fluorescent yield measures the probability of a radiative de-excitation to take place. Light materials preferably emit Auger electrons, while high-Z atoms show a higher fluorescent yield. Auger electrons have a short range and deposit all their energy in the proximity of the original interaction site. X-rays are also generally reabsorbed close to their creation point through the photoelectric effect involving less tightly bound shells in other atoms.

If no radiation escapes from the detector active volume, the sum of the kinetic energy of all the electrons equals the energy of the original photon. This makes the photoelectric effect an optimal mechanism for photon detection, ideally giving rise to a single Dirac function in an energy spectrum. In practical

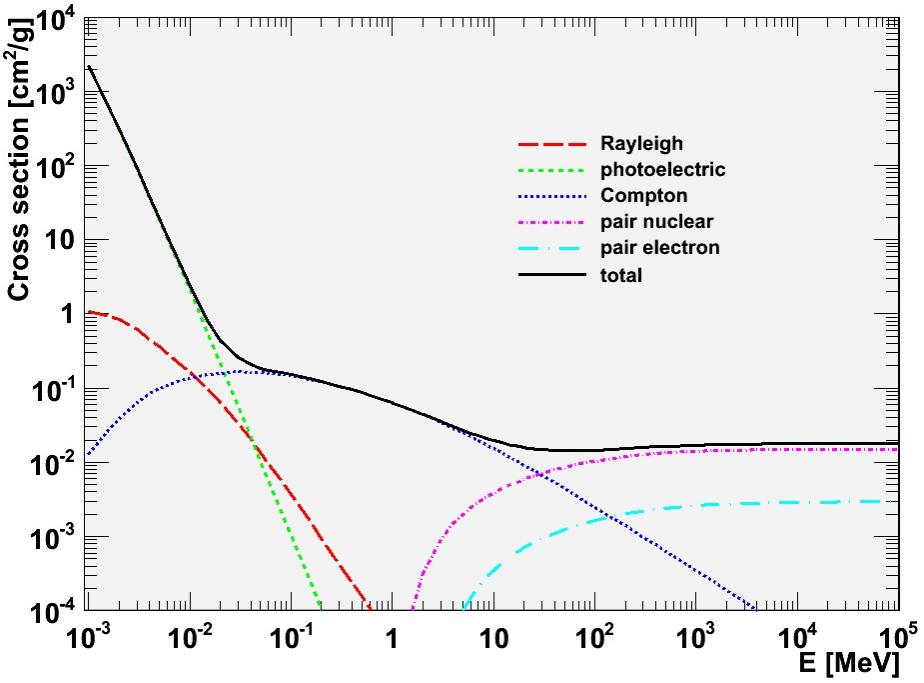

Figure 1.4: Photon cross sections in carbon [11].

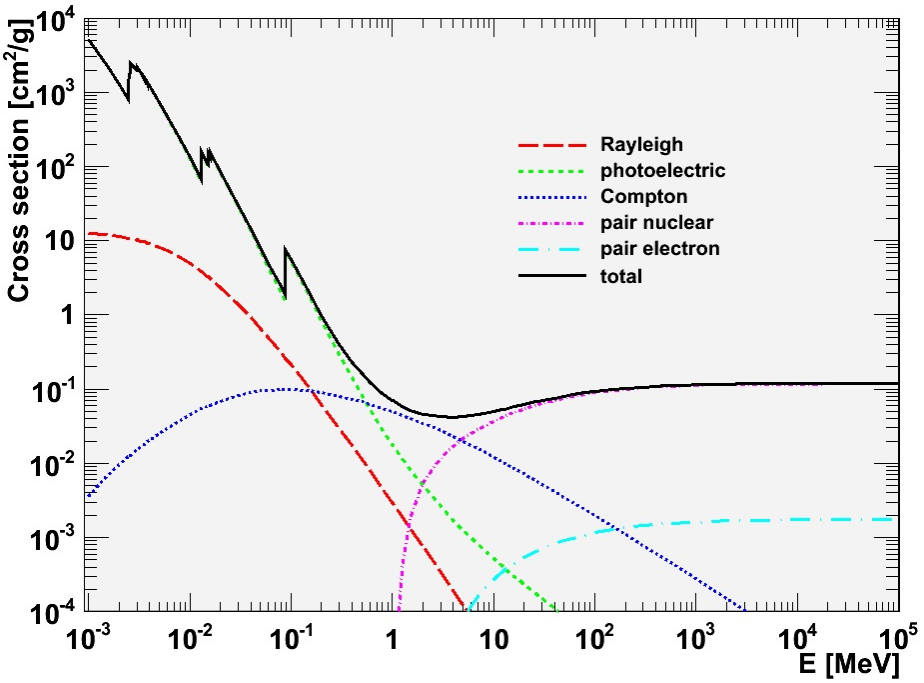

Figure 1.5: Photon cross sections in lead [11].

applications, the detector response smears this delta function, generating a Gaussian distribution that takes the name of photopeak. In case a de-excitation X-ray escapes from the detector, a ghost peak will appear at lower energy, the missing energy corresponding to the undetected radiation. This peak is called the escape peak. The amplitude of an escape peak depends on many factors, including the photon energy, the detector material, its fluorescent yield and the setup geometry.

1.4.3 Compton scattering

In Compton scattering, a photon of energy $E = h\nu$ interacts with an electron and changes its propagation direction by an angle θ. Given the presence of a photon in the final state, the reaction does not need to happen on a bound electron and the process is commonly described assuming the electron to be free and initially at rest.

The Compton differential cross section for the solid angle $\mathrm{d}\Omega$ on a single free electron can be computed using quantum electrodynamics. The lowest-order solution, shown in Eq. (1.15), is known as Klein-Nishina formula [12]. Here r_e is the classical electron radius and ε is the photon energy in units of the free electron mass.

$$\frac{\mathrm{d}\sigma_\mathrm{Compton}}{\mathrm{d}\Omega} = \frac{r_\mathrm{e}^2}{2}\left[\frac{1}{1+\varepsilon\,(1-\cos\theta)}\right]^2\left[\frac{1}{1+\varepsilon\,(1-\cos\theta)} + \varepsilon\,(1-\cos\theta) + \cos^2\theta\right] \qquad \varepsilon = \frac{h\nu}{m_\mathrm{e}c^2} \tag{1.15}$$

For photon energies much lower than the electron rest mass, the Klein-Nishina formula reduces to the Thomson differential cross section reported in Eq. (1.16). This is the angular distribution of elastically scattered radiation by a free charge, as predicted by classical electromagnetism.

$$\frac{\mathrm{d}\sigma_\mathrm{Thomson}}{\mathrm{d}\Omega} = \frac{r_\mathrm{e}^2}{2}\left(1+\cos^2\theta\right) \qquad \varepsilon \to 0 \tag{1.16}$$

The Thomson differential cross section is symmetric for $\theta \leftrightarrow \pi - \theta$, with maxima at $\theta = 0$ and π. As the photon energy increases, the distribution gets a net boost in the forward direction and the probability of having backscattered photons decreases quickly.

The atomic differential cross section is Z times the Klein-Nishina formula, due to the incoherent contributions of the orbital electrons. This is in sharp contrast with the photoelectric cross section, that has a much stronger dependence on the atomic number.

The Compton total cross section is obtained by integrating the Klein-Nishina formula over the full 4π solid angle. This leads to the attenuation cross section, that includes both elastic and inelastic scattering events. The attenuation cross section is maximum for the highest photon wavelengths, where it approaches the Thomson cross section shown in Eq. (1.17), all the interactions being of elastic type.

$$\sigma_\mathrm{Thomson} = \frac{8\pi r_\mathrm{e}^2 Z}{3} \qquad \varepsilon \to 0 \tag{1.17}$$

For higher photon frequencies, the attenuation cross section drops monotonically, while inelastic reactions become more and more important. Equation (1.18) provides an empiric fit to the attenuation cross section as a function of the Thomson cross section.

$$\sigma_\mathrm{Compton} = \frac{8\pi r_\mathrm{e}^2 Z}{3} \cdot \frac{1}{1+3\varepsilon^{0.7}/2} \qquad \varepsilon = \frac{h\nu}{m_\mathrm{e}c^2} \tag{1.18}$$

In particle detection applications, it is sometimes more convenient to introduce the absorption cross section, defined as the cross section of the inelastic events alone. In fact, photon detection relies on

energy transfer to charged particles, while elastic processes have the only effect of changing the photon propagation direction. This distinction is not necessary for photoelectric effect and pair production (cf. Section 1.4.4), in which elastic interactions are not possible, but it is of high relevance for Compton scattering. Figures 1.4 and 1.5 sketch the trend of the Compton absorption cross section. Its relative contribution to the attenuation cross section increases with growing energy.

The energy $E' = h\nu'$ of the photon emerging from an inelastic Compton scattering is given by:

$$h\nu' = \frac{h\nu}{1 + \varepsilon\,(1 - \cos\theta)} \qquad \varepsilon = \frac{h\nu}{m_e c^2} \tag{1.19}$$

This relation can alternatively be expressed in terms of the photon wavelength shift $\Delta\lambda$ following the inelastic collision, by means of the Compton wavelength λ_C, as illustrated in Eq. (1.20).

$$\Delta\lambda = \lambda' - \lambda = \lambda_C\,(1 - \cos\theta) \qquad \lambda_C = \frac{h}{m_e c} \tag{1.20}$$

Conversely, the detectable energy E_e transferred to the electron is described by Eq. (1.21).

$$E_e = \frac{h\nu\varepsilon\,(1 - \cos\theta)}{1 + \varepsilon\,(1 - \cos\theta)} \qquad \varepsilon = \frac{h\nu}{m_e c^2} \tag{1.21}$$

E_e is negligible for vanishing photon scattering angles and exhibits a maximum for $\theta = \pi$. Because of the kinematics involved in the mechanism, the electron cannot acquire the full photon energy, but only a fraction of it, the rest being carried away by the outgoing photon. These peculiarities are reflected in the electron energy spectrum, which presents a continuum from 0 to a the maximum electron energy, where it falls off abruptly with the so-called Compton edge. The gap between the Compton edge and the impinging photon energy approaches $m_e c^2/2$ in the limit of large energies, as from Eq. (1.19).

When the electron binding energy is taken into account, the Compton edge gets smeared off and its sudden decay assumes a finite slope. This effect is more pronounced at low energy, but still negligible in most cases, as it is masked by the finite energy resolution of the detector. The angular momentum of orbital electron also causes a tiny spread in the monoenergetic prediction of Eq. (1.21) for a fixed angle, due to Doppler shift.

1.4.4 Pair production and annihilation

In pair production, a gamma ray of energy $E = h\nu$ interacts with a virtual photon from a nucleus, disappearing and giving rise to an electron-positron pair. The reaction can also happen in the electric field of an electron, but the latter case is of much lower relevance.

The process is kinematically forbidden for photon energies below $2m_e c^2$. Above this threshold, the cross section quickly increases and stabilizes on a plateau value, making pair production the dominant photon conversion mechanism at high energy, as shown in Fig. 1.4 and 1.5. The pair production cross section is closely related to that of bremsstrahlung, since the Feynman diagrams describing the two processes are variants of one another. In the complete screening limit valid at high energy, the pair production cross section can be expressed as a function of the radiation length X_0, as pointed out by Eq. (1.22) [3, 4].

$$\sigma_{\text{pair}} = \frac{7A}{9N_A X_0} \tag{1.22}$$

The formula carries a dependence on Z^2 through the radiation length, according to Eq. (1.5). This is due to the coherent action of the protons in the nucleus.

The photon energy exceeding $2m_e c^2$ is converted into kinetic energy of the produced pair, as stated by Eq. (1.23). This energy is subsequently turned into detectable charge through the interactions of the electron and of the positron.

$$E_{e^-} + E_{e^+} = h\nu - 2m_e c^2 \tag{1.23}$$

After slowing down, the positron will eventually annihilate with an electron, liberating two 511 keV photons. If these photons are reabsorbed and converted into charge in the active volume of the detector, the energy spectrum will present only one peak, corresponding to the energy of the original photon. However, the escape of either or both annihilation photons can lead to missing energy peaks in the spectrum, that take the name of single and double-escape peak respectively. A single-escape peak is located 511 keV below the full-energy peak and a double-escape peak 1022 keV below.

1.5 Interaction of neutrons

Similarly to photons, neutrons are neutral particles and therefore are not subject to Coulomb forces. They can traverse matter without losing energy, with a mean free path ranging from a fraction of a centimetre to tens of centimetres, until they undergo a collision that drastically changes their properties. The interactions happen on atomic nuclei and can be of various nature, from neutron-induced nuclear reactions to elastic or inelastic neutron scatterings, the relative cross sections depending on the neutron energy. A standard classification distinguishes between slow and fast neutrons, the boundary being around 1 eV.

Slow neutrons primarily lose energy through elastic scatterings on nuclei. Given the low transferred momentum, the recoil nucleus does not play any role of relevance. Once the neutron has slowed down to the thermal level (0.025 eV), it can be absorbed by a nucleus and provoke a nuclear reaction, giving rise to a gamma ray, a proton, an alpha particle or provoking a fission. Since the neutron has a negligible energy, the reaction must have a positive Q-value in order to take place.

The cross section of most nuclear reactions drops for fast neutrons, while elastic scatterings become more and more important because neutrons can lose appreciable amounts of energy in collisions. The maximum transferable energy depends on the target nucleus and it is maximum for hydrogen, in which case the neutron can lose up to all its kinetic energy in a single event.

At higher energies inelastic scatterings also come into play. Here the nucleus is raised to one of its excited states and rapidly de-excites emitting a gamma ray.

1.6 Ionization of gas

The operation of gas detectors ultimately relies on the ionization of the gas molecules and the eventual formation of electron-ion pairs. The ionization may be the direct product of the physical processes described in the previous sections, in which case it takes the name of primary ionization. Most of the charge, however, comes from secondary ionization mechanisms, involving either the interaction of delta rays or the relaxation of excited states. An example of the latter case is illustrated in Eq. (1.24), where π^- is the incident particle, * denotes an excited state and e^- is the ionization electron.

$$\pi^- A \rightarrow \pi^- A^* \qquad A^* B \rightarrow A B^+ e^- \tag{1.24}$$

This kind of processes can only occur if the gas mixture contains at least two different species of atoms or molecules A, B and if the excitation energy of A^* is above the ionization potential of B. In gas detectors, A^* is often a metastable state of the noble gas, while B is one of the molecular additives

Table 1.1: W values for various gas molecules [13].

Gas	W [eV]
Ar	26
CO_2	33
CF_4	54

necessary for stable proportional mode operation (cf. Section 1.8). The formation of electron-ion pairs due to energy transfer between different gas species and following de-excitation is known as Penning effect. Penning mixtures are particular gas combinations in which the Penning effect plays an important role and is therefore exploited to increase the liberated charge.

The total charge, that includes both primary and secondary ionization, is usually the relevant parameter for radiation detection purposes. In order to average over all the possible processes, it is convenient to introduce the mean energy, W, spent to create an electron-ion pair. The total number of electron-ion pairs, N, will then be given by Eq. (1.25), where E is the energy deposited by the radiation in the detector active volume.

$$N = \frac{E}{W} \tag{1.25}$$

Since part of the energy is dissipated in non-ionizing events, W is always higher than the ionization energy. The values of W for the gas molecules used in this thesis are reported in Table 1.1. In case of a gas mixture, N can be obtained from a weighted average taking in into account the mixture composition, as shown in Eq. (1.26). Here the sum extends over the gas components and w_i represents the relative abundance of each species. This simple model assumes the gas components to be independent and not interacting, therefore neglecting Penning effects.

$$N_{\text{mixture}} = E \sum_i \frac{w_i}{W_i} \tag{1.26}$$

1.7 Diffusion, recombination and drift of charges

The electrons and the positive ions liberated in ionization processes quickly thermalize in the gas, assuming a random motion. A point-like collection of free charges will then diffuse by multiple collisions with a Gaussian density distribution whose width grows over time. The number of charges, $\mathrm{d}N/\mathrm{d}x$, at a distance x from the original ionization location after a time t is given by Eq. (1.27), where D is the diffusion coefficient.

$$\frac{\mathrm{d}N}{\mathrm{d}x} = \frac{N}{\sqrt{4\pi Dt}} \exp\left(-\frac{x^2}{4Dt}\right) \tag{1.27}$$

Values of the diffusion coefficient for ions at standard temperature and pressure range from some mm^2/s to a few tens of mm^2/s, depending on the gas molecule. Typical values for electrons are three orders of magnitude larger.

Diffusing electrons may attach to gas molecules, creating negative ions. The attachment coefficient is introduced to describe the process, giving the number of attachment events per unit length. Moreover, both electrons and negative ions can interact with positive ions, recombining and mutually neutralizing their charges, that are lost for detection purposes. The recombination rate of either charged species is proportional to the charge density, n, through the recombination coefficient, R, as given in Eq. (1.28). R

is much larger for negative ions than for electrons so that, if an electronegative component is present in the gas mixture, almost all the recombination will happen between ions.

$$\frac{\mathrm{d}n^+}{\mathrm{d}t} = \frac{\mathrm{d}n^-}{\mathrm{d}t} = -Rn^+n^- \tag{1.28}$$

Recombination processes can be distinguished into two types. Initial recombination happens in the close proximity of the ionization site. Following Eq. (1.28), this effect is more pronounced for highly ionizing particles, such as alpha particles and nuclear fragments, than for electrons. Moreover, initial recombination does not depend on the particle rate. On the other hand, volume recombination happens between charges that have already left their production site and therefore increases with the particle rate.

In presence of an electric field, positive and negative charge carriers will separate and drift in opposite directions. The carrier response to the applied electric field is parametrized by the mobility, μ, defined as the ratio between the mean carrier velocity, v_d, and the field strength, E. The mobility of both positive and negative ions does not depend on the field strength and is inversely proportional to the gas pressure. The Einstein-Smoluchowski relation establishes a connection between the mobility and the diffusion coefficient, D, e being the electron charge, k_B the Boltzmann constant and T the absolute temperature:

$$\mu = \frac{v_d}{E} = \frac{eD}{k_B T} \tag{1.29}$$

Conversely, the mobility of an electron depends on its kinetic energy and therefore on the applied electric field. The electron mobility exhibits maxima and minima due to the Ramsauer-Townsend effect, a quantum-mechanical interference phenomenon that comes into play when the electron wavelength, $\lambda = h/p$, approaches molecular dimensions. Appendix A contains plots of the electron drift velocity as a function of the electric field strength for the gas mixtures used in this thesis.

In the presence of an electric field, the diffusion of electrons is not isotropic any more. Equation (1.27) remains valid if the longitudinal and transverse diffusion coefficients are introduced to describe the diffusion processes along the field lines and in the orthogonal direction respectively. Appendix B lists the longitudinal and transverse Gaussian spreads, $\sigma = \sqrt{2Dt}$, of an electron cloud as a function of the electric field strength for the gas mixtures of interest in this research work.

When the drift volume is immersed into a magnetic field, the charges will follow more complicated paths due to the Lorentz force. The angle between the mean drift velocity and the electric field takes the name of Lorentz angle. In case the magnetic field is parallel to the electric field, as in time projection chambers, the Lorentz force suppresses the transverse diffusion, thus allowing for good spatial resolution even over drift distances of several metres.

1.8 Multiplication of charges

The charge carriers liberated in ionization processes undergo many collisions with the neutral gas molecules during their diffusion and drift. Positive and negative ions gain little energy between collisions due to their low mobility. On the other hand, free electrons are easily accelerated by the applied electric field and may acquire significant kinetic energy. If this energy is greater than the ionization potential of a gas molecule, it is possible for an additional electron-ion pair to be created in the collision. The electron liberated in the secondary ionization will also be accelerated and have the possibility to cause further ionization, giving rise to a multiplication process known as Townsend avalanche. The value of the electric field that allows the onset of multiplication is of the order of 10^6 V/m in the most commonly used gases at atmospheric pressure.

The phenomenon of charge multiplication is described by the first Townsend coefficient, α, defined as the number of ionization events per unit length. The first Townsend coefficient is a function of the applied electric field strength, E. It is zero below the multiplication threshold, while above threshold it is well parametrized by Eq. (1.30), where P is the absolute pressure and a, b are positive constants to be experimentally determined [14]. The first Townsend coefficient, as well as the attachment coefficient (cf. Section 1.7) for the gas mixtures used in this thesis are reported in Appendix C as a function of the electric field strength.

$$\alpha = aP \exp\left(-\frac{bP}{E}\right) \tag{1.30}$$

Given a radiation interaction that produces N_0 initial electron-ion pairs, the avalanche will proceed as illustrated in Eq. (1.31). The gain of the charge amplification structure is then defined as $G = N/N_0$.

$$\frac{\mathrm{d}N}{\mathrm{d}x} = \alpha N \qquad N(x) = N_0 \exp \int \alpha \mathrm{d}x \tag{1.31}$$

Just above the multiplication threshold, the gas gain is independent of the initial charge. This implies that the detector output signal is proportional to the energy deposited by the incoming radiation. An increment of the electric field results in a higher gas gain, but the aforementioned proportionality is maintained. The region of electric fields in which the detector exhibits this behaviour defines the proportional mode of operation. Gas amplifications up to 10^6 are possible in proportional mode, even though typical gas amplifications are rather in the range 10^4 to 10^5. As the field is further increased, space-charge effects due to the slowly drifting ions appear, locally decreasing the multiplication field and thus partly destroying the proportionality. At very high fields, the proportionality is completely lost and the detector always generates the same output signal, keeping no memory of the deposited energy. The latter behaviour is known as Geiger-Müller mode of operation. All the tests performed in this research work are carried out in proportional mode.

The collisions of accelerated electrons with neutral gas molecules can lead not only to ionizations, but also to excitations. The development of a Townsend avalanche is therefore accompanied by the emission of de-excitation photons in the visible and ultraviolet spectrum. These photons can cause additional ionization elsewhere in the gas through the photoelectric effect on less tightly bound shells or can produce electrons through interactions with the electrodes or the detector walls. This process is described by the second Townsend coefficient, γ, that gives the probability of creating a photoelectron per electron in the avalanche. When radiative effects are taken into account, the gain G_γ becomes:

$$G_\gamma = G \sum_{i=0}^{\infty} (\gamma G)^i = \frac{G}{1 - \gamma G} \tag{1.32}$$

As the gain increases and $\gamma G \to 1$, saturation effects occur and the detector output signal becomes independent of the initial ionization. Even during proportional mode operation, de-excitation photons from avalanches can lead to after-pulses and a worsening of the space resolution. These undesirable phenomena can be limited by introducing polyatomic additives in the gas mixture. The additives, known as quenchers, have a large cross section for photon absorption due to their many rotational and vibrational modes and dissipate energy without leading to further ionization, thus quenching the photon effects.

If the total charge in a single avalanche becomes too large, the electric field in the front and behind it gets highly boosted. This induces the fast growth of a streamer that can develop into a discharge. The threshold value, of the order of 10^7 to 10^8 electron-ion pairs, is known as Raether's limit and is a constant among gas detectors [15].

1.9 Induction of signal

Moving charges, both electrons and ions, induce currents on all the electrodes present in the detector. The time-dependent current, $I_i(t)$, induced on the i^{th} electrode by a charge q moving at speed $v(t)$ along a trajectory $\boldsymbol{x}(t)$ is given by Ramo's theorem, see Eq. (1.33) [16]. Here $E_i[\boldsymbol{x}(t)]$ is the magnitude of the electric field in $\boldsymbol{x}(t)$ when q is removed, electrode i is set at a potential V_i and all the other electrodes are grounded.

$$I_i(t) = -\frac{qE_i[\boldsymbol{x}(t)]\,v(t)}{V_i} \tag{1.33}$$

Equation (1.33) is exact if all the electrodes are grounded. In case some of them are connected to ground through an impedance network, a correction term must be included to describe the additional couplings.

CHAPTER 2

Micropattern gas detectors: properties, manufacturing and testing

For several decades, gas detectors exploited thin anode wires arranged in convenient configurations to generate the high electric field required for the onset of charge multiplication. The strength of the electric field around a wire is inversely proportional to the distance from its centre. This offers a clear advantage over the parallel-plate geometry, as a much lower voltage is needed to achieve a sufficiently high field region in the proximity of the wires. In wire chambers, the avalanche develops only a few tens of microns from the wire surface. Since the electrons are quickly collected, the signal is entirely induced by the positive ions drifting all the way back to the cathode.

Nowadays wire chambers are widespread detectors. Nevertheless, they have some limitations that restrict their field of applicability. The long ion collection time creates space-charge effects at high particle rates that decrease the effective field around the anode wires, consequently reducing the gas gain and thus limiting the detector rate capability. Micropattern gas detectors (MPGDs) are a class of devices that exploit microscopic structures to obtain charge amplification together with fast ion collection, therefore offering improved performance at high particle rates. Typical figures include a space resolution of a few tens of microns, a time resolution of about 10 ns and a rate capability of several hundred kHz/cm^2.

This chapter gives an overview of the most classical micropattern gas detectors, their properties, their manufacturing techniques and their applications. Section 2.1 introduces the first MPGD: the microstrip gas chamber (MSGC). Section 2.2 focuses on the gas electron multiplier (GEM), detailing the traditional production method, explaining the principle of operation and providing a survey of some applications. The micro-mesh gaseous structure (Micromegas) is presented in Section 2.3, with the subsections expanding on the developments of the Micromegas technology and on a few applications. Finally, Section 2.4 describes the tools and the experimental procedures used in the testing of the MPGD components and the improvements introduced as a part of this research work.

2.1 Microstrip gas chamber

The first type of micropattern gas detector to gain popularity was the microstrip gas chamber, introduced by Anton Oed in 1988 [17]. It is based on the same operating principle as a wire chamber and indeed it resembles a miniaturized multiwire proportional chamber (MWPC). It is constituted of an insulating substrate, of either ceramic or plastic material, on which thin conductive strips act as alternating anodes

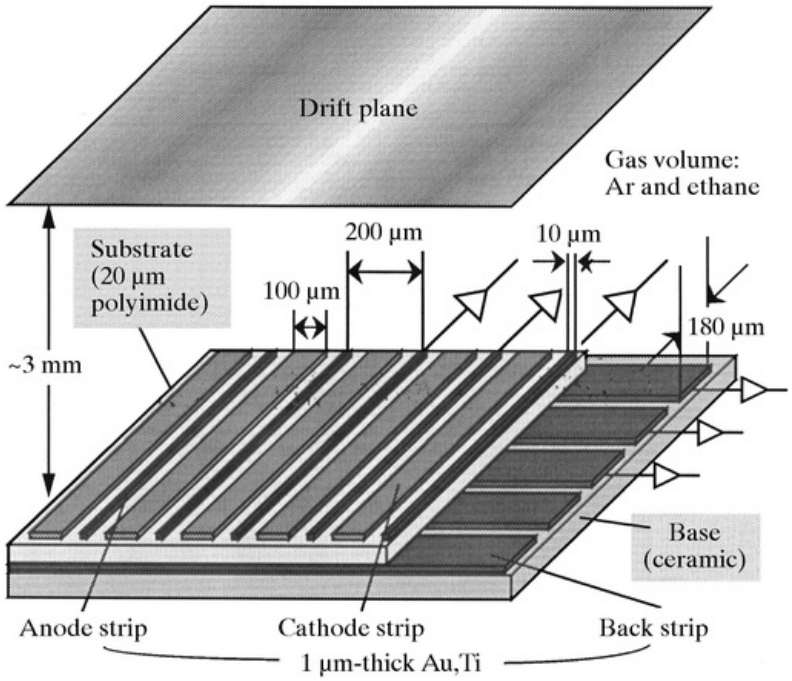

Figure 2.1: Schematic view of a microstrip gas chamber [18].

and cathodes. The exploitation of photolithographic techniques from microelectronics industry allows these elements to be manufactured with a strip pitch as small as 100 μm, more than an order of magnitude lower than the distance between wires in a MWPC. A drift electrode, located a few mm to a few cm from this structure and maintained at negative potential, creates a uniform electric field that defines the detector active volume. A schematic view of a microstrip gas chamber is shown in Fig. 2.1.

Ionization electrons liberated in the active volume are guided by the drift field towards the anode strips. The width of these strips is kept quite narrow, typically around 10 μm, so that the resulting electric field is comparable to the one occurring around a wire. Townsend multiplication is then initiated in the immediate proximity of the anode surface, where nearly all the charge is created. As in conventional proportional counters, electrons are promptly collected and most of the signal is induced by the positive ions formed in the avalanche and drifting away from the anode. Bi-dimensional hit localization can be achieved by adding orthogonal strips on the back side of the substrate, that will pick up signals thanks to capacitive coupling.

An advantage of microstrip gas chambers over multiwire proportional counters lies in the much finer anode pitch, that leads to improved space resolution. Moreover, most of the positive ions from multiplication processes do not travel all the way back to the drift electrode, but are rather quickly drawn to the nearby cathode strips. The fast removal of the corresponding positive space-charge results in a rate capability that is boosted by two orders of magnitude with respect to multiwire proportional chambers, as illustrated in Fig. 2.2.

Although the majority of the charge released in avalanches is collected on the electrodes, a fraction of it ends up on the exposed substrate between anodes and cathodes. Given the insulating nature of the material, these charges cannot easily be removed and tend to build up. The consequent local distortion of the multiplication field, that varies over time as the irradiation continues, decreases the time stability of the gain. This phenomenon is known as charging-up effect and it is common to several types of micropattern gas detectors. In the case of microstrip gas chambers, the problem can be solved by

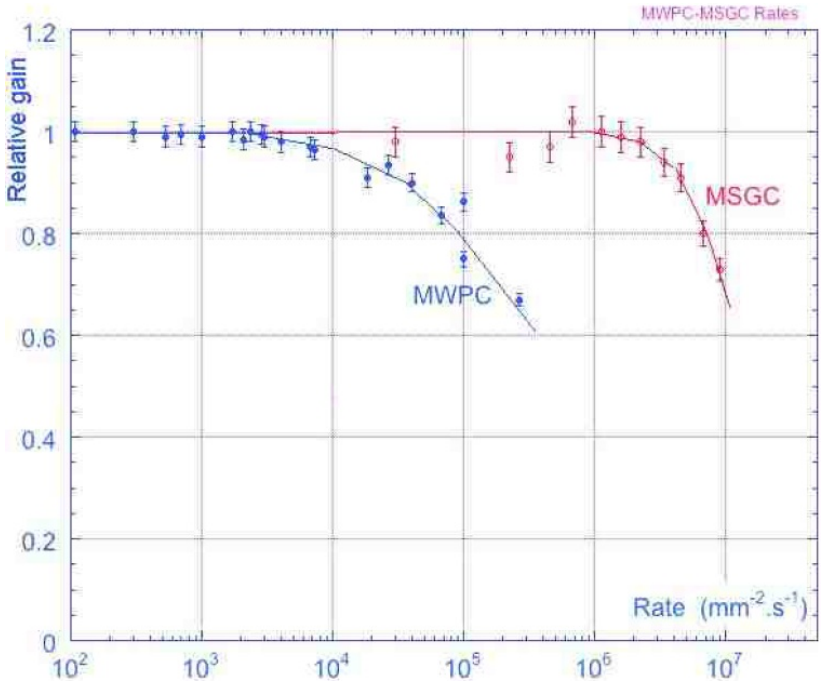

Figure 2.2: Rate capability of MWPCs and MSGCs [19].

reducing the substrate resistivity, either by using slightly conductive glass or by coating the substrate with other materials.

Detector aging is the slow degradation of performance following irradiation and it is a common feature of gas detectors. Figure 2.3 (left) is a close view of a microstrip gas chamber after long-term irradiation. The electrodes appear to be coated with a transparent film and the cathode edges are damaged by micro-discharges. This is understood to be the consequence of polymer formation in avalanches, that stick to the electrodes and to the substrate inducing discharges. A careful selection of the construction materials and of the operating gas mixture can help to reduce the aging and to increase the lifetime of the detector.

Another important issue is the one of sparks, induced either by highly ionizing particles or by high particle rates. Microstrip gas chambers suffer a lot from discharges due to the small spacing between anodes and cathodes. If sufficiently severe, sparks can fatally damage the fragile anode strips, as shown in Fig. 2.3 (right). Although several solutions to this problem have been developed, the MSGC technology was finally abandoned.

2.2 Gas electron multiplier

The gas electron multiplier is a micropattern electron-amplification structure invented by Fabio Sauli in 1997 [20]. It comprises an insulating polymer foil some tens of microns thick, clad on both sides with a few microns of metal. This stack is pierced with a dense regular matrix of holes, arranged either in a square or in a hexagonally packed configuration. Depending on the sample, the hole diameter can range from 50 to 100 µm, while the hole pitch can vary from 100 to 200 µm. The base material, consisting of the metal-insulator-metal sandwich, can be patterned using different techniques, from chemical etching to laser etching.

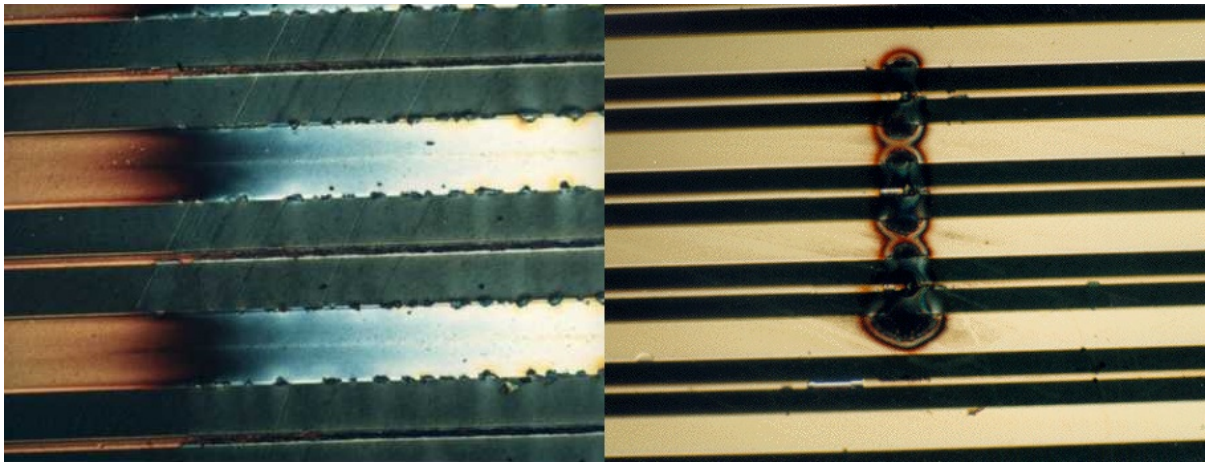

Figure 2.3: Aging and sparks in microstrip gas chambers.

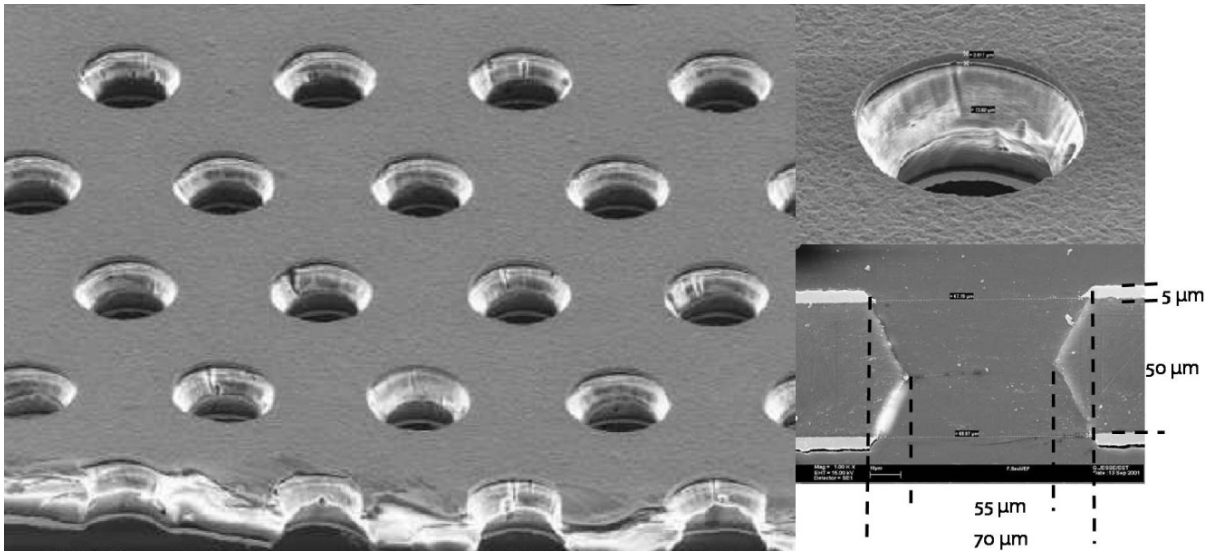

Figure 2.4: Scanning electron microscope pictures of a GEM.

Figure 2.4 (left) is a scanning electron microscope picture of a modern standard GEM. This GEM shares a number of features with the specimens tested during the research work presented in this thesis. They all are produced exploiting photolithographic and chemical wet etching techniques commonly used in the printed circuit board (PCB) industry. The base material is a 50 µm thick polyimide foil, namely Kapton, covered on each side with 5 µm of copper. The holes are organized in a hexagonally packed geometry, with a pitch of 140 µm.

The CERN standard manufacturing process, developed by the CERN TS-DEM-PMT group, makes use of a base material that is delivered in rolls about half a metre wide. The actual width varies slightly among suppliers, the widest currently available on the market being 24 inches or 61 cm. A 15 µm thick photoresist dry film gets laminated on each side of the base material. Negative-tone photoresist is used, meaning that light exposure modifies the photoresist polymeric structure making it insoluble to the developer solution, while the unexposed portion is dissolved by the developer. The lamination is performed with the help of a machine like the one shown in Fig. 2.5 (left). The laminator features two

Figure 2.5: Photoresist laminator and developer.

hot rolls heated up at 100–110 °C, that fix the photoresist by applying pressure. At this stage, attention has to be paid to avoid air trapping between the photoresist and the base material, that would lead to an inaccurate pattern definition. The hole pattern is transferred from photolithographic masks to the photoresist by exposure to UV light. Given the choice of the photoresist tone, negative masks have to be used, consisting in transparent films with black spots corresponding to the hole positions. Both photoresist layers have to be patterned, and careful mask alignment is needed to ensure good pattern matching. The required alignment accuracy depends on the hole diameter, and it should be kept below 10 µm for a good detector quality. The GEM substrate is cured in an oven at about 100 °C for a few minutes to guarantee optimal photoresist adhesion and then moved to the photoresist development, that takes place in a machine like the one in Fig. 2.5 (right). Here a sodium carbonate (Na_2CO_3) rinsing removes the unexposed photoresist, leaving naked copper where holes have to be created. The copper etching is a three-step process, carried out in a dedicated machine, see Fig. 2.6 (left). The GEM is first sprayed with ferric chloride ($FeCl_3$) and rinsed with hydrochloric acid (HCl) to open holes in the copper and then dried with air jets before it exits the machine. At this point, the thin chromium layer used as adhesive between Kapton and copper has to be cleared away from the holes to access the underlying substrate. This is done by dipping the GEM in sodium permanganate ($NaMnO_4$) for 30 s, rinsing with water and bathing the GEM into a neutralizing solution of hydroxylammonium sulfate ($(NH_3OH)_2\ SO_4$), hydrogen peroxide (H_2O_2) and sulfuric acid (H_2SO_4) for 30 s, see Fig. 2.6 (right). After stripping the photoresist with alcohol, the GEM is ready for polyimide etching. Since the Kapton is dug out from both sides, the holes assume a characteristic biconical shape, as it can be seen from Fig. 2.4 (right). The holes of CERN standard GEMs feature an outer diameter of 70 µm and an inner diameter of 55 µm.

The application of a difference of potential between the two metal layers of a GEM gives rise to a dipole electric field. Ionization electrons liberated in the conversion gap are guided towards the GEM by the drift field and focused into the GEM holes by the dipole field. When the voltage difference across the foil is increased above a few hundred volts, the field in the holes becomes strong enough for the onset of Townsend avalanches. Figure 2.7 (left) is a simulation of the resulting electric field, with equipotential lines in green and field lines in yellow. The geometrical parameters are tuned to model a CERN standard GEM. The drift field is 1 kV/cm, the extraction field (the field below the GEM) is 3 kV/cm and the potential difference across the GEM is 400 V. Figure 2.7 (right) illustrates how the electric field intensity changes along the axis of a hole. A complete description of the simulation tools and techniques used in this thesis will be given in Section 3.3.

Figure 2.6: Copper-etching machine and baths for chromium removal.

Figure 2.8 displays two simulated avalanches originated from a single electron. Although the avalanche develops along the whole depth of the hole, most of the charge is generated in the lower part. A fraction of this charge is lost on the polyimide and on the bottom electrode, as it can be seen in the simulations. Furthermore, thermal diffusion can lead conversion electrons to hit the GEM top electrode, reducing the charge that reaches the high-field region. Therefore, when quoting the gas gain of a GEM structure, one usually refers to the effective total gain, that is the convolution of the intrinsic gain with the electron losses on the GEM materials. The effective gain depends not only on the voltage across the GEM, but also on the fields above and below it. Generally speaking, a lower field above the GEM results in a higher field gradient at the entrance of the holes that helps focusing the electrons, therefore reducing the losses on the top electrode and increasing the effective gain. On the other hand, a higher field below the GEM is more effective in extracting charges, limiting losses on the bottom electrode. Experiments show that the effective gain of a single GEM foil can be as high as 10^3, sufficient to detect minimum ionizing particles (MIPs) with a conversion gap a few millimetres thick.

Thanks to the field configuration, most of the positive ions generated in the multiplication processes are guided to the GEM top electrode and collected there. This reduces the space-charge in the conversion gap, making GEM detectors capable of coping with rates as high as 1 MHz/cm^2 [21].

Since a GEM is only a charge amplification device which does not feature any readout structure patterned on it, it leaves complete freedom in the choice of the readout geometry, which can be optimized according to the application. The anode may assume the form of one-dimensional strips or allow for bi-dimensional hit reconstruction with cartesian strips, small-angle-crossing strips, strips on pads, polar coordinates, pads and three-dimensional readout, just to mention a few possibilities. Figure 2.9 presents some of these examples.

The fast collection of positive ions, combined with the decoupling of the readout from the amplification stage, has a strong impact on the signal formation. Contrary to MWPCs and MSGCs, where the signal is almost entirely induced by the ions, in GEM detectors the signal is due to the electrons moving in the induction gap, the volume between the GEM and the anode.

The separation of the charge multiplication from the induction stage also has the advantage of reducing the effect of sparks on the readout electronics. A discharge will cause a short between the two electrodes of the GEM foil, but in general will not directly affect the readout.

GEMs can easily be cascaded to obtain the required gas gain while operating each amplification plane at a lower voltage, with the effect of decreasing the spark probability. Figure 2.10 shows the total

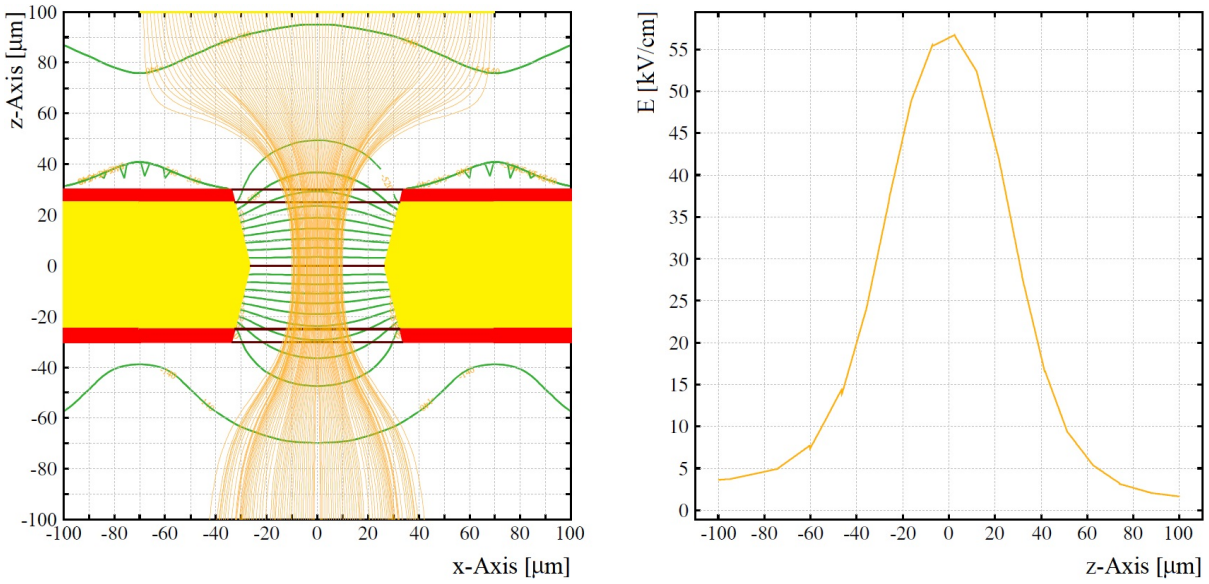

Figure 2.7: Simulated electric field in a GEM. Left frame: equipotential lines (in green) and field lines (in yellow) on the axial plane of a CERN standard GEM. Right frame: corresponding electric field strength along the axis.

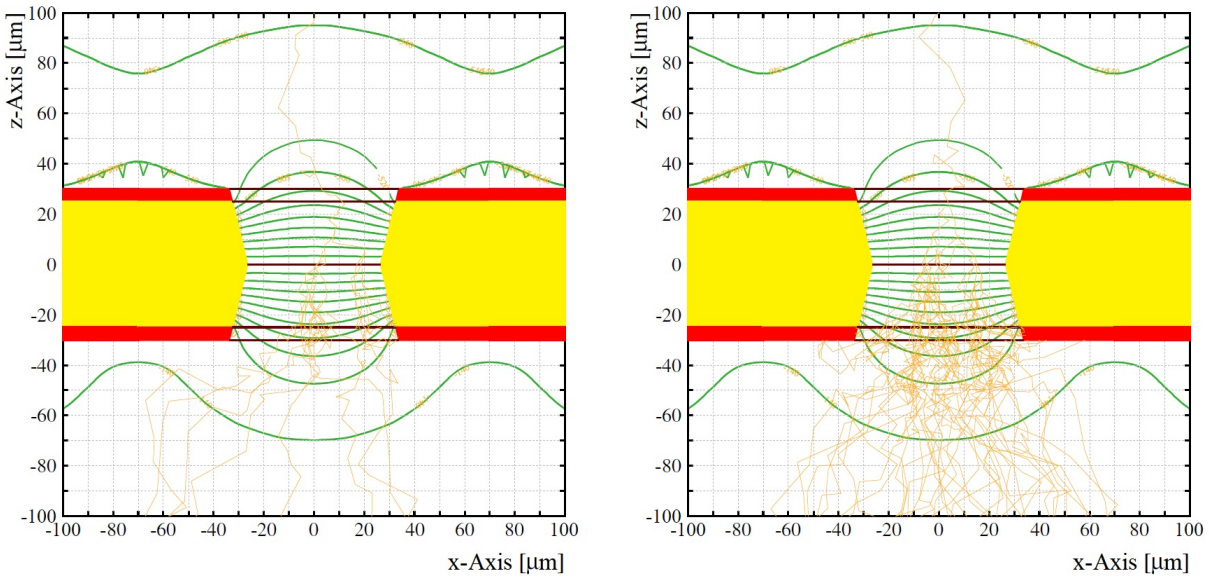

Figure 2.8: Simulated electron avalanches in a GEM.

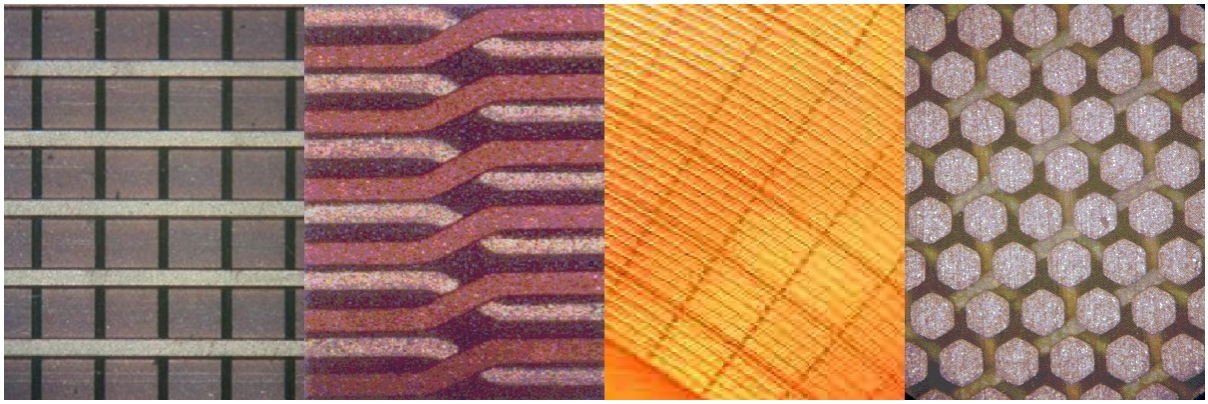

Figure 2.9: Cartesian, small-angle-crossing, polar and three-dimensional readout.

effective gain (solid curves, to be read on the left axis) and the discharge probability (dashed curves, to be read on the right axis) as a function of the potential applied to each layer of a single, double and triple-GEM stack [22]. All measurements are performed in an argon-based gas mixture with 30% carbon dioxide (CO_2) added for quenching purposes. The drift field E_D is set to 2 kV/cm, while the transfer field E_T (the field between two cascaded GEMs) and the induction field E_I are fixed to 3.5 kV/cm. Gains are measured exposing the detectors to soft X-rays, while spark probabilities are determined using alpha particles, as described in Section 2.4.4 and 2.4.6.

Due to its properties, the triple GEM has become the standard configuration for high-rate applications. The research work carried out in the development of the triple-GEM detectors for the COMPASS experiment at CERN has shown that the gain to discharge probability ratio can be further boosted by operating the first stage at about 10% higher voltage and the last stage at about 10% lower voltage with respect to the second GEM [23].

The high-voltage distribution scheme can be designed to contribute to the quenching of discharges and reduce their probability of propagating from an amplification stage to another. The approach developed for COMPASS and become standard practice foresees the introduction of a resistor on the line powering the top electrode of each GEM. Such a component, which takes the name of safety or protection resistor, is usually located in close proximity to the GEM foil and has a typical resistivity in the range 1 to 10 MΩ. In case of a spark, the resistor limits the current that recharges the GEM capacitance, thus quenching the gas discharge. The application of the resistor to the upper side only leads to a voltage drop of the top electrode, while leaving the bottom one at the same potential. The electric field above the GEM therefore increases, while the field below it remains the same. This makes discharge propagation unlikely and reduces even further the probability of a spark reaching the readout electronics.

An additional protection mechanism, that is often combined with the ones above, goes in the direction of limiting the energy liberated in a spark. When a difference of potential is applied between its electrodes, a GEM stores electrostatic energy like a planar capacitor. Given the small thickness of the insulator ($d = 50\,\mu m$) and its high relative electric permittivity ($\epsilon_r = 3.4$), the capacitance of a GEM foil and therefore the electrostatic energy stored in it can be rather high with respect to other micropattern structures. The top electrode is often divided into sectors of less than 100 cm^2, which corresponds to a maximum capacitance of 6 nF or an energy of 3 mJ/kV^2 per sector. Each sector is powered through a separate safety resistor so that, in case of a gas discharge, only the energy stored in the involved sector is released. Low-energy sparks have a reduced probability to damage the GEM foil, while low-capacitance sectors result in a faster voltage recovery, with a time constant $\tau = RC = 60$ ms for a 100 cm^2 sector

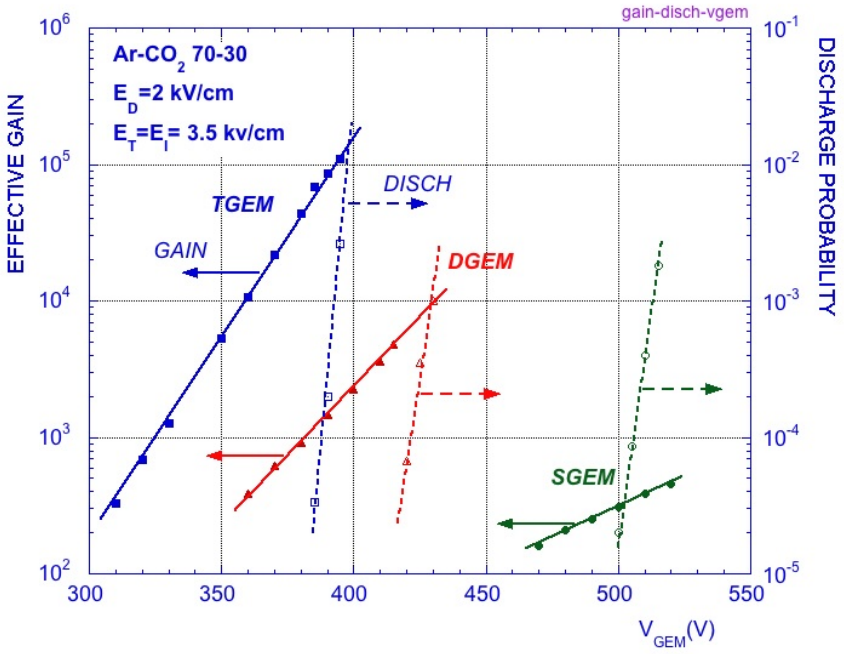

Figure 2.10: Gain and discharge probability of a single, double and triple-GEM stack [22].

powered though a 10 MΩ safety resistor. Moreover, a small clearance of 100 µm between neighboring sectors has been shown to be enough to prevent inter-sector discharge propagation, allowing for reduced dead area following a spark.

A key operation in the construction of a GEM detector is the mechanical positioning of the foils. Since the effective gain depends on the field intensity above and below the GEM, it follows that a good gain uniformity requires the absence of wrinkles and a precise definition of the gap thickness. This is achieved by stretching and framing the foils. Nowadays, there are two possible approaches: thermal stretching and mechanical stretching.

Thermal stretching is performed by firmly attaching the unstretched GEM to a rigid frame made of a material with high linear thermal expansion coefficient, α_L. Figure 2.11 (left) shows a foil clamped to a Plexiglas frame using screws located all around the edges. Plexiglas is often chosen for this purpose given its high $\alpha_L = 80\,\mathrm{ppm/K}$. The assembly is heated up to 45 °C and the stretched GEM is glued to a fiberglass-reinforced epoxy laminate frame (FR4), as illustrated in Fig. 2.11 (centre). The heating and glue curing usually take place in a clean-room oven. An alternative method, recently developed at Florida Institute of Technology (FIT), exploits an array of infrared light bulbs to provide the required heat. A temperature sensor gives feedback to a control unit that limits the current of the light bulbs' power supply, allowing for the maintenance of a stable temperature. This system promises to be a cost-effective alternative to the expensive clean-room ovens. Upon cooling down to room temperature, the foil shrinks with the FR4 frame glued on it, whose α_L is as low as 15 ppm/K. At this point the Plexiglas external frame is removed and the GEM base material exceeding the FR4 frame is cut away. The strain on the framed foil is determined by the difference between the linear thermal expansion coefficient of the two frames and by the temperature excursion during the stretching procedure. Assuming $\Delta T = 25\,\mathrm{K}$, one obtains a strain of 0.16%. Although this is usually sufficient for small-area detectors, when the linear dimensions exceed 10 cm it is common practice to add internal spacers that help keeping the distance between GEMs, at the cost of a decreased local efficiency in particle detection.

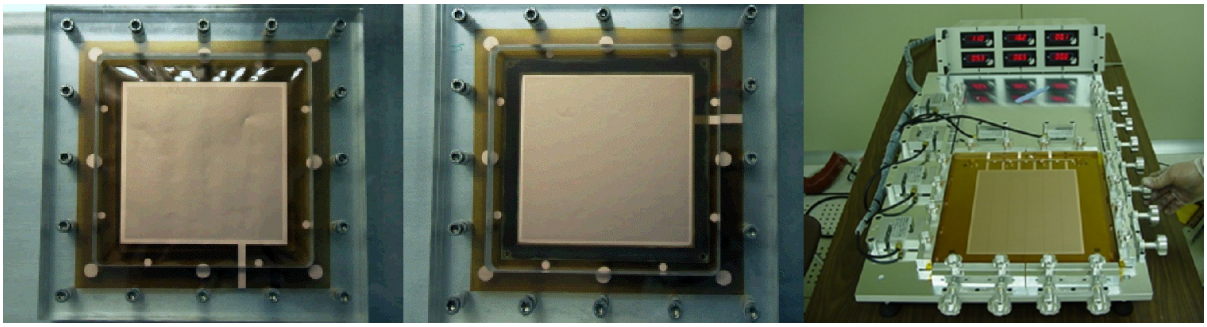

Figure 2.11: Thermal and mechanical stretching of GEMs.

Mechanical stretching was developed by the Frascati INFN group in Italy. It is done on jigs specifically designed to match the size of the GEM foil and featuring jaws to which the GEM is clamped all around the edges. In each pair of opposing jaws, one is fixed, while the other can be moved out to stretch the foil. Sensors located on the fixed parts measure the applied tension, so that the force can be uniformly distributed. Figure 2.11 (right) is a picture of the workbench used to stretch the GEMs for the LHCb detector at CERN. The displays above the jigging bench show the tension measured by the force gauges. Mechanical stretching can generate a strain on the foil four times higher than the one commonly achieved with thermal stretching. Because of this, detectors based on mechanically stretched GEMs usually do not require spacer elements in the active area. This is the case of the LHCb detectors, where the efficiency had to be kept high in order to allow for triggering capabilities.

During the final detector assembly, the stack made up of framed GEMs, readout board and drift electrode is commonly backed up on both sides with stiff panels. The usual choice is a 3 mm thick Nomex honeycomb clad on both sides with 65 µm prepreg (composite fibers impregnated with uncured epoxy) and internally reinforced with a 100 µm thick FR4 layer. This solution presents a good stiffness-to-weight ratio and is electrically insulating.

GEM detectors have been successfully applied in many different fields. A few examples from high-energy physics will follow, without the intent of being exhaustive, but rather to illustrate how the GEM technology can be adapted to different experimental needs.

2.2.1 HERA-B

The first use of GEMs was in the HERA-B experiment at the HERA storage ring at DESY [24]. The HERA-B inner tracking system covered the distance between 6 and 30 cm around the beam pipe, corresponding to polar angles between 10 and 100 mrad. It consisted of 10 stations placed along the beam pipe, some of which were located in a magnetic field $B \simeq 0.85\,\mathrm{T}$. Each station comprised three stereo-oriented layers divided into four independent L-shaped detectors around the beam pipe.

The original proposal based on microstrip gas chambers was discarded because inadequate to the HERA-B environment. In fact, the highly ionizing particles created in the interaction of the HERA proton beam with the wire target of the experiment would have induced a high rate of discharges in the MSGCs, leading to a rapid degradation of the detectors. GEMs were then introduced as preamplifiers above the MSGCs, to split the required gas gain between two stages and reduce the spark probability.

The GEM base material was a 50 µm thick Kapton foil with a 7 µm thick copper cladding on each side. The holes had an outer diameter of 90 µm, an inner diameter of 55 µm and were arranged in a hexagonally packed configuration with a pitch of 140 µm. The 30 cm wide foil, shown in Fig. 2.12 (left) before stretching, was maintained at a distance of 2.8 mm from the MSGC by hollow G10 frames. The

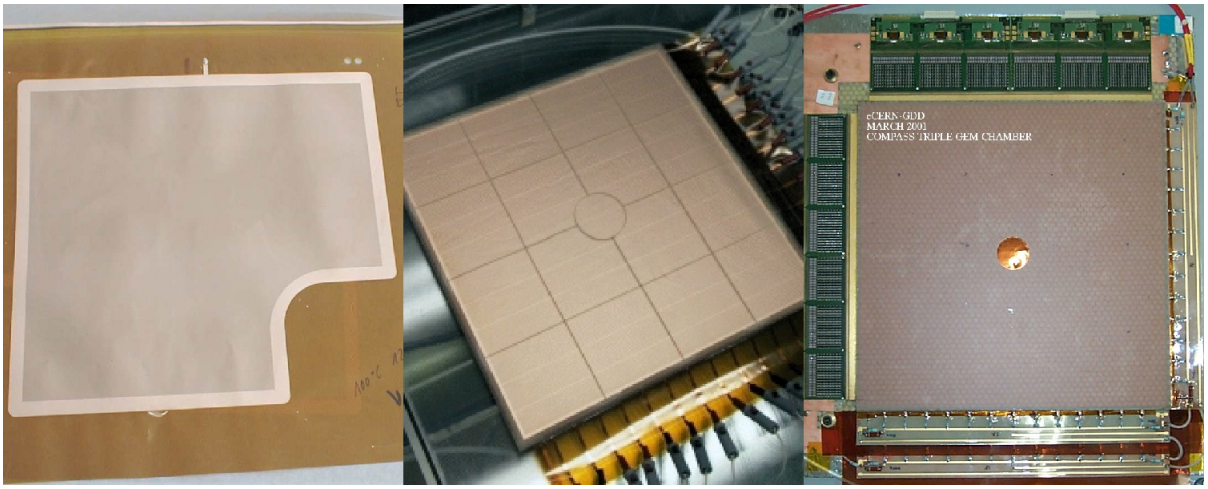

Figure 2.12: HERA-B and COMPASS GEMs.

chosen gas was an argon-based mixture containing 30% carbon dioxide as a quencher. The GEM was operated at a voltage such to provide an effective gain in the range 15 to 50, while the transfer field between the GEM and the MSGC was kept below 6 kV/cm to prevent discharge propagation.

These hybrid detectors could cope with rates of up to 1 MHz/cm^2, reaching a space resolution better than 100 µm with an anode pitch of 300 µm and a single-layer MIP detection efficiency higher than 98%.

2.2.2 COMPASS

The first use of GEMs as detectors on their own is in the aforementioned COMPASS experiment at CERN [23]. The COMPASS small angle tracker, located downstream from the first magnet, is equipped with 20 triple-GEM chambers grouped in 10 stations. Within each pair, one chamber is rotated by 45° with respect to the other to resolve hit ambiguities.

The GEMs have an active area of 31×31 cm^2, with holes following the CERN standard geometry and layout. The top electrode of each foil is segmented into 12 sectors to reduce the capacitance and hence the energy released in case of sparks. The inter-sector distance of 200 µm is enough to prevent discharge propagation between adjacent sectors and at the same time sufficiently narrow to induce only a small perturbation in the detector response uniformity. An additional sector, having the shape of a circle of 50 mm in diameter, is located in the centre of the foil, where the beam and the corresponding halo cross the detector. In this region the particle rate can be such that the readout occupancy becomes too high. A remotely controlled switch can lower the voltage across the central sector of the last GEM by about 200 V, resulting in a complete insensitivity of the region to the beam.

The drift gap is 3 mm thick, while all the other gaps are 2 mm in thickness. The distance between layers is defined by the 7 mm wide fiberglass external frame, while a thin spacer grid made out of the same fiberglass material guarantees the gap uniformity in the active area. The internal spacing elements are 400 µm thick and follow the sector pattern where possible, in order to minimize the impact on efficiency. A groove in the external drift frame supplies and distributes the gas through narrow holes along two sides of the chamber, the gas exhaust consisting of a single larger hole on the readout plane in the opposite corner. Small notches on the internal spacers facilitate the gas circulation in the gaps.

Figure 2.12 (centre) shows the three foils of a chamber, already stretched, framed and stacked, undergoing a high-voltage test. The GEM sectoring and internal spacing elements are here visible.

In order for the COMPASS experiment to carry out its physics program, it is important to limit background-producing secondary interactions. This motivates the low material budget requirement for all of its subsystems, and especially for the ones close to the beam. To achieve a compromise between sufficient mechanical rigidity and low mass, the GEM detectors are supported by front and rear honeycomb plates with a hole cut out in the centre, to further decrease the material budget in the beam region. The honeycomb panels are 33×33 and $50 \times 50\,\mathrm{cm}^2$ in size, with a central hole of 35 and 50 mm in diameter, respectively.

The drift electrode is made out of a single-sided copper-clad Kapton foil, directly glued to the smaller honeycomb plate. The readout features bi-dimensional cartesian strips, deposited on two layers built on top of each other and separated by insulating ridges. The strip pitch is 400 μm in both directions, while the strip width is 80 μm on the top layer and 340 μm on the bottom layer, in order to obtain equal charge sharing between the two coordinates. The readout manufacturing starts from the same base material as a GEM, on which the larger strips are formed. The foil is glued face down onto a 120 μm thick fiberglass support and the second coordinate is patterned on the external copper. The narrower strips are then used as a mask for polyimide etching, leading to the formation of the Kapton ridges and the partial exposition of the lower strips.

Figure 2.12 (right) presents a completed COMPASS chamber, with the resistive divider for high-voltage distribution and the APV25-based readout cards mounted on it. When operated in Ar:CO_2 70:30, the detector has an overall MIP detection efficiency of about 96%, the inefficiencies being mainly due to section boundaries and internal spacers. The achieved space resolution is around 40 μm, while the time resolution is 15.2 ± 0.1 ns.

2.2.3 LHCb

The LHCb experiment at CERN makes use of 12 pairs of triple-GEM chambers in the innermost part of its first muon station [25]. Since these detectors are designed as triggering devices, great care is taken in optimizing their time resolution at high MIP detection efficiency. The required rate capability is about $500\,\mathrm{kHz/cm}^2$ for a peak luminosity of $5 \times 10^{32}/(\mathrm{cm}^2\,\mathrm{s})$, while the efficiency has to be greater than 96% per detector pair in a 20 ns time window.

The LHCb GEMs have the same hole pattern and geometry as the COMPASS foils, with an active area of $24 \times 20\,\mathrm{cm}^2$. The top electrode of each GEM is divided into 6 sectors about $240 \times 66\,\mathrm{mm}^2$ wide, separated by 200 μm. The thickness of the gaps is chosen to enhance the timing properties. The induction gap is slimmed down to 1 mm to achieve a steeper signal rise and thus decrease the time walk, while the thickness of the first transfer gap is reduced to 1 mm to minimize charge conversions that could lead to a premature signal. Both drift and readout electrodes are realized on 1 mm thick standard printed circuit boards and joined to 1 mm thick metalized fiberglass back panels used as a Faraday cage. Since space resolution is not a concern, large pads of $2.5 \times 1\,\mathrm{cm}^2$ are used, coupled to ASDQ-based front-end readout. Figure 2.13 (left) displays a completed chamber. The chosen gas is the ternary mixture Ar:CO_2:CF_4 45:15:40 which, thanks to a high drift velocity and a high primary cluster yield, assures low intrinsic time spread.

This careful design results in a time resolution of 4.5 ns with an efficiency of 90% per chamber, corresponding to 3.5 ns and 97% per detector pair, achieved at a gas gain of only 4×10^3.

2.2.4 TOTEM

TOTEM is one of the experiments on the Large Hadron Collider, and it is integrated into the very forward regions of the CMS experiment [21]. The TOTEM T2 telescopes are located at 13.5 m on both sides of

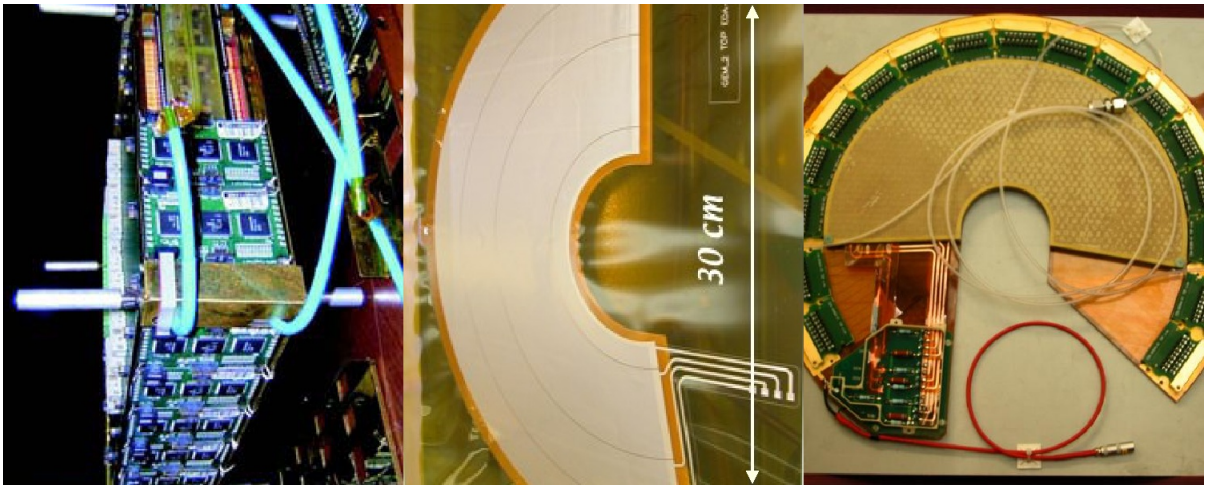

Figure 2.13: LHCb and TOTEM GEMs.

IP5 and cover the pseudorapidity range $5.3 \leq |\eta| \leq 6.5$. They have to be self-triggering devices and feature hit reconstruction capabilities for vertex finding to discriminate against beam-gas background events. A left-right symmetry gives better control over systematic effects. Each of the two telescopes is made up of 20 triple GEMs, grouped into 5 detector pairs on each side of the beam pipes.

The GEM foils are semicircular in shape, the active area covering an azimuthal angle of 192° and extending from 43 to 144 mm in radius from the beam axis, the hole geometry and layout being the same as the COMPASS and the LHCb foils. As shown in Fig. 2.13 (centre), the top electrode is segmented into four separately biased sectors, with the possibility of switching off the innermost region.

The gap configuration follows the COMPASS 3-2-2-2 mm standard, with a 2.4 kV/cm electric field in the drift volume and a 3.6 kV/cm field elsewhere. The induction and transfer gaps present two 500 µm thick internal spacers, asymmetrically machined to minimize dead areas when pairing detectors.

The drift electrode consists in a metalized Kapton foil directly glued to the 3 mm Nomex back panel. The readout board combines tracking and triggering functionalities by exploiting strips and pads in a double-layer structure similar to the COMPASS readout. 1560 triggering pads are arranged in 65 concentric sectors of 24 pads each, connected through metalized vias to radial strips on the back side and read out at the board edge. Tracking is performed thanks to 512 azimuthal strips having a width of 80 µm and a pitch of 400 µm. In order to reduce the occupancy, these strips are divided into two parts covering 96° each and read out at the sides.

The gas connectors are also installed on the readout board, while a system of grooves in the frames distributes the mixture to all of the gaps. The selected compound is Ar:CO_2 70:30, and the operating gain about 8×10^3.

Figure 2.13 (right) displays a completed chamber. The TOTEM GEMs reach a space resolution of about 70 µm and a time resolution of about 18 ns, while being able to cope with particle rates as high as 1 MHz/cm^2.

2.2.5 NA61/SHINE

Given the flexibility of the base material, GEMs can easily be bent into cylindrical shape. Figure 2.14 (left) is a cylindrical triple-GEM prototype having π azimuthal coverage, designed for a possible use in NA61/SHINE, an upgrade of the NA49 experiment at CERN [26].

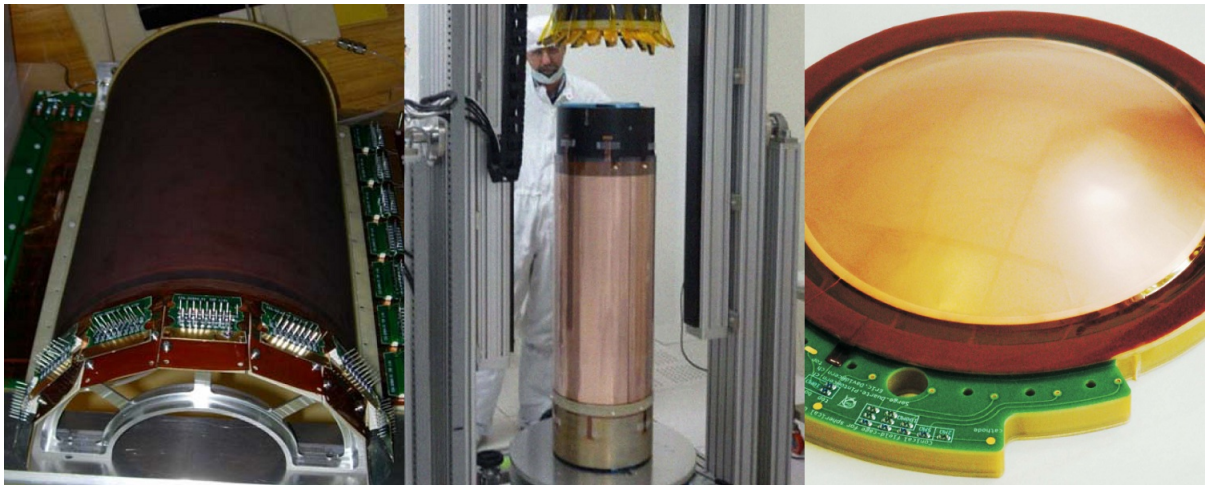

Figure 2.14: Cylindrical and spherical GEMs.

Three COMPASS foils $31 \times 31\,\mathrm{cm}^2$ wide are used, with curved spacers in the active area defining the gap thicknesses. The readout structure is also taken from COMPASS, and features cartesian strips with 400 µm pitch, deposited on two layers separated by 50 µm thick Kapton ridges. The APV25 hybrids are clearly visible in the picture, as well as the high-voltage distribution board.

2.2.6 KLOE-2

KLOE is an experimental apparatus located on DAFNE, the LNF e^+e^- collider operating at a centre-of-mass energy corresponding to the ϕ meson resonance. Following the DAFNE upgrade, with the application of the Crab-Waist scheme for luminosity increase, KLOE will see the insertion of a novel inner tracker into the already existing drift chamber. The new subsystem is immersed in a 0.52 T magnetic field and has to have a low material budget to minimize multiple scattering and thus be profitable for the reconstruction of low-momentum tracks.

The KLOE-2 inner tracker is made up of four cylindrical triple-GEM detectors with 2π azimuthal coverage [27]. The four concentric layers surround the interaction point, extending for 70 cm in the longitudinal direction and ranging from 13 to 23 cm in radius.

The large-area foils, the widest being $135 \times 70\,\mathrm{cm}^2$ in size, are obtained splicing together three GEMs and they required the development of a novel manufacturing technique. The new process, based on single-mask chemical wet etching with electrochemical active corrosion protection, will be described in detail in Chapter 3. The top electrode of each foil is divided into 40 separately biased sectors to reduce the capacitance.

The gap thickness is 3-2-2-2 mm, with no spacers in the active area, resulting in only 0.3% dead zones. The needed mechanical rigidity is provided by a composite shield enclosing each layer and made up of two 90 µm thick carbon fiber sheets spaced by a 3 mm Nomex honeycomb.

The anode is obtained from a 350 µm thick x-v bi-dimensional readout flexible circuit directly glued on the composite shield. The x-strips are axial to the cylinder and have a pitch of 650 µm. The v-strips, with the same pitch, form an angle of 40° with x and are obtained from parallelogram-shaped pads connected on the back side through metalized vias. The y-position is extracted by combining the x- and the v-information.

Figure 2.14 (centre) shows one of the final steps in the detector assembly, where the drift electrode and triple-GEM stack is inserted into the outer shield with the help of a dedicated machine.

The front-end readout is based on the GASTONE ASIC, specifically designed for the detector. The achieved space resolutions are 200 and 400 μm in the azimuthal and longitudinal directions, respectively.

2.2.7 Spherical GEMs

Gas detectors also find applications in X-ray and neutron diffractometry. If the electric field in the drift region is not parallel to the direction of the incoming radiation, the conversion depth uncertainty due to the limited absorption efficiency of gases will give rise to an error in the position reconstruction. Although different approaches to this problem exist, they all avoid the hurdle of creating a spherical conversion gap. Coupling a spherical GEM to a spherical entrance window creates a truly radial drift field, thus solving the parallax problem at the root [28–30].

Spherical GEMs can be manufactured starting from a standard planar foil with circular electrodes. The GEM is at first baked at 150 °C under vacuum for about 10 hours to make the polyimide outgas all the unbound molecules present in its structure. The foil is then clamped to a ring-and-plate structure and forced into the new shape on a spherical mold, in a process similar to thermoplastic heat forming. Forming takes place at a temperature between 350 and 400 °C and an absolute pressure lower than 10^{-3} mbar, in a heat cycle lasting about 24 hours. The procedure does not appear to degrade GEM benchmark figures such as the spark voltage in air and the leakage current per sector, measured to be higher than 600 V and about 2 nA, respectively. Visual inspection with an optical microscope reveals that holes stretch uniformly over the active area, with no visible elliptical deformations. The hole aspect ratio, defined as $depth/width$, is however expected to change and can be corrected for by modifying the hole pitch and width in the original foil.

Given the importance of a radial field in the conversion volume, the GEM is coupled to a conical field cage, made out of a standard rigid multilayer PCB, that helps shaping the drift field at the edge of the active area. Although the formed foil seems to be largely self-supporting, a curved spacer made by stereolithography adds some mechanical rigidity to the structure.

Figure 2.14 (right) shows the GEM, frame and field cage assembly. The prototype, coupled to a flat readout board, has been tested in Ar:CO_2 70:30 at 2 bar, achieving a gas gain of about 30.

The use of a planar readout generates a non-uniform extraction field, resulting in a variation of the effective gain and of the signal induction time over the active area. The design of a spherical flexible readout circuit, based on the recently developed through-hole ChemicalVia technology, can provide a solution and open the way to the production of the first completely spherical gas detector [31].

2.3 Micro-mesh gaseous structure

The micro-mesh gaseous structure is a micropattern gas detector invented by Ioannis Giomataris in 1996 [32]. It consists of a very asymmetrical two-stage parallel-plate avalanche chamber in which the anode gap is slimmed down to sub-millimetric thickness, as schematically shown in Fig. 2.15. The boundary between the two volumes is marked by a 3 μm thick nickel grid with 17 μm wide square openings every 25 μm, resulting in 46% optical transparency, see Fig. 2.16 (left). The micro-mesh is manufactured using electro-forming techniques, that ensure shaping with a precision better than 1 μm. The distance to the anode, between 75 and 230 μm, is maintained by quartz-fiber spacers with a pitch of 2 mm, that define the gap with 2% precision. The readout structure is patterned on a thin G10 layer, although a Kapton foil can be used in case material budget is a concern.

The ionization electrons liberated in the conversion gap, typically a few mm thick, are guided towards the mesh by the drift field, that has an intensity in the order of 1 kV/cm. Thanks to the high field gradient, the electrons are focused in the mesh openings and transferred to the amplification gap, where the field

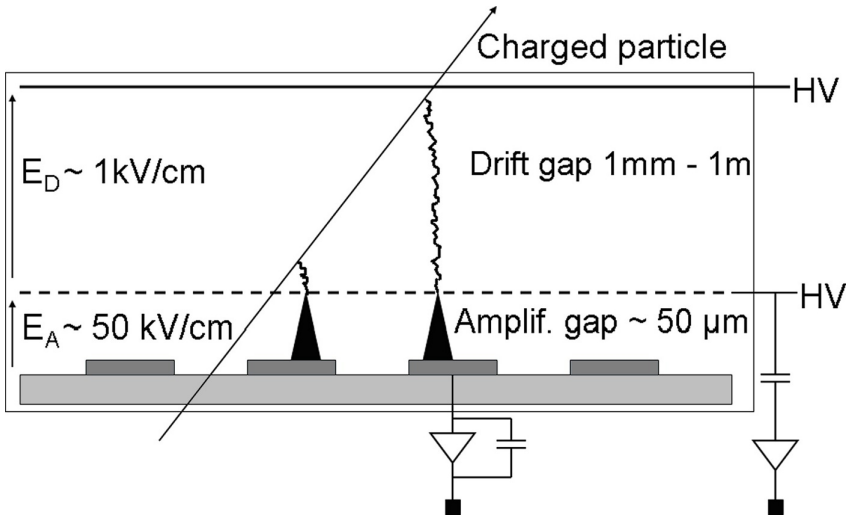

Figure 2.15: Schematic view of a Micromegas detector [33].

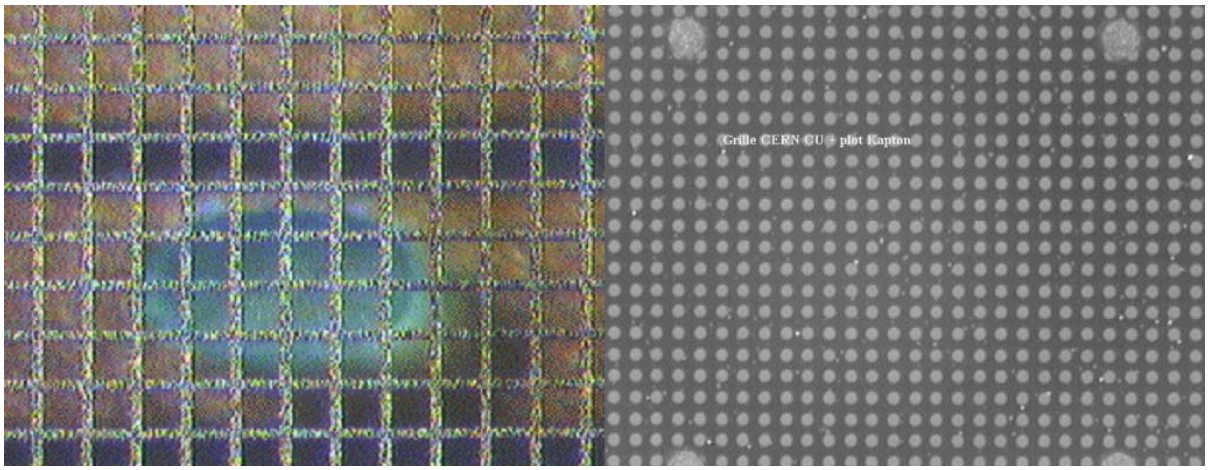

Figure 2.16: Left frame: microscope picture of an electro-formed mesh with pitch of 25 µm [34]. Right frame: microscope picture of a chemically etched mesh with hole pitch of 50 µm [35].

is about two orders of magnitude higher, enabling the onset of Townsend multiplication. The high field ratio between the amplification and drift regions also helps to collect the positive ions left behind by the avalanches on the mesh, quickly removing the corresponding space-charge and making Micromegas detectors capable of coping with high particle rates.

Since the signal induction takes place in the same amplification gap, both electrons and ions will contribute. A typical signal has a very sharp pulse with rise time in the ns range, followed by a tail about 100 ns long due to the positive ions drifting back towards the mesh.

The first tests, performed with a Micromegas having a 140 µm thick amplification gap in an Ar:CH_4 90:10 gas mixture, showed a maximum achievable gain in the order of 10^5 and an energy resolution of 14% full width at half maximum (FWHM) in response to 5.9 keV X-ray photons generated by a ^{55}Fe radioactive source.

High MIP detection efficiency can be achieved, as demonstrated in [36]. Here, $15 \times 15\,\text{cm}^2$ Micromegas detectors with strip pitch of 317.5 µm and inter-strip distance of 70 µm have been tested in the T9

PS beam line at CERN, using 10 GeV negative pions. The amplification gap, 100 μm thick, is defined by cylindrical pillars 150 μm in diameter, spaced with a pitch of 2 mm. The use of a gas mixture containing 90% argon and 10% dimethyl ether (DME, CH_3OCH_3), in combination with a 3 mm conversion gap, results in a wide efficiency plateau above 99%. Filling the detectors with a compound of 92% argon and 8% cyclohexane (C_6H_{12}) gives 99% efficiency with a 3 mm conversion gap and 96% efficiency when the drift volume is slimmed down to 1 mm.

The ultimate attainable space resolution is investigated in [37]. A Micromegas telescope, composed of two test chambers and two tracking chambers, is installed on the T9 PS beam line at CERN and irradiated with 10 GeV pions at 0° incidence angle. All of the four detectors feature an electro-formed nickel micro-mesh with $39\times39\,\mu m^2$ square openings every 50.8 μm, corresponding to 500 lines per inch (LPI). The conversion gap is 3 mm thick, while the amplification gap is 100 μm thick and backed up by a 1.6 mm epoxy substrate. The two tracking chambers have an active area of $14 \times 12\,cm^2$, 317.5 μm strip pitch and 70 μm inter-strip distance. The pillars supporting the micro-mesh are cylindrical in shape, with a diameter of 200 μm and a pitch of 2 mm. The two Micromegas under study, on the other hand, have an active area of $5 \times 4\,cm^2$, 100 μm strip pitch and 50 μm inter-strip distance. The pillars have an oval shape, 100 μm long and 50 μm large, to fit the strip width. They are located on every 6^{th} strip with 600 μm spacing, covering 17% of the strip or 3% of the total area. The detectors, read out via Gassiplex cards, show the best space resolution when filled with 80% CF_4 and 20% isobutane (iC_4H_{10}) and operated with a drift field above 1.5 kV/cm. Simulations suggest that the experimentally achieved record resolution of 14 ± 3 μm is limited by the size of the holes in the mesh and could be reduced to 11 μm with smaller holes. An optimization of the readout with 75 μm strip pitch could lead to a further improvement down to 8.5 μm.

2.3.1 Etched-mesh Micromegas

The micro-mesh and pillar complex can alternatively be produced by exploiting standard photolithographic processes from the printed circuit board industry, as described in [35]. The procedure makes use of a 50 μm thick Kapton sheet, whose faces are plated with 5 μm of copper. The base material is stretched on a frame and laminated together with two foils of 15 μm solid photoresist, one on each side. The mesh is obtained by patterning one copper layer with circular holes having a diameter of 25 μm and a pitch of 50 μm, giving rise to 20% optical transparency. The mesh supporting pillars are formed from the Kapton substrate, that is modeled through wet chemical etching using the second copper layer as a mask. Figure 2.16 (right) is a microscope picture of the etched mesh, where some pillars are visible.

The resulting structure is mounted on top of a grounded copper plate defining the anode electrode and the signal is read out by a calibrated amplifier chain connected to the mesh though a decoupling capacitor. The detector, having a 15 mm thick conversion gap, is filled with Ar:iC_4H_{10} 90:10 and operated at a gain of 5×10^3, with amplification field E_A and drift field E_D in the ratio $E_A/E_D = 200$.

Under these conditions, the Micromegas shows an energy resolution of 11.8% FWHM in response to 5.9 keV ^{55}Mn X-ray photons and of 5.4% FWHM when irradiated with 22 keV ^{109}Ag X-ray photons. The exceptional figures are explained with the superb amplification gap uniformity achieved with this production technique.

2.3.2 Bulk Micromegas

The Micromegas concept underwent a revolution with the introduction of the bulk manufacturing in 2005 [38]. This technology, based on standard photolithography, allows for the production of the entire sensitive detector as an integrated single unit.

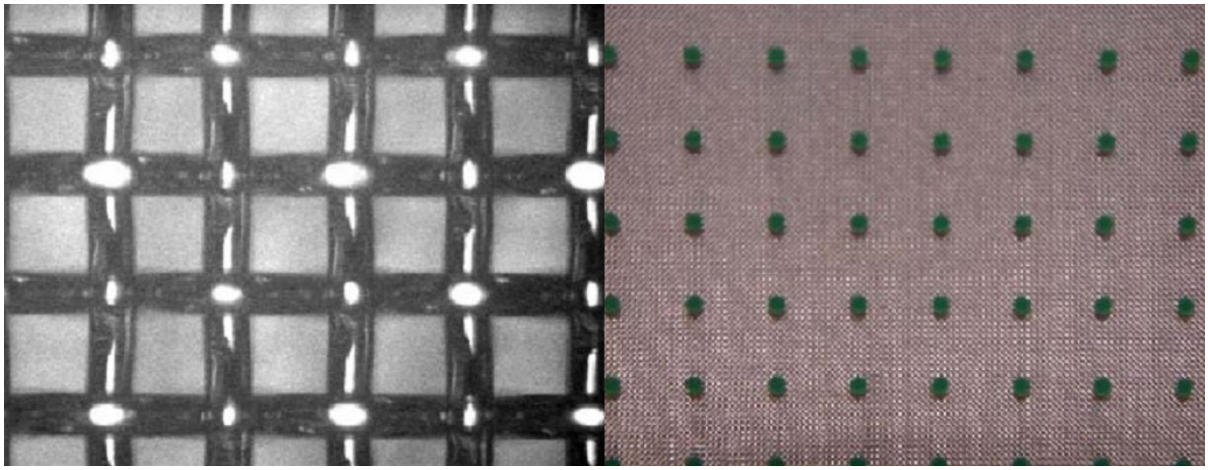

Figure 2.17: Left frame: microscope picture of a woven mesh with wire pitch of 80 μm [38]. Right frame: microscope picture of a bulk Micromegas with pillar pitch of 2 mm.

To obtain a more reliable structure and pave the way to large-area Micromegas, the electro-formed nickel micro-mesh is substituted with a metallic woven wire mesh. Woven meshes are quite robust to handling and stretching and they are delivered in rolls of up to $40 \times 2\,\mathrm{m}^2$. Moreover, they are commonly produced by several companies around the world, they are quite inexpensive and they are available in many materials, such as steel, titanium, iron, nickel, copper and gold. In the bulk process, the wire mesh gets stretched on a frame and laminated at high temperature to the readout board, between layers of photoresist with adequate thickness, typically in the range of several tens of microns. Depending on the desired amplification gap, one or two photoresist sheets are included between the mesh and the readout board, while a single foil is sufficient to externally clothe the mesh. The photoimageable layers are patterned by exposure to UV light and developed to create the pillars, that support and encapsulate the mesh, keeping it under tension.

The involved materials are quite inexpensive and the manufacturing cost is low. Moreover, the procedure can be scaled up to square metre size, enabling the realization of large-area detectors, and it is compatible with industry standards, which makes it suitable for large scale production. On the mechanical side, bulk Micromegas are much more robust than their predecessors and the mesh spacing is more homogeneous than in the original case.

The mesh used in the first bulk prototypes can be seen in Fig. 2.17 (left). It has stainless steel wires 30 μm in diameter, interwoven with a pitch of 80 μm, corresponding to 320 LPI and 39% optical transparency. The pillars, cylindrical in shape and 300 μm in diameter, are evenly distributed over the $9 \times 9\,\mathrm{cm}^2$ active area with a pitch of 2 mm in both the x- and the y-direction, as illustrated in Fig. 2.17 (right), introducing dead zones of only 1.8%. One of the chambers has an amplification gap of 75 μm, while a second one, obtained by laminating two photoresist layers between the mesh and the anode, has an amplification gap of 150 μm.

Both detectors have been tested in combination with a 10 mm thick conversion gap, using Ar:iC_4H_{10} 95:5 and reading out from the mesh the signal generated by 5.9 keV ^{55}Mn X-rays. The ion signal rise time is 60 ns in the first Micromegas and 150 ns in the second, while the maximum achievable gain is about 2×10^4 in both cases. The energy resolution is 20% FWHM and can be improved by flattening down the mesh between two heavy rolls before laminating it to the readout.

2.3.3 COMPASS

The COMPASS experiment at CERN makes use of Micromegas chambers in the section downstream of the beam target and upstream of the first analyzing magnet, where the detectors are traversed by the full spectrum of particles produced in the target, as the low-energy component is not yet deflected out of the acceptance by the magnetic field [39–41]. In order to cope with the different fluxes encountered along the beam radius, the tracking system in this section is divided into three nested subsystems of increasing rate capability. The Micromegas technology has been selected to equip the intermediate zone, called the small-area tracker (SAT). For a typical beam of 200 GeV muons impinging at about 10^8 Hz on the 1.3 m long lithium deuteride (^{6}LiD) polarized target, the integrated particle rate expected on the SAT is about 30 MHz, with a peak flux of 450 kHz/cm^2. Additional requirements for the SAT include a space resolution better than 100 μm and a time accuracy in the 10 ns range, together with a material budget below 0.3% of a radiation length per detection plane.

The SAT is made up of 12 Micromegas chambers with 40×40 cm^2 active area, assembled in back-to-back doublets of perpendicular views, *x*-*y* (0-90°) and *u*-*v* (±45°), as shown in Fig. 2.18. Both the drift and the amplification meshes are electro-formed nickel grids, 4 μm thick, with pitch of 200 and 500 LPI, respectively. They are stretched and glued on glass fiber frames and stacked on the anode, delimiting the 100 μm amplification gap and the 3.2 mm thick conversion gap, while a copper-clad Kapton window stretched on a plastic frame encloses the 61 gas volume. The amplification gap thickness is precisely maintained thanks to cylindrical pillars 150 μm in diameter, made out of insulating etchable resin and fixed to the anode. The readout board is a 100 μm epoxy fiber PCB with 15 μm thick and 200 μm wide copper strips spaced with a pitch of 360 μm in the inner region and of 420 μm in the outer region. A circular dead zone of 5 cm in diameter is located in the centre, corresponding to the beam position, where tracking is performed by scintillating fibers. In order to meet the low material budget requirements, the readout strips are patterned on a very large PCB (120×60 cm^2) and extend 35 cm beyond the active area, allowing the front-end electronics to be moved out of the spectrometer acceptance. Mechanical rigidity is improved by a 5 mm honeycomb support, glued to a 100 μm carbon epoxy sheet and coupled to a 15 μm copper electromagnetic shielding.

Although sparks do not damage Micromegas detectors, they generate dead time and require protection for the electronics. The choice of polarizing the strips through individual resistors lets the potential of the few strips involved in the discharge vary faster than the mesh voltage, thus reducing the dead time. Moreover, since it was shown that the probability of hadron-induced sparks in Micromegas is proportional to the mean atomic number of the gas mixture, the adoption of a neon-based compound offers additional safety. Finally, provided that for a given gas mixture the number of discharges varies exponentially with the gain, efforts were made in achieving high efficiency at a gain not exceeding a few thousand. For this purpose, the SFE16 dedicated amplifier-and-discriminator circuit was designed with a long 85 ns shaping time, to best match the ion-induced signal.

The resulting figures include 99.5% MIP detection efficiency, 65 μm space resolution in the inner region and a 9 ns time jitter.

2.3.4 CAST

The CERN axion solar telescope (CAST) has been using the Micromegas technology for one of its subsystems since 2002 [42, 43]. The purpose is that of reducing background events through the identification of photons in the energy range from 1 to 10 keV. Because one of the main sources of background is natural radioactivity, all weldings are done with low-radioactive soldering and Kapton or Kevlar have been preferred over FR4 epoxy for the readout plane.

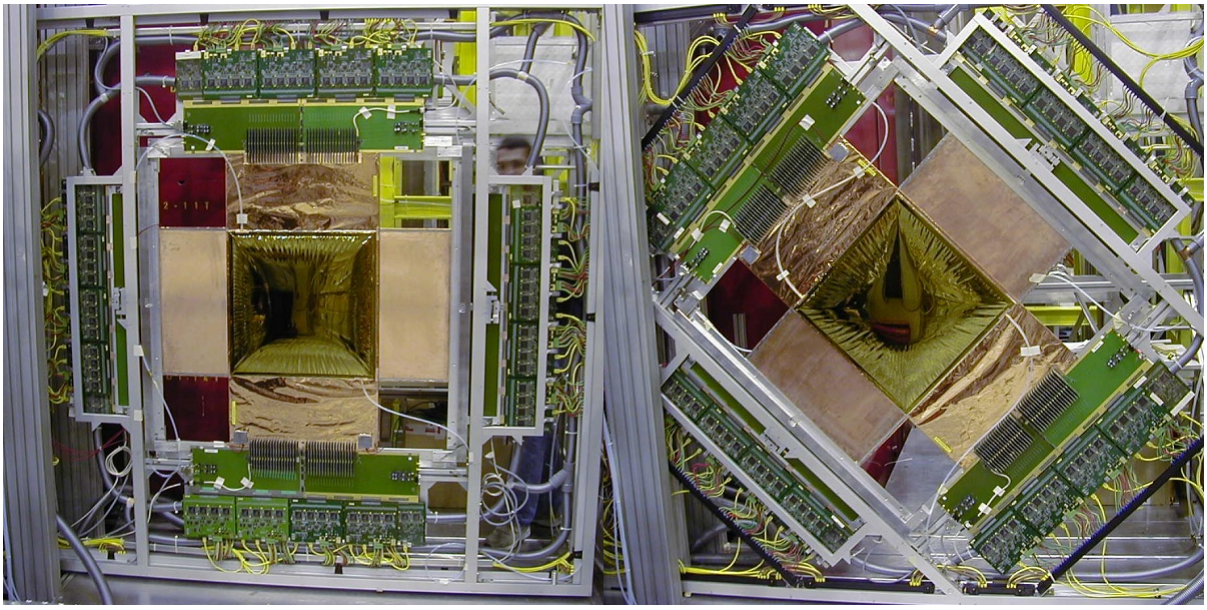

Figure 2.18: COMPASS Micromegas.

The chamber frame is made out of joined Plexiglas cylinders to which the drift and multiplication electrodes are attached. A 4 μm aluminated polypropylene entrance window, glued on a stainless steel strong back and capable of holding the vacuum at the magnet side, encloses the 25 mm thick conversion volume and serves as the cathode, generating the 250 V/cm drift field. The amplification gap, 50 μm in thickness, is defined by a 4 μm copper micro-mesh having 100 μm wide Kapton support pillars patterned on it with a pitch of 1 mm. The anode features bi-dimensional cartesian readout with strips-on-pads configuration, where the y-coordinate is extracted by connecting the pads with strips patterned on the back side of the Kapton support sheet through metalized vias. The 45 cm^2 active area is covered by 192 strips in each direction, spaced with a pitch of 350 μm. Figure 2.19 shows a picture of the micro-mesh (left) and of the anode plane (right). The readout is performed with Gassiplex electronics, triggered by the micro-mesh signal.

When operated in Ar:iC_4H_{10} 95:5, the detector can reach gas gains of up to 10^5, although in normal operation a gain in the range 5×10^3 to 10^4 is sufficient to discriminate 1 keV photons. Under these conditions, the achieved hit-reconstruction accuracy is better than 100 μm along both the x- and the y-coordinate. A signal event, corresponding to a 1–10 keV photon coming from the magnet, creates a charge cluster with a lateral size of 4 to 8 strips in each direction, allowing for the rejection of background events which typically form larger clusters.

In 2003, the detector was upgraded with the introduction of a high-sampling-rate flash analog-to-digital converter (ADC) to record the mesh pulse and discard background events with unexpected shape. The energy resolution, measured with 5.9 keV X-rays from a ^{55}Fe radioactive source, is 16% FWHM when using the mesh signal, but only 30% FWHM when reading out the strips because of cross-talk issues due to unetched copper left on the micro-mesh pillars.

In 2004, an improved Micromegas with a conversion gap of 30 mm and amplification gap of 100 μm was installed on CAST. In the new setup the cross-talk is eliminated by using Kevlar pillars attached to the readout plane instead of Kapton pillars patterned on the micro-mesh. This results in an energy resolution of 19% FWHM from both the mesh signal and the strip signal, which leads to better background rejection capabilities.

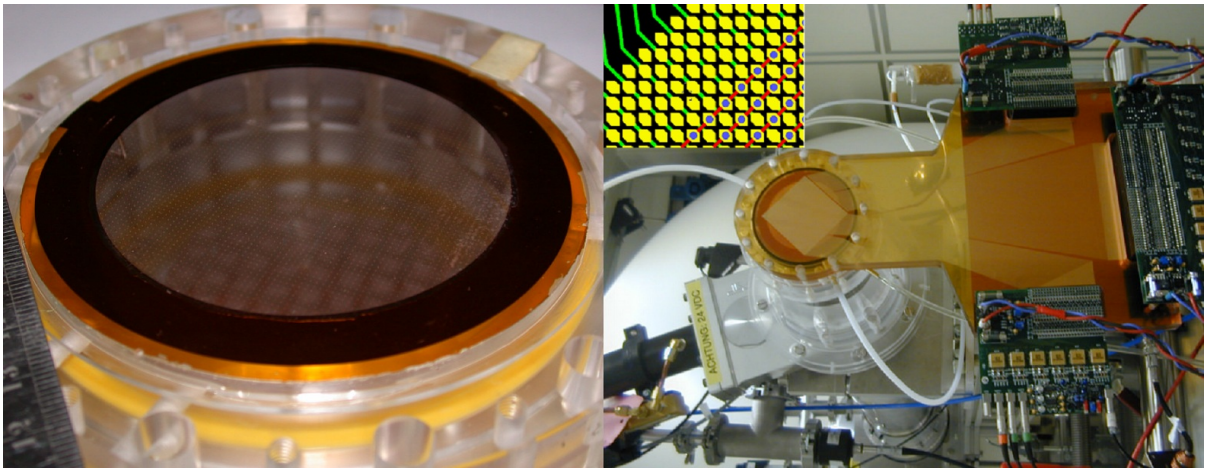

Figure 2.19: Micro-mesh (left) and readout plane (right) of a CAST Micromegas [44].

2.3.5 Other applications

The Micromegas technology finds applications in many other fields. Just to mention a few, it can be used as a readout structure in time projection chambers [45, 46] and serve as a neutron detector when equipped with a convenient converter such as ^{6}Li or ^{10}B [47].

2.4 Detector testing

Testing is a key step at every level of detector research and development, both when exploring new ideas and when aiming at the best exploitation of an existing technology for the needs of a specific application. The purpose of the test can vary hugely, ranging from a proof of feasibility to the study of the detector performance, to the optimization of its parameters. This section provides some guidelines and presents the assembling and testing procedures used throughout the thesis, highlighting the points where particular care should be taken and explaining the physics foundations of the adopted experimental methods.

Section 2.4.1 introduces the standard tools, the assembling procedure and the preliminary operations employed to prepare an MPGD specimen for testing. Section 2.4.2 describes the X-ray sources used in this research work and Section 2.4.3 presents an energy-selective photon filter that I designed to remove spurious components from the spectrum emitted by the employed X-ray gun. Section 2.4.4 details the procedure used to assess the total effective gas gain of the MPGDs, while the gain stability is addressed in Section 2.4.5 and the discharge probability in Section 2.4.6. Finally, beam tests are briefly considered in Section 2.4.7.

2.4.1 Detector assembling

Most of the tests reported in the following chapters are performed on early-stage specimens, with the aim of probing novel MPGD technologies. For this reason, a flexible and easy-to-assemble setup is often used, leaving in the background other aspects that would otherwise be of primary importance in a finalized detector, such as a custom readout structure or a careful planning of the service routings.

The MPGD components under study, mostly $10 \times 10\,\mathrm{cm}^2$ in active area, are mounted in a test box like the one shown in Fig. 2.20. Although the details of such a box depend on the nature of the test, its skeleton follows a standardized scheme. The readout elements are patterned on a PCB about 1 mm

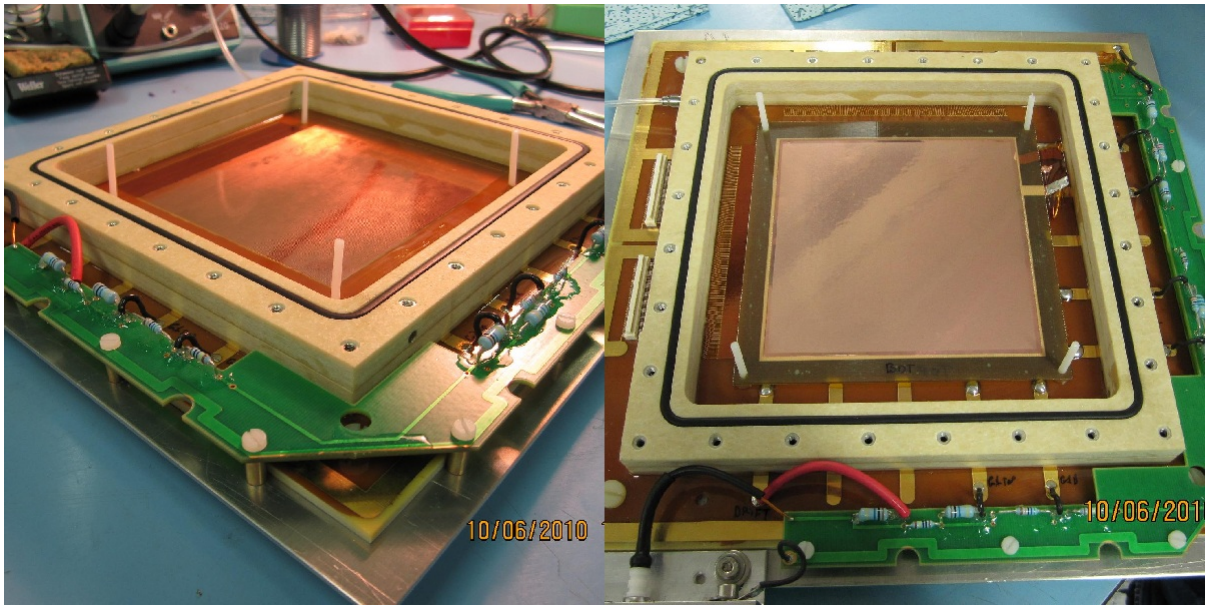

Figure 2.20: Test box with bi-dimensional readout and resistive divider.

thick, together with the feedthrough contacts for high-voltage distribution. In the case of Fig. 2.20 (left), the anode has COMPASS-like bi-dimensional strips with Panasonic P5KS high-pitch board-to-board connectors for signal routing towards the readout ASICs. A gas-tight square frame, most often made out of insulating material, defines the gas volume and provides the gas inlet. A groove in the frame houses the O-ring for coupling to the dismountable roof, where the gas outlet and the Kapton or Mylar entrance window are located. High voltage can be distributed either through a resistive divider, as in Fig. 2.20, or channel by channel with single SHV connectors, in the latter case giving more freedom in the choice of the fields at the cost of an increased number of high-voltage channels. The drift electrode and the GEMs, stretched on fiberglass frames, can be piled up over the anode or the bulk Micromegas mesh using insulating pins for positioning and calibrated washers for precise gap definition, as illustrated in Fig. 2.20 (right).

The assembly has to take place in a clean room, while wearing a clean-room coat, gloves, shoe covers and a facial mask. The MPGD active elements should not be touched directly, but rather handled through their frames, avoiding contact with dirt or hard surfaces that could create shorts. Each component has to pass an inspection under an optical microscope to ensure the absence of visible defects. It is then gently blown with nitrogen in order to remove dust particles possibly stuck between its electrodes, as illustrated in Fig. 2.21 (left). A high-voltage test follows, as shown in Fig. 2.21 (right), to verify the electrical robustness before the piece is mounted into the test box. For example, $10 \times 10\,\mathrm{cm}^2$ GEM foils are required to stand a potential difference of 500 V in dry air, with a leakage current of less than 5 nA. Upon applying the high voltage for the first time, discharges may occur due to manufacturing leftovers or dirt particles. The plasma generated in the spark is often sufficient to burn the impurity and make the detector capable of holding high voltage. Although the observation of a few discharges in a brand new detector element should not raise any worry, repeated sparking in the same position is usually an indication of a local defect that may require chemical cleaning to be removed. Particular care has to be taken when performing electrical connections in the test box, in order to prevent the solder from creating shorts. It is considered good practice in this sense to cover the active area with a clean-room-grade cloth whenever soldering inside the test box and repeatedly blow with nitrogen after each intervention.

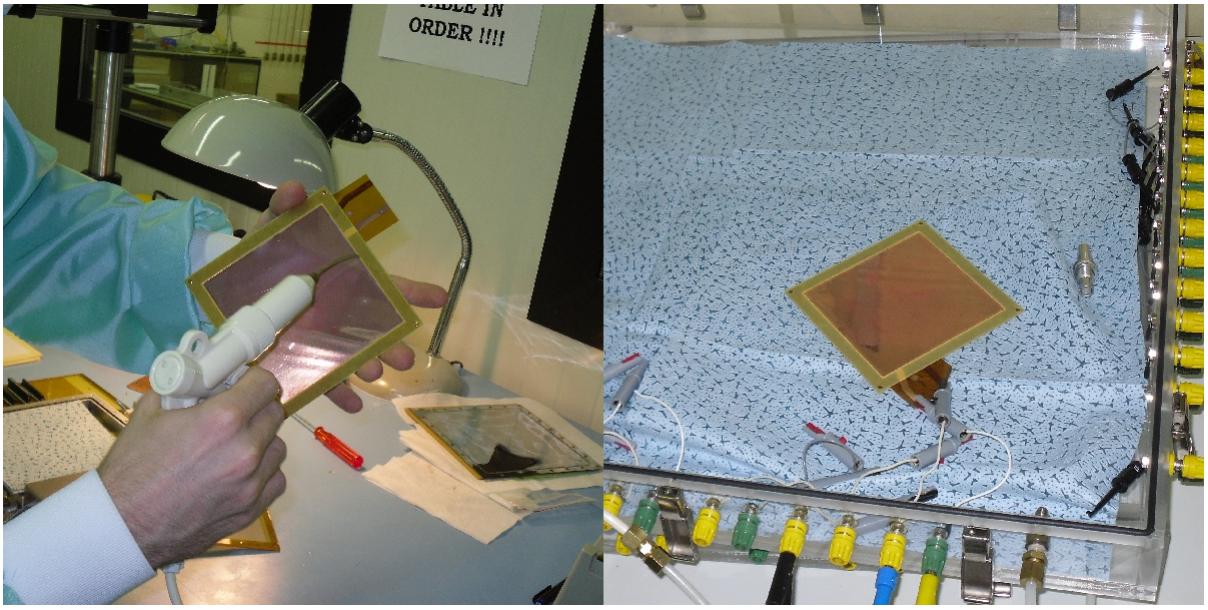

Figure 2.21: GEM cleaning and HV test.

Upon being placed under gas for the first time, the chamber has to pass a gas tightness test, usually performed with the help of a sniffer gun. If a leak is found, it can be closed with insulating conformal coating for electronic circuits, which will penetrate into narrow cavities by capillarity. The detector should be left for a few hours on open-loop gas flow to ensure several gas-volume exchanges before powering. All the tests performed in this research work are carried out in open-loop configuration. In such a case, it is good practice to leave the chamber flushing all the time, even at reduced flow, in order to prevent extraneous particles from entering into the active volume through the exhaust. When this is not possible, the gas inlet and outlet should be sealed or shorted together.

2.4.2 X-ray sources

In spite of the fact that MPGDs are often foreseen and designed for the detection of minimum ionizing particles, many tests are better done with X-rays in the energy range from 1 to 10 keV. The main advantage consists in the tenfold liberated charge, a few hundred electron-ion pairs for soft X-rays against a few tens for MIPs traversing a conversion gap a few millimetres thick with 0° incidence angle. This makes it easier to reach the efficiency plateau with a non-optimized setup and a low gas gain. Moreover, while the charge deposited by MIPs is Landau-distributed, photon conversions have small and Gaussian charge variations, thus enabling the estimation of the energy resolution. In turn, the energy resolution can be used to gather indirect information about the gain uniformity.

Radioactive sources are the simplest and handiest way to generate soft X-rays. They are constituted of isotopes with a relative proton superabundance in the nucleus, but with insufficient energy difference between the parent nuclide and its prospective daughter to allow for a positron emission. Under such conditions, positive beta decay is kinematically forbidden and electron capture is the sole available decay mode, thus removing the otherwise competing beta background.

By far the most widespread radioactive source of soft X-rays for laboratory calibration and test purposes is ^{55}Fe. Figure 2.22 (left) shows one such a source placed on a detector. ^{55}Fe decays by electron capture into ^{55}Mn, with a half-life of 2.737 years. The resulting K shell vacancy is filled by an electron

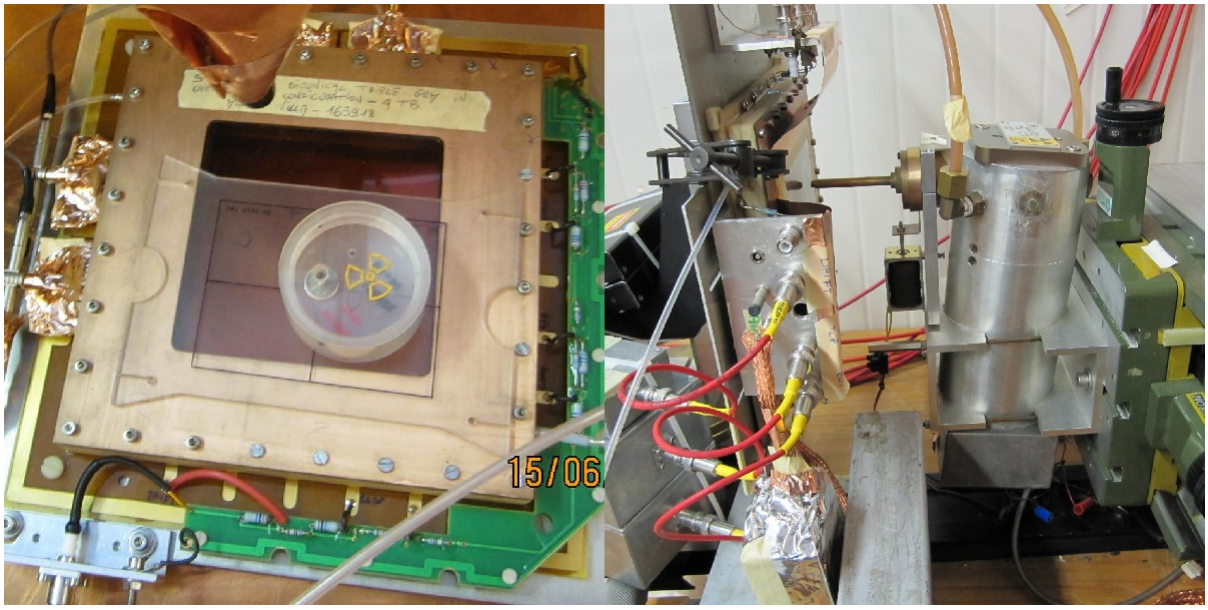

Figure 2.22: Left frame: ^{55}Fe radioactive source on a detector. Right frame: copper X-ray tube with long collimator standing in front of the irradiated chamber.

Table 2.1: Average number of electron-ion pairs liberated in a photon conversion in various gas mixtures.

Gas	Mn K_α	Cu K_α
Ar:CO_2 70:30	212	289
Ar:CO_2 85:15	219	299
Ar:CO_2 93:7	223	305
Ar:CF_4 90:10	215	293

from a higher shell, with the corresponding emission of a 5.19 keV Auger electron (60% probability), a 5.899 keV $K_{\alpha 1}$ X-ray (16.2% probability), a 5.888 keV $K_{\alpha 2}$ X-ray (8.2% probability) or a 6.49 keV K_β X-ray (2.85% probability). The remaining 12% is accounted for by lower-energy Auger electrons and photons from minor transitions. Due to the limited energy resolution of the tested detectors, these lines cannot be resolved and the energy spectra exhibit a single photopeak, plus the argon escape peak about 3 keV below it. The middle column of Table 2.1 gives the average number of electron-ion pairs produced by a ^{55}Mn K_α photon conversion in the gas mixtures used in this research work, obtained combining the values in Table 1.1 according to Eq. (1.26).

X-ray tubes come into play when higher photon rates are needed. An X-ray tube is an evacuated glass bulb in which a tungsten filament connected to an adjustable current generator acts as an electron emitter through the thermionic effect. The released electrons are accelerated towards the target anode, which is maintained at a constant positive potential of several tens of kV with respect to the grounded cathode. An electrostatic lens focuses the electron beam in a small spot on the target surface, while a water cooling circuit dissipates the intense heat generated in the anode by the impinging high-energy electrons. A fraction of the electron energy excites the atoms of the metallic target, which eventually revert back to their ground state by emitting characteristic X-rays. Contrary to radioactive sources, these spectral lines are superimposed on a background continuum due to bremsstrahlung, whose intensity spectrum is roughly proportional to $(E_{\max} - E)/E$, where E is the photon energy and $E_{\max}$ the maximum photon

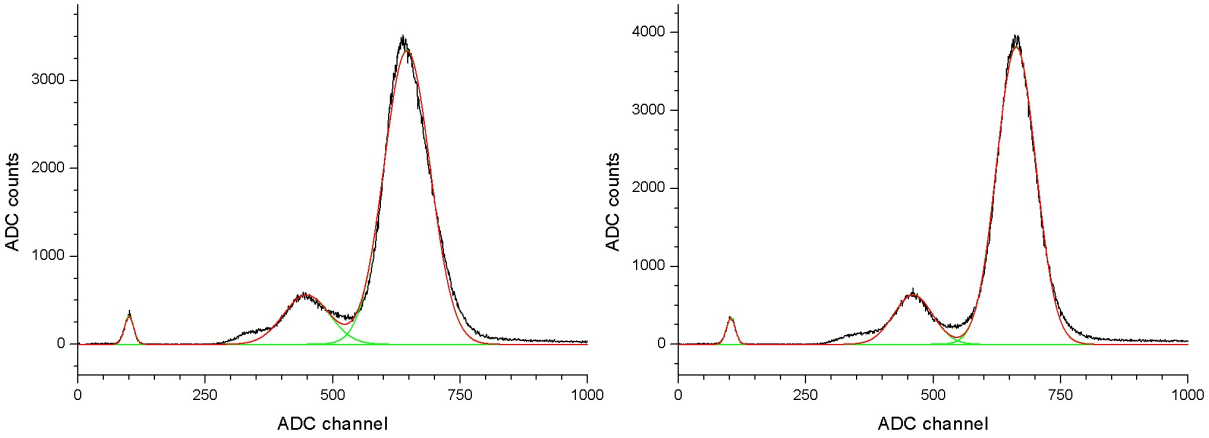

Figure 2.23: Left frame: energy spectrum of a copper X-ray tube. From right to left, the three peaks correspond to the photopeak, the argon escape and the pedestal. Right frame: energy spectrum of the same copper X-ray tube, where the K_β line has been removed with the interposition of a nickel filter between the tube and the detector.

energy. The anode voltage therefore defines the spectrum shape, while the filament current regulates the photon rate. The produced X-rays leave the tube from a thin beryllium extraction window that partly modifies the spectrum, suppressing the low-energy bremsstrahlung components.

The tubes used in this research work have a copper target, emitting 8.048 keV $K_{\alpha 1}$ X-rays, 8.028 keV $K_{\alpha 2}$ X-rays and 8.905 keV K_β X-rays. The last column of Table 2.1 gives the average number of electron-ion pairs produced by a copper K_α photon conversion in the gas mixtures used in this thesis.

2.4.3 Design of an energy-selective photon filter

Figure 2.23 (left) is an energy spectrum acquired with the experimental setup of Fig. 2.22 (right). The copper X-ray tube is here operated at a potential of 15 kV and a cathode current of 0.300 mA. This results in a photon flux of $1542 \pm 6\,\mathrm{Hz/mm^2}$ after the long cylindrical collimator of 1 mm in diameter and a copper absorber. The detector is a $10 \times 10\,\mathrm{cm^2}$ active area double GEM with 4.25 mm thick drift gap, 2.25 mm transfer gap and 2.13 mm induction gap. The foils are mounted in a standard test box of the type described in Section 2.4.1, with an unsegmented anode readout. The chamber is flushed in open-loop configuration with a 5 l/h flow of Ar:CO_2 70:30. The drift and transfer fields are both set to 2 kV/cm, the induction field is fixed to 3 kV/cm and each GEM is biased with 403 V, corresponding to an overall effective gas gain of 1100.

The rightmost peak in Fig. 2.23 (left) is the photopeak, the middle one is the argon escape and the leftmost is the pedestal. The spectrum shows that under low noise conditions the copper K_β line, although not resolved, begins to emerge from the predominant K_α contributions, giving rise to a positively skewed photopeak and thus biasing the estimation of the energy resolution.

Better results can be achieved by cleaning up the X-ray tube spectrum to get an improved monochromaticity. Specifically, this can be done by cutting out the copper K_β line by means of a selective filter that suppresses photon intensities above a selected energy threshold. Figure 2.24 shows the attenuation length, as defined in Eq. (1.12), for nickel, Kapton and copper as a function of the photon energy. Nickel is the only chemical element whose attenuation length presents an abrupt fall between the copper K_α and K_β lines, at an energy of 8.33 keV. Although this unique property makes nickel the sole candidate material for the filter, its fragility when laminated in thin foils requires the presence of a support sheet. The substrate ought to provide mechanical strength and, at the same time, have little or no influence on

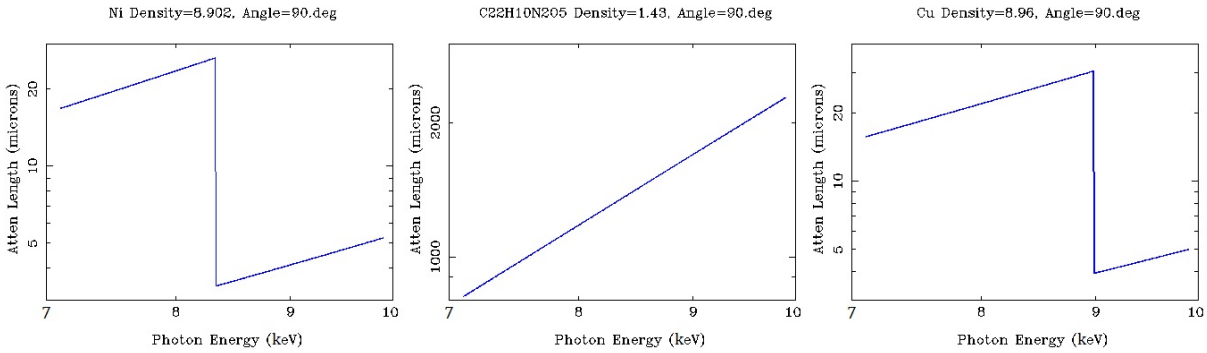

Figure 2.24: Attenuation length of nickel, Kapton and copper [11].

the photon spectrum. The adopted solution is based on the standard double-sided copper-clad Kapton foil that is used as the GEM raw material, on which nickel layers are subsequently deposited by electroplating. Since the filter will also serve as a rate moderator for gain calibrations (cf. Section 2.4.4), the nickel thickness has to be selected to attenuate the copper K_α line by a factor 50 to 100. The most suitable thickness of nickel is determined by combining the data of the three graphs of Fig. 2.24 to obtain the overall photon suppression. Figure 2.25 gives the calculated attenuation factor as a function of the photon energy for a stack with 50 µm of Kapton, 10 µm of copper and different amounts of nickel. The main discontinuity is due to nickel, while the second maximum at 8.98 keV comes from copper.

A picture of the realized filter is shown in Fig. 2.26. The thickness of the deposited nickel is measured to be in the range 86 to 90 µm, corresponding to an attenuation of the copper K_α line by a factor 59 to 70 and of the copper K_β line by a factor 3.0×10^9 to 8.2×10^9. The filter is stretched on a 2 mm thick aluminum frame with a hole at each corner for mechanical fixation to the detector entrance window through support metal pins.

The energy spectrum in Fig. 2.23 (right) is acquired under the same conditions as 2.23 (left), after replacing the copper absorber with the nickel filter and increasing the X-ray tube cathode current to 0.459 mA to get a photon rate of $1523 \pm 4\,\mathrm{Hz/mm^2}$, as similar as possible to the one previously used. The improvement is visible, as the copper K_β line and the bremsstrahlung tail are removed, leaving a purely Gaussian photopeak. This also reflects in the energy resolution extracted from the Gaussian fits, which decreases from 19.5% to 16.2% FWHM.

2.4.4 Gas gain

The estimation of the effective gain is one of the fundamental steps in the characterization of a gas detector. Different gain calibration methods exist, each of them offering some advantages and disadvantages. Throughout the research work presented in this thesis, gain calibrations are performed exploiting an X-ray tube to produce a high enough photon rate to enable the direct measurement of the detector anode current by means of a nanoammeter. In the following, the adopted experimental procedure will be explained in detail, from the physics foundations to the methodological tricks.

The current I_A flowing in the anode of a generic gas detector is given by Eq. (2.1), where N_γ is the number of photons interacting in the time interval Δt, $N_{p/\gamma}$ is the number of electron-ion pairs liberated in a photon conversion as reported in Table 2.1, G is the effective gas gain and e is the electron charge.

$$I_A = \frac{N_\gamma N_{p/\gamma} G e}{\Delta t} \tag{2.1}$$

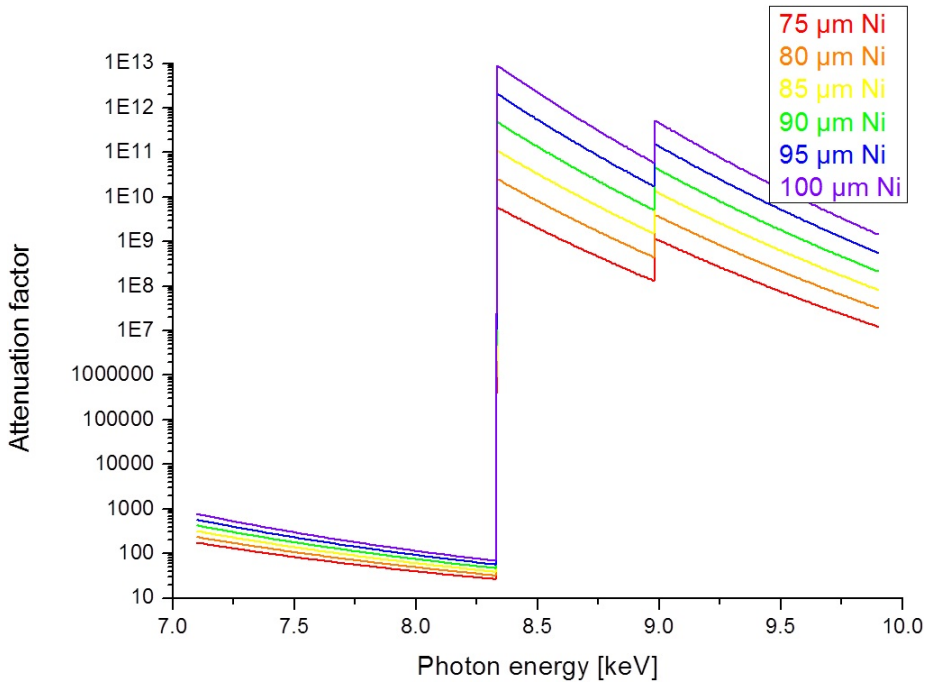

Figure 2.25: Attenuation factor for different nickel thicknesses.

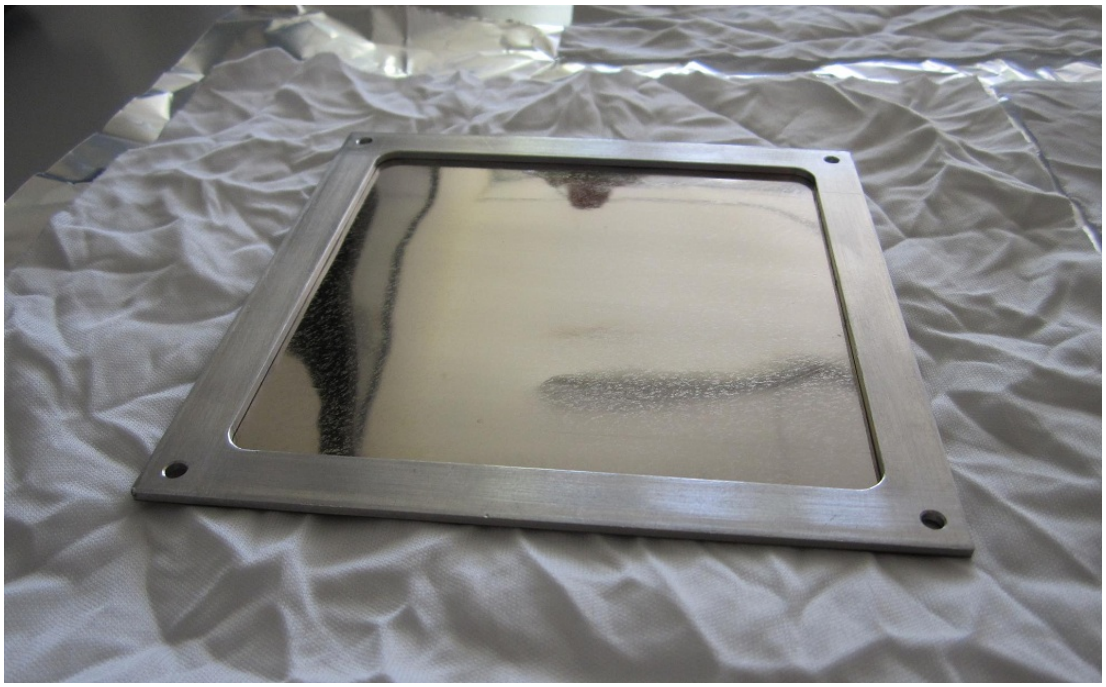

Figure 2.26: Nickel filter.

The anode current is better estimated when the detector is irradiated with an intense photon flux, as the relative error on I_A generally decreases at larger rates. On the other hand, the number of photon interactions per unit time is best measured in the opposite condition, as a high particle flux increases the pile-up probability, leading to an underestimation of N_γ. A calibrated photon absorber can be used to artificially lower the rate and thus reduce the systematic uncertainties. The absorber calibration is done by counting the number of detected anode pulses above threshold when the X-ray tube is operated at the lowest possible cathode current, with ($N^{\text{with}}_{\gamma,\text{low}}$) and without ($N^{\text{without}}_{\gamma,\text{low}}$) absorber. Letting $N^{\text{with}}_{\gamma,\text{high}}$ be the number of anode pulses from the detector that exceed the noise threshold when the X-ray tube is powered with a high cathode current and the absorber is mounted, the number of photon interactions per time unit Δt with high current and no absorber is computed as:

$$N^{\text{without}}_{\gamma,\text{high}} = \frac{N^{\text{with}}_{\gamma,\text{high}} N^{\text{without}}_{\gamma,\text{low}}}{N^{\text{with}}_{\gamma,\text{low}}} \tag{2.2}$$

Due to local thickness variations across the absorber area, it is important to experimentally determine in situ the attenuation factor every time the absorber is used. Moreover, one has to take care not to move the absorber once in place and not to reinsert it after removal. As for the X-ray tube, the cathode current should be changed only once, since the potentiometer-based analog current controller makes it very difficult to revert back to a specific value. Finally, all rate measurements have to be done with and without radiation to allow for background subtraction. All these requirements can be met by adopting the following operative procedure.

1. Set up the readout chain for pulse-height operation by connecting the anode of the chamber under test to a charge preamplifier and to a shaper amplifier in cascade. Keep the signal cable to the charge preamplifier as short as possible to limit the electronic noise. Hook up the output of the shaper amplifier to a threshold discriminator followed by a counter scaler for pulse counting. Optionally, also feed the signal from the shaper amplifier to an ADC for spectroscopy analysis. Operate the X-ray tube at the lowest cathode current, about a few tens of μA, to obtain a photon rate in the order of 1 to 10 kHz/mm^2 after the long collimator of 1 mm in diameter. Record the number of detector pulses that exceed the noise threshold over a chosen time interval Δt. Repeat the measurement several times to accumulate statistics in the presence of radiation (signal and background) and without radiation (background only). Estimate the average number of photons $N^{\text{without}}_{\gamma,\text{low}}$ detected in Δt and the associated uncertainty by computing the arithmetic mean and the corrected sample standard deviation of the mean for the acquired data sets, then subtracting the background contribution and propagating the errors.

2. Mount the absorber in front of the chamber. Estimate the number of photons $N^{\text{with}}_{\gamma,\text{low}}$ detected in the time interval Δt.

3. Increase the cathode current of the X-ray tube to a couple of mA. Estimate $N^{\text{with}}_{\gamma,\text{high}}$.

4. Remove the absorber and switch to current-mode readout by disconnecting the charge preamplifier and inserting a nanoammeter in series between the anode of the chamber and the DC ground. Measure the current I_A flowing in the anode of the detector.

At this point, the effective gas gain is obtained by inserting Eq. (2.2) into Eq. (2.1) and solving for G:

$$G = \frac{I_A \Delta t N^{\text{with}}_{\gamma,\text{low}}}{N_{p/\gamma} N^{\text{with}}_{\gamma,\text{high}} N^{\text{without}}_{\gamma,\text{low}} e} \tag{2.3}$$

One can then get a complete gain curve by varying the bias voltages and recording the corresponding anode current. There is no need to repeat the rate measurements for each voltage setting, as the gain can be inferred by rescaling the calibrated point on the basis of the anode current. Alternatively, one can choose to revert back to pulse-height mode and extract the other points from the photopeak position in the energy spectra. In either case, to ensure the consistency of the results, neither the chamber nor the X-ray tube should be moved throughout the whole calibration and scan procedure. Also, the gain scan should proceed upwards from the lowest voltage, in order to avoid memory effects due to the charging-up of the dielectrics (cf. Section 2.4.5), that typically have long relaxation times. Unless otherwise specified, the gain curves shown in this thesis are measured up to the discharge point, so to determine the maximum applicable voltage and the corresponding maximum achievable gain.

2.4.5 Charging-up

Charging-up is a generic expression that indicates the buildup of charges on the surface of insulating materials in a gas detector. Charges of either sign contribute to the phenomenon, following their drift motion in the applied field or because of diffusion processes in the gas. The charges will maintain their position on the insulators until they get neutralized in an encounter with charges of opposite sign or until they are evacuated through very small surface leakage currents. The equilibrium is reached when there is no net charge flow towards the insulating structures, as formalized by Eq. (2.4), where $N^{\pm}$ indicates the surface charge density of a given species.

$$\left.\frac{\mathrm{d}\left(N^{+}-N^{-}\right)}{\mathrm{d}t}\right|_{\text{drift}}^{\text{eq}} + \left.\frac{\mathrm{d}\left(N^{+}-N^{-}\right)}{\mathrm{d}t}\right|_{\text{diff}}^{\text{eq}} + \left.\frac{\mathrm{d}\left(N^{+}-N^{-}\right)}{\mathrm{d}t}\right|_{\text{recomb}}^{\text{eq}} + \left.\frac{\mathrm{d}\left(N^{+}-N^{-}\right)}{\mathrm{d}t}\right|_{\text{leak}}^{\text{eq}} = 0 \tag{2.4}$$

Because of the nature of the neutralization process, the recombination rates must be the same for both carrier species. Furthermore, by neglecting both the leakage terms due to the long relaxation times and the small diffusion contribution from the positive ions, the previous relation can be simplified as:

$$\left.\frac{\mathrm{d}N^{+}}{\mathrm{d}t}\right|_{\text{drift}}^{\text{eq}} = \left.\frac{\mathrm{d}N^{-}}{\mathrm{d}t}\right|_{\text{drift}}^{\text{eq}} + \left.\frac{\mathrm{d}N^{-}}{\mathrm{d}t}\right|_{\text{diff}}^{\text{eq}} \tag{2.5}$$

The last equation shows that, when equilibrium is reached, the system is not in a static condition, but rather in a dynamic state characterized by zero net charge flow. Since the terms in Eq. (2.5) depend on the intensity of the fields and on the particle rate, it follows that the amount of charging-up will also be a function of such parameters.

Charging-up causes gain variations that, depending on the application, may interfere with the correct functioning of the detector. In the research and development phase it is therefore important to assess the impact of the phenomenon on the detector performance. The parameters that are usually taken into account are the relative gain variation and the characteristic time to reach the dynamic equilibrium.

In this thesis, gain stability tests are performed by setting up the readout in pulse-height operation mode, acquiring several spectra and extracting the relative effective gas gain from the shift of the photopeak position. The detailed procedure is as follows.

1. Bias the detector and energize the X-ray tube several hours before starting the measurement to minimize gain instabilities due to reasons other than charging-up.

2. With the X-ray shutter closed, move the detector to a fresh new spot which was not previously irradiated and start the acquisition.

3. Open the shutter and take data for long enough time without moving the setup.

Table 2.2: Decay chain of ^{228}Th.

Parent nuclide	Half-life	Decay mode	Q-value [keV]
^{228}Th	1.9116 ± 0.0016 a	α	5520.12 ± 0.22
^{224}Ra	3.6319 ± 0.0023 d	α	5788.87 ± 0.15
^{220}Rn	55.6 ± 0.1 s	α	6404.67 ± 0.10
^{216}Po	145 ± 2 ms	α	6906.3 ± 0.5
^{212}Pb	10.64 ± 0.01 h	β^-	569.9 ± 1.9

In order to best sample the exponential-like gain-variation curve, low-statistics spectra are recorded in rapid sequence for the first few minutes, after which time period the data acquisition program automatically switches to longer runs interleaved by pauses of a few minutes.

2.4.6 Discharge probability

As stated in Section 1.8, discharges happen when the total charge in a single avalanche exceeds Raether's limit, corresponding to 10^7–10^8 electron-ion pairs. For this reason, sparks are more likely to be triggered by highly ionizing particles or intense particle fluxes and the discharge probability increases at higher gas gains. The consequences of sparks include possible damage to the amplification structures or the readout electronics and dead time associated with the recharging of the electrodes. Although the discharge probability can be reduced in several ways and precautions can be adopted to minimize potential damages, the stochastic nature of the phenomenon makes it impossible to completely suppress sparks.

Throughout the thesis, the discharge probability is probed by forcing the selected gas mixture to flow through a cavity containing a ^{228}Th radioactive source before entering in the detector volume. ^{228}Th decays with a half-life of about two years according to the scheme reported in Table 2.2. Its second daughter in the decay chain is ^{220}Rn that, being in gaseous state, is transported by the gas flow through the gas line and to the detector active volume. Both ^{220}Rn and its immediate daughter nuclide (^{216}Po) rapidly decay by emitting alpha particles which average energy is around 6.5 MeV. A calibrated rate of alpha particles can therefore be obtained by regulating the gas flow. A detailed description of the experimental procedure used to assess the discharge probability is given in Section 4.3.1.

2.4.7 Beam tests

When it comes to evaluating the MIP detection efficiency or the space resolution, X-rays are not suitable anymore. Cosmic rays may be used for this purpose, but the very low particle rate often leads to prohibitively long data-taking runs. A sometimes better alternative is provided by artificially produced particle beams, where the beam size, energy and composition can be freely chosen within the machine limits. The beam tests described in Section 4.4.4 have been performed on the H6 beam line in the CERN North Experimental Area, using beams of muons and pions with energy in the order of 100 GeV.

CHAPTER 3

Large-area GEMs

Since their invention in 1997, gas electron multipliers (GEMs) have found application in many different fields, inside and outside high-energy physics. In recent years, a growing demand for large-area GEMs has arisen, frequently in combination with a need for large-volume production capabilities. Much of this interest is motivated by the planned increase of luminosity in the upgrade of the Large Hadron Collider (LHC) to HL-LHC. At present, the external tracking systems of the LHC experiments are often based on traditional gas detectors, such as multiwire proportional chambers, resistive plate chambers or drift tubes. Some of the detectors, and especially the ones located in the forward regions, will have troubles coping with the increased particle flux and need to be replaced. Thanks to their properties, and in particular the high rate capability, micropattern gas detectors appear as a natural choice for the next generation of these systems.

The original GEM manufacturing method described in Section 2.2, although regularly used for small detectors, is hardly applicable to large areas. For this reason, in 2007 an effort has started, aimed at finding a novel GEM production process that can be scaled up to square metre size. In addition, the new technique should be compatible with industrial standards in order to allow for large-volume production in a commercial company outside research institutes.

This chapter describes the research work done over the past years, that eventually led to the development of a novel GEM technology based on single-mask wet etching with electrochemical active corrosion protection. The new GEMs perform similarly to the traditional ones in terms of leakage current, robustness against sparks and maximum achievable gain. Since the base material is the same as the one employed for traditional GEMs, one can expect outgassing, aging and radiation hardness to be as good. Moreover, in case of industrialization the price per unit area is expected to drop by more than an order of magnitude.

Section 3.1 explains the limitation of the original GEM manufacturing method and introduces the approach that led to the first large-area triple-GEM prototype chamber. Section 3.2 presents the refinements of the polyimide-etching technique, which led to the second generation of single-mask GEMs. At this stage I joined the research group. My first task, which I describe in Section 3.3, was the simulation of the GEM electrostatic properties as a function of the hole shape in the substrate. Section 3.3.1 to 3.3.3 expand on the employed software tools, on the realized model of a GEM foil and on the utilized simulation techniques, while Section 3.3.4 and 3.3.5 critically compare the results. Section 3.4 to 3.7 focus on the laboratory tests that I performed to complement the simulations and with the purpose of further improving the single-mask technology. Four generations (from the third to the sixth) of single-

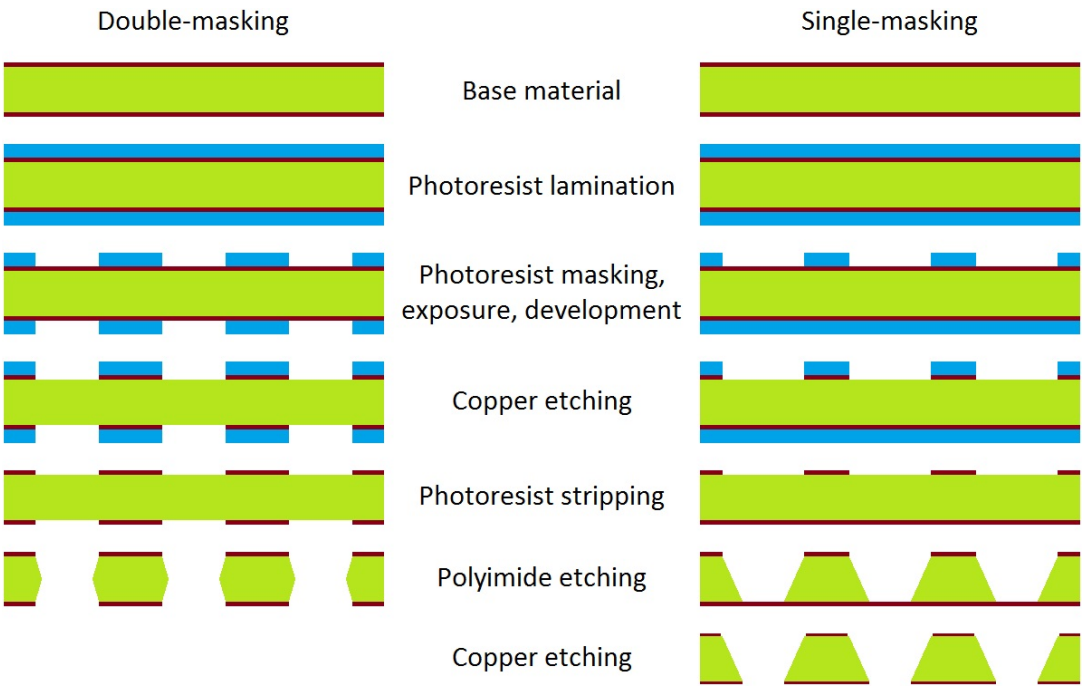

Figure 3.1: Double-mask and single-mask GEM manufacturing.

mask GEMs are considered, showing a steady performance improvement up to the point of making the new technology mature enough for exploitation in a real experiment. For each of these four generations, I explain the goal that we wanted to achieve, I document the innovations in the manufacturing method and I describe the tests that I performed, critically commenting the results. Section 3.8 briefly faces the issue of stretching and positioning the large-area GEM foils. Finally, Section 3.9 summarizes the research and development work that has been done and presents the conclusions.

3.1 Single-mask technology

For more than ten years, gas electron multipliers have been manufactured following the original procedure reported in Section 2.2 and schematically shown in the left part of Fig. 3.1. The base material, consisting of a copper-clad polyimide sheet, is laminated between two negative-tone photoresist dry films on which the hole pattern is subsequently transferred from photolithographic masks by exposure to UV light. The two copper layers are etched at the same time in the same machine. The resulting holes in the copper act as a mask for the polyimide substrate, which is etched simultaneously from above and from below the foil. The alignment of the two photolithographic masks with an accuracy of 10 µm or better is a requisite to ensure a good pattern matching and therefore a good detector quality.

Given the flexibility of both the base material and the two masks, and since the alignment is performed manually with the sole help of an optical microscope, the process becomes more and more involved and time-consuming with the increase of the active area. When the linear dimensions of the sheet exceed about 30 cm, the procedure is not feasible any more.

Instead of trying to improve the mask alignment over large areas, the chosen approach aims at simplifying the production process by using only one photolithographic mask, thus removing any need for alignment. The idea is to pierce the GEM from top to bottom, layer after layer, using the hole pattern

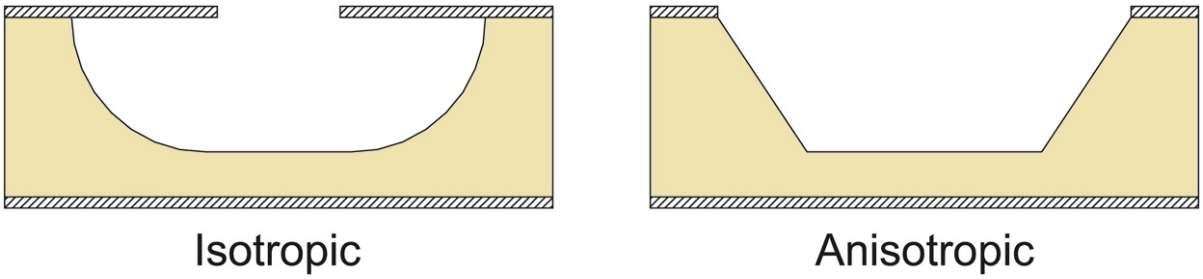

Figure 3.2: Isotropic and anisotropic polyimide etching [48].

produced in one layer as a mask to etch the one right below it. The trick is applied in turn to each layer, until through-holes are formed in the base material. This is in contrast with the original procedure, where the holes are excavated from both sides at the same time. Figure 3.1 provides a schematic comparison between double-masking (left) and single-masking (right).

Although the single-mask concept is simple and neat, it requires proper mastering of the etching techniques to ensure perfect hole definition at the boundary between each pair of layers. Failing in doing so results in irregularities of the hole shape that reflect in a poor gain homogeneity across the active area. The challenge is therefore shifted from the manual alignment of the two photolithographic masks to the refinement of the etching techniques. Once the right combination of chemistries is found, the dimensions are limited only by the size of the base material and of the machinery. Another advantage lies in the fact that the single-mask processing requires very few manual interventions and it can be automatized with the employment of roll-to-roll equipment. As a consequence, while the price of traditional GEMs is dominated by the manpower cost, in case of large-volume production in industry the price of single-mask foils is just slightly higher than the cost of the raw materials.

In single-mask processing the base material is still clothed on both faces with negative-tone photoresist dry films, but the hole pattern is transferred to one side only. The unpatterned photoresist is insoluble to the sodium carbonate development rinsing and protects the bottom copper electrode while the top one gets etched. After clearing the chromium from inside the holes opened in the top copper layer and stripping both photoresists, it is necessary to etch the Kapton substrate. A variety of different chemistries can be used for this purpose.

Potassium hydroxide (KOH) has an isotropic behaviour, which means that material is eroded from the substrate at the same rate in all directions. An isotropic etch undercuts the mask and forms cavities with round sidewalls, as schematically shown in Fig. 3.2 (left). A through-hole created with such an etch is always at least twice as wide as it is deep and hence its aspect ratio, defined as $depth/width$, is very poor. On top of this, the large bias, representing the distance of mask undercutting, exposes the copper edge and makes the GEM more prone to sparking.

Ethylenediamine ($C_2H_4(NH_2)_2$), on the other hand, exhibits an anisotropic behaviour, proceeding faster in the direction perpendicular to the material surface. Although a perfectly anisotropic etch would produce vertical sidewalls, a real situation is more similar to the one shown in Fig. 3.2 (right): the resulting holes have a conical shape, with little or no bias. The aspect ratio depends on the specific etch, and it is not satisfactory for ethylenediamine alone.

Combining the two chemistries, one can increase the aspect ratio of the holes and therefore lower the GEM charging-up by limiting the amount of exposed Kapton, while maintaining a small bias. Moreover, one can change the steepness of the walls within a certain range by tuning the relative concentration of the two compounds. Heat also plays a role, increasing the etching rate of potassium hydroxide with respect to the one of ethylenediamine. Temperatures exceeding about 55 °C should anyway be avoided,

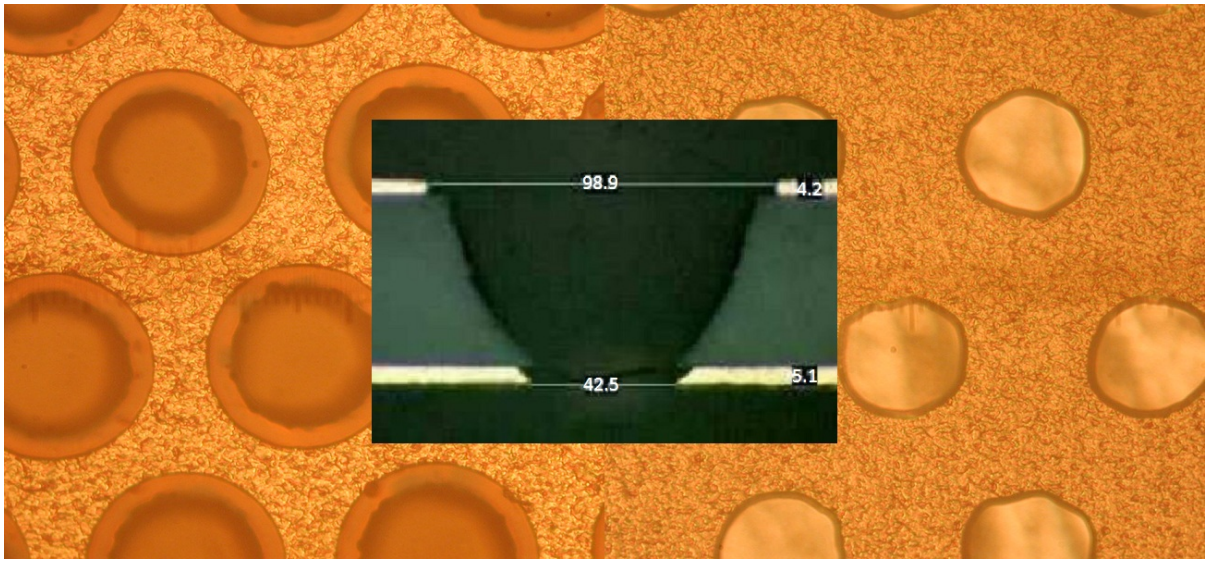

Figure 3.3: 1st generation single-mask GEM. Microscope picture of the top electrode (left frame), of the bottom electrode (right frame) and cross section picture on the axial plane of a hole (central frame). All the dimensions are given in microns.

as local copper delaminations from the polyimide give rise to irregular etching patterns. With optimized parameters, one can make holes with a top diameter of about 90 µm and a bottom diameter of about 45 µm. The foreground of Fig. 3.3 is a cross section microscope picture of such a hole, all the dimensions being given in microns.

The bottom copper layer can be pierced by immersing the sheet into a bath of ammonium persulfate ($(NH_4)_2\,S_2O_8$). Ammonium persulfate is a white-to-yellowish salt, highly soluble in water and with strong oxidizing properties. It is commonly used in the printed circuit board industry as an alternative to ferric chloride for copper etching. Over large areas, it is found to produce copper thickness variations of a few microns across the foil. With single-masking, it generates fluctuations of the hole diameter on the lower GEM electrode, which in turn lead to gain inhomogeneities. On top of this, ammonium persulfate etches more effectively at grain boundaries and therefore increases surface roughnesses and degrades the definition of the copper edges around the holes, making the structure more likely to spark. The use of this chemistry was hence abandoned.

Chromic acid (H_2CrO_4) was found to be a better option, as it solves both issues of inhomogeneity and surface roughness. Figure 3.3 shows a single-mask GEM whose lower electrode (right frame) is etched with chromic acid. The bottom copper layer is etched simultaneously both from the external face and from inside the holes in the polyimide, which act as a mask. Since all the copper surfaces are attacked by chromic acid and get eroded at the same rate, the final sheet has both electrodes slimmed down to half of their original thickness or less. Furthermore, given the isotropic behaviour of chromic acid, a clearance arises on the top electrode around the edge of the Kapton holes, as it can be seen in the left frame of Fig. 3.3. This formation, called the rim, is known to worsen the time stability of the gain due to charging-up of the exposed insulator.

In 2008, the first large-area triple-GEM chamber was built. The detector has an active area of about 2000 cm^2 and was designed such that it could be used in the TOTEM experiment, as a possible upgrade of the T1 tracker. A detailed description of this prototype is provided in [49].

3.2 Polyimide-etching improvement

The second generation of single-mask GEMs sees an improvement of the polyimide-etching technique in the direction of steeper holes. This is achieved with the addition of ethanol (C_2H_6O) to the formerly used ternary mixture of ethylenediamine, potassium hydroxide and water. The reduction of the exposed dielectric area reflects in a lower charging-up and hence in a better gain stability over time.

A further improvement is obtained by etching in two phases with solutions containing the same four constituents in different concentrations. This trick allows for an increased hole steepness and a better control over the hole shape, that can be finely tuned according to one's needs.

The single-mask technology therefore offers freedom of choice for almost all of the GEM geometrical specifications. The Kapton thickness is the sole fixed parameter, given by the selected base material. The electrodes can be slimmed down before etching the holes, leaving the detector performance untouched and making it more suitable for applications with low material budget constraints. The hole pitch is precisely defined by the pattern on the photolithographic mask, that can be changed at will. The same mask also largely defines the hole diameter on the top electrode, even though a fine adjustment is possible at a later stage by tuning the amount of UV light during the exposure. The hole steepness and the diameter on the bottom electrode are determined by the polyimide-etching chemistries and can be changed within a certain range. Finally, the size of the rim is decided when etching the bottom copper layer by adjusting the time in the chromic acid bath.

3.3 Hole-geometry study

While the shape of the GEM holes produced with the single-mask technique can be chosen at will, within certain limits, it is not clear a priori what the optimal shape would be. The best orientation, with the larger diameter towards the cathode or the anode, is also an open question. Moreover, what is regarded as optimal depends on the properties that one wants to enhance for the specific application for which the detector is being designed.

In this framework, numerical simulations can help to gain some knowledge on the influence that the hole geometry has on the GEM performance. The simulations proceed through three consecutive steps.

1. Define the geometry of the GEM elementary cell, fix the material properties and the applied voltages, set the symmetry and boundary conditions and solve the electrostatic problem by means of a finite-element-analysis package.

2. Select a gas mixture and model its properties.

3. Simulate the motion and the interaction of charges in the gas.

In the following, each of these steps is described in detail.

3.3.1 Field-map generation

Since the behaviour of free charges in a GEM depends on the field configuration, it is first of all necessary to deal with the electromagnetic problem of finding the field in each point of the simulation volume. The solution of the Maxwell equations under a set of boundary conditions can be approached in different ways. In this research work, a finite-element-method (FEM) commercial package is used to extract a numerical answer in the form of a field map.

Finite-element methods are numerical techniques for finding approximate solutions to a set of partial differential equations or integral equations. The original set is either approximated with a set of ordinary differential equations which is then numerically integrated using standard techniques or, in case of a steady-state problem, turned into a set of algebraic equations. FEMs are particularly suitable for the solution of partial differential equations when the problem domain has a complicated shape, when it changes over time, when the required precision on the approximate solution varies over the domain, or again when the expected solution has sharp gradients or lacks smoothness. Most FEMs, including the one used in this thesis, proceed by subdividing the domain into a high number of small elements of defined shape, that are called finite elements or primitives. For example, primitives can be triangles and quadrangles for bi-dimensional cases or tetrahedra and hexahedra for three-dimensional cases. The collection of all the primitives constitutes a discretization of the problem domain and is called a mesh. Each mesh element is considered as a homogeneous integration domain, in which the solution is assumed to be the superimposition of polynomial basis functions or shape functions. The coefficients of the shape functions in the linear combination are the unknowns of the algebraic set resulting from the discretization. Although the primitives' shape is fixed, their linear dimensions are not and can vary over the problem domain, thus allowing for higher accuracy near surface boundaries where the solution can be expected to show higher gradients or even discontinuities. In height-FEMs (h-FEMs), the requested precision on the solution is reached by iteratively subdividing the mesh into smaller and smaller elements, while in polynomial-FEMs (p-FEMs) this is done by progressively increasing the degree of the polynomial shape functions. Combining the two methods leads to hp-FEMs, where the polynomials' degree can change from element to element.

The choice of a FEM to compute the field in a GEM detector comes from the fact that the needed accuracy varies over the simulation volume. In fact, the field is almost constant far from the amplification structure, while it is expected to change quickly in both magnitude and direction in the vicinity of the GEM holes and at the surface boundaries. Throughout this research work, the ANSYS package is adopted as the field solver [50].

First, one has to create a geometrical model of the GEM foil and of the surrounding electrodes, namely the detector drift and anode planes. In order to restrict the computational time in the subsequent simulation stages, the model should be kept as simple as possible. Given the hexagonally packed disposition of the holes in all the simulated structures, the most elementary cell is a rectangle of linear dimensions $pitch/2$ and $\sqrt{3}pitch/2$ respectively, including two quarter holes at diagonally opposite vertices. Figure 3.4 illustrates such a minimal cell in a bi-dimensional (left) and three-dimensional (right) view. The GEM periodic pattern is then obtained by mirror symmetry along both the x- and y-direction. Following the same CPU-time optimization philosophy, the extension of the simulation volume along the z-direction can be limited to a few hundred microns, at which distance any distortions due to the holes becomes negligible and the field is uniform.

Let's consider as an example a standard double-mask GEM manufactured at CERN. The base material is a 50 µm thick polyimide layer, clad on the two faces with 5 µm of copper. The holes have a pitch of 140 µm and they are biconical in shape, with an outer diameter of 70 µm and an inner diameter of 55 µm. Along the z-direction, the simulation volume stretches from 500 µm, where the virtual drift electrode is located, to −500 µm, at which position one finds the anode plane. Figure 3.5 is a detail of the ANSYS 3D model, shown in wireframe under two different viewing angles. The two quarters of the biconical holes are visible, the first centered in the origin of the coordinate system and the second at the diagonally opposite corner of the cell. Figure 3.6 is a solid model of the same GEM detail, with the Kapton foil in purple and the gas volume in yellow. The GEM electrodes are not shown in colour because, being metallic, they are equipotential volumes and they have to appear in the simulation only as a set of boundary conditions.

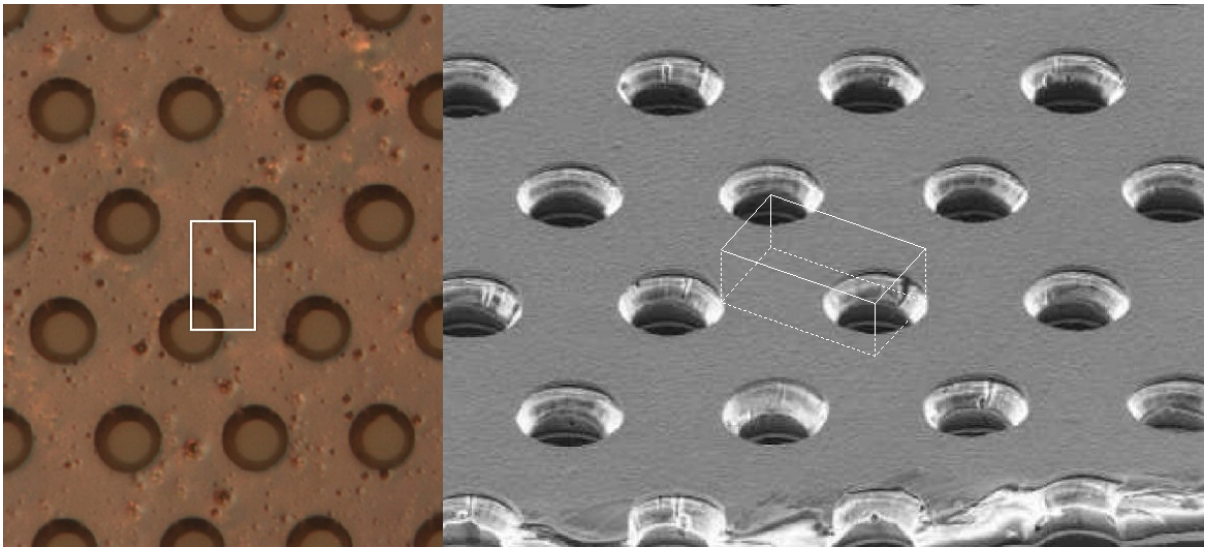

Figure 3.4: Definition of the elementary cell of a GEM.

After defining the material properties, one has to set the electromagnetic state of the cell. In the example under analysis, the difference of potential across the GEM is 400 V, the drift field is 1 kV/cm and the induction field is 3 kV/cm, with no superimposed magnetic field. The virtual drift electrode and the grounded anode are modeled with Dirichlet boundary conditions for the electric potential $\phi(z) = K(z)$ on the top and bottom planes of the simulation volume. Moreover, in order to allow for mirror symmetry of the solution, one has to require the electric potential to satisfy Neumann boundary conditions $-\nabla\phi(\boldsymbol{x}) \cdot \boldsymbol{n}(\boldsymbol{x}) = 0$ on the four lateral faces of the polyimide and gas volumes.

Next, one has to adequately subdivide the problem domain into primitives by meshing the polyimide and the gas volumes. The chosen element type is a 10-node tetrahedral electrostatic solid. Although the meshing is done with the finest primitive size available to the ANSYS smartsize procedure, the solution accuracy can be further improved when necessary by manually refining the mesh. Tests indicate that a small refinement of all the elements appreciably ameliorates the solution with an acceptable burden on the CPU and with no increased risk of meshing problems. Figure 3.7 shows the refined mesh in the elementary cell. The mesh is denser at volume boundaries, where higher precision is needed.

Figure 3.8 and 3.9 visualize the computed electric potential, as a colour map and as equipotential planes, respectively. This solution is then saved into field map files for use at later stages.

3.3.2 Gas-property modeling

Besides the electromagnetic field, the behaviour of free charges in a gas detector depends on the selected gas mixture. In this thesis, the gas attributes are computed using Magboltz version 7.07, called from Garfield version 7.43 [51, 52]. Magboltz is a simulation code written by Stephen Biagi and widely adopted to model with percent accuracy the properties of an almost arbitrary gas mixture by taking into account both elastic and non-elastic cross sections [53].

Appendix A reports the electron drift velocity, Appendix B the electron longitudinal and transverse diffusion and Appendix C the first Townsend coefficient and attachment coefficient as functions of the electric field strength for the gas mixtures used in this research work. In addition, since all the performed simulations use Ar:CO_2 70:30, Appendix D shows the electron energy distribution in such a mixture for electric field strengths from 1 to 100 kV/cm in 10 logarithmically spaced steps.

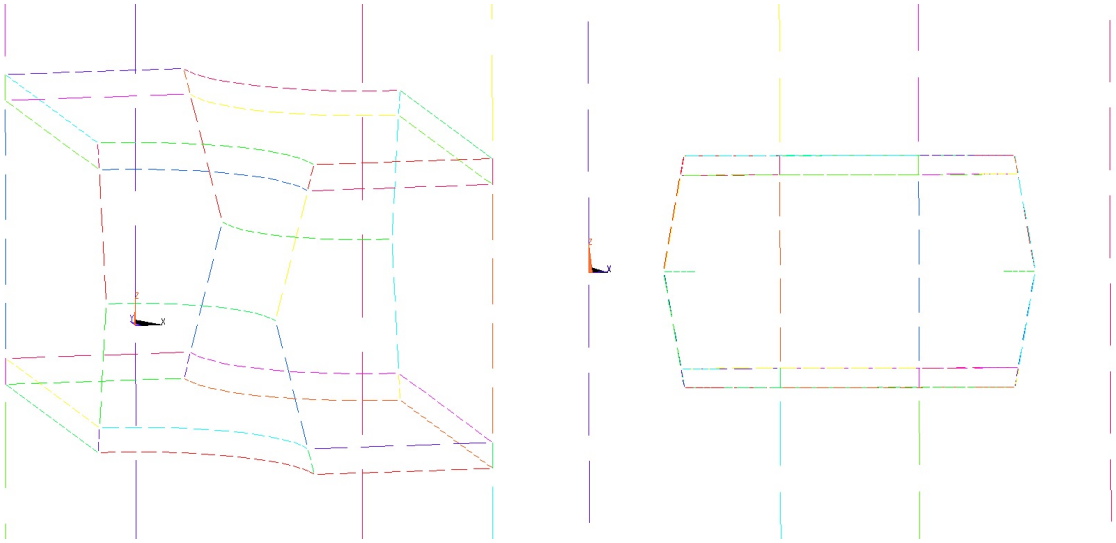

Figure 3.5: ANSYS wireframe model of a double-mask GEM. Left frame: axonometric projection of the elementary cell defined in Fig. 3.4. Right frame: lateral view of the elementary cell, with the two quarter holes shown at the sides.

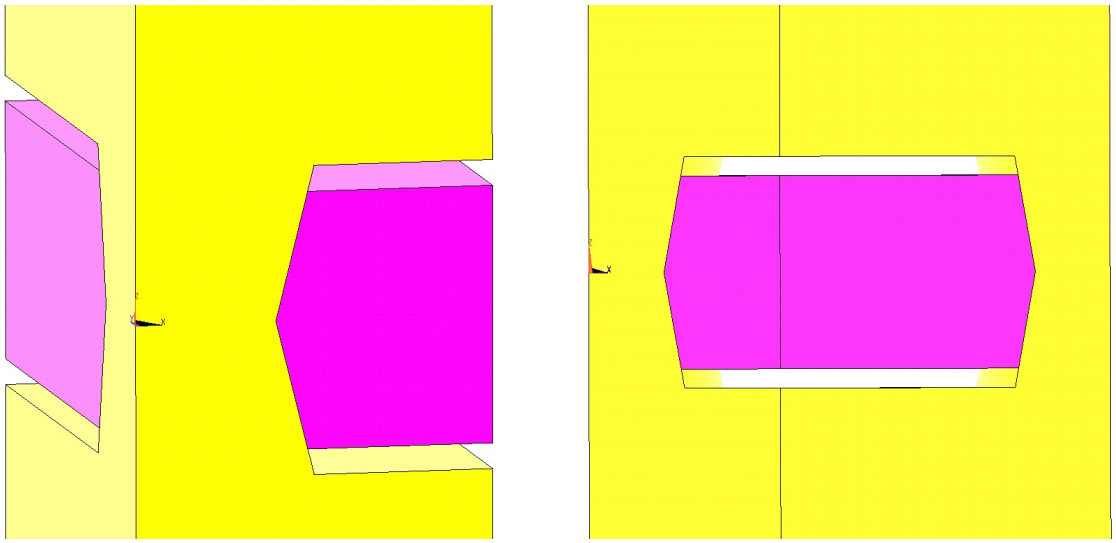

Figure 3.6: ANSYS solid model of a double-mask GEM. The polyimide foil is shown in purple, while the gas volume is in yellow. The electrodes are not shown in colour because they appear in the simulation as a set of boundary conditions.

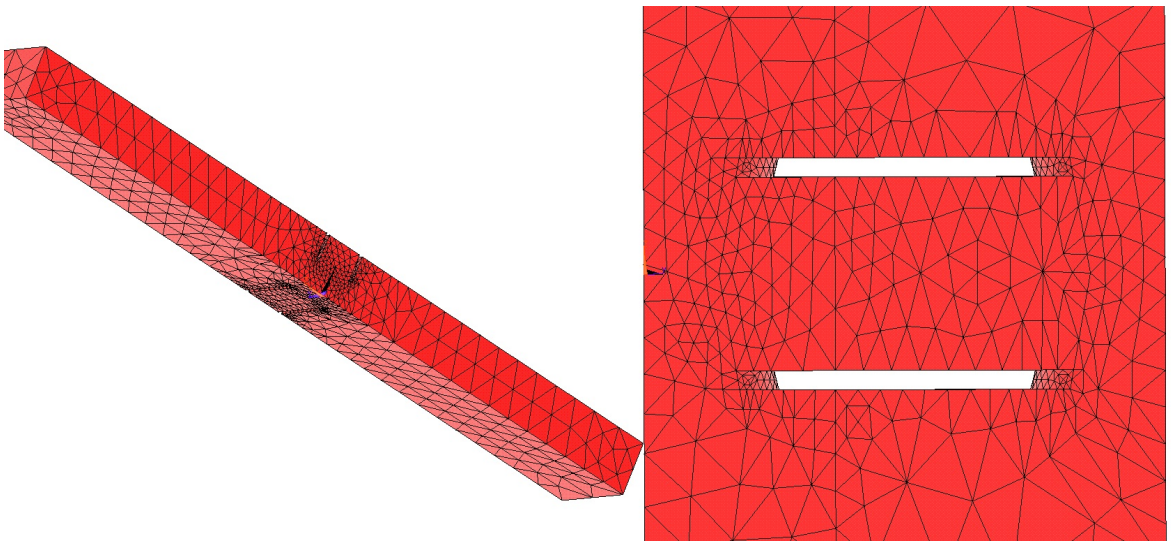

Figure 3.7: ANSYS meshed model of a double-mask GEM. Left frame: axonometric projection of the whole simulation space, stretching from the cathode at $z = 500\,\mu\text{m}$ to the anode at $z = -500\,\mu\text{m}$. Right frame: lateral view of the elementary cell, like in Fig. 3.5 (right) and 3.6 (right). Note that the GEM electrodes are not meshed and that the mesh gets finer at volume boundaries.

3.3.3 Charge motion and interaction

The diffusion of free charges, their drift motion under the action of the applied electric field, their interaction with the molecules of the gas mixture and their Townsend multiplication are simulated using version 7.43 of Garfield, by Rob Veenhof [54].

First, the field map generated with the finite-element-analysis package has to be converted into Garfield format. At this stage, the field map only contains a discrete solution of the electromagnetic problem in the elementary cell defined in Section 3.3.1 and shown in Fig. 3.4. Since the simulation space typically stretches over several elementary cells, the field map is prolonged by mirror symmetry along both the x- and y-direction to fill the entire simulation volume. A geometrical model of all the detector elements also has to be provided. The model has to match the one used in ANSYS, extended to the whole simulation space. The information is needed by Garfield to determine when to stop tracking a drifting particle due to a collision with a detector surface.

After loading the gas file created with Magboltz, one can investigate the field configuration in the GEM by means of a number of different plots. For example, the left frame of Fig. 2.7 displays the equipotential lines (in green) and field lines (in yellow) in the axial plane of a double-mask GEM hole, while the right frame highlights the electric field intensity along the hole axis. Furthermore, Garfield provides the user with three different integration methods for particle tracking.

The first method is based on the Runge-Kutta-Fehlberg algorithm. It is initialized with a starting point, $\boldsymbol{x}_0$, in three dimensions and with the corresponding initial velocity vector, $\boldsymbol{v}_0$, that is retrieved from the Magboltz gas table after extracting the electric field at the starting location from the field map. The method also requires the desired space accuracy, ϵ, to be specified. This parameter, which is set to 1 Å, remains constant throughout the whole integration process and it enters in the calculation of the variable integration time step, Δt_i. The initial time step is conservatively set to $\Delta t_0 = \epsilon / v_0$. The algorithm proceeds by finite moves by computing two estimates of the next position of the particle on the drift line, $\boldsymbol{x}_{i+1}^{(2)}$ and $\boldsymbol{x}_{i+1}^{(3)}$, with second-order and third-order accuracy, respectively. The time step is

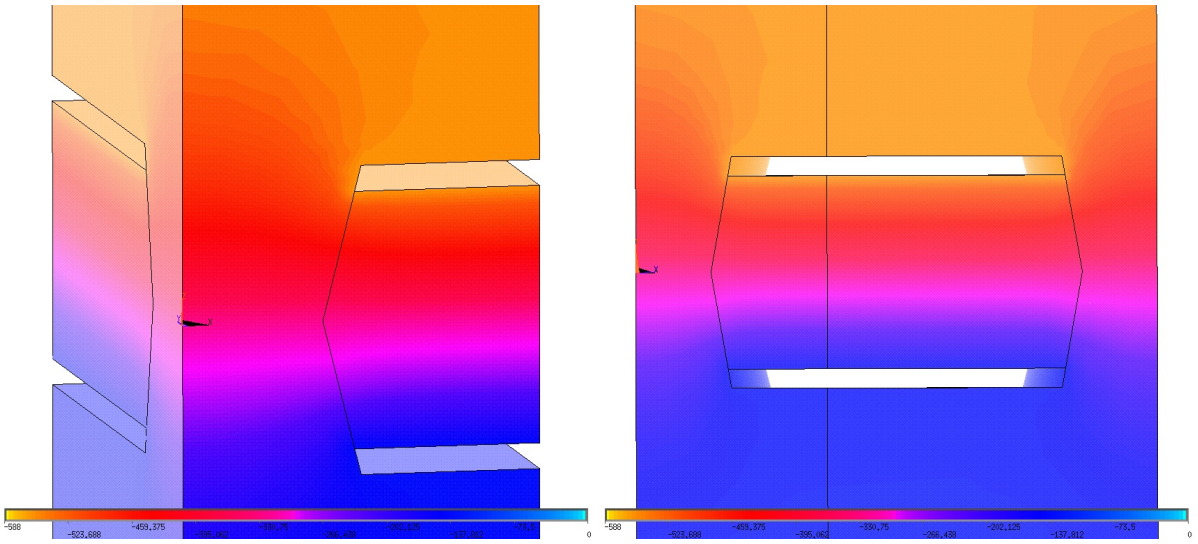

Figure 3.8: Potential map of a double-mask GEM. The colours indicate the electric potential computed by the field solver over the discretized problem domain.

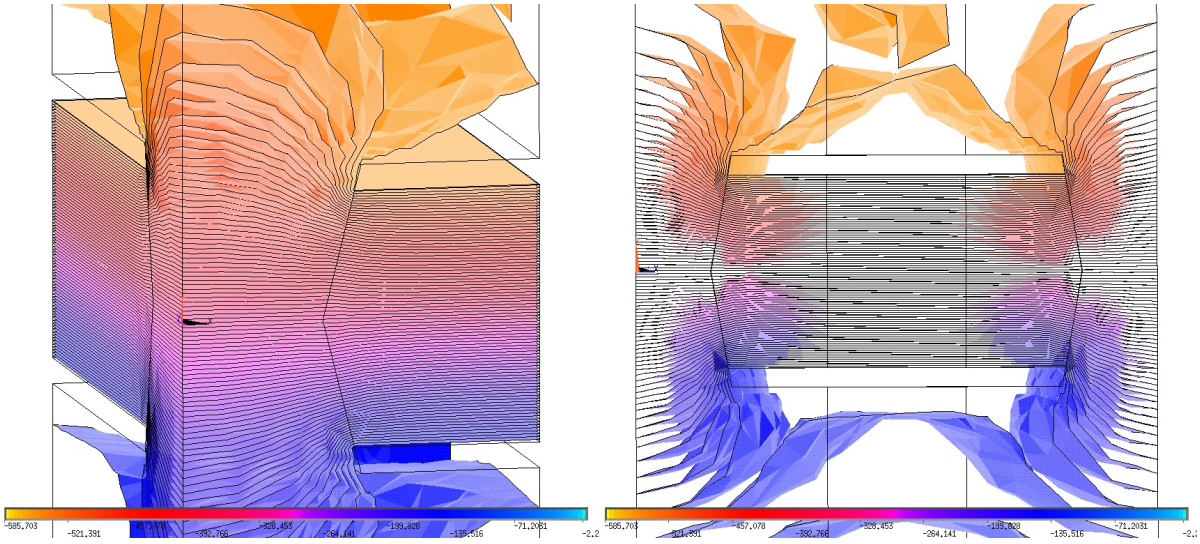

Figure 3.9: Equipotential planes in a double-mask GEM.

then updated by comparing the requested space accuracy with the Euclidean distance between the two estimated points, according to Eq. (3.1).

$$\Delta t_{i+1} = \Delta t_i \sqrt{\frac{\epsilon}{\left\| \boldsymbol{x}_{i+1}^{(2)} - \boldsymbol{x}_{i+1}^{(3)} \right\|}} \tag{3.1}$$

The step is repeated using the new Δt in case the time step shrinks by more than a factor 5 or if the step size exceeds the maximum step length, fixed to 2 µm. Otherwise, the position and the velocity are updated with the second-order estimate and the integration continues. The iteration is stopped if the particle hits a wall, if it exits the simulation volume, if the number of steps reaches the maximum number of steps allowed, if the step size drops below the requested accuracy, or if the velocity becomes zero or negative. This method is well suited for smooth or even analytic fields, where it allows for an improvement of the simulation accuracy, by reducing at the same time the CPU cost thanks to the variable time step. However, one should be careful when using such an algorithm with field maps, that are sometimes not even continuous. Since the Runge-Kutta-Fehlberg integration does not take diffusion into account, it is generally used to trace an approximate profile of the field lines in a chamber, as it was done in Fig. 2.7 (left) for a standard double-mask GEM.

For the use in conjunction with a field map, the Monte Carlo drift-line integration is a more robust alternative, which also considers the charge diffusion processes in the gas mixture. Like the previous algorithm, it is initialized with a starting point $\boldsymbol{x}_0$ and with the corresponding initial velocity vector $\boldsymbol{v}_0$. The time step can be set either explicitly or through a step size, in the latter case giving rise to an almost constant spatial length covered at each step, with small variations due to diffusion and, to a lesser extent, to non-linearities in the field. A third option is to request a variable time step, characterized by an exponential distribution with an average value roughly equal to a specified number of times the mean collision time at the local electric field strength. The step length is then computed assuming the particle velocity to be constant over the time step. Both the longitudinal and the transverse diffusions are also considered to be constant, and their contributions along the drift line and in the two perpendicular directions are taken from three independent Gaussian distributions with spread $\sigma_i = \sqrt{2 D_i \Delta t}$, where D_i is the diffusion coefficient in the considered direction. The particle position is updated by adding the drift and the diffusion vectors and the process iterates. Similarly to the Runge-Kutta-Fehlberg method, the integration is stopped if the particle hits a wall, if it exits the simulation volume, if the number of steps reaches the maximum number of steps allowed, or if the velocity becomes zero. The most important difference between the two described algorithms is that, while the former will always compute the same trajectory for a given set of initial conditions, the latter will return different results due to the random contributions introduced by the diffusion. Although the Monte Carlo method is intrinsically robust and therefore more suited for irregular fields like the ones arising from field maps, great care has to be taken when adjusting the time step. Too large values of the time step make the algorithm inaccurate, while too short steps can cause a premature abortion of the integration in case the maximum number of steps allowed is reached.

The third and most precise integration method performs a microscopic particle tracking at molecular level using Monte Carlo techniques. It is initialized with a starting point, $\boldsymbol{x}_0$, the corresponding initial kinetic energy, E_0, and optionally the direction of the initial velocity vector, $\hat{\boldsymbol{v}}_0$. The step size is the actual free path, as in the real gas, with its natural energy-dependent exponential probability distribution, and with the particle following a vacuum trajectory between collisions. Each collision is classified as either elastic, inelastic, super-elastic, attachment or ionization, with one of the molecular species present in the gas mixture. The choice is made on a probabilistic basis, by taking into account the gas composition and the cross section of each interaction type at the energy just prior to the collision. Since such a

simulation typically proceeds through millions of steps, it is rarely practical to store each of them and so the particle state is recorded every n collisions, with the possibility to set $n = 1$ if desired. In addition, the maximum kinetic energy allowed during the whole procedure has to be provided by the user. If the electron energy exceeds the set threshold, the tracking is terminated before completion. A too small energy limit therefore causes a loss of statistics, while a too large limit makes the algorithm inaccurate. In order to determine such a parameter, one has to find the maximum field strength in the chamber and check the corresponding maximum kinetic energy using probability distributions like the ones reported in Appendix D. In the example of the standard GEM under consideration, the energy limit can be safely set to 100 eV. The microscopic tracking can be somewhat demanding in terms of computational cost, but it provides a very accurate model of the drift and diffusion processes. In Garfield, it is implemented in two different procedures: the first follows only the original electron, while the second also tracks every ionization electron in the Townsend avalanche. Figure 2.8 shows two avalanches simulated with this algorithm.

3.3.4 Field comparison

The software tools introduced in the previous sections can be exploited to investigate the influence of the hole geometry on the properties of single-mask GEMs.

Consider a standard Kapton substrate of 50 μm in thickness, clad on the two sides with 5 μm of copper and perforated by conical holes arranged in a hexagonally packed configuration with a pitch of 140 μm. As formerly done for the standard GEM, the ANSYS elementary cell extends for $pitch/2$ and $\sqrt{3}pitch/2$ in the x- and y-dimension respectively, including two quarter holes at diagonally opposite vertices. Along the z-direction, the simulation volume stretches from −500 to 500 μm, with the virtual anode on the bottom face and the drift plane on the top one. The hole diameter on the GEM lower electrode is fixed to 55 μm, while it varies from 55 to 95 μm in steps of 10 μm on the upper one. The z-mirror-symmetric geometries are also considered, i.e. the ones obtained by flipping over the GEM foil. For each of these configurations, a field map is created, with 400 V across the GEM and 3 kV/cm electric field in both the drift and the induction gaps.

Each of the field maps is converted into Garfield format and the Ar:CO_2 70:30 gas table generated with Magboltz is loaded. Garfield is then used to draw equipotential lines in a hole axial section, on top of which approximated field lines are traced with the Runge-Kutta-Fehlberg integration algorithm. The field strength along the axis for each of the considered geometries is also plotted. The simulation results are given in Appendix E.

As one could expect, the field is z-symmetric in the special case of equal hole diameter on the two GEM faces, that corresponds to a cylindrical geometry. Wider top diameters lead to better field focusing into the hole, with consequent reduction of the electron losses on the GEM upper electrode. However, the number of field lines drawn to the bottom copper layer also grows for larger top diameters. This, in combination with the lateral spread of the charge cloud in a growing Townsend avalanche, can be expected to give considerable electron losses on the polyimide and on the GEM lower electrode. Conversely, wider bottom diameters affect only slightly the electron focusing at the hole entrance, while considerably reducing the charge deposition on the insulator.

The right-handed frames in Appendix E demonstrate that the electric field strength along the hole axis is maximum in the cylindrical configuration, as also indicated by the high concentration of field lines in Fig. E.1. In spite of the variation of about 17% of the field peak intensity along the hole axis, the z-coordinate of the peak does not change appreciably, or does the overall axial-field shape, that is only slightly distorted in asymmetric holes.

3.3.5 Transparency study

A further step can be done by tracking a high number of electrons with one of the integration algorithms described above and recording, for each particle, the final position in the chamber. In this way one can estimate the electron transparency and the losses on the various detector surfaces for the different geometrical configurations.

In order not to bias the Monte Carlo results, the electron starting points have to be homogeneously distributed in the x-y plane. The request can be satisfied, while keeping the computational cost at the minimum, by picking random starting points in the elementary cell shown in Fig. 3.4, which extends for $pitch/2$ and $\sqrt{3}pitch/2$ in the x- and y-dimension, respectively. Moreover, the initial z-coordinate has to be chosen far enough from the GEM, in a region of uniform field. A good compromise is $z = 100\,\mu\text{m}$, that is only $70\,\mu\text{m}$ above the foil, but already enough to meet the field homogeneity requirement.

The Monte Carlo can build on the ANSYS field maps and on the Magboltz gas table created for the study previously described in Section 3.3.4, while the Garfield code has to be adapted to the requirements given above. The simulation volume still ranges from -500 to $500\,\mu\text{m}$ along the z-coordinate, but in the x- and y-direction it is extended up to $7pitch/2$ and $5\sqrt{3}pitch/2$ respectively, thus covering the whole area shown in Fig. 3.4 (left). This is necessary because the charges generated in the elementary cell can diffuse to neighboring GEM holes, which hence have to be defined as Garfield solids and taken into account during the tracking process.

For each of the considered geometries, 1000 electrons are tracked using the microscopic drift procedure and their final positions are recorded. The tracking is stopped and the electron is considered collected by the anode if it crosses the plane $z = -100\,\mu\text{m}$, while it is labeled as lost on a detector wall if its last tracked position is less than $1\,\mu\text{m}$ from a material surface. Other possible final states include attachment to a gas molecule and a series of very rare errors due to local poor-quality meshing or algorithm failure.

Figure 3.10 is a stacked-area chart showing the Monte Carlo outcomes as a function of the geometry, expressed in abscissa through the upper and lower hole diameters. As pointed out in the previous section, wide conical openings facing the cathode have good electron-focusing properties, that result in negligible losses on the GEM top electrode. However, the bending of the field lines inside the hole, together with the transverse diffusion of electrons, cause a significant charge deposition on the middle and bottom layers. When moving from wide conical holes towards more cylindrical configurations, these phenomena cause an increase of the number of particles collected on the upper electrode and a parallel drop in the number of collisions with the polyimide and lower copper layer. The slight decrease of attachment events is understood with the shorter average integrated path covered by the particles. In the geometries with larger holes facing the anode, wider openings follow in a better way the transverse diffusion of electrons, resulting in reduced losses on the Kapton. On the other hand, the charge collected by the two electrodes does not change significantly with the hole shape. As regarding the overall electron transparency, it does not appear to depend strongly on the geometry.

3.4 Mechanical protection

The first and second generation of single-mask GEMs, described in Sections 3.1 and 3.2 respectively, differ in the polyimide-etching technique, but they both get their bottom electrode pierced by means of chromic acid. As explained at the end of Section 3.1, chromic acid is an excellent copper etch for large-area single-mask GEMs, as it solves both the issues of thickness inhomogeneity and of surface roughness that arise with ammonium persulfate. Chromic acid also slims down both electrodes to less than half of their original thickness and it creates a rim around the edge of the Kapton holes, that

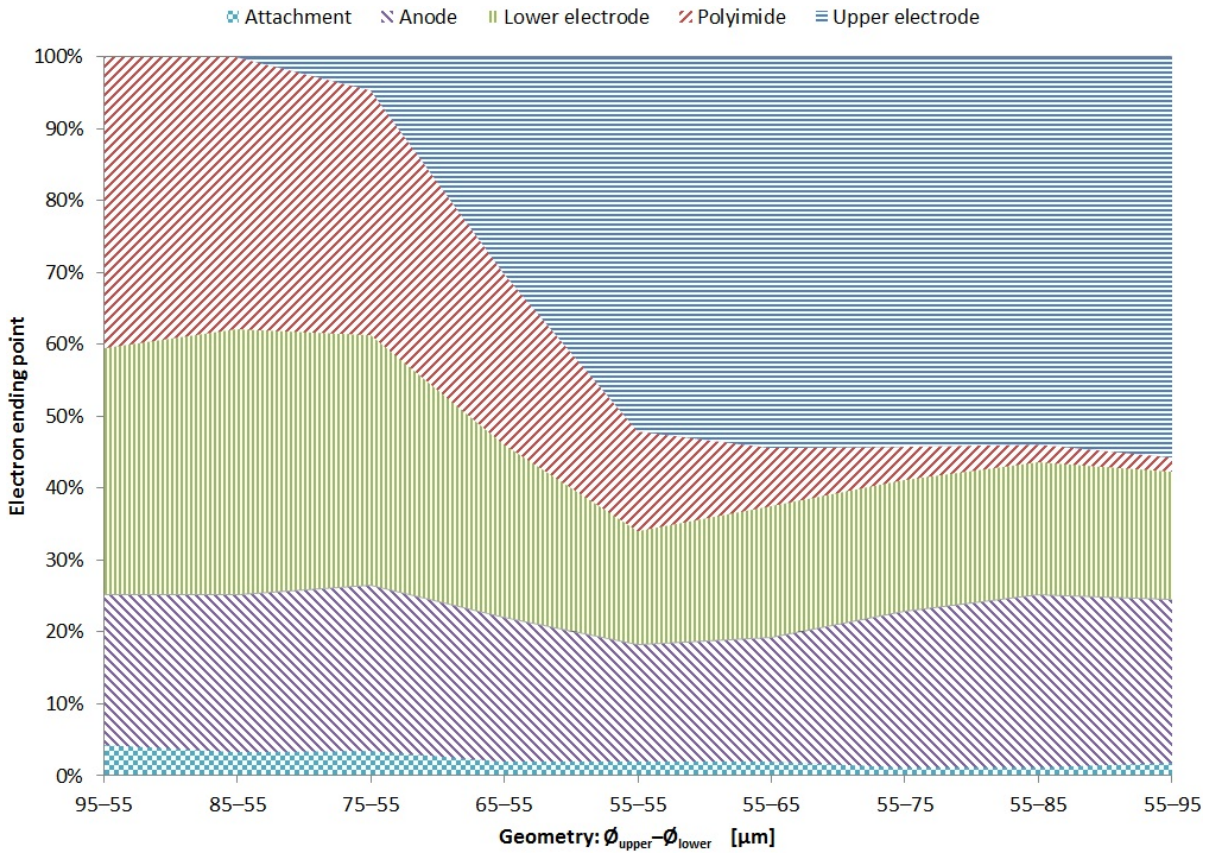

Figure 3.10: Electron ending point for different conical hole shapes.

degrades the time stability of the gain due to charging-up of the exposed insulator. If necessary, the rim size on both electrodes can be increased by moderate over-etching. Although a well-timed etching can set the lower rim to zero, the upper one cannot be reduced below half of the original copper thickness. This is due to the isotropic behaviour of the chemistry, together with the fact that all the copper surfaces are attacked by the acid. In order to enhance the gain stability and avoid potentially undesired electrode thinning, it is necessary to protect the GEM top layer and the external face of the bottom one during the second etching phase, with the openings being excavated from the inside of the holes only.

From the third generation of single-mask GEMs, the outer side of the lower electrode is shielded by laminating a photoresist foil that acts as a mechanical barrier to the chromic acid. This solution is simple, effective and cheap and it is therefore maintained in the following generations, which are presented in Section 3.5 to 3.7.

In the third generation of single-mask GEMs, a mechanical protection is applied also to the upper electrode. As photoresist would seal the holes and prevent the acid from reaching the GEM bottom layer, gold plating is used instead. The plating is applied to the top layer only, after etching the polyimide and before proceeding with the second copper-etching phase. Figure 3.11 shows a microscope picture of the upper (left) and lower (right) electrodes of such a GEM, together with an axial cross section of a hole. A comparison with Fig. 3.3 reveals the great improvement in polyimide etching introduced with the second generation, that results in much steeper walls. Third generation single-mask GEMs have an average top diameter of $101 \pm 17\,\mu m$ and an average bottom diameter of $66 \pm 10\,\mu m$, against 90 and $45\,\mu m$ for the first prototype described in Section 3.1.

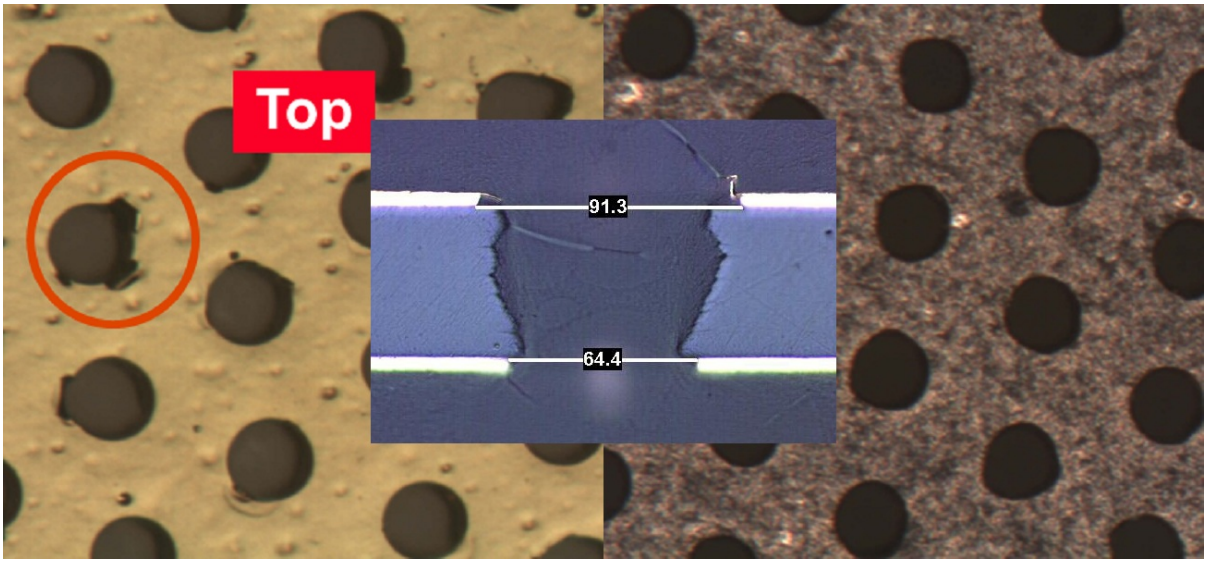

Figure 3.11: 3rd generation single-mask GEM. Microscope picture of the top electrode (left frame), of the bottom electrode (right frame) and cross section picture on the axial plane of a hole (central frame). All the dimensions are given in microns.

Gold plating has a high cost and the added layer is hard to remove. Due to the difficulty of stripping the cladding, gold-plated GEMs often have metal flakes stretching out into the holes, as shown in the central frame of Fig. 3.11. The consequent high discharge probability prevents the GEM foils from reaching sufficient gas gains. These inconveniences could be solved by substituting gold with tin that is cheaper and can be easily eliminated in post-production. Both with gold and tin, however, it is difficult to ensure perfect tightness of the plating at the junction between copper and Kapton. The slightest delamination creates a leak through which the acid can attack the electrode, leading to copper etching under the shielding. This results in the formation of dents that degrade the hole shape on the GEM top electrode, as highlighted in the left frame of Fig. 3.11. The mechanical protection of the upper copper layer was therefore abandoned in favour of more suitable schemes based on electrochemical processes.

3.5 Reverse electroplating

In the fourth generation of single-mask GEMs, the lower electrode is externally laminated with a photoresist shielding and subsequently etched through reverse electroplating.

Electroplating, also known as electrodeposition, is an electrochemical process used to coat a conductive object with a thin layer of metal, in order to bestow a desired property to a surface or to build up thickness on undersized parts. The object to be plated is used as a cathode in a galvanic cell acting in reverse, where the anode is made of the material to be deposited on the part. A power supply, in the form of a battery or more commonly of a rectifier, injects a direct current into the anode, oxidizing the zero-valence metal atoms to form cations. The cations are dispersed in the electrolyte, where they combine with the dissolved anions. Free ions migrate in the cell under the action of the electric field, resulting in a net movement of metal ions towards the cathode. At the cathode the opposite process takes place, with cations getting reduced and sticking onto the object. In this process the anode is dissolved at a rate that is equal to the metal deposition rate on the cathode and proportional to the electric current flowing in the circuit.

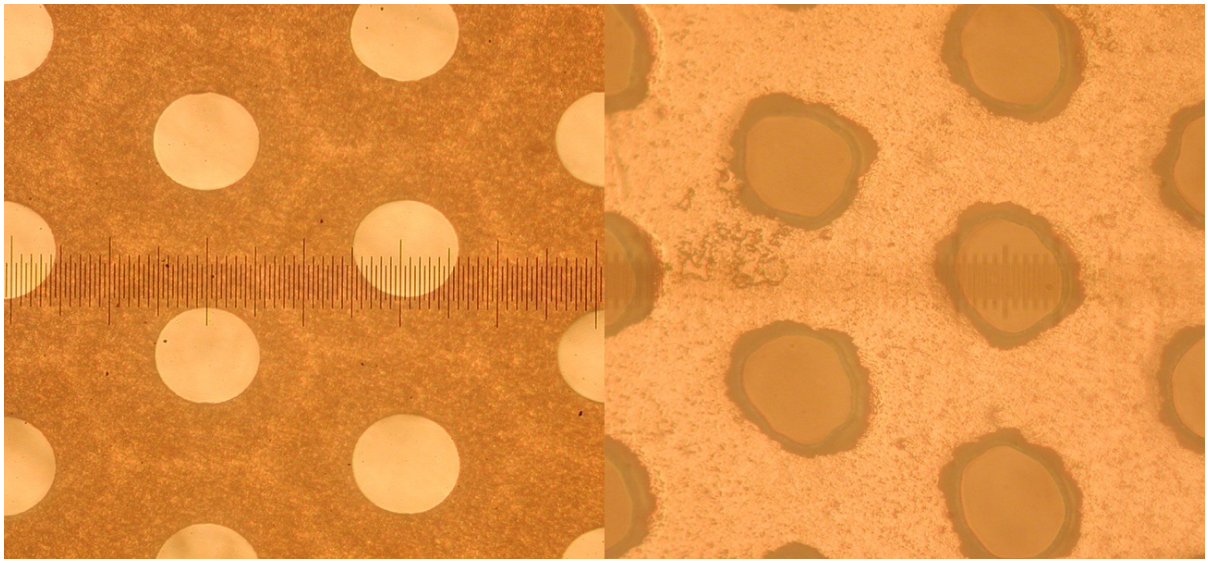

Figure 3.12: 4^{th} generation single-mask GEM. Microscope picture of the top electrode (left frame) and of the bottom electrode (right frame).

In the present case, the GEM is immersed into an acidic copper sulphate ($CuSO_4$) solution and its bottom electrode is connected to the positive terminal of a power supply. The unprotected upper copper layer is mildly eroded, while the lower one is quickly electroetched on the internal face only, the external one being shielded by the photoresist. The supplied current stimulates the oxidation of the zero-valence metallic copper, that dissolves in the electrolyte as doubly charged Cu^{2+} cations, which then combine with free SO_4^{2-} anions.

When the electroetching starts, the electric field in a GEM hole is rather homogeneous, the field lines are approximately parallel to each other and they are evenly distributed in a cross sectional plane. This leads to a uniform etching of the GEM bottom copper layer, with the insulator acting as a mask. After a few minutes, the electrode thinning locally modifies the resistance, creating a region of higher resistivity in the centre of the hole. The field lines deviate towards the edges, following the lowest-impedance path and giving rise to a radial electric field gradient. As the process continues, the hole centre progressively increases its resistivity and becomes harder to erode, while the growth of current density at the border produces quick and irregular etching-rate variations. This causes a significant over-etching, degrades the hole contour and leaves spikes that make the GEM more likely to discharge. Figure 3.12 shows microscope pictures of an electroetched GEM. Although its top electrode (left frame) has well-defined holes, the pattern on the opposite side (right frame) is highly irregular and cannot be considered satisfactory.

3.6 Electrochemical active corrosion protection

In the words of Ulick Richardson Evans, the British chemist who is often considered as the father of the corrosion science:

> "Corrosion is largely an electrochemical phenomenon, [which] may be defined as destruction by electrochemical or chemical agencies."

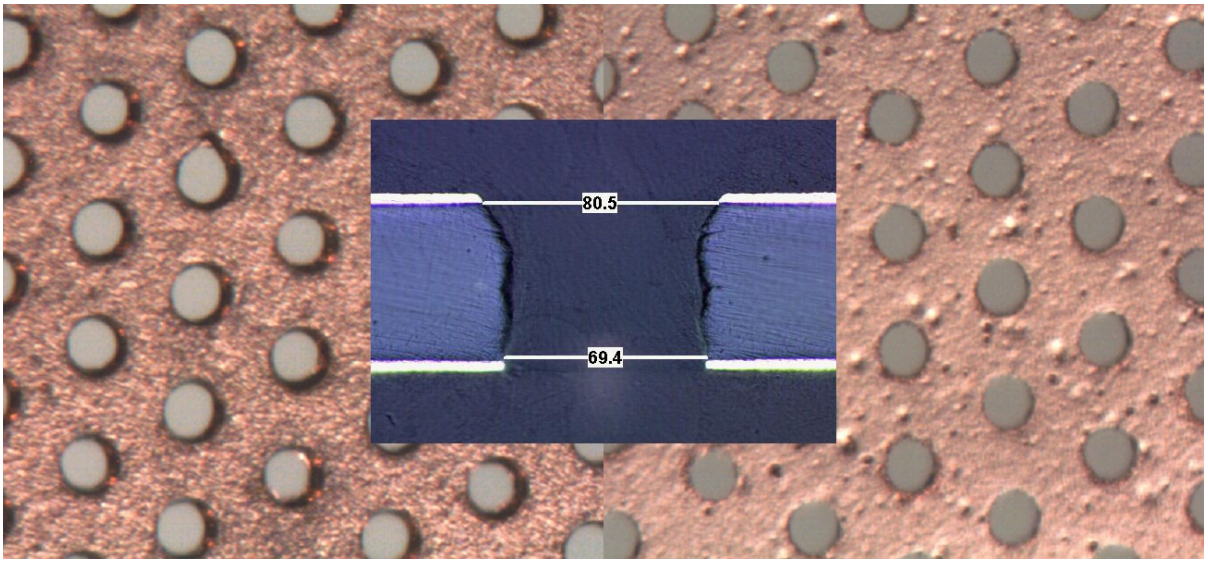

Figure 3.13: 5th generation single-mask GEM. Microscope picture of the top electrode (left frame), of the bottom electrode (right frame) and cross section picture on the axial plane of a hole (central frame). All the dimensions are given in microns.

Indeed, when a metal is immersed into a corrosive liquid, a voltage drop appears between the object and the metallic walls of the etching bath. By applying a greater potential with reverse polarity through an external power supply, one can stop the reaction and make the object totally inert to the chemicals. This technique, known as electrochemical active corrosion protection, finds application in several industrial fields, from the protection of boat hulls against sea water to the protection of pipes against corrosion in humid ground.

The approach can be adapted to the manufacturing of single-mask GEMs, by grounding the upper electrode of a foil immersed into a chromic acid solution, while supplying a positive voltage of 3 V to the lower electrode and to the walls of the bath. The inverse current drawn from the GEM top copper layer protects it against corrosion, while the bottom one is externally shielded by photoresist and internally etched from the apertures in the polyimide, that act as a mask. This is in sharp contrast with the reverse electroplating technique presented in the previous section, where the upper electrode of a GEM immersed into an appropriate electrolyte is left unprotected and the lower one is electroetched by the injection of a direct current. The exploitation of the traditional isotropic chemical etching based on chromic acid solves the issues caused by electroetching in the 4th generation of single-mask GEMs.

The time required to fully etch the holes varies from 5 to 10 minutes, depending on the copper thickness. The process is stopped only when the hole diameter on the bottom layer equals the hole width on the top one. This copper over-etching leaves large rims on the lower face, that can be removed with a fast polyimide etching (about 30 s) after stripping the photoresist. In this way very steep holes can be made, with almost no rims on either sides.

Figure 3.13 shows the top (left) and bottom (right) electrodes of a 5th generation single-mask GEM, as well as a representative cross section picture (centre). The holes in both copper layers are perfectly defined, with no over-etching or spikes. The average upper diameter is $85 \pm 6\,\mu m$, while the lower one is $69 \pm 3\,\mu m$.

Moreover, the electrochemical active corrosion protection technology is compatible with roll-to-roll processing and therefore suitable not only for large-area, but also large-volume productions.

Table 3.1: Maximum voltage and leakage current of 5th generation single-mask GEMs. V_{max} is the lowest difference of potential that causes the onset of discharges in dry air without radiation. I_{leak} is the corresponding leakage current at the sparking limit.

Specimen	No rim		$\simeq 1\,\mu$m rim		$\simeq 2\,\mu$m rim	
	V_{max} [V]	I_{leak} [nA]	V_{max} [V]	I_{leak} [nA]	V_{max} [V]	I_{leak} [nA]
1	590	3.42			600	9.15
2	600	0.73	635	5.35	670	10.10
3	590	6.10	645	4.07	675	11.40
4	600	0.69			660	11.20

The second and third columns of Table 3.1 give the discharge voltage in dry air and the corresponding leakage current at the sparking limit for four specimens with active area of $10 \times 10\,\text{cm}^2$. The tests, performed in a clean room according to the procedure described in Section 2.4.1, classify all of the specimens as eligible for use in a detector. Nevertheless, when housed in a test box and operated in Ar:CO_2 70:30 in the presence of ionizing radiation, the foils appear to be very delicate. Even though they are not particularly prone to discharging, the chance for a single spark to cause significant damage is quite high. In fact, within a few minutes of operation, a discharge event has a fairly large probability to create a low-resistivity bridge between the two GEM electrodes, making it impossible for the power supply to maintain the required high-voltage difference. One can attempt to recover the foil by using a low-voltage generator to inject an intense current and burn the ohmic contact like a fuse. However, this has to be considered as an emergency procedure and does not provide a lasting solution. The GEM robustness against sparks can be improved by introducing a non-zero, but still very small rim. For example, dipping the foil into chromic acid for about 30 s results in a rim a few microns wide, enough to ensure sufficient robustness against discharges. The rightmost columns of Table 3.1 show the performance boost in terms of maximum sustainable voltage that originates from a modest rim. The higher leakage current at the sparking limit is a normal consequence of the increased difference of potential and should not raise any worry, as it remains in the order of a few nA. Although many efforts have been done to eliminate the rim, it has been demonstrated that in 5th generation single-mask GEMs a minimal rim of a few microns is mandatory for safe operation. The electrochemical active corrosion protection technology provides us with a powerful and precise method to finely tune the rim according to the needs.

Once safe detector operation is secured thanks to a satisfactory tolerance to discharges, one can probe the GEM performance, identify the possible weak points and eventually further develop the technology. The studies are best done on a single-GEM chamber, in order to disentangle the intrinsic properties from other effects due to the coupling between adjacent foils. However, the first laboratory tests carried out on a single-GEM prototype reveal poor gas gains even at the highest applicable voltages, to the point that the signal cannot always be easily discriminated from the background random noise. For this reason, the measurements presented in the rest of the current section are based on a double-GEM structure.

The chamber is assembled using a standard test box like the one described in Section 2.4.1. The anode is a $10 \times 10\,\text{cm}^2$ unsegmented copper plane with a feedthrough contact that extends until outside the box frame. The contact is in turn wired to a LEMO 00 female chassis socket[1], mounted on the patch-panel sitting just outside the chamber wall. The same patch-panel also accommodates several SHV male chassis sockets[2], connected to the high-voltage feedthrough contacts with 1 MΩ safety resistors. The

[1] LEMO type ERA.00.250.NTLW, Fischer type D 101 A004, Huber-Suhner type 22 QLA 01-0-2
[2] Radiall type R317.580, Suhner type 22 SHV 50-0-2

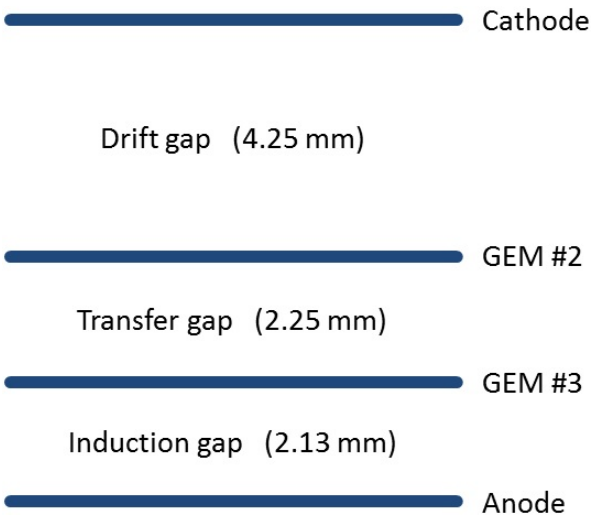

Figure 3.14: Schematic view of the double-GEM detector. From top to bottom: the cathode (or drift electrode), the drift gap (or conversion gap), the GEM specimen 2, the transfer gap, the GEM specimen 3, the induction gap and the anode, which is used as the readout electrode.

use of several high-voltage channels biased by independent power supplies is usually preferable over the alternative resistive divider approach in the early R&D phase. The adopted solution, although more complex to setup and operate, offers much greater freedom in the choice of the voltages, thus enabling the investigation of a wider range of detector aspects. The fiberglass frame of the test box houses the gas inlet and presents on its top face a groove with an O-ring for coupling to the dismountable roof, where the gas outlet and the Kapton entrance window are located. The GEM specimen 3 is stretched on a frame and placed over the anode at a distance of 2.13 mm. The GEM specimen 2 is then positioned 2.25 mm above it. The stack is completed by the drift electrode, made out of a single-side copper-covered Kapton foil, that delimits the 4.25 mm thick conversion gap. Figure 3.14 shows a schematic view of the detector.

The measurements reported in the rest of this section are performed in Ar:CO_2 70:30 at standard ambient temperature and pressure. The chamber is flushed in open-loop configuration with a gas flow of about 5 l/h. The water content, surveyed by means of a hygrometer placed at the end of the gas line, is in the order of 100 ppm. Figure 2.22 (right) is a picture of the realized double-GEM detector, hooked up to the gas, high-voltage and readout lines and fixed to a movable stand in front of the copper X-ray tube that is used as the radiation source throughout the characterization. The photon beam is shaped by a long collimator of 1 mm in diameter, which is also visible in the picture.

As mentioned in Section 3.3, when dealing with asymmetrical holes it is not in principle clear which GEM orientation would be the best, if with the larger diameter towards the cathode or the anode. In the former case, the GEM is colloquially said to be in “open top” configuration, while the latter condition is referred to as “open bottom”. The GEM performance will be studied for both orientations, taking care to apply the same environmental conditions, the same voltage settings and similar radiation fluxes, in order to allow for a critical comparison.

Figure 3.15 displays two spectra acquired with the double GEM in open top (left) and open bottom (right) configuration, respectively. In both cases, the drift field is set to 3 kV/cm, the transfer and the induction fields are 2 kV/cm and the voltage difference across the foils is fixed to 430 V. The achieved energy resolution, extracted from Gaussian fits to the energy spectra, is 23.5% full width at half maximum (FWHM) in the first case and 20.8% FWHM in the second.

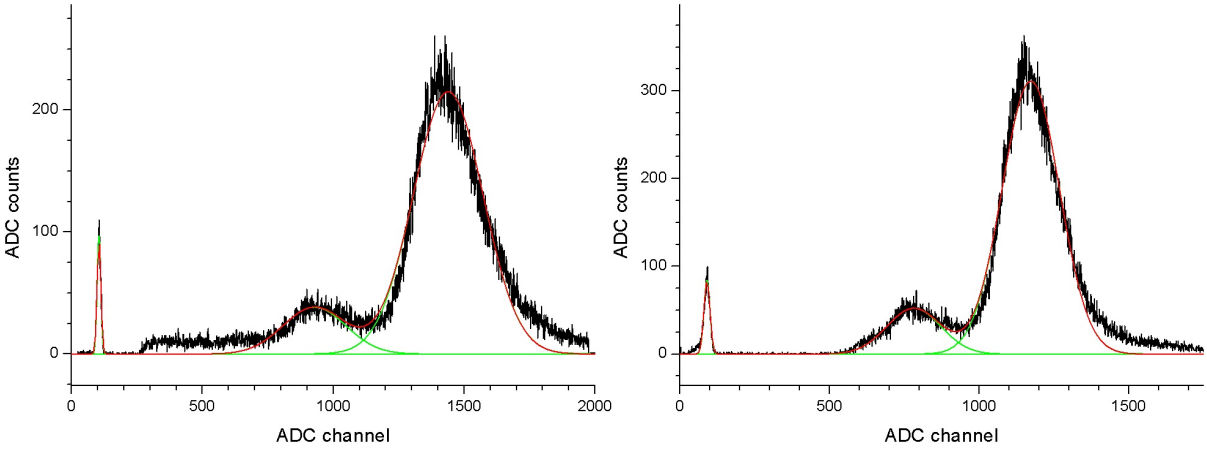

Figure 3.15: Energy spectra of a 5th generation single-mask double GEM.

It is interesting to observe how the different electric fields influence the effective gas gain and the energy resolution. For this purpose, the chamber is prepared with the two GEMs in open top configuration and it is hooked up to a pulse-height readout chain comprising a charge preamplifier, a shaper amplifier and an analog-to-digital converter, in cascade. The voltage difference across each foil is maintained at 430 V, while the drift, transfer and induction fields are alternatively scanned. For each set of fields, an energy spectrum is acquired and subsequently fitted with three independent Gaussian curves corresponding to the photopeak, the argon escape peak and the pedestal. The fit parameters are then used to compute the variation of the effective gain and the energy resolution.

Figure 3.16 is obtained fixing the transfer field at 2 kV/cm, the induction field at 3 kV/cm and letting the drift field vary from 0.25 to 6 kV/cm. For low drift-field values, both the effective gas gain and the energy resolution are, within the experimental uncertainties, in a plateau region. Around 4 kV/cm, however, the effective gain starts to drop and the corresponding energy resolution becomes worse. This can be understood by considering that a higher field in the conversion gap reflects in a less efficient electrostatic focusing at the entrance of the first amplification stage, leading to progressively more important losses of ionization electrons on the GEM copper layer facing the cathode.

Figure 3.17 summarizes the results obtained when setting both the drift and the transfer field to 2 kV/cm and changing the induction field between 0.25 and 8.5 kV/cm. The energy resolution is better than in Fig. 3.16 thanks to the interposition of an energy-selective photon filter between the radiation source and the chamber, which cleans the spectrum emitted by the X-ray tube by removing the copper K_β line (cf. Section 2.4.3). The trend of the two curves in Fig. 3.17 is explained with an increasing electron extraction efficiency from the second amplification stage.

Finally, in Fig. 3.18 the transfer field is scanned from 0.25 to 8.5 kV/cm, while keeping the drift field at 2 kV/cm and the induction field at 3 kV/cm. The behaviour is the convolution of an increasing extraction efficiency from the first amplification stage and a progressive loss of charge on the second one as the field value increases. The inversion of the trend manifested in the gain growth at very high transfer fields is due to the extension of the Townsend multiplication region outside the GEM holes and into the transfer gap for both amplification stages.

Figure 3.19 shows the total effective gas gain as a function of the voltage across each stage of the double amplification structure, for the open top and the open bottom configurations. The two curves are obtained following the procedure detailed in Section 2.4.4, scanning the bias voltage up to the discharge point and taking care to apply similar experimental conditions for both GEM orientations. Throughout

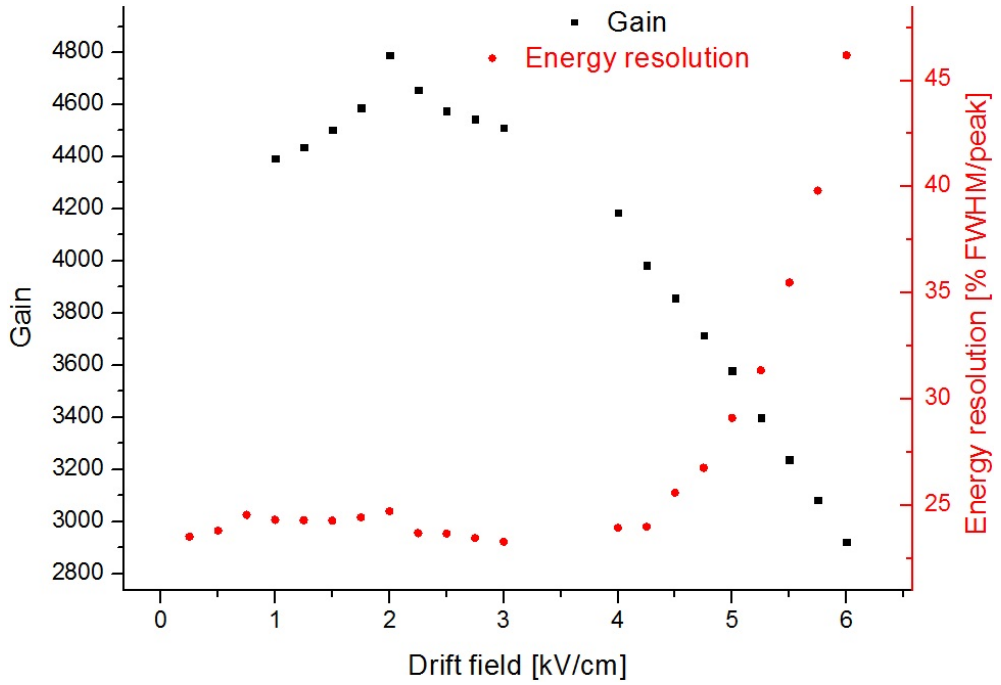

Figure 3.16: Drift-field scan of a 5th generation single-mask double GEM.

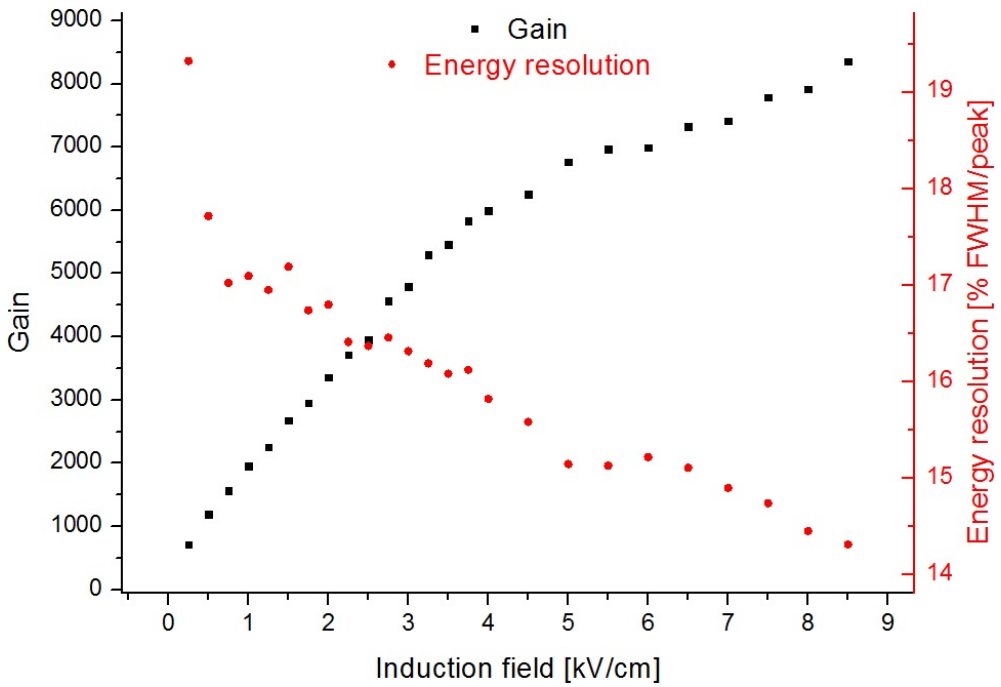

Figure 3.17: Induction-field scan of a 5th generation single-mask double GEM.

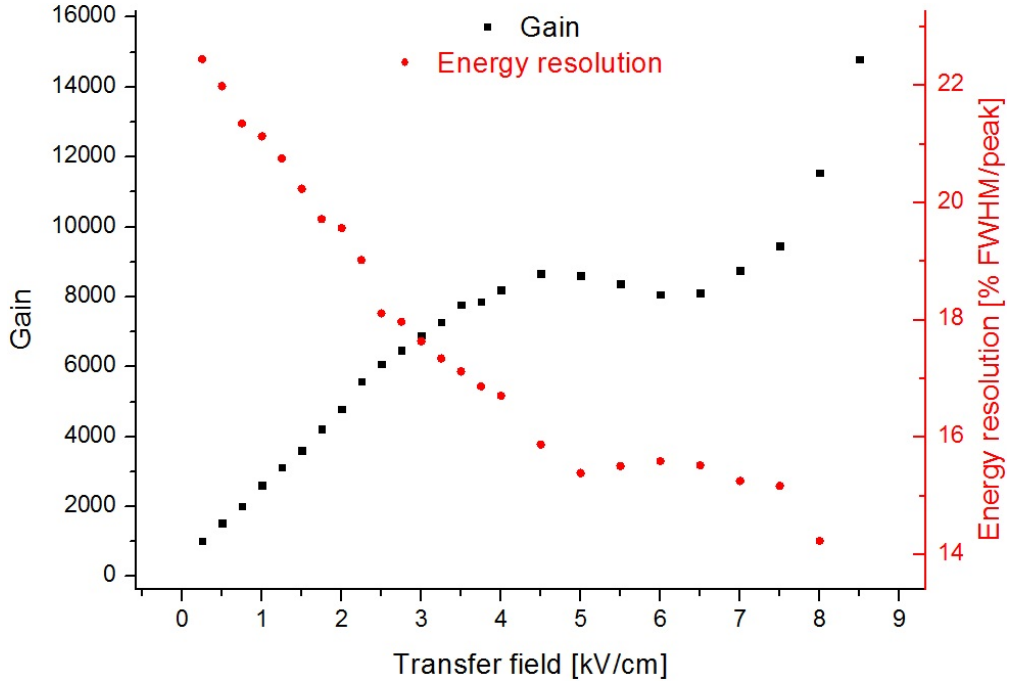

Figure 3.18: Transfer-field scan of a 5th generation single-mask double GEM.

the data taking, the drift and transfer fields are maintained at 2 kV/cm and the induction field at 3 kV/cm. The absolute value of the gain is calibrated with 430 V on the foils in open top and with 425 V in open bottom configuration, while the current-mode measurements are performed with a copper X-ray rate of $152.9 \pm 1.2\,\mathrm{kHz/mm^2}$ in open top and of $208.1 \pm 2.1\,\mathrm{kHz/mm^2}$ in open bottom configuration. The gain error is computed by combining the rate uncertainty with the uncertainty on the measured anode current. The experimental data are then fitted with a curve of the form of Eq. (3.2), where G_c, G_e and V_e are the fit parameters. The constant term models the deviation of the gain from a purely exponential behaviour at the lowest voltages.

$$G = G_c + G_e \exp \frac{\Delta V}{V_e} \tag{3.2}$$

The values in Fig. 3.19 represent the effective gas gain at which the detector stabilizes a while after the beginning of the irradiation. In the very first moments, however, the amplification factor changes over time due to charging-up phenomena. Figure 3.20 depicts this effect for an open top (left) and an open bottom (right) double GEM. The data, showing the relative gain variation as a function of the time elapsed from the start of the irradiation, are obtained with the method illustrated in Section 2.4.5. In order to allow for a comparison to be made, it is important to perform the two gain-stability scans with the chamber in the same conditions. The drift and transfer fields are fixed to 2 kV/cm and the induction field to 3 kV/cm. Since the charging-up is rate-dependent, one has to ensure that each amplification stage sees the same electron flux in the two configurations. For the first GEM this is achieved by irradiating with similar copper X-ray rates: $1591 \pm 6\,\mathrm{Hz/mm^2}$ in the open top and $1523 \pm 4\,\mathrm{Hz/mm^2}$ in the open bottom configuration. To satisfy the condition also on the second stage, one has to operate the first GEM at the same effective gas gain in the two configurations. In turn, the different behaviour highlighted in Fig. 3.19 requires a voltage specific to the orientation. Using the fit parameters of Eq. (3.2), it results that a gain of 1100 is achieved with 394 V across the open top and 403 V across the open bottom foils. The experimental data in Fig. 3.20 cannot be fitted with only one exponential curve, presenting a very

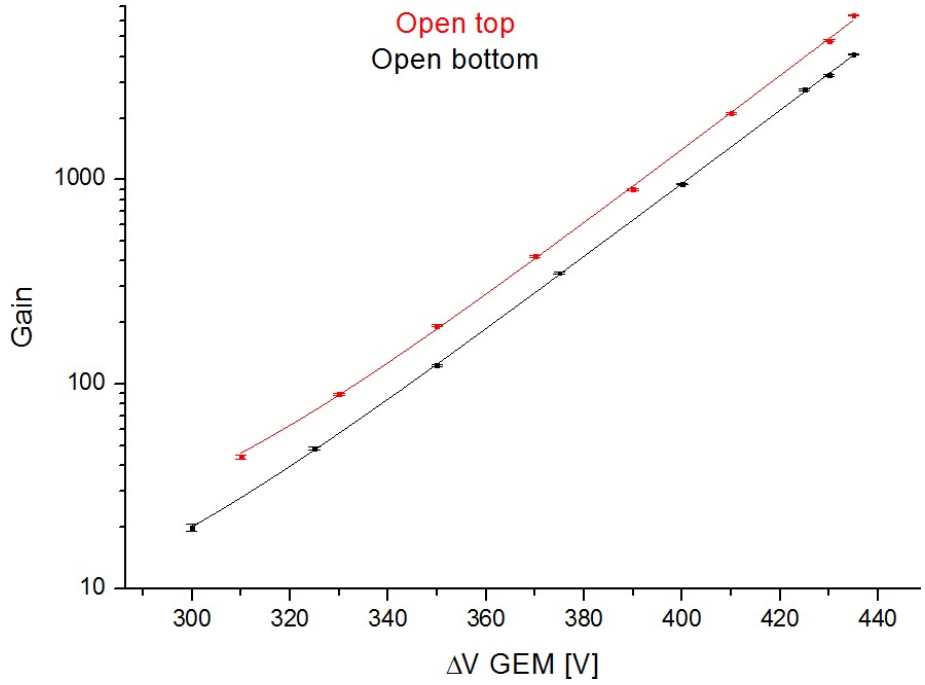

Figure 3.19: Gain curves of a 5th generation single-mask double GEM.

steep initial decay followed by a milder exponential decrease. The gain variation is significant in both GEM orientations, and much more important than in double-mask foils.

As it can be seen from the plots, 5th generation single-mask GEMs have quite different performance depending on their orientation. This is not surprising and it is a consequence of the conical shape of the holes. The maximum applicable voltage in Ar:CO_2 70:30 at atmospheric pressure is 435 V, as the discharge probability becomes too high at 440 V. This corresponds to a maximum achievable gain of 6370 ± 50 and 4100 ± 40 in the open top and open bottom configuration, respectively, a result considerably worse than for traditional GEMs. Moreover, the charging-up appears to be significant, strongly affecting the gain stability.

3.7 Hole biconical remolding

The perfected polyimide-etching chemistry, in conjunction with the electrochemical active corrosion protection, proved to be a valid approach to the manufacturing of single-mask GEMs. Combining the two techniques, it is possible to create neat and precise holes, while leaving clean and polished electrode surfaces. The hole diameters can be finely tuned, the wall steepness can be modified within a wide range and up to high aspect ratios and the rim size can be chosen according to the needs. Lastly, the procedure is cheap, reproducible, it has a high production yield and it is compatible with industrial standards and roll-to-roll processing, thus making it suitable for large-volume productions.

The downsides highlighted at the end of the previous section have to be attributed to the conical shape of the holes and not to the technology itself. For example, the lower gas gain with respect to traditional GEMs originates from the lack of field-focusing elements inside the apertures. The biconical shape of double-mask GEM holes indeed has the effect of squeezing the field lines, giving rise to a higher electric field in the central region that enhances the charge multiplication. Instead of looking for

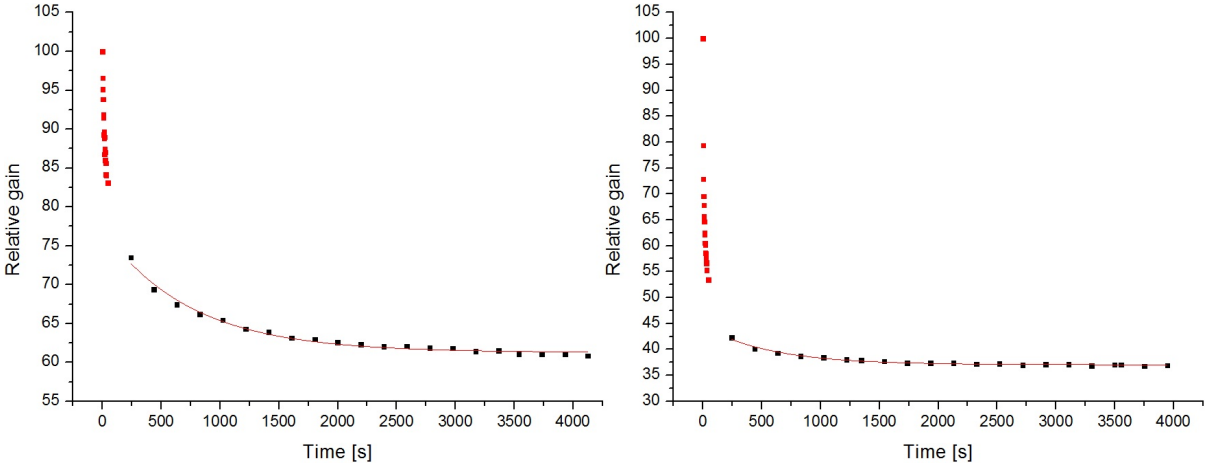

Figure 3.20: Gain stability of a 5th generation single-mask double GEM in open top (left frame) and in open bottom (right frame) configuration.

a different manufacturing technology, one should rather address the low-gain problem by tweaking the polyimide etching and the electrochemical protection to reproduce biconical openings.

The forming of biconical holes through single-mask processing is done following the steps delineated in Section 3.6. The key point is the revision of the composition of the polyimide-etching chemistry, that has to be adjusted in order to create cavities with much lower aspect ratio. In this way the Kapton post-processing, originally introduced to remove the excess insulator after the second copper-etching phase, now has the effect of remolding the apertures into a double-conical shape.

Figure 3.21 shows a microscope picture of the upper (left) and lower (right) electrode of a 6th generation single-mask GEM, together with an axial cross section (centre) of a hole. The photos of the electrodes refer to a foil with $10 \times 10\,\mathrm{cm}^2$ active area, while the cross section comes from a $1 \times 1\,\mathrm{cm}^2$ specimen intended for destructive analyses. The specimens are used in a technology assessment for a possible upgrade of the $1.6 \leq |\eta| \leq 2.4$ region of the CMS experiment at CERN [55–58]. The holes, although produced with the single-mask technology, have a biconical shape that resembles the one of double-mask GEMs. The average opening diameters, measured on several holes, are also comparable to the double-mask characteristic values: $70 \pm 6\,\mu\mathrm{m}$ on the top layer, $69 \pm 2\,\mu\mathrm{m}$ on the bottom layer and $51 \pm 3\,\mu\mathrm{m}$ in the middle point. The lower electrode, corresponding to the upper layer in the cross section picture, presents slight copper thickness variations around the holes. This is understood to be an edge effect taking place on the materials attacked during the electrochemically protected etching. Since the phenomenon affects only the most external zones, it is significant in the small-area specimen, but it is expected to be much weaker in larger foils. Moreover, its effects can be minimized by introducing an additional hole pattern a few centimetres outside the detector area. In this way the anomalous etching will interest only the external holes, leaving the active area untouched.

The images in Fig. 3.22 pertain to a full-size GEM as the ones for the KLOE-2 inner tracker (cf. Section 2.2.6). This sample did not meet the quality standards and was therefore used for tests. The foil has an active area of about $1 \times 0.7\,\mathrm{m}^2$, that exceeds by far the dimensional limits of the double-mask technology. Both electrodes appear to be well polished, with uniform and perfectly defined apertures. The cross section picture in the foreground displays a flawless symmetrical biconical hole, where it is almost impossible to tell which side was patterned first. Given the large area of the specimen, no copper thickness variation is noticeable. The diameters, averaged over several openings, are 74 ± 3, 79 ± 9 and $48 \pm 5\,\mu\mathrm{m}$ on the top, bottom and in the middle point, respectively.

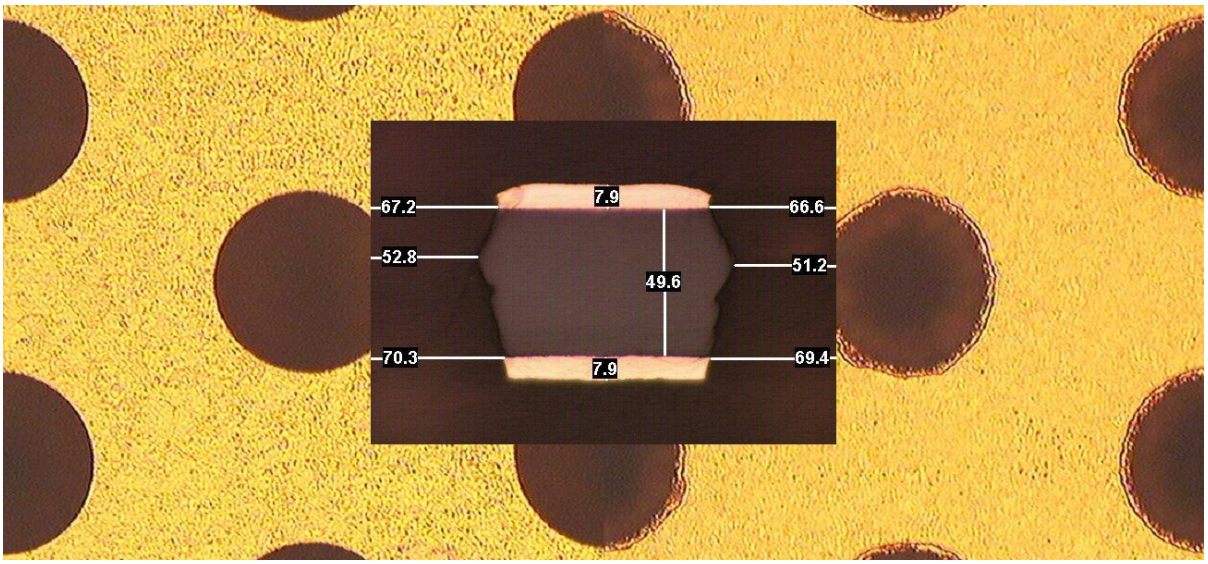

Figure 3.21: 6th generation single-mask GEM for CMS. Microscope picture of the top electrode (left frame), of the bottom electrode (right frame) and cross section picture (central frame). As opposite to Fig. 3.3, 3.11, 3.13 and 3.22, the cross section picture is not centred on a hole, but rather shows two holes at the sides. All the dimensions are given in microns.

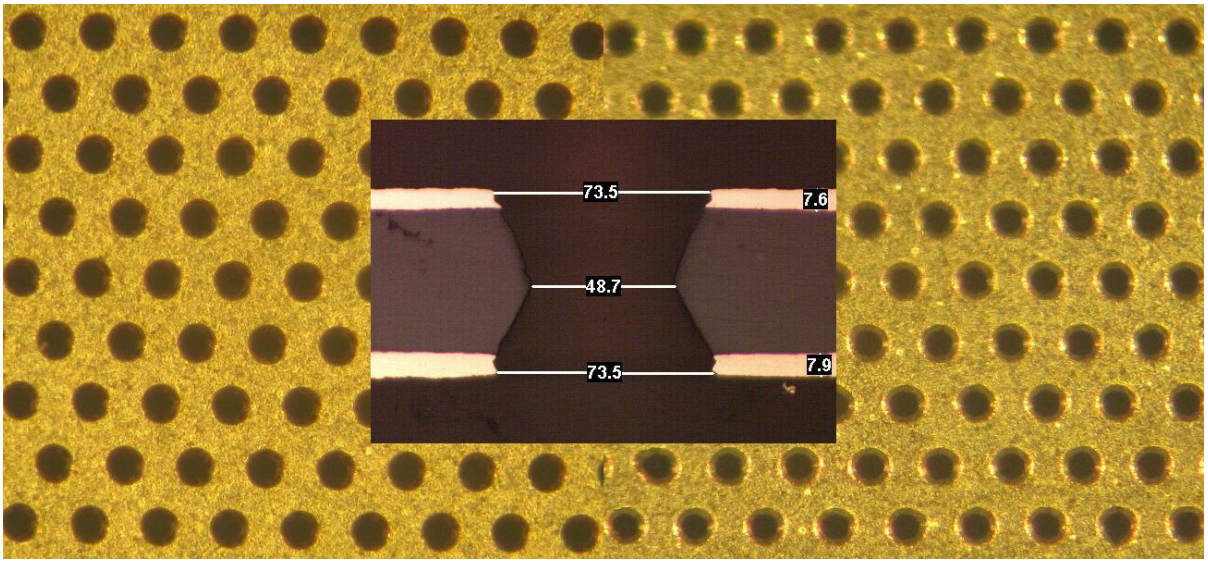

Figure 3.22: 6th generation single-mask GEM for KLOE-2. Microscope picture of the top electrode (left frame), of the bottom electrode (right frame) and cross section picture on the axial plane of a hole (central frame). All the dimensions are given in microns.

Table 3.2: Leakage current of 6th generation single-mask GEMs at 510 V. The measurements are performed in dry air without radiation.

Specimen	V [V]	I_{leak} [nA]
1	510	0.4
2	510	0.3
3	510	0.2
4	510	0.2

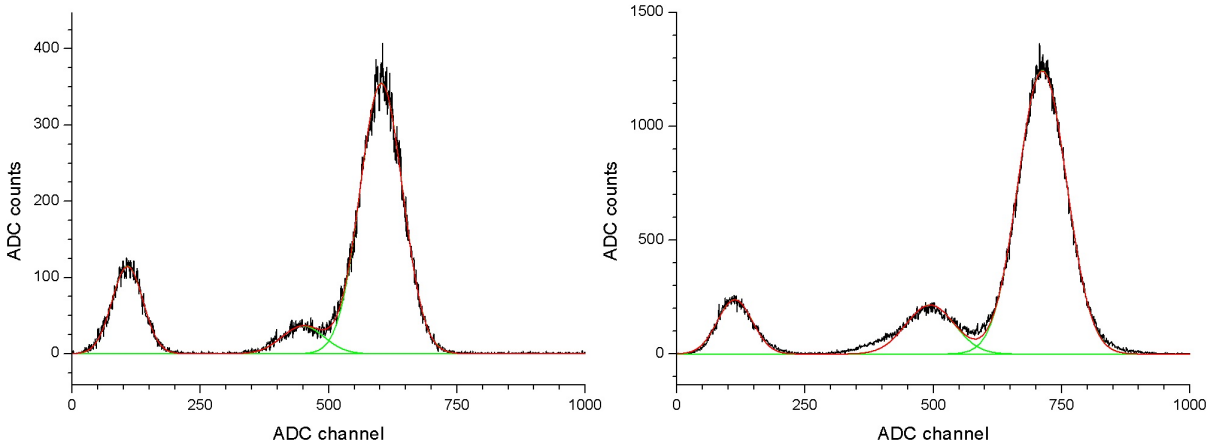

Figure 3.23: Energy spectra of a 6th generation single-mask single GEM.

The measurements reported in the following are performed on $10 \times 10\,cm^2$ GEMs of the type in Fig. 3.21. Table 3.2 summarizes the leakage current in air at standard ambient temperature and pressure with 30% relative humidity for the four tested foils. Given the advanced development stage reached at this point, the purpose is here to validate the specimens rather than to determine the breakdown voltage. For this reason, a maximum difference of potential of 510 V is used, even though no sparks are observed and higher voltages could be applied.

The specimens are first characterized in the single-GEM configuration, thanks to the improved charge multiplication capability expected from the better electrostatic lensing properties of the biconical holes. The GEM specimen 1 is chosen to be mounted in a test box similar to the one described in Section 3.6. In the chamber, a $10 \times 10\,cm^2$ unsegmented copper plane located 2.15 mm below the foil serves as the anode, while a single-sided copper-clad Kapton sheet stretched on a frame defines the 3.05 mm thick conversion gap. The readout plane is maintained at ground potential and the other three electrodes are biased with independent high-voltage power supplies through 1 MΩ safety resistors.

The chamber is flushed in open-loop configuration with about 5 l/h of Ar:CO_2 70:30 at standard ambient temperature and pressure. The water content is surveyed by means of a hygrometer placed at the end of the gas line, and it is in the order of 100 ppm. The radiation source is an X-ray tube with a copper anode, whose beam is trimmed by a long cylindrical collimator of 1 mm in diameter. The photons reaching the detector's active volume have a monochromatic spectrum, thanks to the employment of the nickel filter described in Section 2.4.3.

Figure 3.23 presents two energy spectra acquired applying a drift field of 2 kV/cm, an induction field of 3 kV/cm and a voltage difference of 480 V across the GEM. The resulting energy resolution is 19.7% FWHM in open top configuration (cf. Fig. 3.23 left) and 18.6% FWHM in open bottom configuration (cf. Fig. 3.23 right).

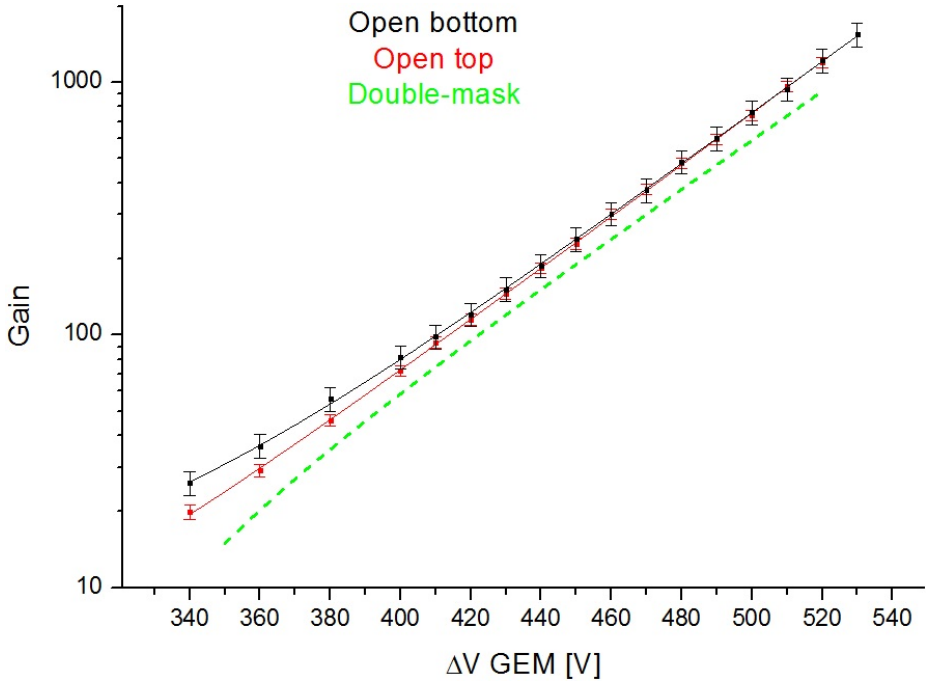

Figure 3.24: Gain curves of a 6th generation single-mask single GEM.

The presence of field-focusing elements in the holes of 6th generation single-mask GEMs is expected to boost their charge multiplication capability with respect to that of their predecessors. Moreover, the z-symmetry of the biconical apertures can anticipate a similarity in behaviour between the two possible orientations of the foil. These conjectures are shown to be true in Fig. 3.24, which displays the gain curves for the single-GEM detector in open top and open bottom configuration. The gain curve of a standard double-mask single-GEM chamber, flushed with the same gas mixture and operated under similar experimental conditions, is also shown as a benchmark. The data are acquired following the procedure detailed in Section 2.4.4, with the voltage scans ranging up to the discharge point. The drift field is constantly kept at 2 kV/cm and the induction field at 3 kV/cm. The absolute value of the gain is calibrated with 480 V across the foil for both GEM orientations, while the current-mode measurements are carried out with a copper X-ray rate of 18.0 ± 0.9 kHz/mm^2 in open top and of 21.2 ± 2.3 kHz/mm^2 in open bottom configuration. The fitting functions are exponentials of the form of Eq. (3.2).

Figure 3.25 complements the information provided by the gain curves, illustrating the effective gas gain variation over time. The data are sampled following the procedure described in Section 2.4.5, with the detector irradiated by a photon flux of about 1 kHz/mm^2. The high-voltage power supplies are set to maintain 2 kV/cm in the conversion region, 3 kV/cm in the induction region and 480 V across the GEM in open top configuration, corresponding to a stabilized gain of 480.

Summarizing, the 6th generation of single-mask GEMs marks a significant technological advancement. The remolding of the holes into biconical shape is performed simply by adjusting the composition of the polyimide-etching solution, without adding any supplementary manufacturing steps. Therefore, the whole procedure remains compatible with roll-to-roll machinery industrial standards, that are necessary for the production of large detector volumes at no cost increase. The biconical shape, which results in more dielectric material inside the openings, drastically reduces the discharge probability and makes the foil more robust against the effects of sparks. As a consequence, zero-rim apertures can be used, resulting in an improved gain stability over time, as demonstrated in Fig. 3.25. The new profile of the

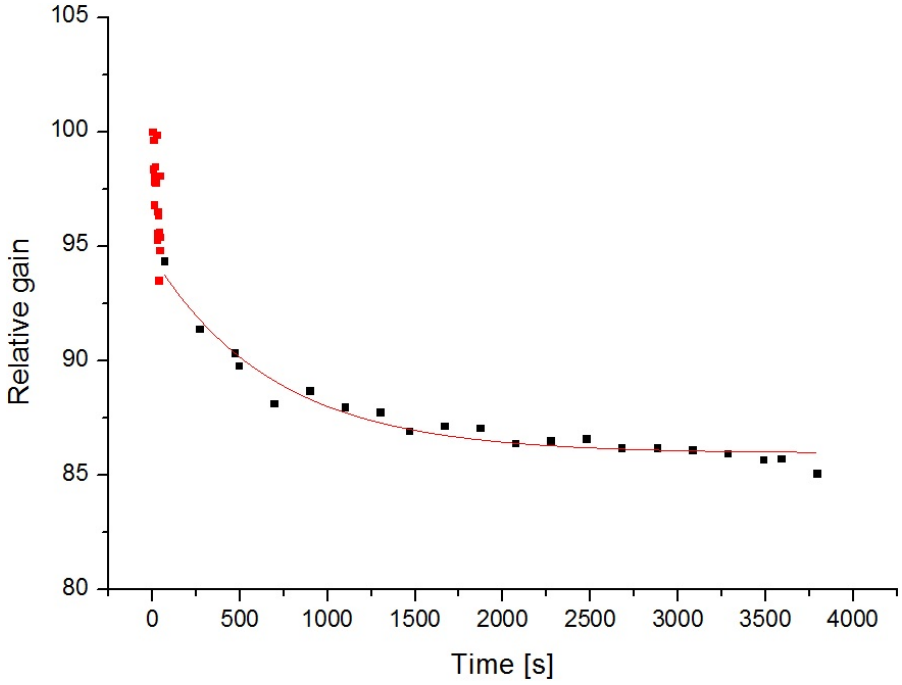

Figure 3.25: Gain stability of a 6th generation single-mask single GEM.

insulator has better electric field lensing properties that greatly enhance the charge multiplication capabilities with respect to the previous generations. Figure 3.24 shows that 6th generation single-mask GEMs provide gas gains that are compatible with the ones of the traditional double-mask foils, both for a given bias voltage and in terms of maximum achievable gain. At the same time, the z-symmetry of the holes grants equal behaviour in the two possible GEM orientations, thus simplifying the detector assembly. As from Fig. 3.24, the maximum applicable voltage is 520 V in open top configuration, corresponding to an effective gas gain of 1200 ± 60, and 530 V in open bottom, with a gain of 1540 ± 160.

Given the widespread use of cascaded amplification stages in the form of triple-GEM detectors, studies have been performed also in such layout. The employed test box has COMPASS-like bi-dimensional cartesian strips, on two levels, linked to Panasonic P5KS high-pitch board-to-board connectors for signal routing to the readout ASICs. During the laboratory measurements reported in following, all the channels are shorted together on the interface boards plugged to the Panasonic connectors and they are all read out through one single charge preamplifier. The chamber houses the GEM specimens 1, 2 and 3, stacked on top of each other and topped by an unsegmented drift electrode made out of a single-sided copper-clad Kapton foil. The GEMs are in open bottom configuration, because of the slightly better performance seen with this orientation during the tests carried out on the single-stage detector. The induction gap is 2.15 mm thick, the lower transfer gap is 2.23 mm thick, the upper one is 2.22 mm wide and the conversion region extends for 3.25 mm. The high voltage is distributed to the seven non-grounded electrodes through a resistive divider designed on the COMPASS model, with the first stage operating at about 10% higher voltage and the last stage at about 10% lower voltage with respect to the second GEM, in order to decrease the discharge probability [23]. A 10 MΩ safety resistor is applied to the drift bias line and to each line supplying the top electrode of a foil.

The detector is flushed in open-loop configuration with about 5 l/h of Ar:CO_2 70:30 at standard ambient temperature and pressure. Since the copper X-ray gun was not available at this time, a different X-ray tube with a silver target had to be used as the radiation source. The tube emits $K_{\alpha 1}$, $K_{\alpha 2}$ and K_{β}

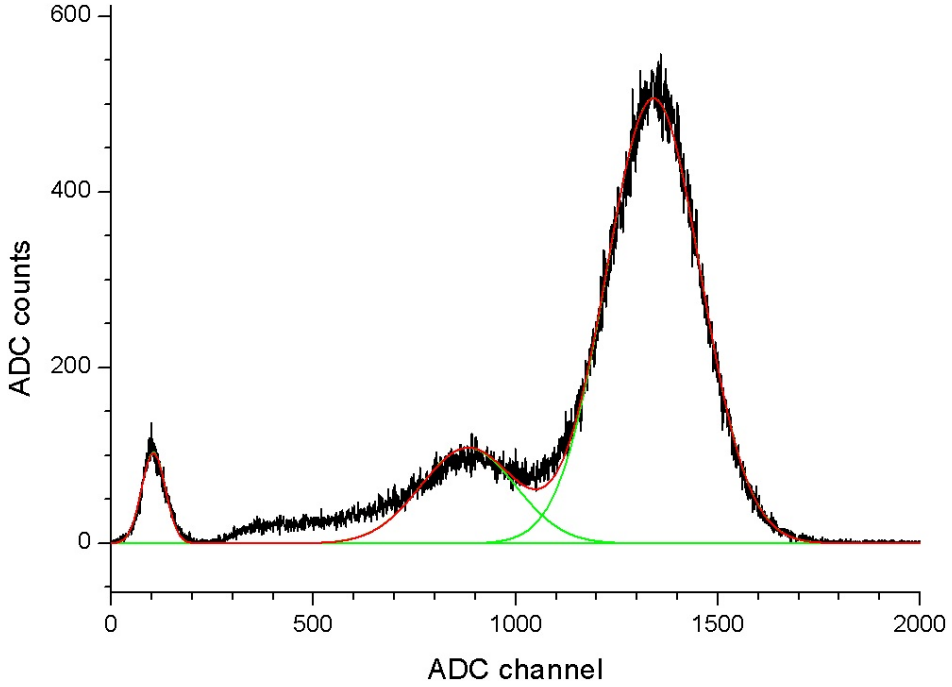

Figure 3.26: Energy spectrum of a 6th generation single-mask triple GEM.

photons of 22.163, 21.99 and 25.004 keV, respectively. Given the poor detection efficiency of the selected gas mixture at such high photon energies, the spectrum is modified with the insertion of a copper sheet after the X-ray tube collimator, which converts part of the incident radiation into copper fluorescence photons. A nickel absorber (cf. Section 2.4.3), placed just in front of the chamber, then reduces the particle rate, removes the copper K_β contribution and suppresses both the bremsstrahlung and the high-energy silver lines, giving rise to a photon spectrum better suited to the experimental needs.

Figure 3.26 shows an energy spectrum acquired with the realized single-mask triple-GEM chamber. The current flowing through the resistive divider is 693 µA, generating a difference of potential of 391, 354 and 309 V across the upper, middle and lower foil, respectively. The drift field is about 2 kV/cm, while the transfer and induction fields are all around 3 kV/cm. The energy resolution extracted from the fit is 22.3% FWHM. Since copper fluorescence photons are emitted in all directions and illuminate all the detector surface, the achieved resolution provides an experimental proof of the good gain homogeneity across the $10 \times 10\,cm^2$ active area.

Figure 3.27 displays the gain curve as a function of the total applied voltage. The calibration is performed in the same regime as Fig. 3.26, with the power supply at 4200 V, while the photon rate used during the current-mode measurements is 419 ± 4 kHz over the whole active area. The fitting function is an exponential of the form of Eq. (3.2). Note that in this case the voltage scan does not extend up to the discharge point and therefore the maximum achievable gain is higher than shown in the graph.

3.8 Stretching and positioning

As stated in the previous sections, the single-mask technology enables the manufacturing of large-area GEMs and, thanks to absence of manual interventions and to the compatibility with roll-to-roll machinery, it also opens the way to the industrialization of the process. In case of large-volume production,

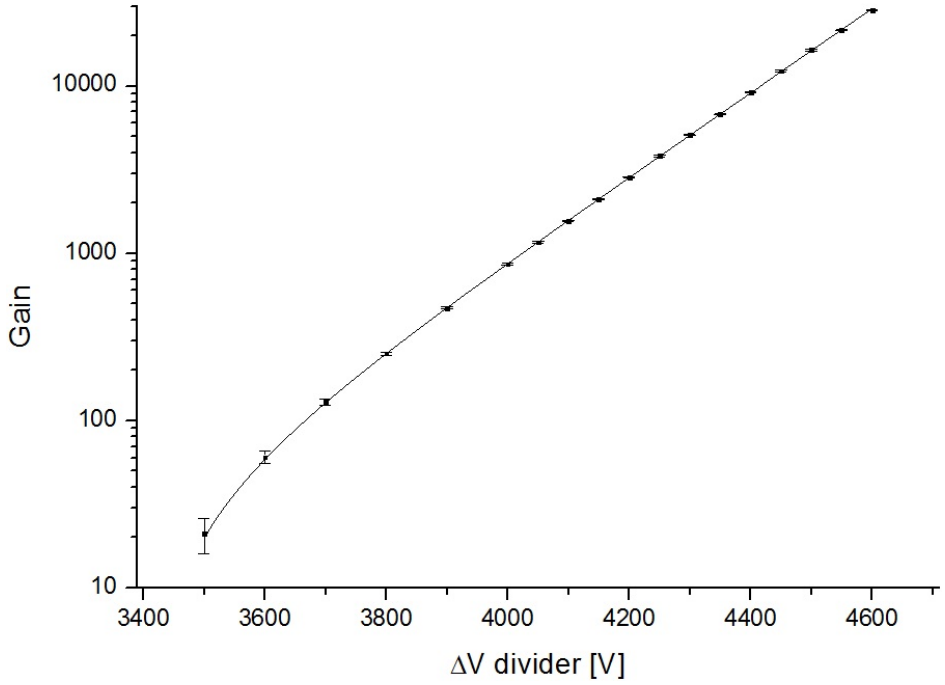

Figure 3.27: Gain curve of a 6th generation single-mask triple GEM.

the bottleneck will be the stretching and framing of the foils, that at the moment of writing this thesis cannot be completely automated.

A possible solution to this hurdle is the use of many very thin spacers distributed over the whole detector surface. These elements work both as spacers and as support structures, maintaining the shape of the GEMs and the distance between them, eliminating the need for external tension. The chamber is assembled simply by laying the unstretched foils on top of each other, housed between two support layers. The first material that comes to mind for this purpose is Nomex honeycomb, the same substance already employed as a reinforcement in the backing of cathode and readout electrodes.

A triple-GEM chamber with $10 \times 10\,\mathrm{cm}^2$ active area has been set up in a standard test box, using double-mask foils separated by honeycomb with cell size of 6.1 mm. No stability problem is noticed during operation with soft X-rays. However, a fine position scan with 25 µm step size, performed using a narrow photon beam from an X-ray tube, reveals severe local efficiency losses, as shown in Fig. 3.28. The cell structure of the honeycomb occupying the drift region is clearly visible from the two count rate drops around 2 and 8 mm in the y-direction. Along the x-axis, on the other hand, no periodic pattern can be identified because the walls of the honeycomb cells are not perpendicular to the scanning line.

The effective width of the honeycomb walls is much greater than their physical thickness of about 15 µm, due to the transverse diffusion of the drifting electrons. The rate never drops to zero because the X-ray collimator has a diameter larger than the honeycomb wall, but the efficiency loss is not negligible. Better results can be achieved with wider cell spacings, slimmer transfer gaps and gas mixtures with a lower transverse diffusion.

The results are at present not satisfactory, but efforts are continuing to validate and optimize this method for use in those applications where cost-effectiveness and ease of production are more important than full efficiency.

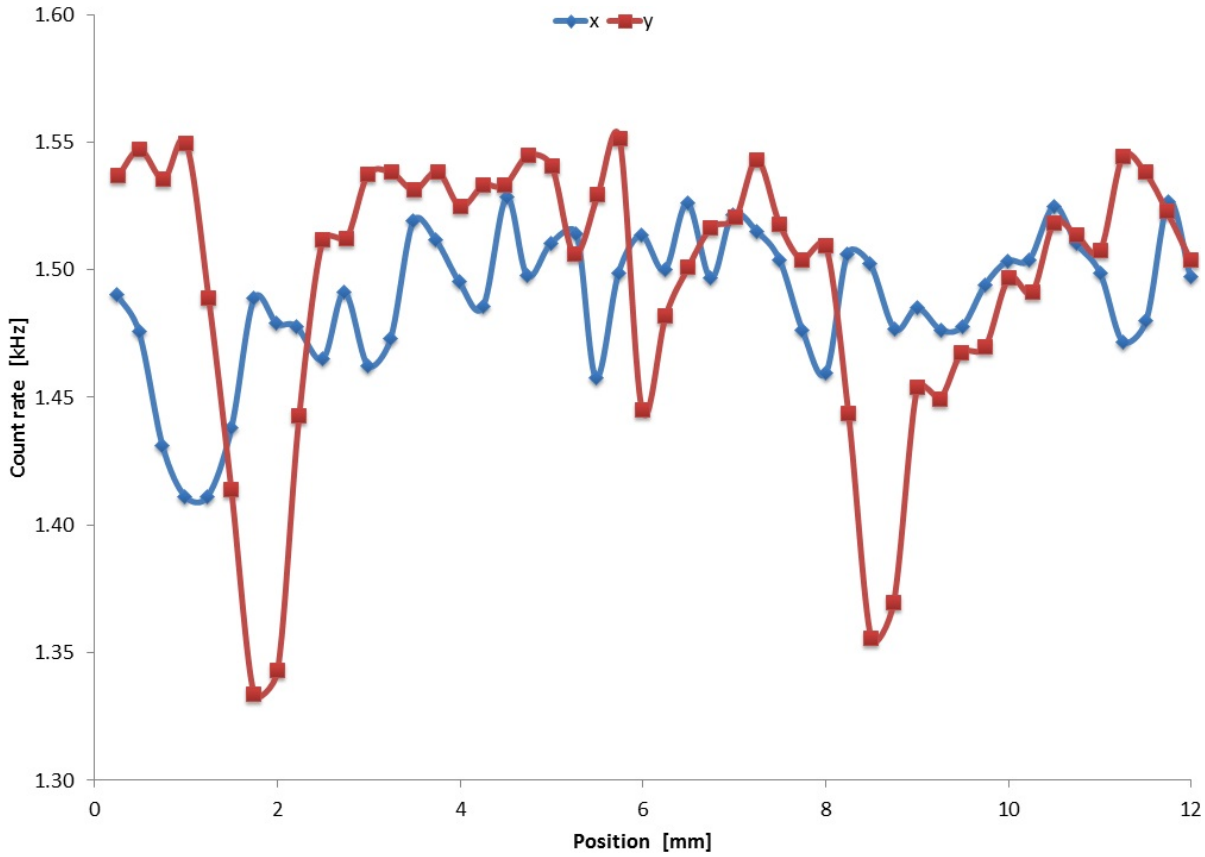

Figure 3.28: Position scan of a double-mask honeycomb triple GEM. The chamber is irradiated with a narrow photon beam and the count rate is measured in different points of the detector. Two scans are performed, proceeding with steps of 25 μm along straight lines corresponding to the x- and y-direction, respectively.

3.9 Conclusions

The original manufacturing procedure of gas electron multipliers requires involved and time-consuming manual interventions that limit the maximum linear dimensions of the foils to about 30 cm. Given the growing demand for large-area GEMs, an effort has started in 2007 to find a new production method that is scalable up to square metre size. The bottleneck, identified in the manual alignment of the two photolithographic masks, is tackled at the root by using one mask only, thus removing any need for alignment. In this novel approach, that goes under the name of single-masking, the foil is pierced layer after layer, from one side to the other. This has required extensive research and testing of the various chemistries available for the etching of the polyimide and of the copper.

The first working prototype, having an active area of about 2000 cm^2, was realized in 2008. The triple-GEM detector, intended for an application in the TOTEM experiment as a possible upgrade of its T1 tracker, attracted a lot of interest in the micropattern gas detector community, but it also showed some flaws, such as lower gas gains with respect to double-mask foils and longer stabilization times. This behaviour was tracked down to the suboptimal shape of the GEM holes, that were widely conical, and to their large rim.

The aspect ratio of the conical openings is increased with the adoption of a quaternary polyimide-etching solution and later with a two-stage etching, that also gives the possibility to finely tune the wall

steepness according to the needs. This attainment has triggered a simulation activity that has highlighted the electric properties of different hole geometries.

The rim problem is faced at first with mechanical protection and then with reverse electroplating, but both techniques turn out to be unsatisfactory. The electrochemical active corrosion protection, on the other hand, gives complete control over the rim size on both faces of the foil, creating perfectly defined apertures, while leaving clean and polished electrode surfaces. However, the laboratory tests reveal a low gas gain, due to the absence of field-focusing elements inside the conical holes, and an improved but still insufficient gain stability, due to the small rim necessary for safe operation. Both issues are solved by adjusting the etching parameters in order to mimic the biconical shape of double-mask GEMs.

The final performance is compatible with the one of traditional foils, and the method can be extended up to square metre size. The dimensions are in principle limited only by the size of the base material, that is delivered in rolls 24 inches (61 cm) wide and about a hundred metres long. Since the base material is the same as the one employed for traditional GEMs, one can expect outgassing, aging and radiation hardness to be as good. Moreover, the new process is compatible with roll-to-roll equipment, thus enabling the production of large detector volumes in industry. A price drop between one and two orders of magnitude is expected in this case.

The new technology has already been adopted by several experiments and upgrade projects. These range from forward tracking and triggering for a CMS upgrade [55–58] to barrel tracking with cylindrical GEMs in KLOE-2 [27, 59], from ILC digital hadron calorimetry [60] to cosmic muon tomography for detection of high-Z materials [61], from time projection chamber readout [62] to various nuclear physics experiments.

CHAPTER 4

Discharge-tolerant Micromegas

The second long shutdown of the Large Hadron Collider (LHC), scheduled for 2018, will see an upgrade of the accelerator to increase its luminosity beyond the design value and up to $2 \times 10^{34}/(\text{cm}^2\,\text{s})$ in the following running period. The high-luminosity LHC (HL-LHC), whose installation is expected in 2022–2023, will push the luminosity even further, reaching at least $5 \times 10^{34}/(\text{cm}^2\,\text{s})$. During the 2018 technical stop, the ATLAS experiment will install a new pair of so-called Small Wheels, replacing the current ones. The intervention is meant to significantly improve the performance of the muon system in the forward region, enhancing the level-1 muon trigger and the muon tracking precision. The reason for designing and building new Small Wheels lies in the impossibility to achieve the desired performance with cheaper upgrades of the present system, such as the addition of further detector layers, different readout electronics or better radiation shielding. Micropattern gas detectors appear as a possible technological solution and a project based on the micro-mesh gaseous structure (Micromegas) has been submitted as a candidate implementation of the new system.

Micromegas are scalable up to square metre size and their manufacturing relies on standard photolithographic methods, thus enabling large-volume production in a commercial company. However, the high discharge probability in the ATLAS environment may limit the use of Micromegas-based detectors. For this reason, a research and development activity has started, aimed at enhancing the Micromegas technology to make it spark-tolerant, while maintaining the performance and the compatibility with industrial processing.

This chapter describes my contribution to the development of the Micromegas for the ATLAS new Small Wheels. Section 4.1 gives an overview of the ATLAS muon spectrometer, while Section 4.2 lists the requirements for the detectors in the new Small Wheels and points out the main challenges faced in the development of the Micromegas technology for this application. Section 4.3 presents the study that I made on a preamplified Micromegas, where an electron-amplification structure is fitted on top of the Micromegas mesh with the purpose of splitting the total gas gain over two stages and reduce the discharge probability. Section 4.4 focuses on the novel spark-resistant bulk Micromegas. I first introduce the new technology and then detail the analysis that I made on test-beam data collected with a resistive chamber and with a standard bulk Micromegas, taken as benchmark. I prove the superior performance of resistive Micromegas in terms of immunity to discharges and I demonstrate the remarkable improvement of both the detection efficiency and the space resolution. Finally, Section 4.5 summarizes my research activity and draws the conclusions.

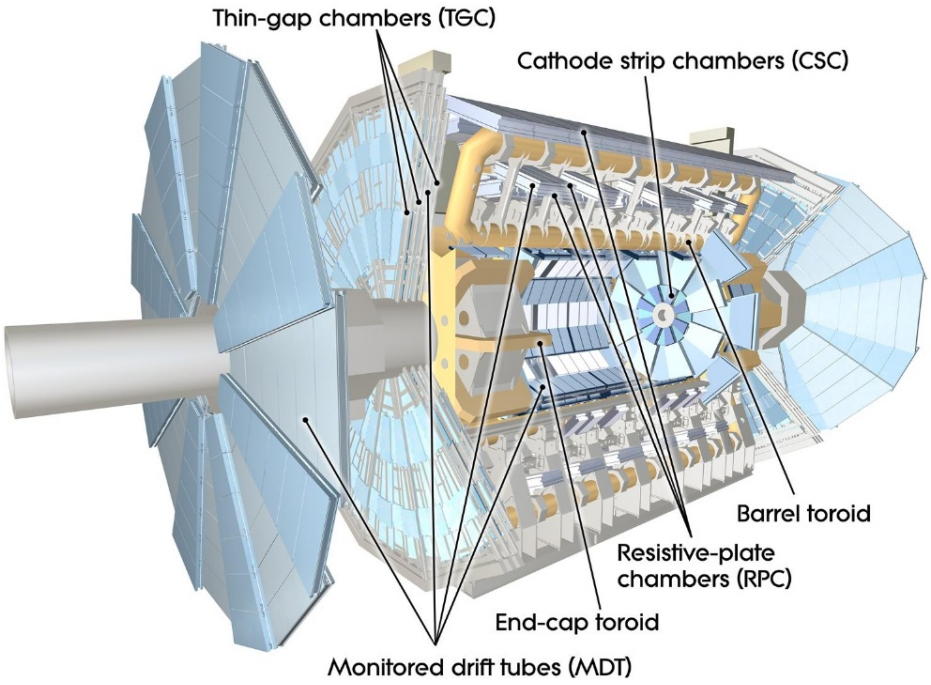

Figure 4.1: Cut-away view of the ATLAS muon spectrometer.

4.1 ATLAS muon spectrometer

ATLAS (a toroidal LHC apparatus) is a general-purpose experiment operating at the Large Hadron Collider at CERN [63]. The experiment's coordinate system is centred on the nominal interaction point, with x pointing towards the centre of the LHC ring, y upwards and z along the counterclockwise beam. The muon spectrometer is the most external subsystem of ATLAS, meant to detect charged particles exiting from the barrel and the end-cap calorimeters. It is conceived to combine tracking and momentum reconstruction capabilities for $|\eta| \leq 2.7$ with trigger functionalities for $|\eta| \leq 2.4$. These tasks are performed by two distinct sets of chambers, equipped with different detection solutions. Figure 4.1 details the spectrometer configuration and highlights the four employed detector technologies.

The bending force required by the muon spectrometer is furnished by three large air-core superconducting toroids. The barrel toroid is made up of eight coils, housed in eight individual cryostats and arranged radially and symmetrically around the beam axis. Each of the two end-cap toroids is also composed of eight coils, but they are cold-linked and assembled as a single cold mass, housed in a large cryostat. The end-cap toroids are inserted at the two ends of the barrel system, with the coils rotated by $\pi/8$ with respect to the barrel ones in order to provide radial overlap and optimize the field in the interface zone.

The purpose of the tracking system is that of providing a precise measurement of the track coordinate along the intersection between the bending plane and the detection plane up to $|\eta| \leq 2.7$. In the following, the barrel and end-cap components are briefly described.

The barrel tracking chambers are arranged in three concentric cylindrical shells, with average radii of approximately 5, 7.5 and 10 m and with a ϕ symmetry that follows the octant structure of the barrel toroid. Each octant is in turn made up of two azimuthal sectors with slightly different lateral extension, commonly referred to as large and small modules. The partial overlap between adjacent chambers ensures 2π azimuthal coverage and allows for a precise determination of the relative positions of the

modules using events recorded by both large and small sectors. The adopted detection technology is that of monitored drift tube chambers (MDTs), which combine simplicity of construction with predictability of mechanical deformations.

The end-cap tracking system is made up of three large disc-shaped detection planes on each side of ATLAS. These stations are located at $|z| = 7.4$, 14 and 21.5 m and they are commonly referred to as the end-cap inner (EI), the end-cap middle (EM) and the end-cap outer (EO) layer. The EI station is also called the Small Wheel, while the EM layer is alternatively called the Big Wheel. Due to the constraints imposed on the maximum diameter of the EO station by the dimensions of the experimental hall, the EI layer does not project into the EO one at the lower edge of the end-cap $|\eta|$ coverage. In order to enable momentum measurement in this pseudorapidity window, an extra ring-shaped station is inserted at $|z| = 10.8$ m, surrounding the end-cap toroid. The azimuthal sectoring of the end-cap tracking system mimics the one of the barrel system, with large and small chambers. The MDT technology is used almost everywhere. The EI station, that is located just downstream of the calorimeter and in front of the end-cap toroid, has to withstand a higher rate with respect to the others. Its innermost region, corresponding to $2 \leq |\eta| \leq 2.7$, is traversed by a flux exceeding the safe operation rate for MDTs, which is about 150 Hz/cm^2. For this reason, here cathode strip chambers (CSCs) are used instead, thanks to their higher rate capability, which ranges up to about 1 kHz/cm^2, their good time, space and double-hit resolution and their low neutron sensitivity.

The muon spectrometer must also have trigger capabilities over the region $|\eta| \leq 2.4$ and deliver coarse track information within a few tens of ns of the passage of a particle, to be used in the trigger logic. For this reason, the tracking system is complemented by a set of trigger chambers, designed to perform different tasks. In first place, they have to provide a well defined p_T threshold and bunch crossing identification with $\geq 99\%$ probability. They have to produce a rough hit position reconstruction in the bending plane for use in the high-level trigger stages and complement the precision tracking with a second coordinate in the non-bending plane. Finally, robustness against neutron and gamma-induced background is mandatory. Since the required readout granularity is much higher in the end-cap then in the barrel, different detection technologies have been implemented in the two regions.

Barrel triggering is performed with three concentric cylindrical shells covering the pseudorapidity interval $|\eta| \leq 1.05$ and following the azimuthal symmetry of the tracking system, with a large and a small sector per octant. The modules of the first and second trigger layers are anchored to the middle shell MDTs, covering their internal and external faces, while the third trigger layer is attached to the outer MDTs. In the barrel, resistive plate chambers (RPCs) have been chosen for their good space and time resolution, adequate rate capability and ease of construction.

The end-cap trigger system is made of three disc-shaped stations per side, mounted on the Big Wheel. The first disc is installed directly upstream of the middle MDT layer, while the other two are located just downstream. The discs are segmented into twelve azimuthal sectors and they are radially divided into two rings, an end-cap ring at $1.05 \leq |\eta| \leq 1.92$ and a forward one at $1.92 \leq |\eta| \leq 2.4$. The selected detector technology is that of thin gas chambers (TGCs), which offer a finer granularity and a rate capability much higher than RPCs.

4.2 Small Wheel upgrade

Figure 4.2 shows the single-plane counting rate, expressed in Hz/cm^2, as a function of the radius in the Small Wheels, at a centre-of-mass energy $\sqrt{s} = 7$ TeV and a luminosity $L = 9 \times 10^{32}/(\text{cm}^2\,\text{s})$. The Monte Carlo simulation is in fairly good agreement with the experimental data collected from the large sectors during the LHC runs. According to the data of Fig. 4.2, the highest rates experienced by the

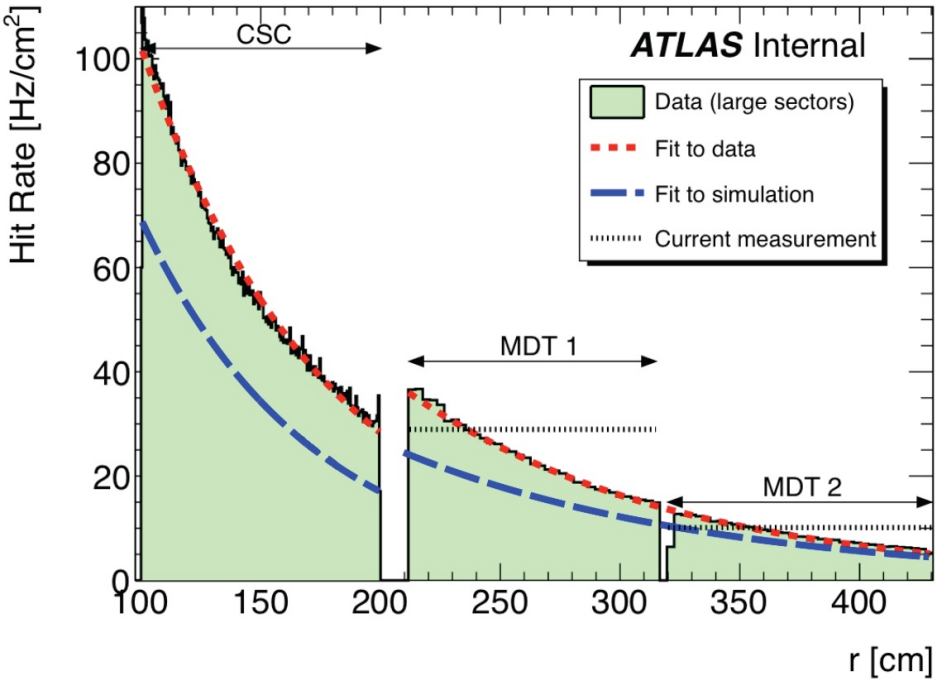

Figure 4.2: Single-plane counting rate, expressed in Hz/cm^2, as a function of the radius in the Small Wheels, at a centre-of-mass energy $\sqrt{s} = 7$ TeV and a luminosity $L = 9 \times 10^{32}/(\text{cm}^2\,\text{s})$.

MDTs and the CSCs are about 35 and 100 Hz/cm^2, respectively. When scaled up to $\sqrt{s} = 14$ TeV and $L = 10^{34}/(\text{cm}^2\,\text{s})$, these figures become 550 and 1.6×10^3 Hz/cm^2. Considering that the MDTs are validated up to 150 Hz/cm^2 and the CSCs up to 1 kHz/cm^2, it is clear that these detectors are already approaching their occupancy limit and they are not suitable for operation in the HL-LHC environment. Hence the need for new Small Wheels, that are foreseen to replace the present ones in the second long LHC shutdown.

The new Small Wheels will have the same dimensions as the ones currently installed in ATLAS, placed right upstream of the end-cap toroid magnet and covering the pseudorapidity interval $1.3 \leq |\eta| \leq 2.7$. The required rate capability is obtained by extrapolating the maximum particle flux in Fig. 4.2 to $\sqrt{s} = 14$ TeV and $L = 5 \times 10^{34}/(\text{cm}^2\,\text{s})$ and adding a safety factor of 2 to keep into account the increase of background events. This rather conservative estimate evaluates to about 16 kHz/cm^2.

The new Small Wheels are also expected to significantly enhance the level-1 trigger by suppressing fake high-p_T (≥ 20 GeV) muons. In the present trigger scheme, the direction vector of a particle traversing the end-cap muon system is extracted from the reconstructed hit positions in the three TGC planes, located on the EM station. The momentum is then computed under the assumption that the track originates in the interaction point. Random background can easily trick this algorithm and generate fake triggers. Currently, more than 95% of the forward high-p_T level-1 triggers have indeed no track associated with them. The flaw can be removed by having Small Wheels capable of providing a second direction vector, thus imposing tight constraints on real tracks. Moreover, a pointing resolution better than 1 mrad will improve the resolution on the transverse momentum, allowing for the application of sharper thresholds.

Additional requirements for the new chambers include a detection efficiency of more than 98% per plane for minimum ionizing particles (MIPs), trigger capability, good resistance to radiation and good aging properties.

All these requirements can be met using Micromegas chambers. The muon ATLAS Micromegas activity (MAMMA) is an R&D collaboration born in 2007, with the aim of exploiting and adapting the Micromegas technology for the ATLAS Small Wheel upgrade. In 2012 resistive Micromegas have been selected as the primary tracking detectors for the new Small Wheels, where they will be complemented by small-strip thin gas chambers (sTGCs) as the primary trigger detectors.

The Micromegas concept takes advantage of the fast evacuation of the space-charge created in the amplification gap, as the vast majority of the positive ions from the Townsend avalanches is drawn to the mesh electrode within a typical time of the order of 100 ns. Hence, the high rate capability. Micromegas can also provide the second direction vector that is needed to suppress fake high-p_T tracks and enhance the level-1 trigger. This can be done even with a single conversion gap by operating the detector in micro-time-projection-chamber (μ-TPC) mode, that is, by measuring the arrival time of the signals from different primary clusters. Knowing the drift velocity in the selected gas mixture and the strip pitch, one can work out the track inclination and thereafter the direction vector. Furthermore, a careful choice of the chamber structural and running parameters enables high detection efficiency for minimum ionizing particles, good space resolution and a time resolution sufficient for triggering. The history of Micromegas has shown good aging properties and the possibility to use non-flammable and cheap gases at atmospheric pressure, like the Ar:CO_2 93:7 mixture already employed in the present MDTs. From the manufacturing point of view, Micromegas rely on photolithographic methods that are industrial standards, which makes it possible to produce high volumes of large-area detectors at a cheap price and to take advantage of the quality insurance tools of the printed circuit board (PCB) industry.

At the time when the first institutes participating to the MAMMA collaboration started to develop the original idea, there appeared to be two main points to work on. The first is the scalability of the Micromegas technique to square metre size, with the bottleneck being the dimension of the machines needed for the manufacturing. After a few attempts and with the upgrade of the CERN PCB workshop in 2012, it is now possible to produce chambers with an active area of about $2 \times 1\,\mathrm{m}^2$.

The second hurdle has to do with discharges. As pointed out in Section 1.8, when the total charge in a single Townsend avalanche becomes important, the electric field in the leading and trailing areas of the charge cloud gets highly boosted. This induces the fast growth of a streamer that can develop into a spark. The minimum amount of charge in a single avalanche that leads to a discharge is found to be a constant among all gas detectors. This threshold is known as Raether's limit and its value is in the order of 10^7 to 10^8 electron-ion pairs [15]. In the proposed application for the upgrade of the ATLAS Small Wheels, Micromegas are required to detect minimum ionizing particles with high efficiency, which asks for an effective gas gain of the order of 10^4. Since Micromegas are single-stage amplification structures where the effective gain is about the same as the intrinsic gain, it follows that ionization processes liberating about 10^3 electrons along the lateral extent of an avalanche carry the risk of sparking. Such ionization levels are easily reached by low-energy alpha particles or charged debris from the interactions of background radiation in the detector gas or materials. Considering the negative impact that discharges can have on the dead time, on the readout electronics and on the chamber itself, it appears necessary to enhance Micromegas detectors to make them capable of coping with high charge deposition densities.

4.3 Preamplified Micromegas

The case presented at the end of the previous section can be tackled in several ways. A possible approach aims at decreasing the absolute number of undesired occurrences, by extending the dynamic range of ionization charge in which the detector can be safely operated to include the high charge deposition events. In other words, one seeks to raise the gas gain for a fixed discharge probability, or equivalently

to reduce the spark rate for the required amplification factor. For a given charge deposition and a given gas gain, the discharge probability grows with the density of free electrons in the multiplication region, as denser charge clouds make it more likely to reach the Raether's limit and cause the onset of a streamer. The longitudinal and transverse diffusion of the electrons in the gas can be exploited in different manners to spread the charge. Firstly, one can tune the gas composition and the electric fields for the largest diffusion. This solution alone is however not sufficient to guarantee safe operation in the ATLAS environment. In the following, we do not attempt to find the best gas mixture and field configuration, but we rather make use of a charge preamplification structure above the Micromegas mesh to distribute the required gas gain over two stages and take advantage of the diffusion in the transfer gap. Our purpose is that of assessing the effectiveness of such a preamplified detector, by comparing its performance to that of a standard Micromegas, taken as benchmark.

The idea is explored using a standard test box equipped with a bulk Micromegas, see Fig. 4.3 (left), on top of whose mesh a charge preamplification structure can optionally be fitted. The anode is segmented into 360 one-dimensional strips 10 cm long and 150 μm wide, spaced with a pitch of 250 μm. The readout pathways are clustered in 5 groups of 72 channels each and routed to 5 ERNI female connectors of type SMC 1.27 mm. Every connector features 80 pins, arranged in two rows of 40. The central 72 pins are used as signal channels, while the 4 most external pins at the two ends of the connector are grounded. The $10 \times 9\,\mathrm{cm}^2$ anode active area is covered by a stainless steel mesh having 18 μm thick wires interwoven with a pitch of 63 μm, corresponding to 400 lines per inch (LPI) and 51% optical transparency. The mesh is laminated using the bulk technique at a distance of 128 μm from the anode and kept under mechanical tension thanks to cylindrical pillars having a diameter of 300 μm and a pitch of 2.5 mm in both x- and y-direction, resulting in only 1.1% of dead material on the active area. The drift electrode is also made out of the same type of mesh, stretched on an FR4 frame and maintained at a fixed distance from the Micromegas by plastic washers at the four corners. The gas volume is defined by an aluminum frame housing the gas inlet and outlet and by the dismountable roof with Mylar window, that can be coupled to the aluminum frame with an O-ring to ensure gas tightness. A plastic layer covers the flexible Mylar sheet in order to provide mechanical protection and furnish a support structure for radioactive sources. The chosen preamplification structure is a standard $10 \times 10\,\mathrm{cm}^2$ double-mask gas electron multiplier (GEM) of the type described at the beginning of Section 2.2 and depicted in Fig. 2.4. The foil is stretched on an FR4 frame and optionally inserted between the Micromegas and the cathode, as shown in Fig. 4.3 (right), with the gap thicknesses defined by washers. Four SHV male chassis sockets[1] provide enough power lines to bias the mesh, the two GEM electrodes and the cathode.

All the measurements are performed using a premixed argon-based gas with 10% of added tetrafluoromethane (CF_4), supplied to the chamber in open-loop configuration. Two flow meters, one placed at the input of the line and the other inserted right before the exhaust, are used as monitors against gas leaks. The water content is not measured, as the hygrometer is not fluorine-compliant.

In the next sections, the Micromegas is at first characterized in standalone configuration, tracing its gain curve as a function of the mesh voltage and probing its behaviour in the presence of highly ionizing radiation. The composite detector obtained by adding the preamplification stage is in turn considered, and its properties critically compared to the ones of the sole Micromegas.

4.3.1 Standalone Micromegas

For the Micromegas standalone tests, the drift electrode is mounted directly above the Micromegas mesh, at a distance of 3.3 mm. Figure 4.4 (left) shows a schematic view of the detector. The chamber is

[1] Radiall type R317.580, Suhner type 22 SHV 50-0-2

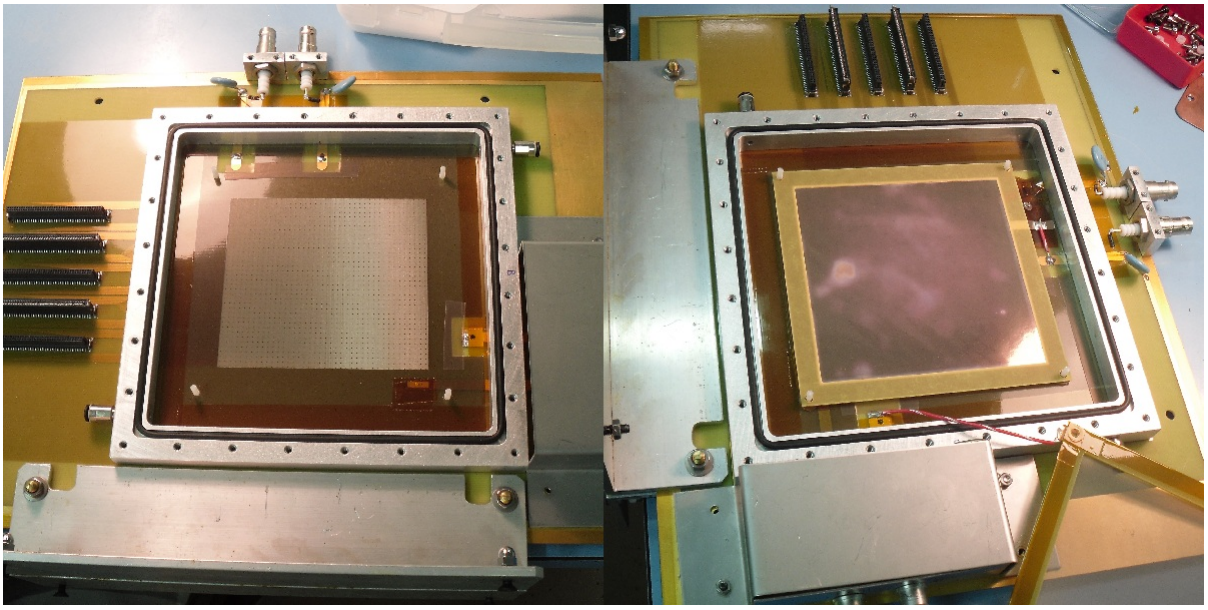

Figure 4.3: Test box of the preamplified Micromegas. The left frame shows the PCB with the bulk Micromegas, the signal and the high-voltage connectors and the aluminum frame that defines the gas volume. The right frame shows the GEM, stacked on top of the Micromegas, and the drift electrode in the lower right corner, soldered to the high-voltage feedthrough contact and ready to be mounted above the GEM.

fastened in a vertical position on a *x*-*y* adjustable bench and hooked up to the gas and high-voltage lines, as shown in Fig. 4.5 and 4.6 (left). An X-ray tube with copper target and a collimator of 1 mm diameter stands in front of the detector and is used as the radiation source for most of the measurements.

During operation with soft X-rays, the central 72 channels are shorted together and read out through a single charge preamplifier, while the remaining 288 strips are grounded through ERNI male connectors plugged on the chamber. When irradiating only the central part of the active area, this readout scheme allows for detecting all of the signal events, while reducing the electronic noise associated with the detector capacitance by a factor of 5. Figure 4.7 displays the energy spectrum obtained in response to 5.9 keV photons from a ^{55}Fe source, when the Micromegas is biased with 500 V and the drift field is 1.25 kV/cm. The attained energy resolution, extracted from a Gaussian fit to the photopeak, is 30.4% full width at half maximum (FWHM).

The gain curve is traced following the procedure explained in Section 2.4.4. The gain calibration is performed in the presence of a collimated beam of copper photons from the X-ray tube, with the Micromegas mesh at a negative potential of 520 V with respect to the grounded anode and the drift field maintained at 1.25 kV/cm. The experimental points at different voltages are then obtained by comparing the position of the pedestal-subtracted photopeak in ^{55}Fe energy spectra. The results, reported in Fig. 4.8, show that the maximum applicable voltage is 550 V, corresponding to a gas gain of 2070.

The discharge properties of the Micromegas are probed with highly ionizing alpha particles emitted by unstable gas nuclides, that are produced outside the chamber, coalesced with the employed mixture and transported into the active volume by the gas flow, as described in Section 2.4.6. Figure 4.6 (right) presents the experimental setup. The ^{228}Th radioactive source sits in the left branch of the double pipe noticeable in the foreground. The three helium-leak-free valves serve to force the gas through one of the two pipes alternatively, thus permitting to easily toggle between the original gas mixture and the ^{220}Rn-enriched one. For the discharge studies, it is sufficient to close the cutoff on the right branch and

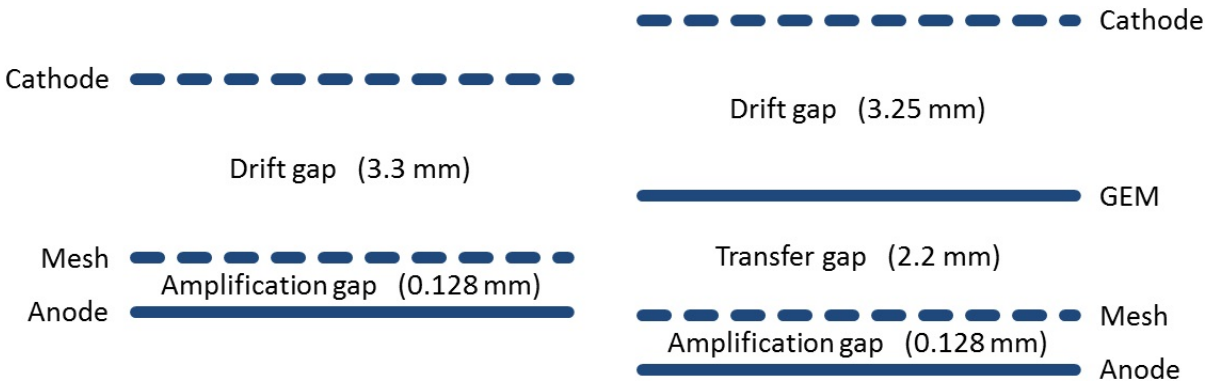

Figure 4.4: Left frame: schematic view of the standalone Micromegas. From top to bottom: the cathode (or drift electrode), the drift gap (or conversion gap), the amplification mesh, the amplification gap and the anode, which is used as the readout electrode. Right frame: schematic view of the combined detector. From top to bottom: the cathode (or drift electrode), the drift gap (or conversion gap), the GEM foil, the transfer gap, the amplification mesh, the amplification gap and the anode, which is used as the readout electrode.

fully open the two valves on the left pipe. Within about ten minutes, the detector is subject to a steady flow of ^{220}Rn, that results in a constant rate of alphas. When switching back to the uncontaminated gas mixture, however, it is important to keep in mind the characteristic decay chain of ^{228}Th, reported in Table 2.2. Although ^{220}Rn has a half-life of 55.6 ± 0.1 s and its immediate daughter nuclide ^{216}Po has a decay time of only 145 ± 2 ms, the second daughter ^{212}Pb is much longer lived, with a half-life of 10.64 ± 0.01 h. As a consequence, it is necessary to flush the chamber with clean gas for 24 h to reduce the amount of radioactive lead deposited inside the detector by an order of magnitude.

Since ^{228}Th has a half-life of 1.9116 ± 0.0016 a, its decay rate falls appreciably over time, decreasing by 1% every week. The rate of alpha particles released inside the chamber varies accordingly and hence needs to be experimentally determined at the moment of performing the discharge study. The knowledge of such rate is of primary importance to compute the discharge probability by normalizing the measured spark rate. For this purpose, the detector is read out in pulse-height mode, its shaped anode signal is fed to a voltage threshold discriminator for noise removal and the number of outgoing digital pulses is recorded for different biasing voltages. Since the alphas are produced at random locations in the active volume and with an isotropic velocity distribution, it is important to read out the entire anode, by shorting together all of the strips. The rate estimation is complicated by the fact that the deposited energy, and therefore the signal amplitude, covers the whole range from zero to the Q-value. This requires a careful choice of the discriminator's threshold, that in turn is not straightforward due to the low conversion rate of the alpha particles. Figure 4.9 reports the number of counts in a 10 s time window for different biasing voltages, with the drift field set to 1.25 kV/cm. The data are fitted with a logistic sigmoid function of the type of Eq. (4.1), where R is the rate at the biasing voltage V, while R_M, R_m, V_0 and ΔV are the fitting parameters, representing the maximum and minimum rate, the sigmoid flex point and its width, respectively. The maximum rate extracted from Fig. 4.9 is 123 counts in 10 s, or 12.3 Hz.

$$R = \frac{R_M - R_m}{\exp\left[\left(V - V_0\right)/\Delta V\right] + 1} + R_m \tag{4.1}$$

The spark-rate measurement is done together with the alpha-particle counting, for each high-voltage configuration. For operative purposes, a discharge is defined as a high-charge-depositing event that initiates a streamer in the gas volume and creates an electrical short between two or more electrodes, triggering a voltage trip of the power supply. The time between consecutive sparks is recorded and

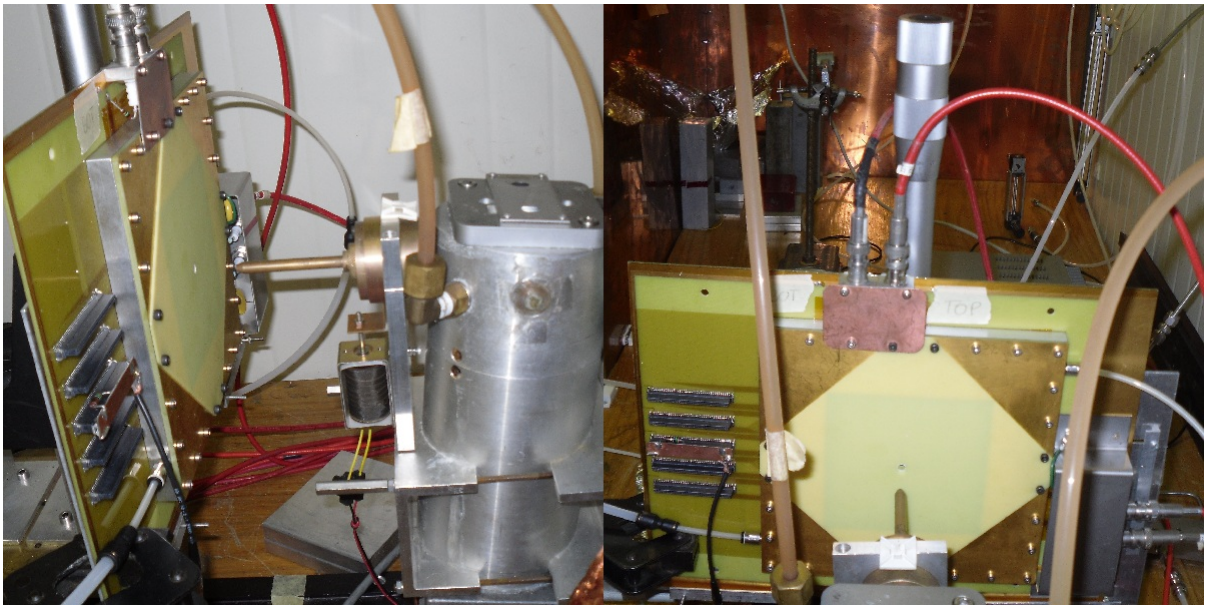

Figure 4.5: Micromegas on the X-ray test bench. Left frame: side view of the chamber, fastened in a vertical position on the *x*-*y* adjustable bench and hooked up to the gas, high-voltage and readout lines. The X-ray tube is visible on the right-hand side of the picture. Right frame: front view of the detector. In the background, one can see the copper cage used as a radiation shielding when the X-ray tube is energized.

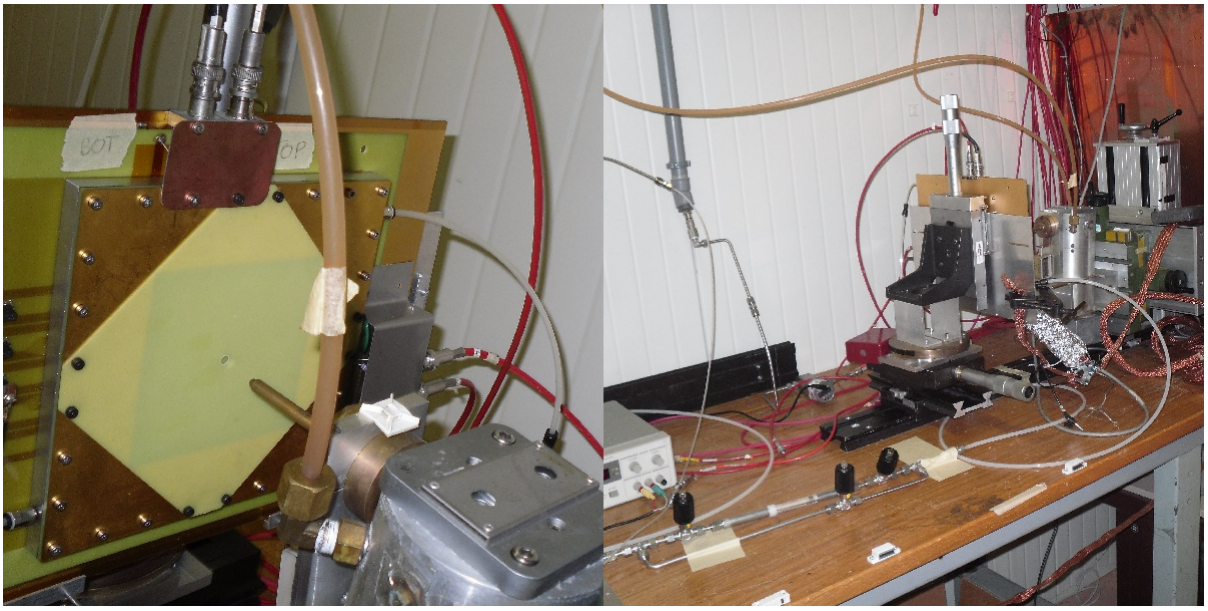

Figure 4.6: Left frame: detail of the detector, standing in front of the X-ray tube. The long collimator used to trim the photon beam is visible in the centre of the picture. Right frame: view of the experimental setup for the discharge studies, seen from behind the chamber. The ^{228}Th radioactive source sits in the left branch of the double pipe noticeable in the foreground.

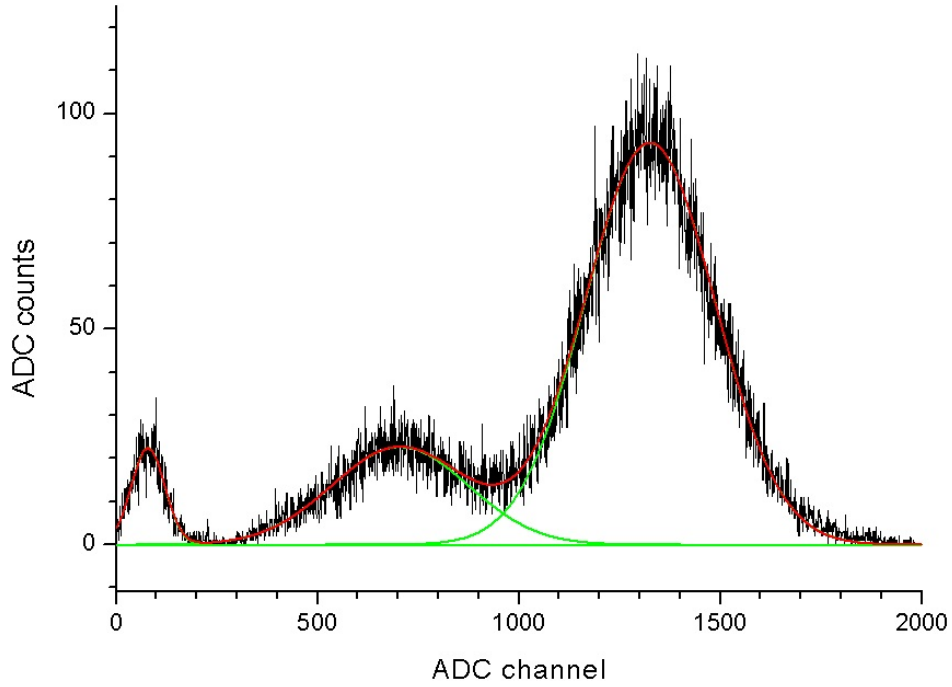

Figure 4.7: Energy spectrum of the standalone Micromegas. Drift field $E_d = 1.25\,\mathrm{kV/cm}$, mesh voltage $V_{\mu\mathrm{M}} = 500\,\mathrm{V}$. From right to left: the photopeak, the argon escape peak and the pedestal.

averaged over about 10 times. The reciprocal of the mean value, normalized with the alpha rate, gives the searched discharge probability.

Given the adopted operative definition of discharge, it is mandatory to test any possible correlations of the measured spark rate with the current-limit setting of the power supply. The discharge study is therefore repeated, varying the current limit while keeping the Micromegas at 525 V and the drift field at 1.25 kV/cm, which results in a fixed charge amplification factor of 840. Figure 4.10 shows that the time between consecutive sparks, averaged over 10 measurements, does not depend on the chosen current limit over the scanned range, that covers two orders of magnitude.

4.3.2 Combined detector

The idea of a preamplified Micromegas is explored by inserting a double-mask GEM foil of $10\times10\,\mathrm{cm}^2$ active area, stretched on an FR4 frame, between the Micromegas and the cathode. The combined detector has a drift gap of 3.25 mm in thickness, that is kept as similar as possible to the one of the standalone Micromegas formerly characterized. This ensures the same average charge deposition by highly ionizing particles and thus enables the comparison of the discharge probabilities. The transfer gap can be slimmer, and it is fixed to 2.2 mm. Figure 4.4 (right) shows a schematic view of the chamber.

Before performing a discharge study on the combined detector and comparing the results with the ones of the standalone Micromegas, it is necessary to understand the operational limits of the new chamber and find an appropriate working point. The preamplified Micromegas has several parameters that can be changed at will and that have to be tuned in order to take the best advantage of the preamplification stage. A bad choice of the working point may indeed diminish or nullify the benefits brought by the GEM to the overall spark probability. For parameter tweaking, the detector is hooked up to the gas and high-voltage lines, illuminated with a ^{55}Fe radioactive source and read out in pulse-height mode

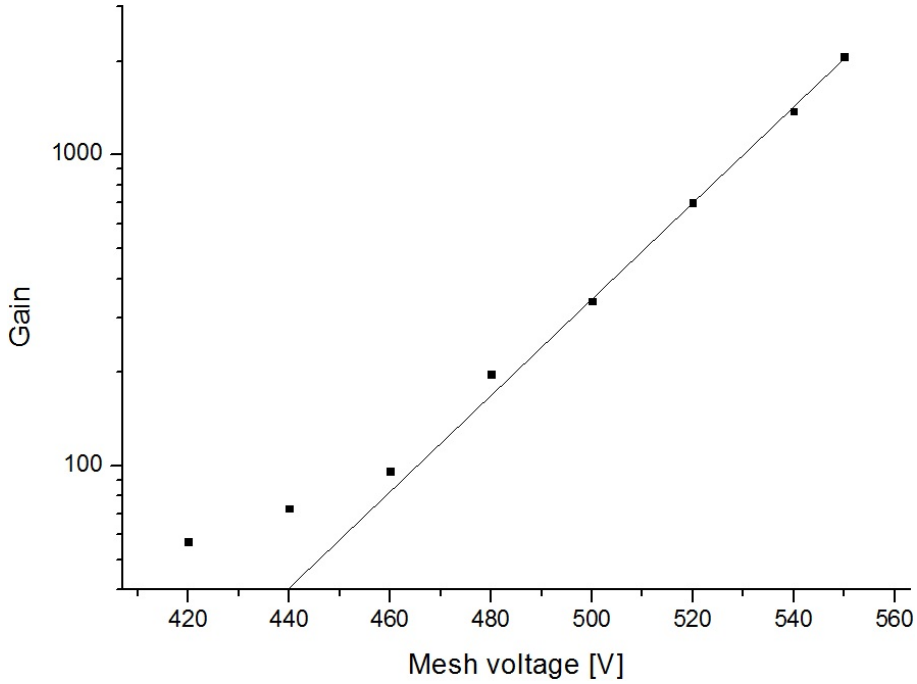

Figure 4.8: Gain curve of the standalone Micromegas. $E_d = 1.25\,\mathrm{kV/cm}$.

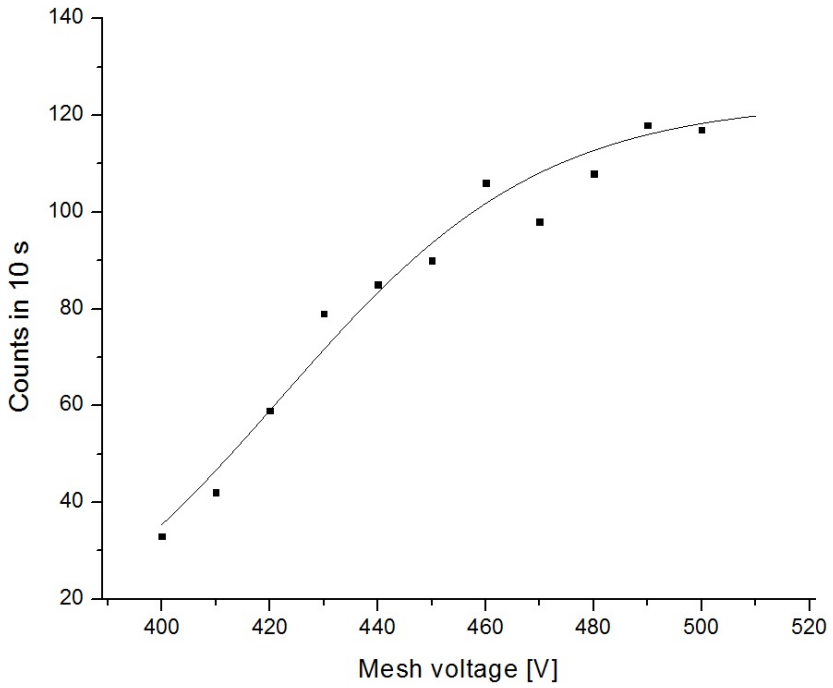

Figure 4.9: Measured counts of alpha particles in a 10 s time window as a function of the difference of potential across the amplification gap. $E_d = 1.25\,\mathrm{kV/cm}$.

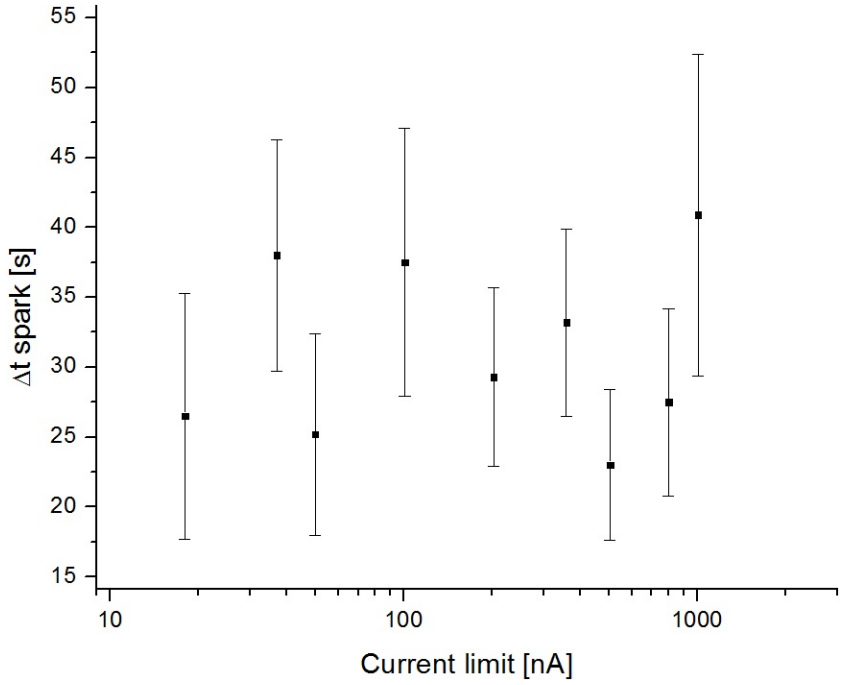

Figure 4.10: Average sparking time vs power-supply current limit. E_d = 1.25 kV/cm, $V_{\mu M}$ = 525 V.

through a charge preamplifier. The integrated anode signal is fed to a shaper amplifier and then to an oscilloscope, on which the signal amplitude is gauged at different parameter values.

Figure 4.11 is a scan of the voltage difference across the GEM, from 0 to 410 V. The Micromegas is maintained at a negative voltage of 500 V with respect to the grounded anode, while the drift and transfer fields are 0.62 and 0.45 kV/cm respectively. The vertical axis, showing the gas gain of the combined detector, is rescaled according to the gain calibration described later in this section. Up to 225 V, the GEM has an effective gain lower than one and the anode signal is only due to those X-rays converting in the transfer gap, with charge amplification provided by the sole Micromegas. At about 250 V, the GEM crosses the unitary-gain threshold and the contribution from photons converting in the drift gap becomes the dominant one. The overall gain then increases exponentially and reaches 6300 at the sparking limit, corresponding to 410 V across the GEM.

Figure 4.12 shows a Micromegas voltage scan, where the GEM is biased with a fixed potential difference of 325 V. The drift and transfer fields are also constant and their intensities coincide with the ones used above. The total gain increases exponentially up to the sparking limit at 570 V, where the amplification factor reaches 14 800.

Having drawn the detector operational limits in terms of the maximum applicable voltage on the GEM and on the Micromegas, one can move on to tweaking the fields. Although the optimal field configuration has a slight dependence on the voltages applied on the two amplification stages, for the sake of discharge studies it is possible to set a common working point for all of the measurements.

Figure 4.13 is a transfer-field scan performed with the Micromegas and the GEM biased at 500 and 325 V respectively and with a drift field of 0.62 kV/cm. An optimum is clearly identifiable at 1.25 kV/cm. Below this value, the transfer field is not strong enough to efficiently extract electrons from the GEM and a significant fraction of charge is lost on the foil's lower electrode. Above the optimal value, on the other hand, the ratio between the Micromegas field and the transfer field decreases to a point where the mesh electron transparency begins to drop, causing charge losses on the mesh itself.

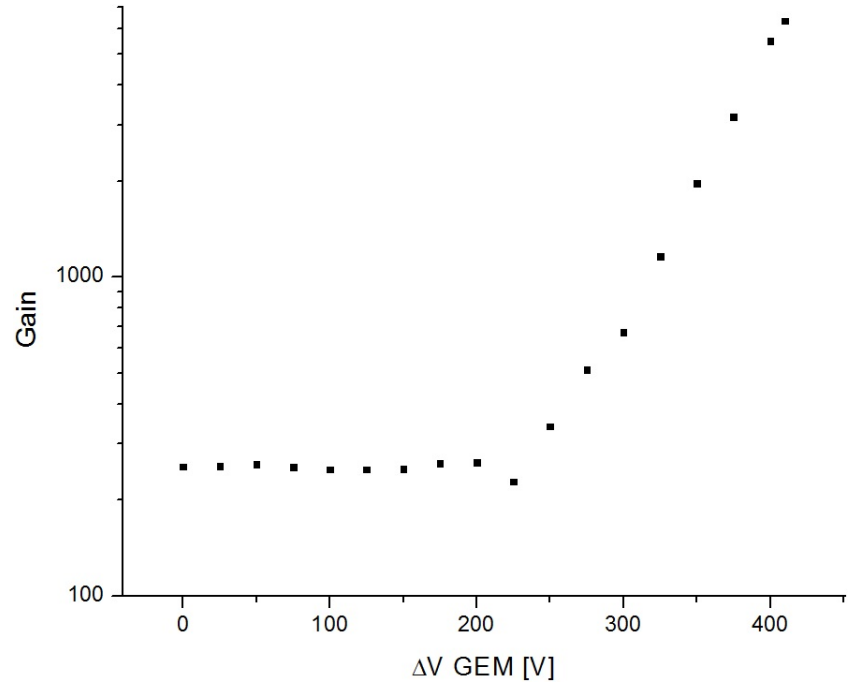

Figure 4.11: GEM voltage scan for the combined detector. $E_d = 0.62\,\mathrm{kV/cm}$, transfer field $E_t = 0.45\,\mathrm{kV/cm}$, $V_{\mu\mathrm{M}} = 500\,\mathrm{V}$.

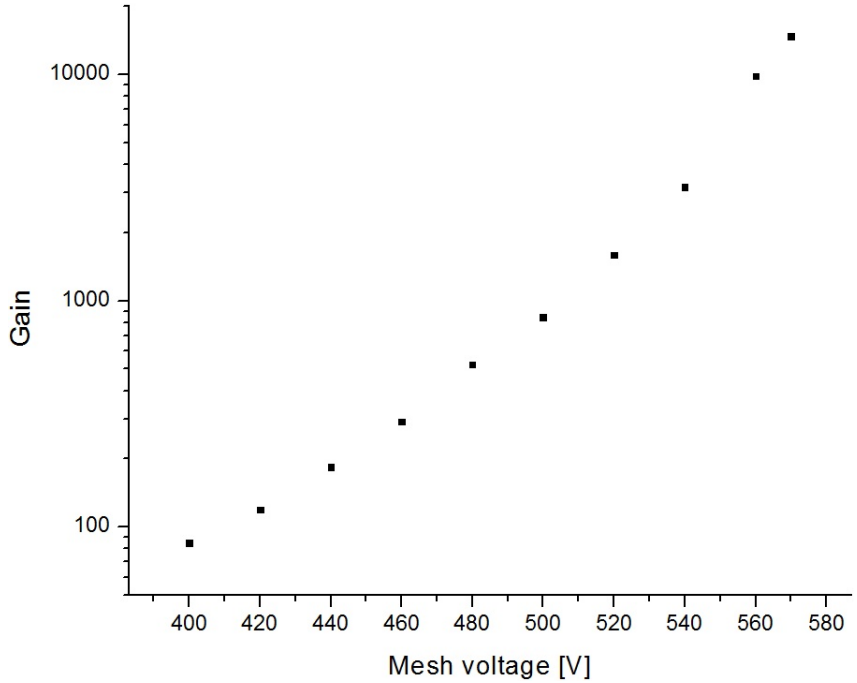

Figure 4.12: Micromegas voltage scan for the combined detector. $E_d = 0.62\,\mathrm{kV/cm}$, GEM voltage $\Delta V_{\mathrm{GEM}} = 325\,\mathrm{V}$, $E_t = 0.45\,\mathrm{kV/cm}$.

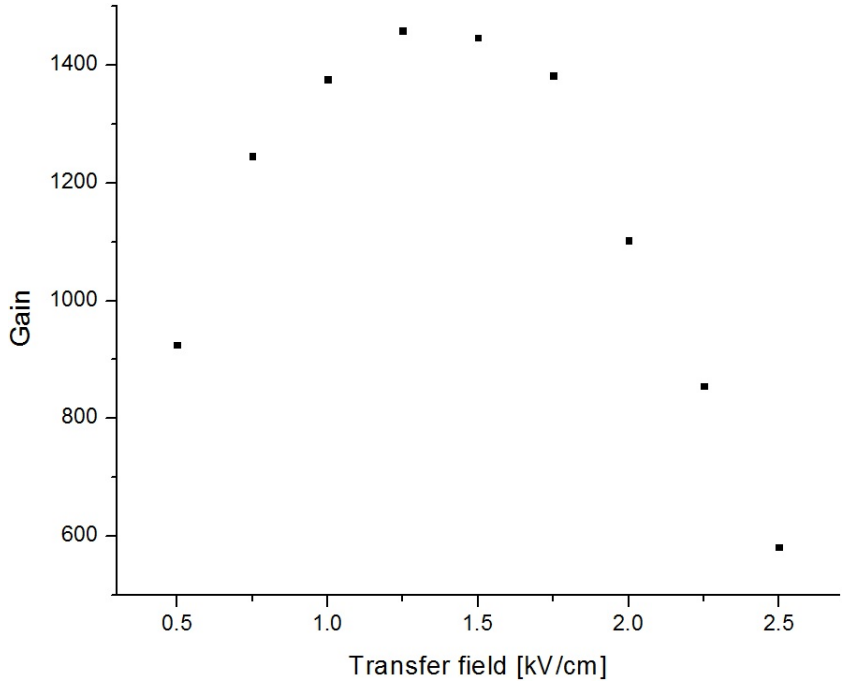

Figure 4.13: Transfer-field scan for the combined detector. $E_d = 0.62\,\mathrm{kV/cm}$, $\Delta V_{\mathrm{GEM}} = 325\,\mathrm{V}$, $V_{\mu\mathrm{M}} = 500\,\mathrm{V}$.

Figure 4.14 displays a drift-field scan. The voltages across the two amplification stages are the ones used for the previous scan, whereas the transfer field is now maintained at its optimal value of 1.25 kV/cm. The gain drop at high drift fields is due to a decreased electron transparency of the GEM, that becomes less efficient at focusing ionization charges into its holes, leading to losses on the foil's upper electrode.

A preliminary, heuristic evaluation of the enhancements brought by the preamplification stage can be made by repeating the Micromegas voltage scan without powering the GEM. By comparing the results with the gain curve of Fig. 4.12, one can assess the maximum achievable boost of the effective gain. The scan is executed with an inverted drift field of 0.31 kV/cm and the GEM reversely biased with 20 V. The transfer field is set to 0.45 kV/cm, in order to attain the same mesh electron transparency as in Fig. 4.12. The signal now originates from X-rays converting in the transfer gap, whose liberated charge is amplified by the Micromegas alone. Considering that the transfer gap thickness d_T is small compared with the photon attenuation length of the employed gas mixture, it is possible to expand the exponential interaction law of Eq. (1.12) in a Taylor series, finding that to a first approximation the number of X-rays converting in the gap is proportional to d_T. Let's indicate with $A_2(V_M)$ the amplitude of the anode signal when the Micromegas is running at a negative potential, V_M, with respect to the grounded anode, providing a gas gain $G_M(V_M)$. Let's also denote with $A_1(V_M)$ the amplitude of the signal measured during the scan of Fig. 4.12, which has a contribution from the transfer gap (thickness d_T), amplified by a factor $G_M(V_M)$, and a contribution from the drift gap (thickness d_D), amplified by a factor $G_D(V_M)$. In both scans, the only dependence is on the Micromegas biasing voltage, as the potential difference across the GEM is fixed. Expressing the effective gain of the whole structure as $G_D(V_M) = G_G G_M(V_M)$ and assuming the GEM to have an effective gain G_G significantly larger than one, it is possible to write:

$$\frac{A_1(V_M)}{A_2(V_M)} = \frac{d_T G_M(V_M) + d_D G_D(V_M)}{d_T G_M(V_M)} = \frac{d_T G_M(V_M) + d_D G_G G_M(V_M)}{d_T G_M(V_M)} \simeq \frac{d_D}{d_T} G_G \tag{4.2}$$

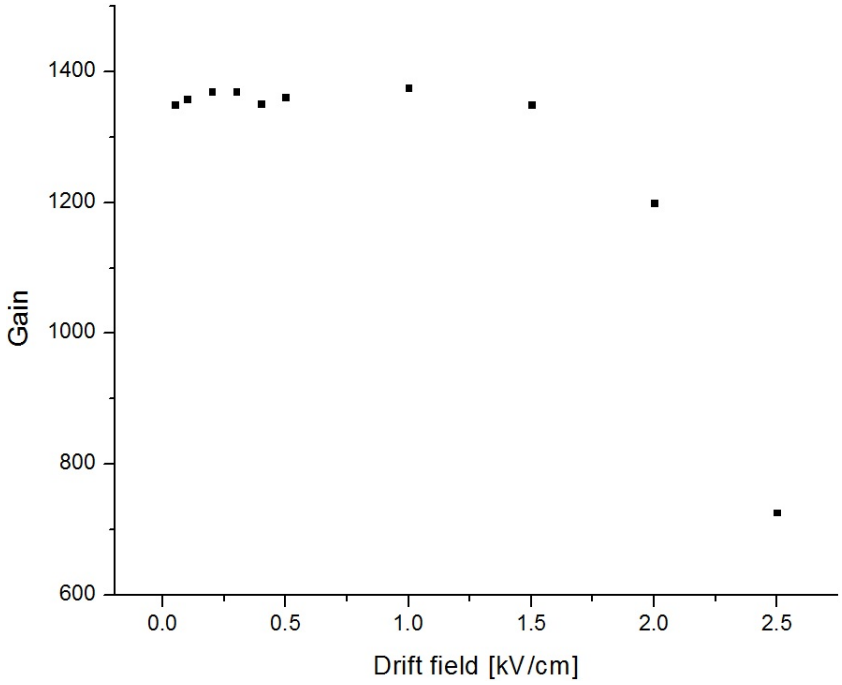

Figure 4.14: Drift-field scan for the combined detector. $\Delta V_{\mathrm{GEM}} = 325\,\mathrm{V}$, $E_t = 1.25\,\mathrm{kV/cm}$, $V_{\mu\mathrm{M}} = 500\,\mathrm{V}$.

By inverting the relation, one can get the effective gain of the preamplification stage operated at 325 V. Scaling this up to the GEM sparking limit, one obtains that the maximum achievable gain boost in the described configuration is 13.

In order to get a deeper understanding of the benefits carried by the preamplification stage, one has to proceed with a systematic study of the discharge behaviour of the composite detector. On the basis of what was done for the standalone Micromegas, one has to calibrate the total effective gas gain, trace the gain curve with soft X-rays and determine the spark probability in the presence of highly ionizing particles. During these measurements, the drift field will be maintained at 0.62 kV/cm, while the transfer field will be fixed to 1.25 kV/cm. The former condition allows the GEM to maximize its input electron transparency, while the latter setting guarantees the best coupling between the two stages and at the same time reproduces the mesh electron transparency of the standalone Micromegas characterization, thus enabling the comparison of the results.

Figure 4.15 shows the typical pulse-height response of the chamber to 5.9 keV X-ray photons from a ^{55}Fe radioactive source, when the first amplification stage is operated at low gain. From right to left, it is possible to recognize the full-energy photopeak and the argon escape peak from photons converting in the drift gap, the photopeak and the escape peak from photons converting in the transfer gap, and the pedestal. The second and the third peak from the left appear to be squeezed towards lower energies because the charge liberated in the transfer gap does not benefit from the GEM action and therefore undergoes a smaller amplification with respect to the charge liberated in the drift gap. In the limit of unitary effective gain in the preamplification stage, these two peaks will overlap the rightmost ones, while in the case of significant voltage across the GEM, the contribution from the transfer gap will disappear below the trigger threshold. The energy resolution extracted from a fit to the spectrum is 22.2% FWHM, obtained with 492 V on the Micromegas and 310 V across the GEM. The best energy resolution reached during the tests is 16.2% FWHM, achieved with 427 and 435 V on the Micromegas and on the GEM, respectively.

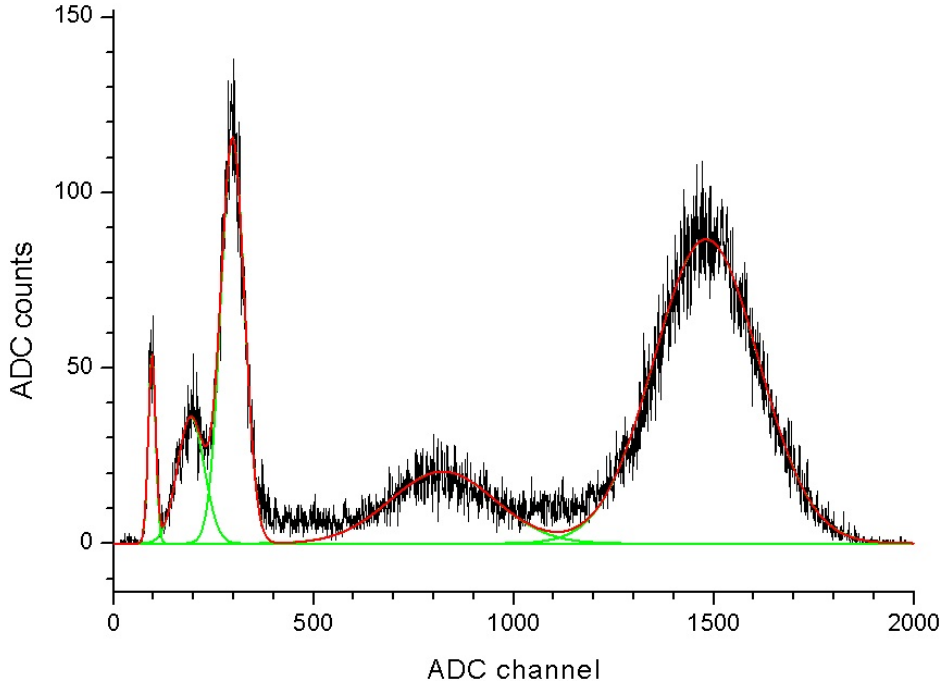

Figure 4.15: Energy spectrum of the combined detector. E_d = 0.62 kV/cm, ΔV_{GEM} = 310 V, E_t = 1.25 kV/cm, $V_{\mu\mathrm{M}}$ = 492 V. From right to left: the photopeak and the argon escape peak from photons converting in the drift gap, the photopeak and the escape peak from the transfer gap, and the pedestal.

As previously done for the standalone Micromegas, the gain is measured following the experimental procedure detailed in Section 2.4.4. The gain calibration is carried out by illuminating the detector with a collimated photon beam of 1 mm in diameter, generated using an X-ray tube with copper target. Through the whole procedure, the drift and transfer fields are maintained at 0.62 and 1.25 kV/cm respectively, while the voltage across the first and second amplification stages are fixed to 325 and 540 V. In order to effectively accomplish its purpose, the GEM should ideally operate at a gain significantly higher than one. For this reason, it is convenient to consider the discharge probability due to the ionization created in the drift gap only, removing the contribution from photons converting in the transfer gap. This can be done by rescaling the measured anode current, I_A, and the number of photon counts, N_γ, according to the properties of the energy spectrum acquired during the calibration. Specifically, since the number of counts is given by the area under the spectrum, while the anode current is proportional to the number of photons times the charge amplification factor, the correction factors are given by Eq. (4.3) and (4.4). Here E_i and A_i are the centre and the area of the i^{th} peak in the spectrum, as extracted from the multi-Gaussian fit and counting upwards from the pedestal.

$$N_{\gamma,\mathrm{drift}} = \frac{\sum_{i=4}^{5} A_i}{\sum_{i=2}^{5} A_i} N_{\gamma,\mathrm{total}} \tag{4.3}$$

$$I_{A,\mathrm{drift}} = \frac{\sum_{i=4}^{5} E_i A_i}{\sum_{i=2}^{5} E_i A_i} I_{A,\mathrm{total}} \tag{4.4}$$

Figure 4.16 shows the gain curve obtained by keeping the GEM at 325 V and scanning the negative voltage applied to the Micromegas mesh from 400 to 570 V, where the total gain reaches 31 300. The points are extracted from the position of the pedestal-subtracted photopeak in the ^{55}Fe energy spectra.

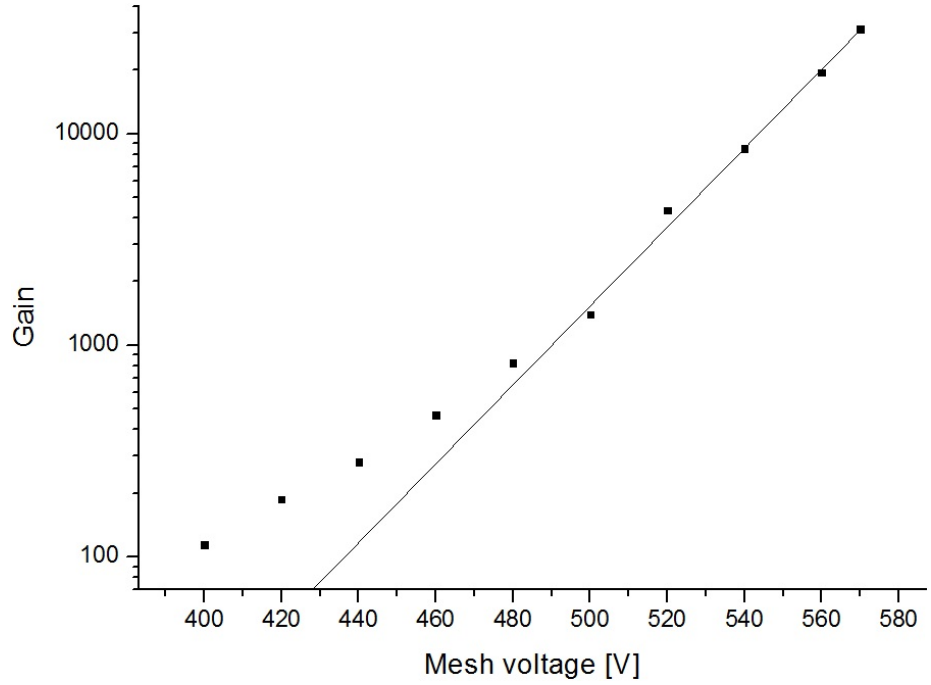

Figure 4.16: Gain curve of the combined detector. $E_d = 0.62\,\mathrm{kV/cm}$, $\Delta V_{\mathrm{GEM}} = 325\,\mathrm{V}$, $E_t = 1.25\,\mathrm{kV/cm}$.

The discharge behaviour of the combined detector is probed using the experimental setup depicted in Fig. 4.6 (right) and explained in Section 4.3.1. Figure 4.17 (left) displays two energy spectra, acquired with a drift field of 0.62 kV/cm, a potential difference of 325 V across the GEM, a transfer field of 1.25 kV/cm and a negative potential of 440 V on the Micromegas mesh with respect to the grounded anode, from where the induced signal is read out. The solid-filled red spectrum is obtained in response to 5.9 keV X-rays from a ^{55}Fe radioactive source, and exploited for calibration purposes. Contrarily to the spectrum in Fig. 4.15, only the photopeak and the escape peak from photons converting in the drift gap are visible because, despite the relatively low gain of the preamplification stage, the signals from interactions in the transfer gap are cut out by the discriminator threshold. The black curve is the spectrum generated by the alpha particles, acquired under the same conditions. Figure 4.17 (right) is an alpha spectrum in which the signal is attenuated by 18 dB to explore the high-charge-deposition events. Comparing the three graphs, one can see a strong low-energy component and a clear peak around 500 keV, above which value the number of recorded events drops with an exponential tail reaching a few MeV. The trend is understood considering that, oppositely to X-rays, the spectrum of alpha particles strongly depends on the chamber geometry. In this specific case, the energy deposit is significantly lower than the Q-value because the alphas are produced uniformly with an isotropic momentum distribution and because the conversion gap is thin compared to the average alpha range (cf. [64]).

The interaction rate of the alpha particles is estimated by fitting a logistic sigmoid function of the type of Eq. (4.1) to the number of event counts in a Micromegas voltage scan. The extracted parameter is then used to compute the discharge probability by normalizing the spark rate measured with the same procedure utilized in Section 4.3.1. In order to compare the discharge behaviour of the standalone Micromegas to the one of the composite detector, the gain data of Fig. 4.8 and 4.16 are fitted with exponential curves and the amplitudes and voltage-step constants are extracted. These parameters are then employed to compute the effective gas gain for the various voltage settings applied during the spark-rate measurements. The discharge probability as a function of the gain for both detector configurations

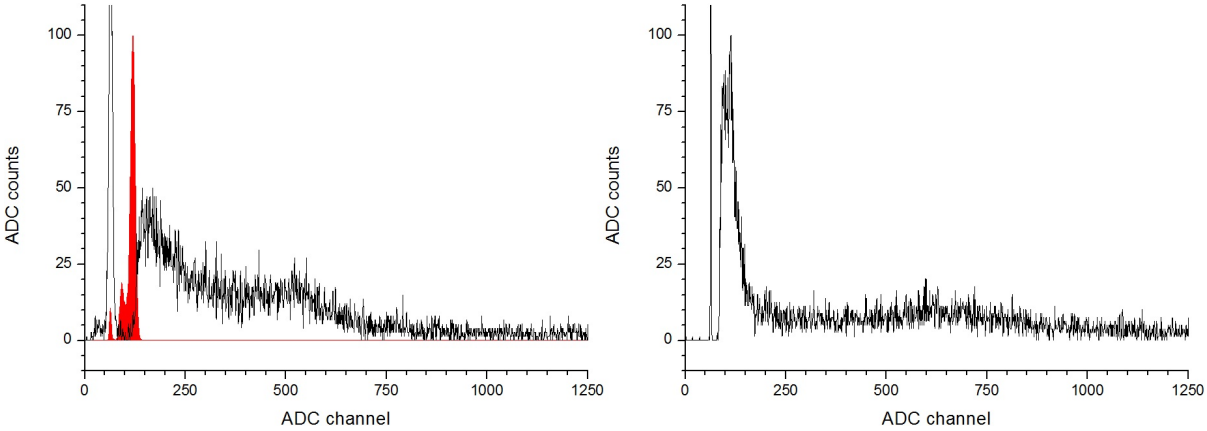

Figure 4.17: Energy spectra of ^{55}Fe (in red) and alpha particles (in black). $E_d = 0.62\,\mathrm{kV/cm}$, $\Delta V_{\mathrm{GEM}} = 325\,\mathrm{V}$, $E_t = 1.25\,\mathrm{kV/cm}$, $V_{\mu\mathrm{M}} = 440\,\mathrm{V}$.

is summarized in Fig. 4.18. The black squares trace the behaviour of the standalone Micromegas, taken as benchmark chamber. The red triangles refer instead to the combined detector, where the GEM is operated at a fixed voltage of 325 V. The spark reduction, although visible, is rather modest and cannot be considered satisfying. This is not a surprise and should not be regarded as a disproof of the double-stage approach, as the preamplification structure is here operated at a relatively low voltage and therefore brings only marginal benefits. The next section explains how to get the best out of the GEM to improve this result.

4.3.3 Parameter optimization

The scarce performance improvement in terms of discharge probability observed in Section 4.3.2, following the introduction of the preamplification stage above the Micromegas mesh, is understood to be due to the low gain boost added by the GEM. In turn, this is a consequence of keeping the potential difference across the foil at a low and constant value through the Micromegas voltage scan. Such an explorative choice was aimed at probing the detector properties in safe electrostatic configurations and getting familiar with its behaviour as a function of the different parameters. When operating a multi-stage amplification device, however, it is common practice to change the bias of each layer at the same time. The purpose is that of varying the gain of each amplifying structure by the same relative amount, avoiding to overload one specific station and thus reducing the risk of sparks.

In order to apply this philosophy to the combined GEM and Micromegas chamber under test, it is first of all necessary to find the characteristic voltage step that increases the effective gas gain of each stage by a fixed amount. Since Townsend charge multiplication in the proportional regime is governed by the exponential law of Eq. (1.31), it is natural to take as characteristic voltage step the difference of potential that raises the gain by a factor of e. As for the GEM, the parameter is extracted from an exponential fit to the data of Fig. 4.11, giving $50.7 \pm 1.3\,\mathrm{V}$. As regarding the Micromegas, both the graph in Fig. 4.8 and the one in Fig. 4.16 are fitted and the results combined to yield $24.9 \pm 0.5\,\mathrm{V}$. The data of Fig. 4.12 are not used, as the measurement precision is by far lower than for the other two samples.

Once the characteristic voltage steps are known, one has to establish how best to split the total effective gas gain among the different layers making up the multi-stage detector. In the case of triple GEMs, for example, the research work carried out in the development of the chambers for the COMPASS experiment at CERN has shown that the gain-to-discharge-probability ratio is optimized by operating the

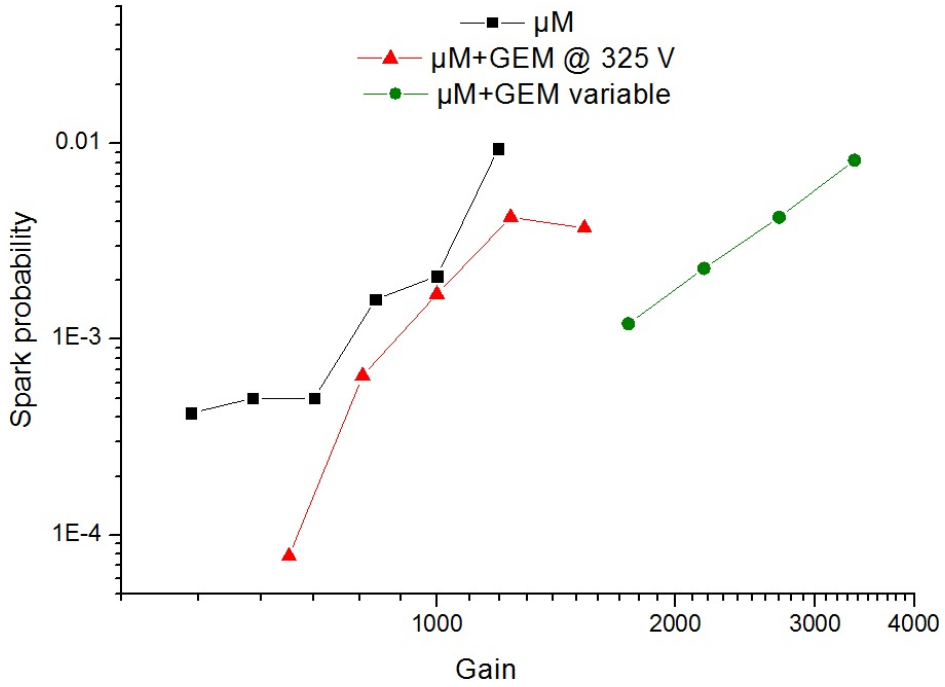

Figure 4.18: Spark probability vs gain.

first stage at about 10% higher voltage and the last stage at about 10% lower voltage with respect to the second GEM [23]. In the present case, a good starting point is given by the sparking limits observed in Section 4.3.2. Figure 4.11 indicates that the limit is 410 V for the GEM, while Fig. 4.12 and 4.16 give a limit of 570 V for the Micromegas. Voltage scans are then performed starting from these values and receding by multiples or submultiples of the characteristic voltage steps.

Figure 4.19 shows such a double voltage scan, where the lower abscissa shows the Micromegas negative potential with respect to the grounded anode and the upper horizontal axis is the corresponding bias applied to the GEM. The vertical axis records the number of detected copper X-rays per unit time. During the scan, the drift field is maintained at 0.62 kV/cm, while the transfer field is fixed to 1.25 kV/cm. The figure demonstrates that, under low-noise conditions and with an appropriate discriminator threshold, signals generated by the conversion of 8 keV photons can be clearly distinguished from noise already with 310 V on the GEM and 518 V on the Micromegas mesh.

In a similar fashion, Fig. 4.20 is a gain curve traced by changing the voltages on both amplification stages. The drift and transfer fields are the same used to acquire the data of Fig. 4.19. The gain is calibrated following the steps listed in Section 2.4.4 and applying the corrections of Eq. (4.3) and (4.4). The chamber is illuminated with a narrow photon beam, generated in an X-ray tube with copper target and trimmed with a long collimator of 1 mm in diameter. Taking into account the counting plateau of Fig. 4.19, the calibration is performed biasing the cascaded stations with 360 and 544 V, respectively. The rest of the curve is obtained by rescaling the gain at the calibration point according to the position of the pedestal-subtracted photopeak, as extracted from copper X-ray spectra acquired at different voltages and at a fixed photon rate of $1070 \pm 27\,\mathrm{Hz/mm^2}$. The behaviour is perfectly exponential, as shown by the fitting curve superimposed on the experimental points. The maximum achievable gain is 31 200, reached with 373 V on the GEM and 551 V on the Micromegas.

At this point one can move on to measuring the discharge probability. The method employed is the same used for both the standalone Micromegas and the first study of the combined detector. The gas

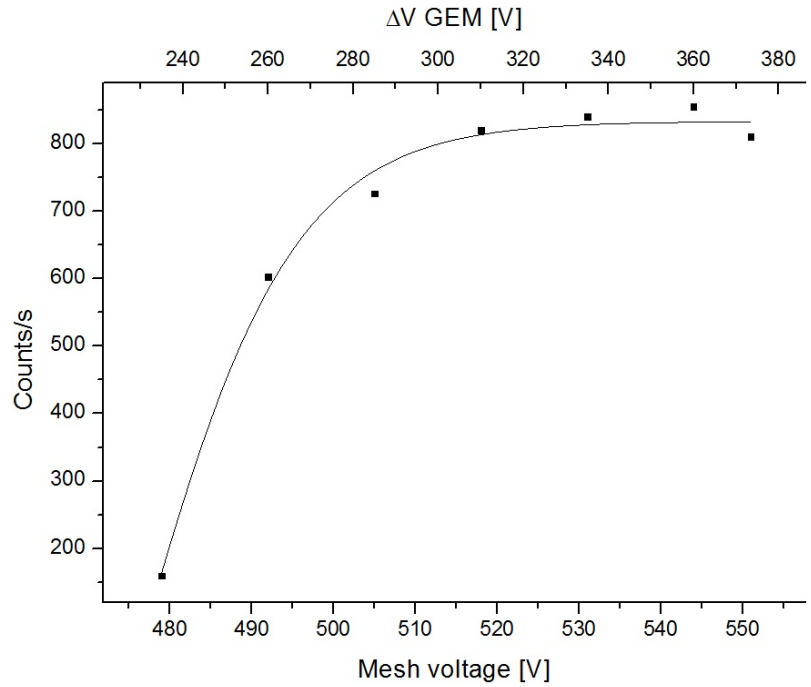

Figure 4.19: Measured rate of copper X-rays. $E_d = 0.62\,\mathrm{kV/cm}$, $E_t = 1.25\,\mathrm{kV/cm}$.

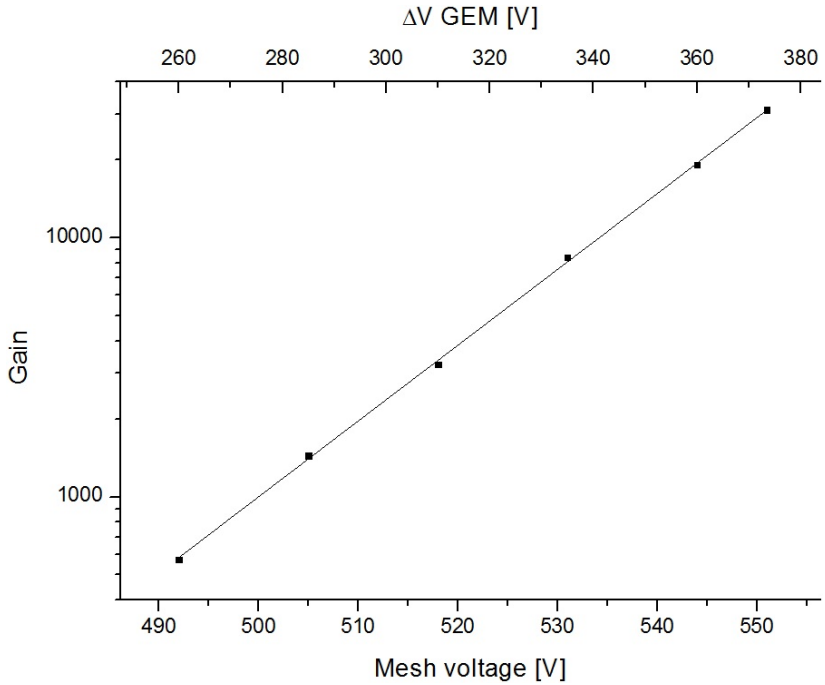

Figure 4.20: Gain curve of the combined detector (double voltage scan). $E_d = 0.62\,\mathrm{kV/cm}$, $E_t = 1.25\,\mathrm{kV/cm}$.

mixture is contaminated with unstable ^{220}Rn nuclides, that are transported inside the detector active volume with the gas flow and eventually decay by emitting alpha particles with a Q-value of about 6.5 MeV. The alpha interaction rate is determined with a voltage scan, as done in Fig. 4.19 for X-rays. Defining a spark as a high-charge-deposition event that provokes a breakdown of the gas dielectric strength and causes a short between electrodes, one can get the spark rate from the average time between consecutive voltage trips of the power supply. The discharge probability is then computed by normalizing the measured spark rate with the number of alphas per unit time. The gain curve of Fig. 4.20 is fitted with an exponential function and the extracted parameters are exploited to compute the gain at the voltages used during the discharge study.

The results, expressed in terms of spark probability as a function of the total effective gas gain, are summarized in Fig. 4.18, together with the curves discussed at the end of Section 4.3.2. Comparing the green circles to the black squares representing the standalone Micromegas, taken as benchmark, it appears that the discharge probability is reduced by more than one order of magnitude at a gain of 10^3, and that the spark suppression factor increases at higher gains.

In order to get the maximum benefit from the double amplification structure operated with variable voltage on both stages, it is necessary to determine how to best distribute the total effective gas gain between the GEM and the Micromegas. So far, this has been done by taking the sparking points measured in Section 4.3.2 as maximum settings and subtracting multiples or submultiples of the characteristic voltage steps extracted from the fits to the gain curves. Now that the detector behaviour in terms of gain and discharge probability has been delineated, it is possible to test the ansatz against experimental data and tweak the gain partitioning if needed. For this purpose, the voltage of the two amplification layers is scanned in opposite directions, in such a way to maintain the total gain constant, while changing the contribution of the two structures. For each voltage configuration, the average time between consecutive power trips in presence of alpha particles is measured and recorded. Figure 4.21 shows the results obtained for a fixed gain of 1440, previously achieved with a drift field of 0.62 kV/cm, a voltage of 285 V across the GEM, a transfer field of 1.25 kV/cm and 505 V on the Micromegas mesh. Here, the drift and transfer fields are maintained at the same values, while the GEM voltage is scanned from 235 up to 410 V and the Micromegas potential from 531 down to 440 V with respect to the grounded anode. The spark rate clearly increases as the gain load gets heavier on the first stage, in which case the discharges are observed to originally take place on the GEM and subsequently propagate to the Micromegas with delayed streamers. As the gain share is shifted towards the second amplification stage, sparks are observed only on the Micromegas and their rate tends to stabilize. On first approximation, one can say that the discharge probability remains relatively low as the GEM voltage is scanned from 235 to 323 V and the Micromegas from 531 to 486 V. This validates the original ansatz on the gain splitting and confirms that the data of Fig. 4.18 represent the behaviour of a detector with optimized operating parameters.

In conclusion, the double-stage approach reduces the discharge probability by more than an order of magnitude at an effective gain of 10^3, and the suppression factor grows at higher gains. However, this is not sufficient to guarantee safe operation in the ATLAS environment. Additional downsides appear when moving to the design of a full-size chamber. The use of a GEM spoils one of the Micromegas' most attractive features, namely the easy, fast and clean mounting procedure, that is often as simple as positioning the drift electrode and sealing the gas volume. On the contrary, a large-area GEM requires lengthy and complex stretching and framing procedures, and the use of glues and spacing frames in the gas volume. Alternative approaches based on stretch-free and/or spacer-free GEMs can be studied, but the research in these fields is still in a very early stage. The increased mechanical sophistication coming from the use of a preamplification structure inevitably reflects in higher manpower cost and longer assembly time. Also, the added services have to be taken into account when considering implementation into the ATLAS new Small Wheels.

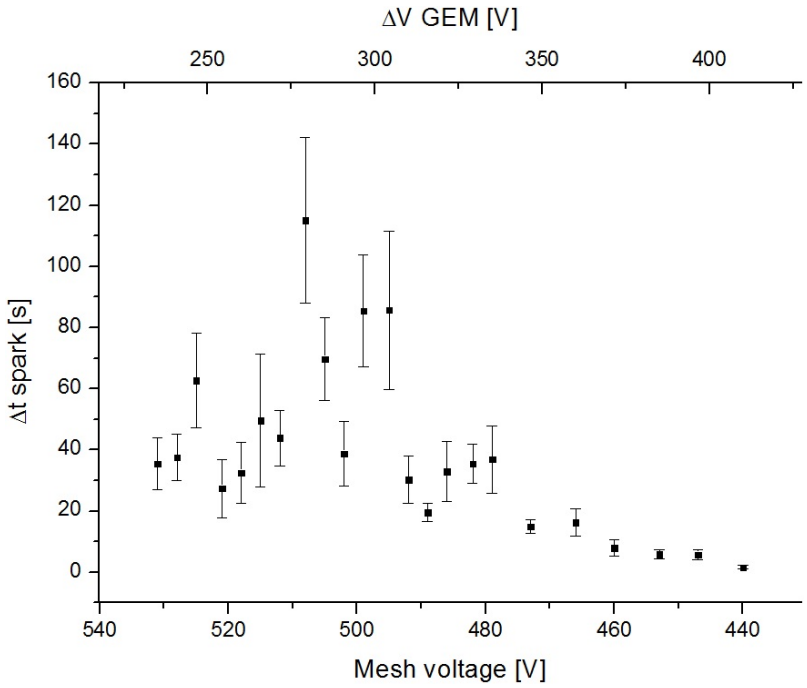

Figure 4.21: Optimization of the relative bias voltages. $E_d = 0.62\,\mathrm{kV/cm}$, $E_t = 1.25\,\mathrm{kV/cm}$.

4.4 Resistive Micromegas

The considerations made at the end of the previous section make the double-stage approach inadequate for the detectors of the ATLAS new Small Wheels. Given the specific application, scalability to square metre size and possibility of large-volume production in a commercial company are a must. In order to ease the chamber design, fabrication, assembly and commissioning, a single-stage technology similar to the original Micromegas concept is also desirable.

In a single-stage detector, the charge multiplication will take place only in the Micromegas' amplification gap. Given the stringent requirements on the MIP detection efficiency for the chambers of the ATLAS Small Wheels, one will be forced to operate the Micromegas at a higher gain with respect to a preamplified detector, thus inevitably increasing the discharge probability. When developing an alternative approach not involving preamplification structures, one therefore has to abandon the idea of reducing the absolute number of sparks and rather focus on mitigating their effects. With this in mind, it is helpful to analyze in some detail the possible consequences of a discharge.

In the first place, physical damage to the components of the micropattern gas detector may happen. This was a primary issue in microstrip gas chambers, whose anode strips proved to be very fragile due to their reduced width, which could be as low as 10 µm. Micromegas, on the other hand, are among the most spark-proof micropattern gas detectors. A discharge creates a short between the Micromegas mesh and the anode, causing the dumping of the energy stored in the mesh, held at a negative potential, on the grounded readout elements. For the standard amplification gap thickness of 128 µm, the Micromegas capacitance is about $0.7\,\mathrm{nF/dm^2}$ and the corresponding stored energy about $0.1\,\mathrm{mW/dm^2}$ at a normal operating voltage of 540 V. Although the amount of energy stored and released in case of spark is not negligible, the simple and robust mechanical structure, together with the minimal amount of insulating materials in the active area, make Micromegas capable of standing thousands of discharges without suffering any damages.

Secondly, sparks represent a potential threat for the delicate readout electronics. Since in Micromegas the amplification gap coincides with the induction gap, discharges always involve the readout elements and thus have a direct impact on any circuits connected there. Nowadays, various protection schemes exist that allow Micromegas to be operated with no danger for the electronics. As a general rule, it is anyway considered a good design choice to equip the readout board with protection diodes that would dump to ground any excess currents before they reach the most sensitive parts of the electronics.

Lastly, sparks are a source of dead time. The power supply will take a finite amount of time to recharge the Micromegas mesh after its voltage has dropped as a consequence of a short circuit with the anode. The recovery speed strictly depends on the chosen bias distribution scheme. For example, both universal multichannel power supply mainframe systems and programmable NIM high-voltage power supplies feature built-in ramp-up speed regulators that can be set individually for each channel. In such case, the mesh reload time is usually approximately equal to the voltage drop times the ramp-up speed. Conversely, non-programmable NIM high-voltage power supplies do not provide this functionality. Therefore, when such a simpler solution is used, the recharge time will be a function of the voltage drop, the power-supply current limit, the capacitance of the Micromegas and of the SHV cables and the number and type of high-voltage filters applied. Depending on the scenario, the recovery process can be as quick as a few ms or require several seconds. During this time lapse, the Micromegas mesh voltage is too low to deliver a charge amplification sufficient to efficiently detect MIPs. In LHC applications, even a dead time of a few ms is enough to make the chamber blind for a large number of bunch crossings, thus completely spoiling its trigger capabilities.

From what has been said, it appears that the employment of single-stage Micromegas in the ATLAS new Small Wheels, although desirable because of the simple and neat mechanics, critically depends on the ability to reduce the dead time. A research effort in this sense has started in 2009. The basic idea is that of limiting, and whenever possible altogether averting, mesh voltage drops after a discharge. This is done by physically separating the metallic readout elements from the gas volume and interposing some kind of resistive structure. Within this scheme, significant voltage drops of the mesh are avoided by preventing streamers from creating direct short circuits to ground.

In the rest of the chapter, the resistive technology is presented. The novel resistive Micromegas are capable of operating at gas gains of up to about 10^4 and with more than 98% detection efficiency even in presence of sparks. Additionally, they show an improved performance in terms of space resolution with respect to standard chambers. The manufacturing procedure is scalable up to square metre size and it makes use of standard photolithographic methods, thus enabling large-volume production in a commercial company. The next two sections introduce the resistive approach, while the following ones present some tests carried out with soft X-rays and describe a beam test and the consequent data analysis.

4.4.1 Early resistive schemes

The resistive scheme was first tried in 2009 on three small test chambers, whose active area was limited to $10\times10\,\mathrm{cm}^2$ [65]. The detectors, named R1, R2 and R3, are very similar to a standard bulk Micromegas with one-dimensional readout. The copper anode strips are topped with 50 µm thick resistive traces matching the readout pattern and they are interleaved with insulating traces filling the inter-strip space from the PCB to the upper edge of the resistive elements (cf. Fig. 4.22 a). On top of this structure the Micromegas mesh is stretched and laminated in bulk technique, as it would be done for a non-resistive detector. The difference between R1, R2 and R3 lies in the resistance of the covering traces, which is 100 kΩ, 10 MΩ and 20 GΩ, respectively. All three chambers provide clear signals in response to soft X-rays, but none of them offers sufficient reliability, as discharges seem to easily penetrate at the boundary between the resistive and the insulating traces, causing permanent breakdown of the resistive material.

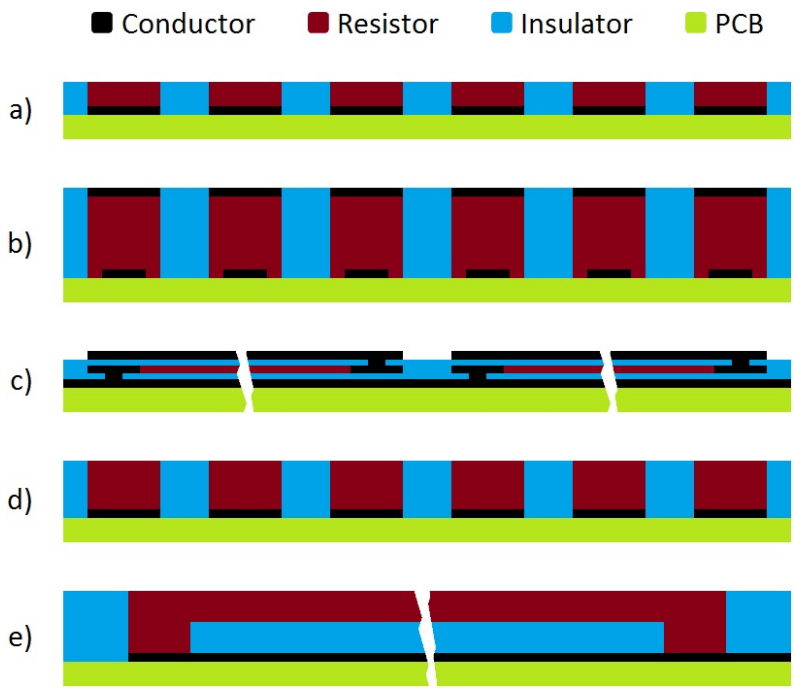

Figure 4.22: Schematics of early resistive Micromegas. a) cross section of R1, R2 and R3; b) cross section of R4; c) longitudinal section of R5; d) cross section of R6, R7 and R8; e) longitudinal section of R9 and R10.

The fragility issue is addressed in R4. The width of the copper anode strips is slightly reduced, while the lateral extension of the resistive traces is maintained at 150 µm (cf. Fig. 4.22 b). In this way, a resistive path is created between the readout and the insulating traces, improving the electrical hermeticity. Moreover, the vertical thickness of the resistive traces is increased from 50 to 150 µm. Finally, the resistive traces are topped with rectangular metallic pads 150 µm wide and 1.5 mm long, running in the trace direction. In the case of sparks, the metallic pads are expected to help spreading the charge along the readout element, thus reducing the density of the current flowing to ground. Laboratory tests show that the modifications do not bring any benefits, as the resistive structures still get easily damaged by sparks.

With R5, a different strategy is attempted to increase the robustness of the resistive elements against discharges. The copper anode strips are covered with a Kapton sheet of 40 µm in thickness and topped with rectangular metallic pads of $1.5 \times 0.15\,\mathrm{mm}^2$, the same size used for R4 (cf. Fig. 4.22 c). The polyimide layer introduces an insulating barrier with a breakdown voltage of more than 1 kV. A 1 mm long resistor, whose breakdown voltage is also ranked higher than 1 kV, is located under each pad, embedded in the Kapton and running along the pad length. Finally, two microvias in the polyimide create electrical bridges that connect each pad to the resistor below it and the resistor to the readout strip. Although no signs of rupture are observed during the detector tests, the overall performance is not satisfactory, as the power supply often trips as a consequence of a spark, like in non-resistive Micromegas. The reason for this behaviour is probably to be found in the low resistance from pad to ground, that is only 2 kΩ. Given the difficulty to increase such value with the same production procedure, this approach is not further pursued.

The next three chambers, named respectively R6, R7 and R8, see a return to the original resistive scheme. Although the layer structure and most geometrical parameters of these detectors are the same as for R1, R2 and R3, the thickness of the resistive layer is increased to 100 µm and different values of

resistivity are tried (cf. Fig. 4.22 d). Moreover, the resistor deposition technique is improved. Again, all three chambers are rapidly deteriorated by discharges.

The evidence collected so far seems to indicate that the witnessed material fragility is not the consequence of a poor choice of the resistivity value, neither it can be fixed by enhancing the manufacturing method. For this reason, a different structural layout is adopted for the following generation of detectors: R9 and R10. The readout board consists of a standard PCB with one-dimensional copper strips of 10 cm in length and 150 μm in width, patterned with a pitch of 250 μm. The anode is clothed with a 64 μm thick photoimageable coverlay[2] and topped with resistive traces matching the readout pattern (cf. Fig. 4.22 e). The traces have a resistance of 1 MΩ/cm and are connected to the anode strips only at the two extreme edges, outside the active area. This alternative scheme gives much better results, drastically reducing the effects of sparks. In case of a discharge, in fact, the short circuit between the Micromegas mesh and the resistive traces will result in a transient decrease of the trace voltage, while the mesh potential will drop only slightly. Moreover, the high impedance of the resistive traces to ground is enough to quench the streamer, preventing the power supply from tripping. After extended tests, however, also these chambers show signs of degradation. A visual inspection of the readout structure reveals that all the breakdown damage occurs near the edge of the active area, close to the points where the resistive traces connect to the anode. Here, the resistance to ground is minimum and therefore the spark current is maximum. Contrary to the previous detectors, this is not due a material weakness, but rather to a layout flaw that can be easily fixed. The modifications, described in Section 4.4.2, lead to the type of Micromegas that has been proposed for the ATLAS new Small Wheels.

4.4.2 Spark-resistant bulk Micromegas

The idea of separating the readout elements from the resistive structures, introduced at the end of the previous section and explored with R9 and R10, is the first at least partially successful attempt to mitigate the undesired effects of discharges in a single-amplification-stage Micromegas. The concept is further investigated with R11, R12 and R13, which borrow the original notion and develop it to address the weakness noticed at the edge of the active area of R9 and R10. The resulting layout, shared by R11, R12 and R13, is at the base of the novel spark-resistant bulk Micromegas technology [66].

Figure 4.23 displays two schematic views of this new type of Micromegas, in a cross sectional plane orthogonal to the strips (left) and in a plane including one strip (right). Similarly to R9 and R10, the readout board is a 3 mm thick standard PCB with 360 one-dimensional copper strips of 10 cm in length, 150 μm in width and 18 μm in thickness, patterned with a pitch of 250 μm. The pathways departing from the readout elements are clustered in 5 groups of 72 channels each and routed to 5 ERNI female connectors of type SMC 1.27 mm. Each connector features 80 pins, arranged in two rows of 40. The central 72 pins are used as signal channels, while the 4 most external pins at the two ends of the connector serve as grounding points. The $10 \times 9\,\mathrm{cm}^2$ anode active area is coated with a 64 μm thick insulating layer, consisting of a sheet of DuPont Pyralux PC 1025 photoimageable coverlay. This stratum is then topped with 64 μm thick resistive traces matching the geometry of the readout pattern. The value of resistance per unit length varies between R11, R12 and R13 as summarized in the second column of Table 4.1. The 100 μm wide inter-strip gaps are filled by additional insulating coverlay of the same thickness, thus creating a flat surface across the entire active area. One important novelty with respect to the previous schemes is that the resistive structures here have a ohmic connection to the chamber ground rather than to the anode elements. Moreover, since the fragility of the resistive structures observed in both R9 and R10 is due to the relatively low peripheral resistance to ground, the ohmic contact is not direct, but

[2] DuPont Pyralux PC 1025

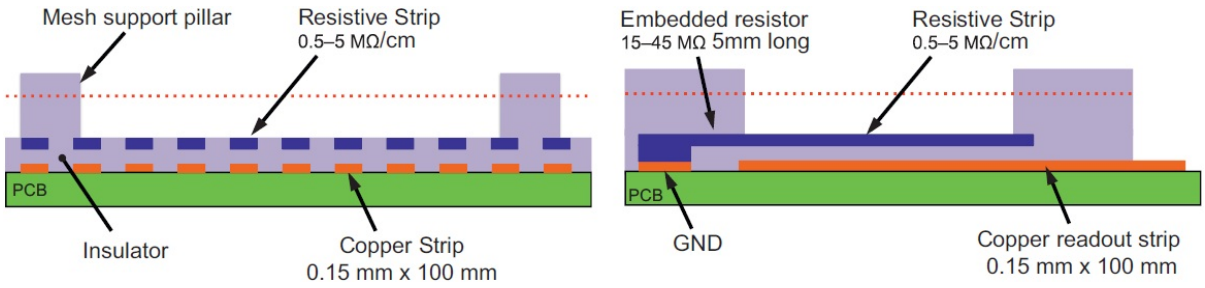

Figure 4.23: Schematic of a spark-resistant bulk Micromegas.

Table 4.1: Resistance specifications of R11, R12 and R13.

Chamber	R_{trace} [MΩ/cm]	R_{ground} [MΩ]	R_{sheet} [kΩ/□]
R11	2	15	30
R12	5	45	75
R13	0.5	20	7.5

rather realized through high-value resistors that limit the current intensity in case of sparks at the edge of the active area. Each such resistor consists of a 5 mm long section of the resistive trace, manufactured with higher resistivity and located outside the detector active area. The values of the grounding resistors of R11, R12 and R13 are reported in the third column of Table 4.1. The Micromegas is completed by a stainless steel mesh having 18 µm thick wires interwoven with a pitch of 63 µm, corresponding to 400 LPI and 51% optical transparency. The mesh is laminated in bulk technique at a distance of 128 µm from the resistive readout and kept under mechanical tension thanks to cylindrical pillars having a diameter of 400 µm and a pitch of 2.5 mm in both x- and y-direction, resulting in only 2% of dead materials on the active area.

Figure 4.24 sketches the equivalent circuit of a resistive Micromegas [67]. The model presented is qualitative only and not based on a detailed simulation. Moreover, the values assigned to the components, although representative of the real chambers, are not meant to be accurate. In spite of this, the analysis of the schematic provides useful insights on the detector operation principles and enables making some predictions of its properties. R_1 is the grounding resistor of a single resistive trace, while R_2 represents the section of the resistive trace included between R_1 and the point where the charge is induced. Therefore R_2 is not constant, but depends on the event location. C_1 is the mesh capacitance to ground. Considering that the mesh stretches a bit outside the active area and approximating the relative permittivity of the coverlay to 4, C_1 evaluates to about 4 nF, which is very large compared to the other capacitances inside the chamber. C_2 is the mesh capacitance to a single resistive trace, whereas C_3 is the capacitance between the resistive trace and the anode element below it. The capacitances to the farther readout strips are much smaller and hence neglected in this model. C_2 and C_3 depend on the relative permittivity of the interposed materials, the vertical position of the layers within the stack, the strip pitch and the charge spread along the resistive traces. In turn, the latter parameter is a function of the gas transverse diffusion at the operative field and of the trace resistance per unit length. More specifically, a smaller transverse diffusion or a higher trace resistivity result in a reduced charge spread and therefore in a lower capacitance. Although the actual values of C_2 and C_3 may be difficult to estimate, their ratio is constant, depending only on the relative permittivities and the distances between the electrodes. In the detectors under analysis $C_3/C_2 \simeq 8$, which means that about 90% of the signal will flow through C_3 independently of the trace resistivity, the adopted gas mixture and the operative bias

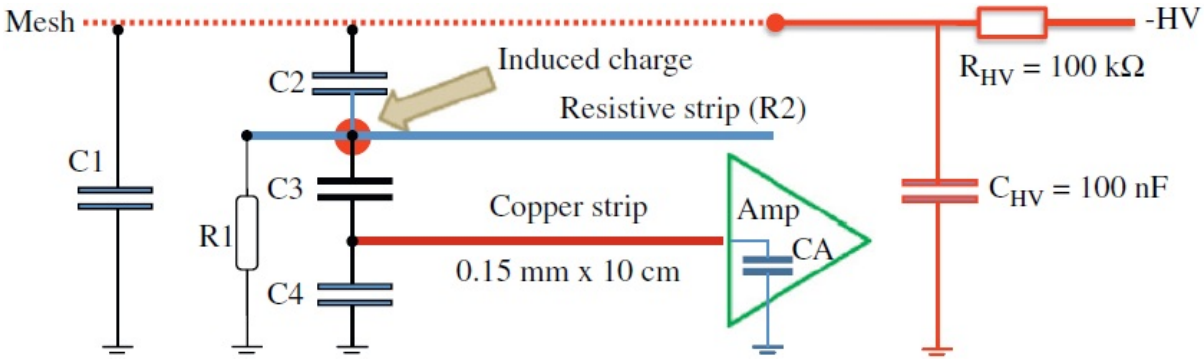

Figure 4.24: Equivalent circuit of a spark-resistant bulk Micromegas.

voltages. C_4 is the anode strip capacitance to ground, whose value is of the order of a few pF, and C_A is the input capacitance of the charge preamplifier. Finally, $R_{\mathrm{HV}} = 100\,\mathrm{k\Omega}$ and $C_{\mathrm{HV}} = 100\,\mathrm{nF}$ are discrete components mounted on the power line just outside the chamber, which make up a simple low-pass filter with cut frequency $f_c = 1/(2\pi C_{\mathrm{HV}} R_{\mathrm{HV}}) \simeq 16\,\mathrm{Hz}$ and attenuation of $-20\,\mathrm{dB/decade}$.

The employment of resistive structures is not new in the Micromegas community [68–70]. However, most of the earlier resistive detectors exploit a solid and uniform resistive layer covering the whole readout board to spread the charge over several anode elements and thus reach a good space resolution with wider and fewer readout channels. Resistive meshes have also been tested for spark protection [71]. The idea behind the new resistive Micromegas is different. The resistive plane is segmented into traces matching the anode pattern in order to prevent the charge spread in the direction perpendicular to the strips, even though spreading along the strip length is still present.

The movement of electrons and ions in the amplification gap induces signals on the resistive traces, which are read out through the capacitive coupling to the anode strips, where the charge preamplifiers are connected. The charge collected on the resistive trace then flows to ground through R_1. In the simple model presented above, only the coupling to the readout element located right underneath each resistive trace is considered. The approach is in first approximation correct, but the couplings to the farther anode strips significantly improve the space resolution, as described in Section 4.4.4.11.

In a resistive Micromegas there is no attempt to reduce the discharge probability, which is the same as in a non-resistive chamber. In case of sparks, the resistive structures limit the current flowing to ground, thus quickly and effectively quenching the streamers before they can cause any significant drop of the mesh voltage. Moreover, the segmentation of the resistive layer allows the area affected by the discharge to be contained. The overall effect is that of drastically reducing the dead time and boosting the detection efficiency. At the same time, the exploitation of high-value grounding resistors secures high DC impedance to ground for efficient spark quenching, while enabling the use of a low surface resistance for high rate capability. The sheet resistance of R11, R12 and R13 are shown in the rightmost column of Table 4.1.

4.4.3 Laboratory tests

To evaluate the performance of R11, R12 and R13, each readout board is paired to a drift electrode, made out of a stainless steel mesh having 20 µm thick wires interwoven with a pitch of 73 µm, corresponding to 350 LPI and 53% optical transparency. The mesh is stretched on an FR4 frame and maintained at a distance of 4 mm (in R11) or 5 mm (in R12 and R13) from the Micromegas, thanks to plastic washers and nuts mounted on fixation screws at the four corners. The gas volume is defined by a 20 mm tall

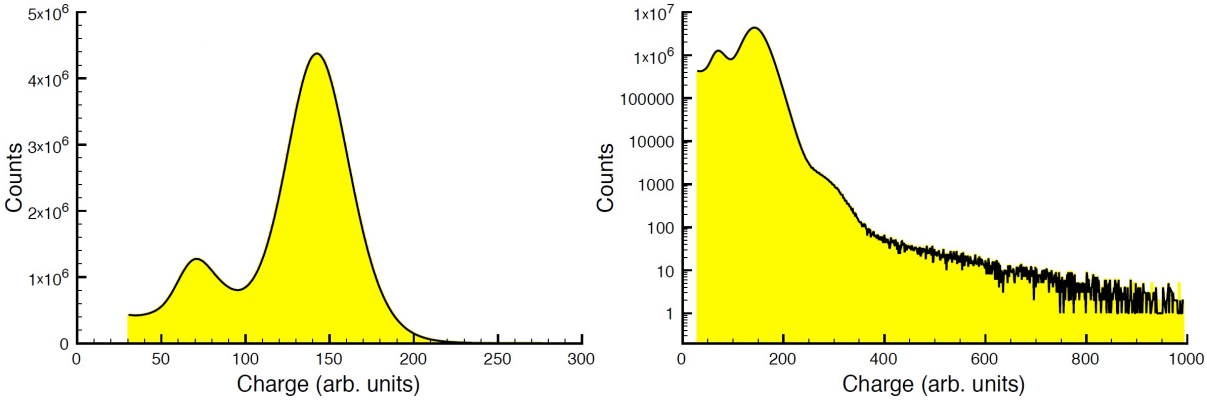

Figure 4.25: Energy spectrum of R11, in linear (left) and logarithmic (right) scale. From left to right: the argon escape peak and the photopeak. The shoulder around 300 charge units in the logarithmic plot is compatible with two-photon events.

aluminum frame and a dismountable roof featuring a 50 µm thick Kapton window. Both couplings are made with fitted O-rings to ensure gas tightness. The gas inlet and outlet are housed in the aluminum frame, located at opposite corners, while two SHV male chassis sockets[3] mounted just outside the frame provide the power connections for the Micromegas and the drift meshes.

In order to compare the behaviour of the three resistive Micromegas to that of a traditional detector, a fourth chamber (S3) is prepared, manufactured with non-resistive bulk technology. Since S3 is meant to be used as a benchmark, its design strictly follows that of R11, R12 and R13. The readout board has the exact same layout, from the geometry of the anode strips and the routing of the signal pathways, to the type and position of the readout connectors. Given that in S3 both the insulating and the resistive structures are missing, the Micromegas mesh is laminated right on top of the anode strips. The Micromegas and the drift meshes, the aluminum frame, the dismountable roof and the high-voltage connections are also the same. The only differences lie in the diameter of the mesh support pillars, that is 300 µm instead of 400 µm and the drift gap thickness, that is fixed to 4 mm as in R11.

Figure 4.25 presents an energy spectrum, drawn in both linear (left) and logarithmic (right) scale, obtained by illuminating R11 with 5.9 keV photons from a ^{55}Fe radioactive source. The source is placed at about 20 mm from the drift electrode, separated from the gas volume by the 50 µm thick Kapton entrance window located on the chamber's dismountable roof, and produces an integrated rate of about 2.5 kHz on the whole active area. The detector is flushed in open-loop configuration with an argon-based gas mixture containing 15% of carbon dioxide. The drift field is 0.275 kV/cm, while the Micromegas mesh is biased with 590 V, resulting in an effective gas gain of about 8750. The full-energy photopeak and the argon escape peak are clearly visible in both graphs. In the logarithmic plot it is also possible to distinguish a shoulder around 300 charge units, that is compatible with two-photon events. The energy resolution extracted from the Gaussian fit to the photopeak is about 25% FWHM.

In Fig. 4.26, the gain curves of the three resistive Micromegas chambers R11, R12 and R13 are compared to each other and confronted with the gain curve of the non-resistive benchmark detector S3. The characterization is repeated with two gas mixtures containing argon and carbon dioxide in different proportions: 93:7 and 85:15. The 72 signal lines terminating on each of the 5 readout connectors are shorted together on the SMC 1.27 mm ERNI male plugs. The four most external groups of lines are grounded, while the central cluster, corresponding to an active area of $10 \times 1.8\,\mathrm{cm}^2$, is wired to a

[3] Radiall type R317.580, Suhner type 22 SHV 50-0-2

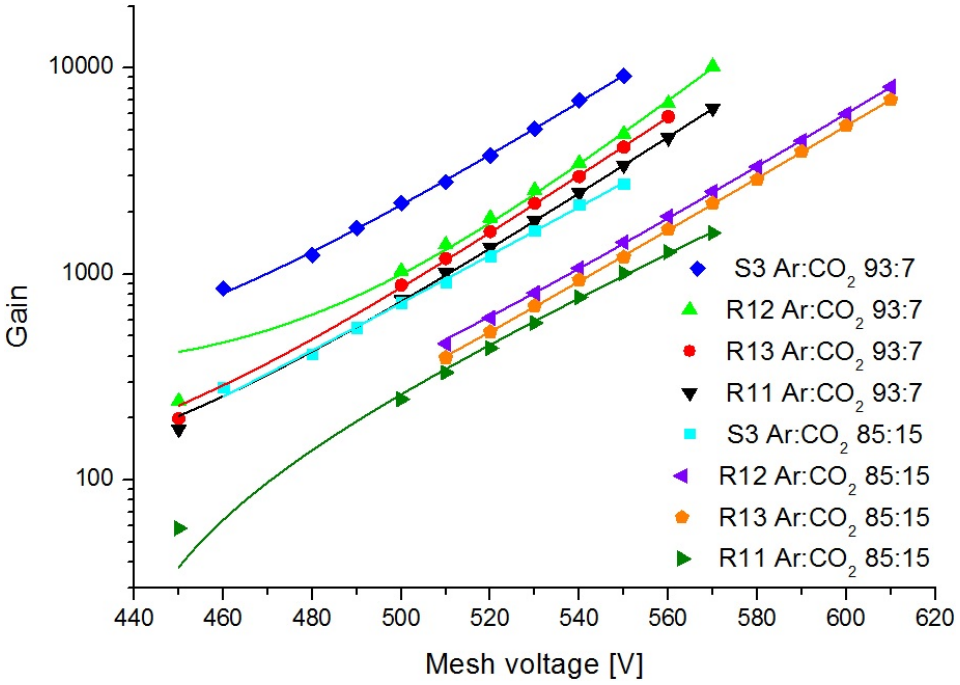

Figure 4.26: Gain curves of R11, R12, R13 and S3.

custom-made charge preamplifier with a rise time of about 10 ns. The signal is then fed to a shaper amplifier with integration and differentiation times of 500 ns and acquired with a multichannel analyzer. The gain calibration is performed by injecting voltage pulses of known amplitude into the test input of the same charge preamplifier. The gain curves are built from the position of the photopeak in the energy spectra obtained in response to 5.9 keV photons from a ^{55}Fe radioactive source at different Micromegas mesh voltages. The fits to the gain curves are based on a function of the type of Eq. (3.2), where G_c, G_e and V_e are the fit parameters, the constant term modeling the deviation of the effective gas gain from a purely exponential behaviour at the lowest voltages.

A detailed analysis of Fig. 4.26 reveals various properties of the resistive Micromegas, provides insights on their working mechanism and gives useful hints for tuning the detector parameters in order to achieve the required performance figures. Before proceeding with such analysis, it is important to expand on the meaning of the variables plotted in the graph. The abscissa is the modulus of the voltage difference between the metallic anode strips, grounded either through the readout electronics or on the ERNI male plugs, and the Micromegas mesh, hold at negative potential. For each voltage setting, the y-value in the chart represents the measured effective gas gain, which should not be confused with the charge amplification factor. The latter quantity is defined as the mean ratio between the number of electrons reaching the anode and the number of charges entering in the amplification region. The effective gas gain, on the other hand, is the average ratio between the total charge induced on the anode elements and seen by the readout electronics and the ionization charge produced in the interaction gap. Although in a non-resistive chamber having a relatively high electric-field gradient in the proximity of the amplification mesh these two quantities can be numerically very close, they are conceptually different. The effective gas gain depends on the charge amplification factor, but it also takes into account the electron losses on the Micromegas mesh. Moreover, in case of R11, R12 and R13, the charge induced on the resistive traces is not the same as the one seen by the readout electronics, due to the various resistive and capacitive couplings highlighted in Fig. 4.24.

The first thing one notices from Fig. 4.26 is that the effective gas gain is systematically greater in Ar:CO_2 93:7 than it is in Ar:CO_2 85:15. This is mainly because of the different value of the first Townsend coefficient α in the two gases. For a mixture of argon and carbon dioxide and for a given electric field, α grows with the relative abundance of argon, thus enhancing charge multiplication in argon-enriched gases. For reference, confront Fig. C.1, C.2 and C.3, which show the first Townsend coefficient as a function of the electric field strength in binary mixtures containing variable amounts of argon and carbon dioxide.

By comparing the four detectors, it is clear that S3 always achieves the greatest effective gain for a given gas mixture and a given set of bias voltages. This is understood to be a consequence of the different resistive and capacitive impedances seen by the signal in standard Micromegas and in resistive Micromegas. In the former type of chamber, the movement of electrons and positive ions in the amplification gap induces a signal directly on the metallic anode elements to which the charge preamplifiers are connected. Oppositely, in the latter kind of detector the signal is induced on the resistive traces and only part of it is transmitted to the readout strips via capacitive coupling, as shown in Fig. 4.24 and as it was discussed in Section 4.4.2.

Another interesting observation is made by measuring the amplitude of the anode signal when irradiating the active area close to and far from the grounding points. Data are taken with R11, R12 and R13. For a given chamber, variations are of the order of 10% and do not show any systematic trend. This means that the trace resistivity does not significantly affect the signal read by the charge preamplifiers. In order to justify this behaviour, one can consider the equivalent circuit of a resistive Micromegas that was given in Fig. 4.24. Remembering that the signal induced by the electrons has a rise time in the ns range and that the ion tail is about 100 ns long, it is possible to work out the values of the capacitive impedances, which turn out to be much lower than the resistive ones. Therefore, the resistive traces can be made fairly long without changing the detector response.

Lastly, a gain stability study is performed illuminating the chambers with the same ^{55}Fe radioactive source previously used to trace the gain curves of Fig. 4.26. The effective gas gain slowly decreases over a few minutes after the beginning of the irradiation and it stabilized on a value about 10% lower than the initial one. Also, the time constant is a function of the particle rate. It ranges from 10 to 15 min for photon rates of the order of 100 Hz and it decreases to less than a minute for rates in excess of 1 kHz. Since the effect is observed in both standard and resistive Micromegas, it is considered to be due to the charging-up of the insulator between the strips, either metallic or resistive, leading to a reduction of the electric field in the amplification gap.

4.4.4 Beam tests

One of the key requirements for the chambers of the ATLAS new Small Wheels is the achievement of a detection efficiency of more than 98% per plane for minimum ionizing particles in a hadron environment. The ability of resistive Micromegas to accomplish this task can be proven only by comparing the position of the hits in the chamber against the particle trajectories reconstructed by an external tracker. This can be done either with a cosmic-ray setup or in a beam test. Given the low flux of cosmic rays and the small solid angle subtended by a tracking setup, the latter solution has been preferred.

In order to study the difference of performance between leptons and hadrons, the beam tests are carried out with both kinds of particles. The selected location is the H6 beam line at CERN, which is part of the Super Proton Synchrotron (SPS) North Experimental Area and can provide tertiary beams of muons and pions with energy in the order of 100 GeV. The energy chosen for the beam tests is $\simeq$ 100 GeV for muons and 120 GeV for pions. The detectors are set up in the PPE 146 experimental zone, also called H6A zone, housed in the EHN1 hall.

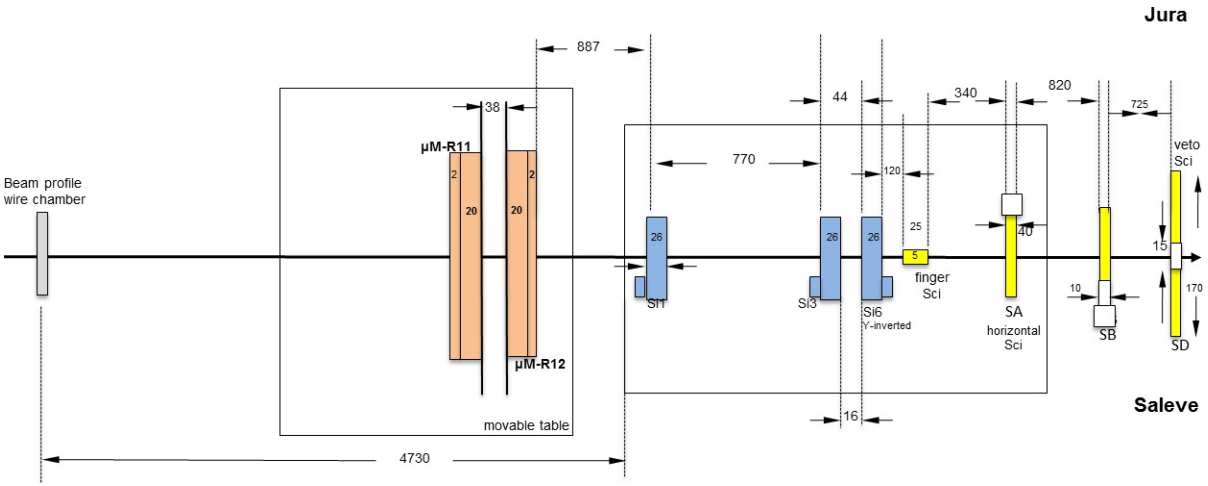

Figure 4.27: Test-beam setup.

Figure 4.27 schematically sketches the layout of the experimental setup in July 2010. The beam enters from the left side of the drawing and points rightward, defining the z-axis of the right-hand coordinate system, with y up and x towards the Jura side. The particles firstly traverse a multiwire proportional chamber, which is used to monitor the beam size and position, and then hit the Micromegas. The detectors under study stand on a movable table that can be displaced along both the x- and y-direction to allow for alignment with the trigger area. A hardware switch enables toggling between local control, which is good for a preliminary coarse alignment, and remote command from the control room, which is more convenient for fine position tuning during data taking. Additionally, the Micromegas sit on a goniometric rotating support, that allows for precisely setting the beam incidence angle. Although different incidence angles are used, all the data analyzed in this thesis are acquired with the Micromegas perpendicular to the beam direction.

Downstream of the Micromegas, the beam traverses a tracking telescope, whose purpose is that of providing x and y hit information on different z-planes to allow for offline reconstruction of the particle trajectories [72]. The tracker, commonly referred to as Bonn ATLAS telescope (BAT), is made up of three equal and independent stations, distributed along the beam axis and sitting on a solid table separated from the movable one used for the Micromegas. Each station consists of a commercially available double-sided, AC-coupled silicon strip sensor type S6934 with integrated polysilicon bias resistors manufactured by Hamamatsu photonics. On each side, 640 n-side strips isolated by p^+-stop implantations are patterned with a pitch of 50 μm, giving rise to a sensitive area of $3.2 \times 3.2\,\mathrm{cm}^2$. The structures on a side are rotated by a nominal stereo angle of 90° with respect to the ones on the opposite side, thus offering bi-dimensional hit localization. The three stations, in order of increasing z-position, are named BAT1, BAT3 and BAT6. BAT6 is taken as the reference plane, with $z = 0$ mm. As from Fig. 4.27, BAT3 is located at −44 mm, BAT1 at −814 mm and the two Micromegas at −1726 and −1784 mm, respectively. Such a configuration, with BAT3 and BAT6 close to each other, optimizes the precision of the extrapolated reconstructed tracks on the Micromegas planes.

The detector setup is completed by a series of plastic scintillators which, together with the tracking telescope, provide the signals used in the trigger logic. Directly downstream of the BAT, a vertical and a horizontal finger scintillator define the trigger area, rectangular in shape, about 5 mm wide and 9 mm tall. The third station in the line takes the name of scintillator B (SB) and it has an active area of $10 \times 10\,\mathrm{cm}^2$. Given its wide coverage with respect to the typical beam size, which is an ellipse 2.5 cm wide and 1 cm

tall, the detector is exploited to measure the number of particles traversing the setup per beam spill. The last station is a very large detector with a small circular aperture in the centre precisely aligned with the beam axis and it is labeled as scintillator D (SD) or, because of its negative-logic selective function, veto scintillator or again halo scintillator.

4.4.4.1 Voltage and current monitoring

Both the reference detector and the three resistive chambers need two independent high-voltage lines, one for the amplification mesh and one for the drift electrode. The required biases are provided by a universal multichannel power supply mainframe system[4], equipped with a high-voltage power supply board[5] that offers up to 12 individually adjustable channels. The set voltage can be selected in the range 0 to −3 kV with a granularity of 250 mV, which corresponds to the voltage-monitoring resolution. The ramp-up and ramp-down speeds can be chosen in the interval 1 to 500 V/s, with steps of 1 V/s. A hardware dip-switch on the board allows the user to toggle between low and high-current mode. In the former case, the current limit of all channels can range up to 20 μA in steps of 2 nA, while in the latter case it can range up to 200 μA in steps of 20 nA. In both cases, the current-monitoring resolution coincides with the current-setting step. Throughout the beam test, the ramp-up speed is fixed to 50 V/s and the current limit is set to 4 μA in low-current mode.

A critical analysis of the monitored high voltage and current drawn by the amplification mesh over time unveils interesting behaviours that shed light on the physics processes taking place inside the detector and at the same time enables a qualitative comparison between resistive and non-resistive chambers to be made. If operated in a beam of muons with energy of the order of 100 GeV, standard Micromegas like S3 perform very well even at high gas gains and high particle fluxes. When switching to a pion beam of similar energy and intensity, however, considerable voltage drops appear in coincidence with high current spikes. Figure 4.28 shows such a behaviour in the monitored high voltage (red points, right scale) and current (blue points, left scale) drawn by the amplification mesh of a non-resistive Micromegas, flushed with Ar:CO_2 85:15 and exposed to a beam of 120 GeV pions. On average, the set voltage of 560 V drops by 70 V 5 times within a 10 s time window, and the whole phenomenon repeats every 40 s. Since the software only records variations of the measured values, the voltage and current are actually constant in the 30 s long time intervals between consecutive groups of spikes, despite inclined lines are shown in the graph. The period of the repeated pattern and the time span in which the spikes are concentrated find a clear match with the SPS cycle length and the duration of the beam spill respectively, which suggests a correlation between the observed events and the presence of incoming hadrons. Further evidence, emerging from in-depth data analysis and discussed in detail in the following sections, indicates that highly ionizing particles are produced by hadronic interactions both in the reference detector and in the resistive chambers. In the former detector type, the streamer following the high-density charge deposition creates a short between the amplification mesh and the unprotected copper anode strips, which causes a sudden dump of part of the stored energy to ground and results in a drop of the mesh voltage for a short time.

Figure 4.29 shows the monitored high voltage (black line, left scale) and current (red squares, right scale) drawn by the amplification mesh of R12, flushed with Ar:CO_2 85:15 and exposed to a beam of 120 GeV pions. The set voltage is scanned from 480 to 600 V in steps of 10 V. The performance improvement with respect to the non-resistive chamber is remarkable. No voltage drops are observed with a bias of 560 V and only a few dips at the volt level can be spotted when applying biases above 580 V. The current is also reduced by more than one order of magnitude, rarely exceeding a few hundred

[4] CAEN nuclear, model SY2527
[5] CAEN nuclear, model A1821N

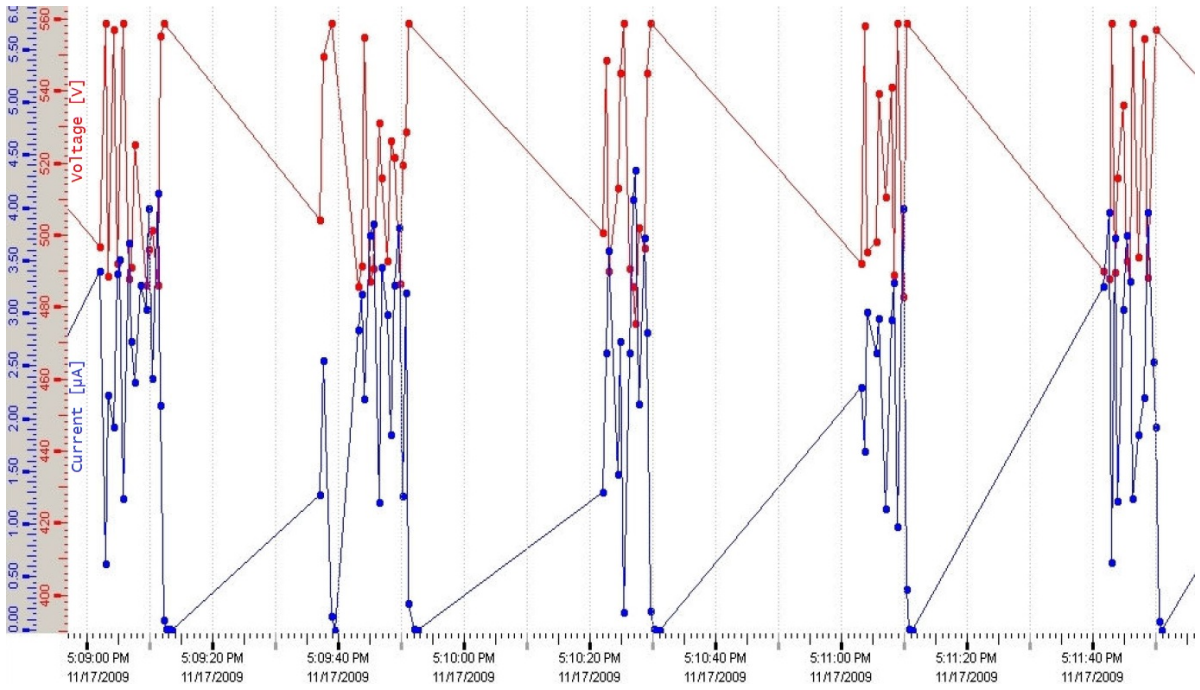

Figure 4.28: Monitored high voltage (red points, right scale) and current (blue points, left scale) drawn by the amplification mesh of a non-resistive Micromegas, as a function of time. The set voltage is 560 V.

nA. The enhancement is secured thanks to the resistive structures, that limit the current flowing to ground in case of a discharge and thus effectively quench the streamer before it causes a drop of the voltage on the amplification mesh.

4.4.4.2 Micromegas readout

In order to enable detection-efficiency and space-resolution studies to be made, the anode elements of the Micromegas have to be read out individually. The extracted performance figures are not only influenced by the data-analysis software algorithms which will be detailed in the next sections, but they also depend on the type and characteristics of the readout hardware. The rest of the current section is therefore dedicated to the description of the electronics chain, from the online analog signal conditioning to the digitizer.

Given the limited number of channels available on the electronics cards at disposal, only 64 out of the 360 anode strips of a Micromegas chamber are read out, while the remaining 296 are shorted to ground. Each of these 64 strips is hooked up to a discrete charge-sensitive preamplifier that is in turn connected to the front-end electronics (FEE) [73]. Two FEE cards are available, each of them housing 32 custom-configured shaper amplifiers and two digitizer chips.

The FEE cards were originally designed with a shaping time of 1 µs for use in the ALICE photon spectrometer (PHOS), which is an electromagnetic calorimeter based on lead tungstate crystals coupled with avalanche photodiodes (APDs). A modified version of the electronics, with shaping time reduced to 100 ns, has also been adopted by the ALICE EMCal detector with the same APD readout.

The FEE input stage is a differentiator with pole-zero cancellation for the charge-sensitive preamplifier. The differentiator is implemented as a first-order passive high-pass filter whose components C_0 and R_0 are chosen for a shaping time $\tau_c = C_0 R_0 = 100\,\text{ns}$, thus providing an attenuation of 20 dB/decade

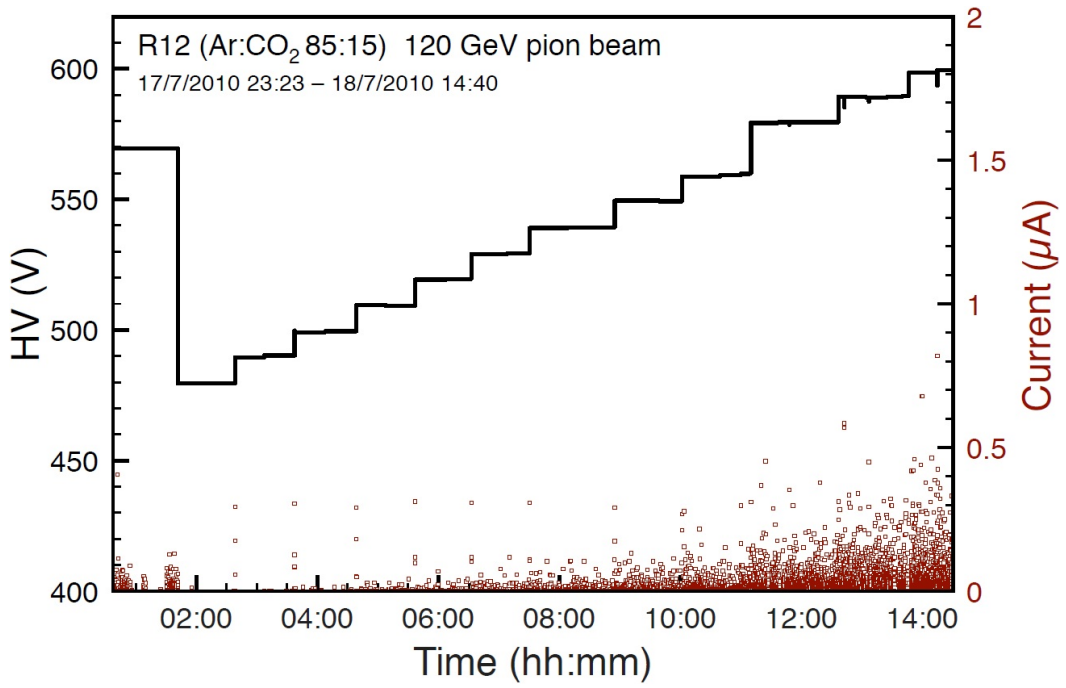

Figure 4.29: Monitored high voltage (black line, left scale) and current (red squares, right scale) drawn by the amplification mesh of a resistive Micromegas, as a function of time. The set voltage is scanned from 480 to 600 V in steps of 10 V.

below the cut frequency $f_c = 1/(2\pi\tau_c) \simeq 1.6\,\text{MHz}$. The pole-zero cancellation for the charge-sensitive preamplifier is performed by introducing a resistor R_z in parallel to C_0 so that $C_0R_z = C_pR_p$, where C_p and R_p are respectively the feedback capacitor and the discharge resistor of the charge-sensitive preamplifier. The ultimate value of R_z deviates slightly from the theoretical prediction and it is finely tuned by experimentally adjusting to zero-undershoot the circuit response to a step pulse. The stage is terminated by a low-noise operational amplifier[6], which is employed to set up a buffer with closed-loop gain of 2.

The analog signal conditioning is completed by two parallel integrators with different gains, cascaded to the described differentiator. Each integrator is a second-order active low-pass filter based on a single operational amplifier with multiple-feedback architecture, offering an attenuation of −40 dB/decade above the cut frequency $f_c \simeq 1.6\,\text{MHz}$. The two integrator branches have the same shaping time and electronic gains in the ratio 16:1 in order to extend the effective dynamic range of the digitizer. The differential output, required for the analog-to-digital converter (ADC), is implemented by inverting and non-inverting drivers.

The response of a CR-RC^n circuit to a step function from the pole-zero-compensated charge-sensitive preamplifier can be analytically computed with the tools of the Laplace analysis. The general solution $V_n(t)$ in the time domain is a Gamma function of order n, as shown in Eq. (4.5). Here, Q is the charge induced on the anode element connected to the considered readout channel, C_p is the feedback capacitor of the charge-sensitive preamplifier, A is the total electronic gain of the band-pass filter and τ_c is the corresponding shaping time.

$$V_n(t) = \frac{QA^n}{n!C_p}\left(\frac{t-t_0}{\tau_c}\right)^n \exp\left(-\frac{t-t_0}{\tau_c}\right) \tag{4.5}$$

[6] Analog devices, model AD8039

The peak amplitude is proportional to the detected charge Q, while the peaking time equals $n\tau_c$. Hence, for the considered CR-RC^2 circuit, the peaking time is 200 ns and the output waveform is:

$$V_2(t) = \frac{QA^2}{2C_p}\left(\frac{t-t_0}{\tau_c}\right)^2 \exp\left(-\frac{t-t_0}{\tau_c}\right) \tag{4.6}$$

The digitization stage of each FEE card is based on two ALICE TPC readout (ALTRO) chips [74]. In a single chip, the analog signals from 16 channels are digitized, processed, compressed, and stored in a multi-acquisition memory. The analog-to-digital converters embedded in the chip have a dynamic range of 10 bits that, together with the aforementioned dual integrator featuring parallel branches with gains in the ratio of 16:1, deliver a total effective dynamic range of 14 bits and a single-ADC-count sensitivity of 1160 electrons on the high-gain branch. The maximum sampling rate of the ADCs is 40 MHz, but they are here operated at a reduced frequency of 10 MHz. The digitized waveforms are stored into a pipeline holding 16 events, with 64 charge samples per event and per channel. The first 15 of these are pre-trigger samples, acquired thanks to the ADC strobe latency in order to allow for channel-by-channel and event-by-event determination of pedestals and RMS noise.

4.4.4.3 Data acquisition and run-naming conventions

The trigger pulses are generated by combining the information from the BAT modules with the signals from the scintillators, and they are then distributed to the test-beam data acquisition (DAQ) system. Upon the receipt of a trigger, the DAQ system records the information from four different detectors, namely the three BAT stations and the Micromegas chamber. The BAT data are processed and stored on a Windows computer sitting next to the silicon tracking telescope in the experimental area, while the Micromegas data are processed and stored on a Linux machine located in the control room. The Micromegas DAQ software is based on DATE, the ALICE DAQ framework. No raw-data selection is performed by this software and thus the digitized waveforms from all the 64 instrumented channels are saved to disc.

Appendix F lists the test-beam data runs analyzed in this thesis. Runs acquired under the same experimental conditions are grouped into a run set. For simplicity, each run set is identified with a short label that summarizes the experimental conditions. Let's consider, for example, the run set R12-85:15-π-2.20-6010. This set gathers the runs acquired with R12, flushed with a mixture of argon and carbon dioxide in the ratio of 85:15. The detector is irradiated with pions at 2.20 kHz/cm^2 and it is operated at a gas gain of 6010. Run sets that differ from each other only in the gas gain of the Micromegas are then grouped into a data set. The naming convention for data sets is similar to the one for run sets. For example, the run set considered above belongs to the data set R12-85:15-π-2.20. Additional information, such as the drift field of the Micromegas, is given in Appendix F.

4.4.4.4 Data synchronization

The BAT data and the Micromegas data are merged by the offline data processor[7], which takes care of retrieving the correct runs from the two machines and combines them into a single file. As mentioned in Section 4.4.4.3, at the moment of acquisition a Micromegas event is stored as 64 raw digitized waveforms including some pre-trigger samples. The offline data processor executes a numerical fit on each waveform, using as target function a second-order Gamma of the type of Eq. (4.6) with non-zero

[7] Author: Woochun Park, wpark@sc.edu

baseline, and stores only the resulting parameters in the output file, discarding the raw data. Additionally, the RMS value of the noise is computed on a channel-by-channel and event-by-event basis by exploiting the pre-trigger samples. Finally, some preliminary event reconstruction is performed. Given the multi-event structure of a run, the natural data format adopted by the offline processor is that of a ROOT TTree [75].

The ROOT run file produced by the offline data processor therefore contains, amongst other information, four main data streams, three from the BAT stations and one from the Micromegas chamber. A preliminary, manual examination of the collected data by means of a simple event displayer soon highlights recurring desynchronization issues between these streams. Although the hit positions in the four detection layers are always consistent with each other in the very first events of each run, a data stream often appears to skip one or more events at a random time and show in their place the following ones. Such observations find explanation in the occasional loss of one or more consecutive trigger signals in one of the four stations. When this happens, three out of the four data buffers get regularly filled, while no information is stored where the triggers fail to be delivered. When all the trigger lines restart working correctly, the data storage is performed for all the four stations, with the memory filling proceeding from the first empty location of each buffer.

The desynchronization of the data streams constitutes a major obstacle to any further analysis involving more than a station at a time. Since the four data streams are always in sync at the beginning of a run, one can consider performing the combined analysis only on the run section previous to the first trigger loss. Such a workaround does not provide a real fix to the desynchronization problem, but only avoids the undesired effects at the cost of a considerable reduction of the statistics. It is therefore not suitable for data-analysis purposes.

Another possible approach is that of exploiting an event displayer to manually identify the first desynchronization point and feed the event number, the station ID and the desynchronization amplitude to a program that takes care of shifting back the faulty branch. Given the difficulty of identifying a second possible desynchronization point before fixing the first one, the whole procedure has to be iterated several times. Although feasible, the whole process turns out to be very time-consuming, requiring 20 min to several hours to resynchronize a single run. Taking into account the high number of collected runs, that is in the order of a few hundred, the need for an automated tool is clear.

Losses of trigger signals can in principle take place in any of the stations in the test-beam setup and indeed desynchronization phenomena have been observed in different data streams. Additionally, multiple trigger losses are not uncommon, leading to consecutive events missing from the affected memory buffer. For all these reasons, the automated software tool not only has to to identify the desynchronization point, but also has to tag the TTree branch that runs out of sync with respect to the others and quantify the number of missing events. The algorithm described in the rest of the current section is able to find and correct for desynchronizations in any runs taken with particles hitting the Micromegas under 0° incidence angle.

Several approaches to the desynchronization problem are possible. The paradigm at the basis of the implemented solution is that of keeping the algorithm simple and neat, optimizing at the same time the computational speed by avoiding CPU-demanding numerical minimizations. For each detector, the residual between the interaction point and the average hit position in the other three stations is calculated, giving rise to four symmetrical equations, one for each data stream. By denoting with x_i and r_i respectively the event coordinate and the residual of the i^{th} station along the x-direction and by using a simple arithmetic mean as the estimator for the average value, one gets:

$$r_i = \frac{\sum_{j \neq i} x_j}{3} - x_i \tag{4.7}$$

The hit position can in turn be written as $x_i = n_i p_i + o_i$, where n_i is the event coordinate in channel number, p_i the readout pitch and o_i the alignment offset of the i^{th} station. The pitch of the three BAT modules is fixed to 50 µm by construction, while the offsets can be neglected as they are not useful for desynchronization finding. Moreover, since the algorithm does not necessitate locating the hit position with high precision, one can speed up the procedure by taking n_i to be the number of the channel that detects the maximum charge, without going through a time-consuming event reconstruction. Under these conditions, and considering that in the three BAT stations the channel number is inverted with respect to the Micromegas, the residual expressions for the four data streams become:

$$r_{\mu\text{M}}\ [\mu\text{m}] = -\left[\frac{(n_{\text{BAT1}} + n_{\text{BAT3}} + n_{\text{BAT6}}) \cdot 50\,\mu\text{m}}{3} + n_{\mu\text{M}} p_{\mu\text{M}}\right] \tag{4.8}$$

$$r_{\text{BAT1}}\ [\mu\text{m}] = \frac{n_{\mu\text{M}} p_{\mu\text{M}} - (n_{\text{BAT3}} + n_{\text{BAT6}}) \cdot 50\,\mu\text{m}}{3} + n_{\text{BAT1}} \cdot 50\,\mu\text{m} \tag{4.9}$$

$$r_{\text{BAT3}}\ [\mu\text{m}] = \frac{n_{\mu\text{M}} p_{\mu\text{M}} - (n_{\text{BAT1}} + n_{\text{BAT6}}) \cdot 50\,\mu\text{m}}{3} + n_{\text{BAT3}} \cdot 50\,\mu\text{m} \tag{4.10}$$

$$r_{\text{BAT6}}\ [\mu\text{m}] = \frac{n_{\mu\text{M}} p_{\mu\text{M}} - (n_{\text{BAT1}} + n_{\text{BAT3}}) \cdot 50\,\mu\text{m}}{3} + n_{\text{BAT6}} \cdot 50\,\mu\text{m} \tag{4.11}$$

In order to ensure the validity of the above equations, a few basic selection cuts are applied. Specifically, the channel numbers n_i of the three BAT modules are validated by requiring the corresponding detected charge to be greater than zero. The Micromegas data are validated by accepting only events with one charge cluster, defined as a group of neighboring firing strips, as to avoid complications arising from double-track occurrences.

Figure 4.30 shows the residual, expressed in µm and plotted as a function of the event number, for the four detector stations. The data are from the BAT run 4226 and the Micromegas run 4962, which contain about 10^4 events. Here, R12 is flushed with Ar:CO_2 85:15 and it is biased with a negative potential of 570 V on the amplification mesh and of 940 V on the drift electrode, with respect to the grounded anode. These settings give rise to a drift field of 0.74 kV/cm and a gas gain of 2490. The Micromegas is exposed to a beam of pions with energy of 120 GeV, which cross the chamber with 0° incidence angle. The average particle flux over the trigger area is 2.79 kHz/cm^2.

The residuals are scattered around an average value, which depends on the reciprocal alignment offsets of the four detectors along the x-axis. The four average values indeed sum up to zero and they would all vanish if the modules were aligned in space. Although important for further physics analysis, these constants do not play any significant role in desynchronization finding. The residual RMS, on the other hand, strongly depends on the synchronization between the data streams. When one of the memory buffers goes out of sync, the RMS values suddenly increase, with the increment being considerably larger for the station where the trigger signals are lost. This is a consequence of the way in which the residual expressions are built, with three variables contributing to the average with a weight reduced by a factor of 3 with respect to the fourth variable.

The implemented algorithm evaluates Eq. (4.8) to (4.11) for each event passing the selection cuts and estimates the residual spreads around the average values over a moving window of N events. The four spreads extracted from the first N events are stored as reference values. Remembering that the memory buffers are always synchronized at the beginning of a run and keeping N sufficiently small, one can assume with good confidence that these values are representative for synchronized data streams. The desynchronization point is then found by checking when the RMS values exceed k times the reference parameters. The module that runs out of sync is identified as the one with the largest RMS after the trigger losses.

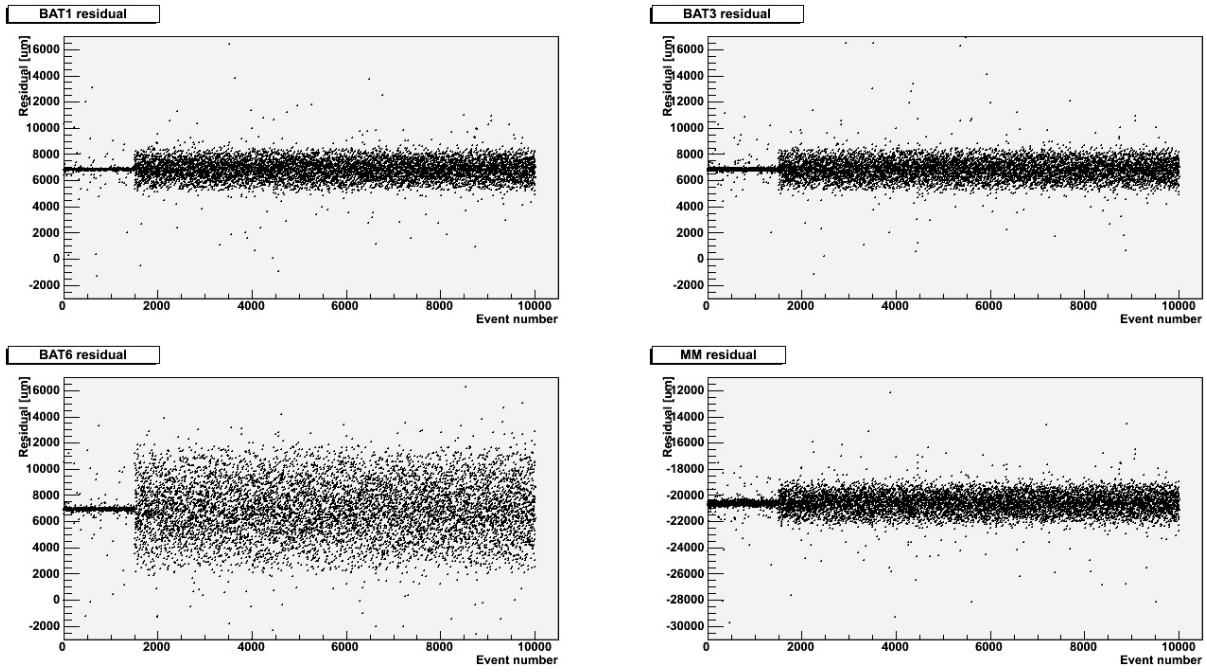

Figure 4.30: Residual distributions before resynchronization.

Considering that four residual spreads have to be estimated for each event passing the selection cuts and that each RMS evaluation requires a square-root extraction, the variance provides a more CPU-efficient solution of equal statistical significance. Taking the arithmetic mean $\bar{r}_i|_j$ as the estimator for the average residual of the i^{th} station at the j^{th} event, the variance $\sigma^2(r_i)\big|_j$ is:

$$\sigma^2(r_i)\big|_j = \frac{\sum_{k=j}^{j+N-1}\left(r_i|_k - \bar{r}_i|_j\right)^2}{N-1} \tag{4.12}$$

Assuming $N \gg 1$:

$$N^2\,\sigma^2(r_i)\big|_j = N\sum_{k=j}^{j+N-1} r_i|_k^2 - \left(\sum_{k=j}^{j+N-1} r_i|_k\right)^2 \tag{4.13}$$

The latter expression is a good implementation of the spread estimator over a moving window, as it can be updated on a event-by-event basis by simply adding and subtracting a few terms, with no need to recompute the whole sum. The corresponding threshold for desynchronization tagging is:

$$N^2\sigma^2_{\text{thr}}(r_i) = k^2N^2\,\sigma^2(r_i)\big|_0 \tag{4.14}$$

The variance, including the modified version of Eq. (4.13), is not a robust estimator of the data dispersion around the average value. A single far outlier can in fact cause a significant increase of the variance, possibly leading to a false desynchronization positive. For this reason, the data undergo a further selection cut that excludes all the events j in which at least one of the four $r_i|_j$ lies outside a window of user-defined half width w and centered around the residual average. For the same reason, the average values used to define the cut windows cannot be estimated using arithmetic means, but are rather obtained from the most probable value of the distributions of the first $N-1$ residuals.

Once the desynchronization point j_d is found and the data stream i_d that goes out of sync is identified through the above algorithm, it is necessary to establish the desynchronization offset because, as previously mentioned, it is not unusual that several trigger signals are lost in sequence on the same station. This is done by shifting forward the desynchronized memory buffer by a given offset and computing the corresponding variance. The number of lost triggers is the smallest offset that satisfies $N^2\ \sigma^2\left(r_{i_d}\right)\big|_{j_d} \leq N^2\sigma^2_{\text{thr}}\left(r_{i_d}\right)$.

The faulty TTree branch is then realigned, the residual mean values and the variance thresholds are reevaluated and the procedure is reiterated until another desynchronization is found or until the end of the file is reached.

It is important to note that the developed algorithm, although flexible and efficient, cannot identify the exact time when the trigger signals are lost. Two are the reasons. Firstly, if a trigger is lost in one of the events that do not pass the selection cuts, the desynchronization effects will only become detectable from the following accepted event. Secondly, even if a careful tuning of the variance thresholds through the k parameter usually results in Eq. (4.13) exceeding the thresholds as soon as an anomalous occurrence is processed, it is still possible that more than one event is necessary to reveal a desynchronization. Hence, all the events within the boundaries of the moving window are removed upon resynchronizing the data streams. In a similar fashion, a certain number of events at the very end of the run are not guaranteed to be synchronized. Depending on the specific conditions, the software therefore takes care of deleting from the end of the run the minimum number of events that ensures synchronization. In a typical case, a few hundred events may be removed from a file counting some tens of thousands of events, resulting in a negligible reduction of the total statistics.

Finally, parameter adjustment is necessary to make the algorithm capable of coping with the diverse desynchronization scenarios observed in the experimental data. There are three main parameters that control the algorithm behaviour. The first is the number N of events over which Eq. (4.13) are evaluated. Too small values of N provide a poor estimate of the variance that may lead to false positives, while too large values result in a considerable fraction of the statistics being cut out during resynchronization. A good compromise is about 100 events. The second parameter is the half width w of the window used in residual selection, which has be be about 1 mm. The third parameter is the k factor entering in the definition of the RMS thresholds. Here, too small values give rise to false positives, while too large values lead to false negatives. The optimum is empirically determined to be 3.5.

With the selection cuts described above and with the parameters so tuned, the algorithm has been able to fix the desynchronizations in all of the processed runs, that amount to several tens of files. An example is provided by Fig. 4.31, which shows the four residual distributions for the BAT run 4226 and the Micromegas run 4962 after the file has been processed. The five blank gaps in each graph correspond to the events that have been removed during the resynchronization. Moreover, the vertical scales are zoomed with respect to Fig. 4.30 because all the desynchronizations have been corrected and the residuals are therefore less scattered around their average values.

4.4.4.5 Gain homogeneity

The resynchronized runs are fed to the BAT reconstructor[8], which takes care of finding the charge clusters, defined as groups of neighboring firing strips, in the three modules of the tracking telescope. For each cluster, the program computes the centre of gravity and corrects for the estimation error introduced by the discrete segmentation of the readout by applying an η_2 algorithm (cf. Section 4.4.4.8). Finally, the software performs the alignment of the stations, reconstructs the particle trajectories along

[8] Author: Marcin Byszewski, marcin.byszewski@cern.ch

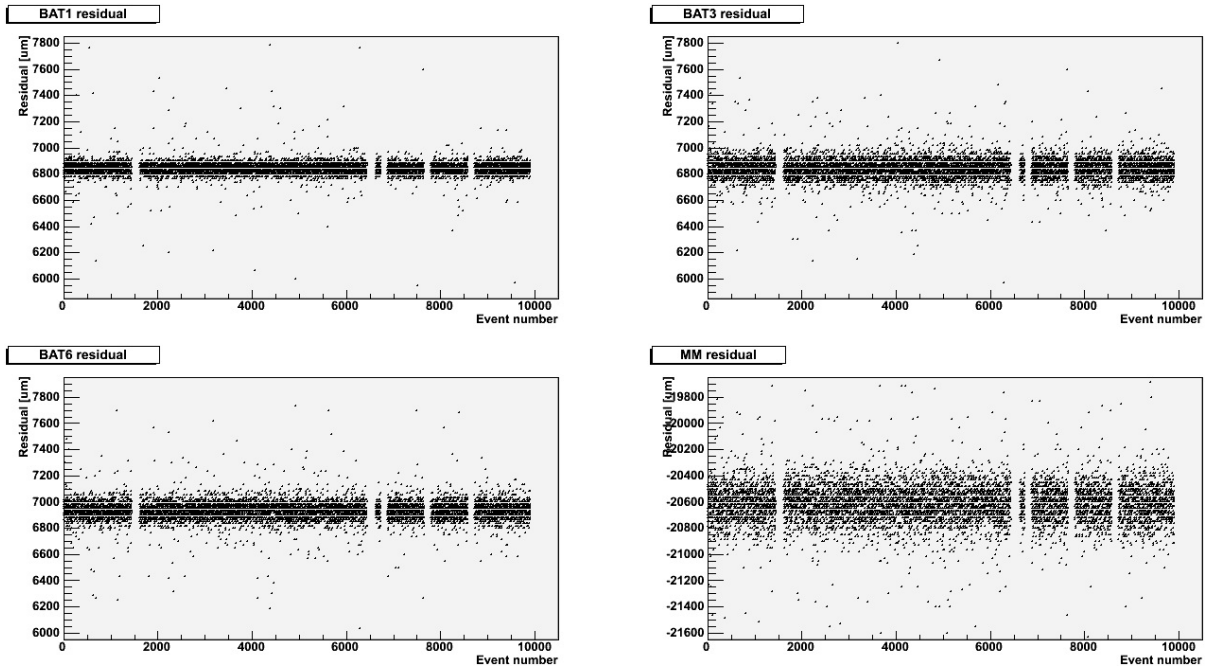

Figure 4.31: Residual distributions after resynchronization.

the x- and y-direction using independent simple linear regressions and stores the results in new branches of the ROOT TTree.

Having synchronized data files containing complete information on the particle tracks traversing the telescope, it is possible to proceed to investigate the properties of the resistive Micromegas. A first study that does not require accurate event reconstruction in the Micromegas is the gain homogeneity. More specifically, the goal is that of analyzing on a strip-by-strip basis the gain variation of the system composed of the chamber itself and the readout electronics, with the purpose of evaluating the uniformity of its response and identifying possible anomalies and their origin.

A simple and straightforward way to perform the gain-homogeneity study is that of taking, for each event, the readout strip on which the maximum charge is recorded. The maximum charge has the advantage of not being biased by the clustering and centre-of-gravity algorithms and of being promptly available in the ROOT file. The drawback of this choice lies in the fact that, since the charge information of only one anode element per event is considered, most of the available data remains unused.

The maximum charge of each event is validated by requiring the corresponding strip position to be within 500 µm of the extrapolated x-coordinate of one of the particle trajectories reconstructed in the tracking telescope. This helps to remove fake hits due to random noise in case of Micromegas inefficiency. The values passing the selection cut are then used to fill a histogram for each channel. The resulting patterns resemble Landau distributions, as shown in Fig. 4.32 for channel 31 of the run set R12-85:15-π-2.20-6010 (cf. Table F.6).

The average differential energy loss by ionization per unit of path length along the track of a heavy charged particle is given by the Bethe formula, see Eq. (1.1). The Landau distribution provides an approximated theoretical model for the fluctuations around the average energy loss in thin layers of matter [76]. Although the maximum charge is not strictly described by such distribution, numerical maximum-likelihood fits performed using a Landau as target function yield a satisfying representation of the experimental data, as seen in Fig. 4.32.

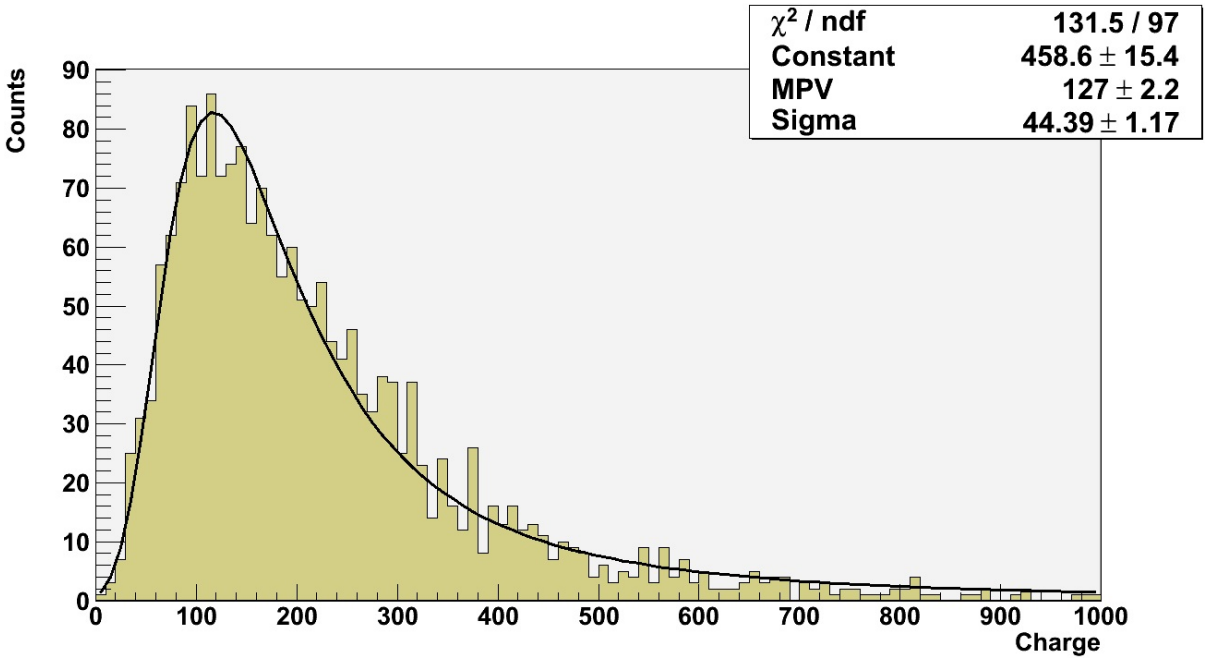

Figure 4.32: Distribution of the maximum charge for a single readout strip.

Figures 4.33 and 4.34 show the aggregate effective gain of the Micromegas chamber and the readout electronics, expressed in ADC bins, as a function of the strip channel number. Since the moments of a Landau distribution are undefined, the values and the uncertainties plotted in the graphs are extracted from the first fit parameter, which approximately coincides with the most probable value of the distribution, and from the associated fit error. Figure 4.33 is based on the run set R12-85:15-π-2.20-2490, while Fig. 4.34 is obtained from the run set R12-85:15-π-2.20-6010 (cf. Table F.6).

In both Fig. 4.33 and 4.34, the abscissa ranges from channel 22 to 42. This reflects the extension of the trigger area along the x-coordinate, which is defined by the vertical finger scintillator and which is 5 mm wide, thus covering about 20 strips. Conversely, the values on the vertical axis are much larger in the latter graph because of the higher effective gas gain. The errors on the data points are relatively large due to the difficulty of determining the parameters of a Landau distribution with high precision. The gain-uniformity study is in fact normally performed with a narrow collimated beam of soft X-rays that, depositing all their energy in a single photoelectric interaction, give rise to a Gaussian distribution in the energy spectrum, whose peak can be fitted with good precision. However, the evaluation of the gain homogeneity with the same test-beam data subsequently used for the space-resolution and efficiency studies has the great advantage of enabling a proper offline compensation of the gain if needed.

The five runs in each of the two graphs are, within the errors, all compatible with each other. It is therefore possible to merge their statistics in order to improve the Landau fits and consequently reduce the uncertainties on the extracted parameters. The results are shown by the purple bands of Fig. 4.33 and 4.34, which represent the one-sigma intervals. It is clear from the graphs, especially when combining the statistics, that the aggregate effective gain of the Micromegas chamber and the readout electronics cannot be considered as constant. A periodic pattern is clearly identifiable, showing a significant gain drop every 10 strips, with dips around channel 23 and 33, and with a possible further drop around channel 43. Moreover, the pattern appears to be independent of the gas gain, thus suggesting that it does not originate from charge-multiplication processes, but it is rather a hardware feature.

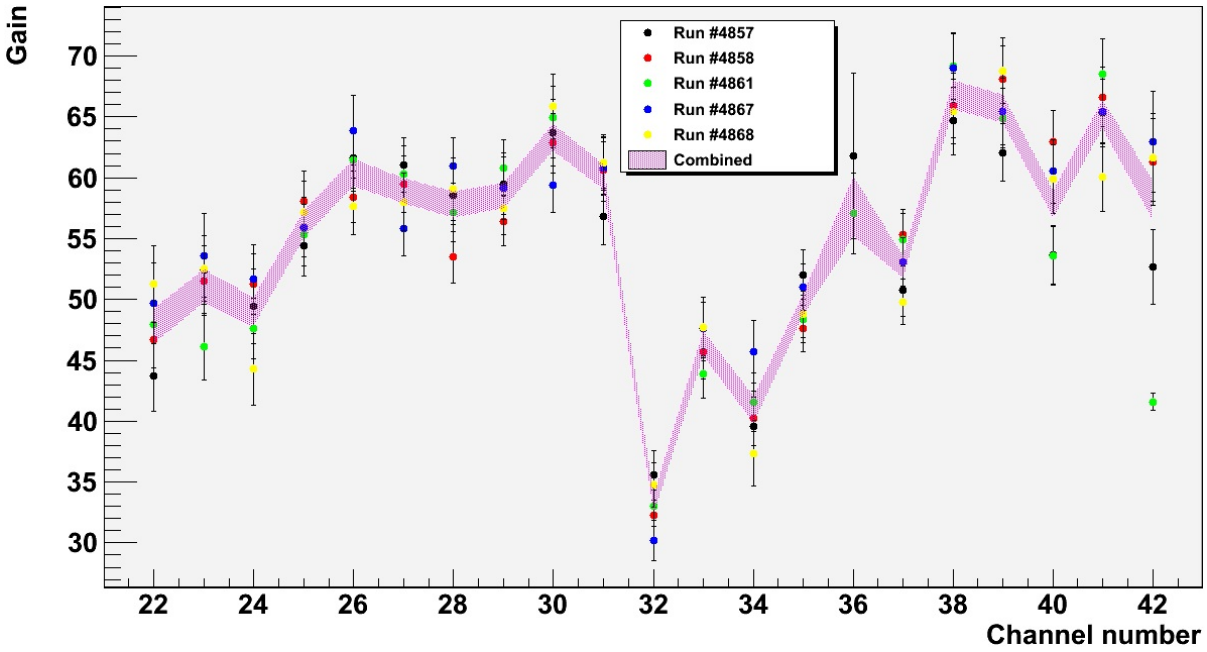

Figure 4.33: Aggregate gain of R12 and the readout electronics at an effective gas gain of 2490. The values, expressed in ADC bins, are shown as a function of the strip channel number.

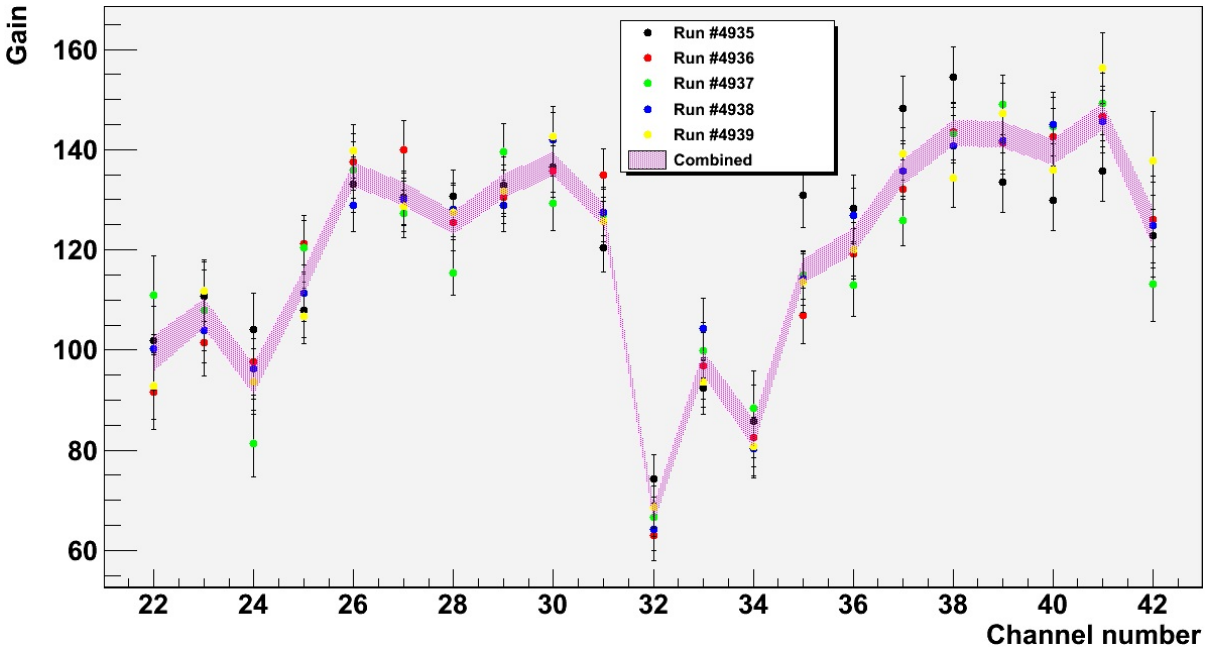

Figure 4.34: Aggregate gain of R12 and the readout electronics at an effective gas gain of 6010. The values, expressed in ADC bins, are shown as a function of the strip channel number.

The explanation for the observed pattern has to be searched for in the periodic matrix of pillars which sustain and keep under mechanical tension the amplification mesh of a bulk Micromegas. When a drifting electron hits one of these support structures, either in the conversion or in the amplification gap, its charge is lost for detection purposes and the effective gas gain appears to drop. Moreover, the dielectric nature of the material introduces local distortions of the electric field that make the affected area slightly larger than the geometrical coverage. As stated in Section 4.4.2, the pillars of all the three resistive Micromegas under study have a diameter of 400 μm and a pitch of 2.5 mm in both the x- and the y-direction. Remembering that the pitch of the anode strips is 250 μm, and considering that the orientation of the matrix of support structures matches that of the readout pattern, one expects the pillar effect to be spread over three strips and to repeat periodically every 10 strips, which is in agreement with the observed behaviour.

Figure 4.35 and 4.36 corroborate the above hypothesis. They show the position of the particle trajectories, reconstructed in the tracking telescope and extrapolated to the Micromegas plane, which have no matching event detected by the chamber under study within 500 μm. Figure 4.35 is based on the run set R12-85:15-π-2.20-2490, while Fig. 4.36 is obtained from the run set R12-85:15-π-2.20-6010 (cf. Table F.6). The vertical axes of the two plots are in mm, while the abscissa scales are expressed in strip channel number to ease the comparison with the previous gain-homogeneity graphs. The resulting scatter plots give a qualitative impression of the variations of detection efficiency over the active area of the Micromegas, demonstrating that the inefficiencies are clustered in circular zones forming a bi-dimensional periodic matrix. Both the diameter and the pitch of these areas are compatible with the specifications of the pillars supporting the amplification mesh. Furthermore, the locations of the pillar columns along the x-axis match the positions of the gain drops in Fig. 4.33 and 4.34.

Combining the data regarding the maximum charge detected in each event, which were used to produce Fig. 4.33 and 4.34, with the information on the particle trajectories reconstructed in the tracking telescope, it is possible to extend the gain-homogeneity study to two dimensions. Despite the tested Micromegas being equipped with one-dimensional readout only, one can take advantage of the bi-dimensional hit-localization capability of the tracking telescope to subdivide the statistics of the maximum-charge distribution relative to each strip into several histograms according to the y-coordinate of the reconstructed track extrapolated to the Micromegas plane. The histograms are then fitted with Landau distributions like in Fig. 4.32 and the extracted position parameters are used to fill a bi-dimensional map. Figure 4.37 shows the results for the run set R12-85:15-π-2.20-2490, while Fig. 4.38 shows the results for the run set R12-85:15-π-2.20-6010 (cf. Table F.6). Due to the limited statistics in some histograms, a few fits fail, giving rise to isolated pixels whose apparent gain is significantly above or below the one of their neighbors. The gain is otherwise uniform over the illuminated active area, with consistent drops only corresponding to the pillars.

The bi-dimensional maps of Fig. 4.37 and 4.38 provide a general overview of the gain homogeneity across the section of active area irradiated by the beam and defined by the trigger logic. They allow to qualitatively judge the overall level of gain uniformity and the effects of the structures supporting the amplification mesh. Because of the poor precision of the parameters extracted from the Landau fits, these maps are however inadequate to quantitatively evaluate the gain homogeneity of the resistive Micromegas in the areas not affected by the pillars. The estimation is done instead by dividing the total statistics of each readout channel into two subsets, according to the distance of the particle trajectory reconstructed in the tracking telescope and extrapolated to the Micromegas plane from the nearest row of pillars. The outcome of this study is shown in Fig. 4.39 and 4.40 for the run set R12-85:15-π-2.20-2490 and R12-85:15-π-2.20-6010, respectively (cf. Table F.6). The black band labeled as "no selection" is the same one-sigma interval shown in Fig. 4.33 and 4.34 for the combined statistics, while the other bands are grouped in complementary pairs with three different values of distance threshold from the

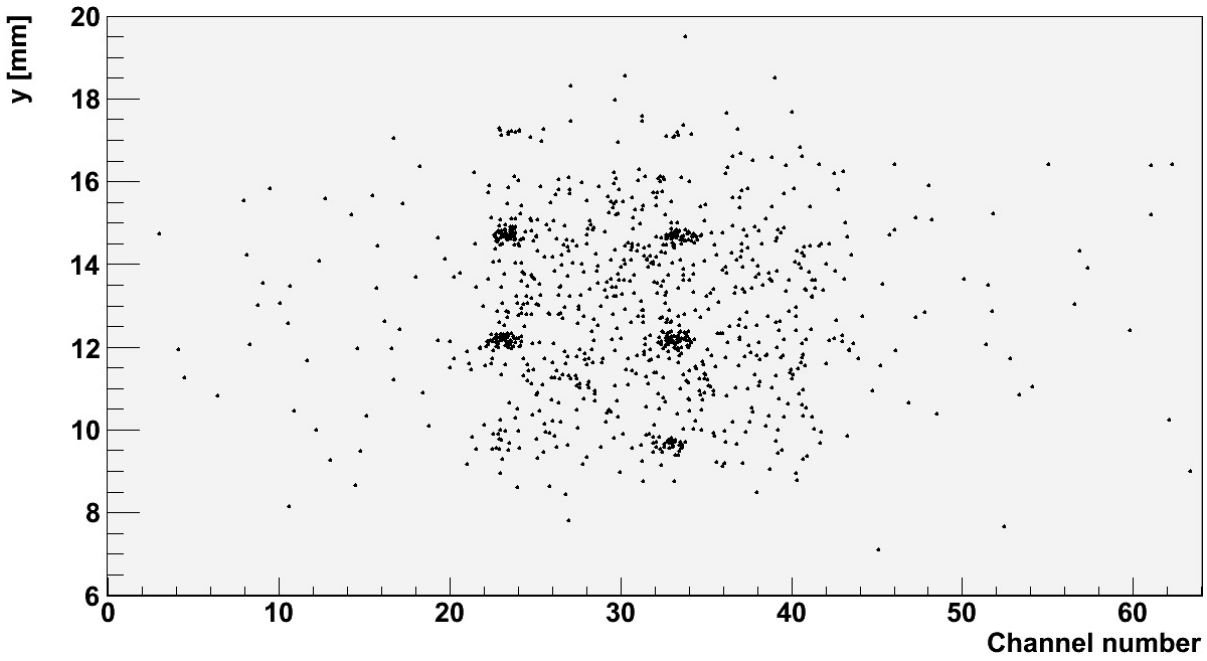

Figure 4.35: Inefficiencies of R12 at a gas gain of 2490. The scatter plot shows the *x*-*y* position of the tracks, reconstructed in the beam telescope and extrapolated to the Micromegas plane, with no matching event in R12.

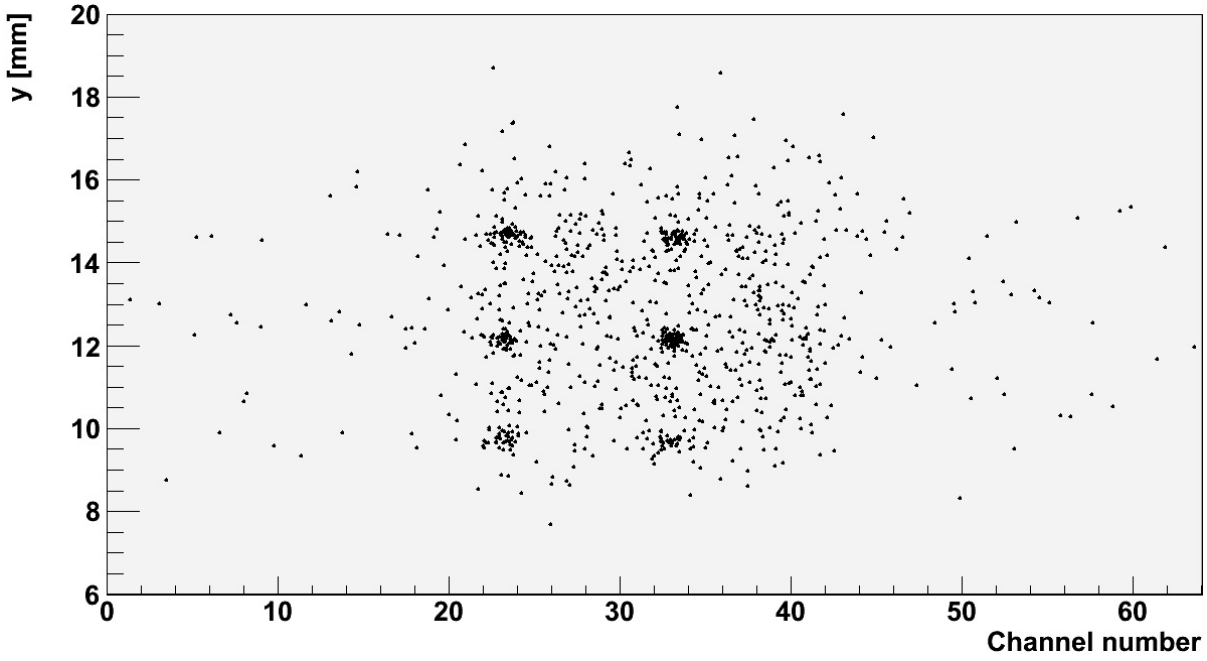

Figure 4.36: Inefficiencies of R12 at a gas gain of 6010. The scatter plot shows the *x*-*y* position of the tracks, reconstructed in the beam telescope and extrapolated to the Micromegas plane, with no matching event in R12.

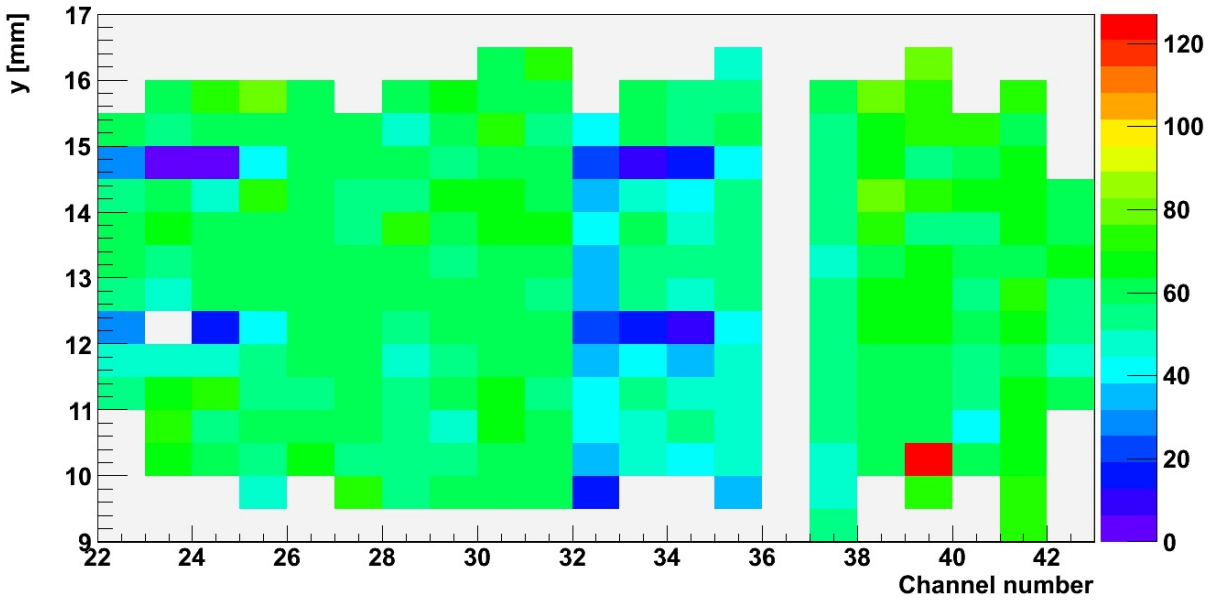

Figure 4.37: Aggregate gain of R12 and the readout electronics at an effective gas gain of 2490. The values, expressed in ADC bins, are colour-coded and shown in a bi-dimensional map as a function of the x (in strip channel number) and the y (in mm) spatial coordinates.

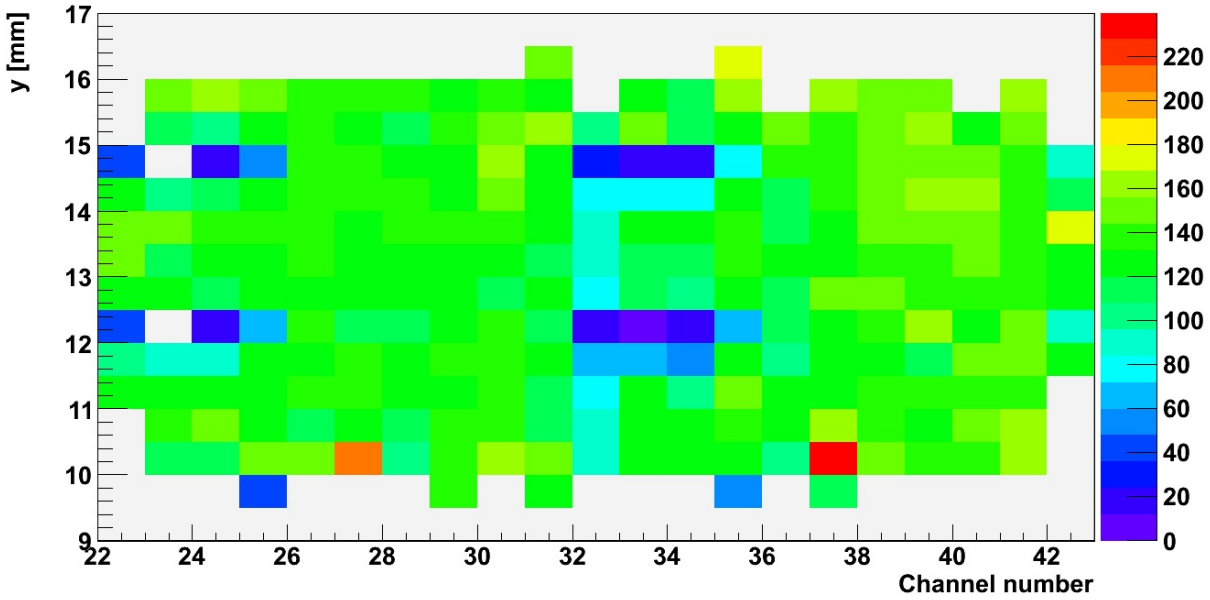

Figure 4.38: Aggregate gain of R12 and the readout electronics at an effective gas gain of 6010. The values, expressed in ADC bins, are colour-coded and shown in a bi-dimensional map as a function of the x (in strip channel number) and the y (in mm) spatial coordinates.

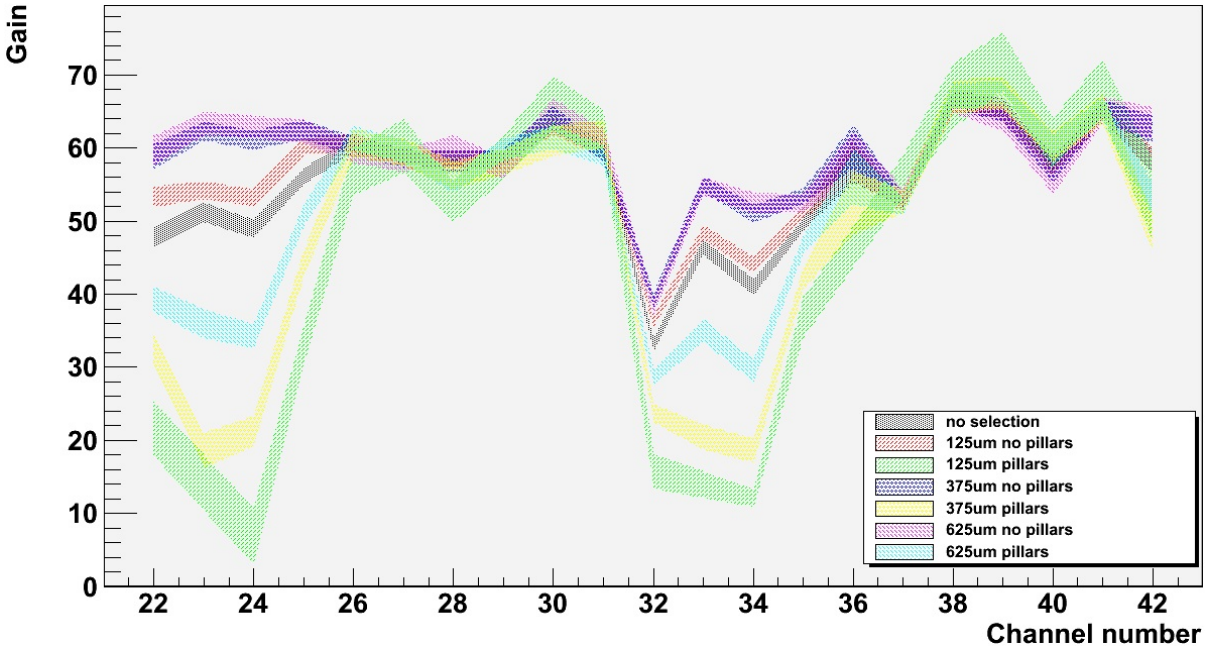

Figure 4.39: Aggregate gain of R12 and the readout electronics at an effective gas gain of 2490. The values, expressed in ADC bins, are shown as a function of the strip channel number. The bands are one-sigma intervals obtained from the hits with a given distance from the nearest row of pillars.

nearest row of mesh support structures. For instance, in the pair labeled "625 µm pillars/no pillars" the statistics is subdivided into two groups of horizontal belts having equal width of $2 \cdot 625\,\mu\text{m} = 1.25\,\text{mm}$, the former ones centered around the mesh support structures and the latter ones located in between. In the other two pairs, the belts containing the pillars become thinner, while the ones in between get larger. As one can expect, the gain variation from channel to channel is maximum in narrow belts around the mesh support structures, where the effective amplification drops almost to zero. The effect gets smeared out as the belt thickness increases, while the behavior on the strips far from the pillars remains the same. The gain uniformity is best etimated in the gaps between pillar rows, using the largest cut threshold of 625 µm. Excluding channel 32, which shows an anomalous behaviour, the variation is around 23% for both gas gains.

A deeper analysis of the bands from which the above result is extracted reveals that there is no common pattern between the data taken at different bias voltages. Since the relative gain variation from channel to channel is expected to be independent of the gas amplification, one can conclude that the quoted value is dominated by statistical fluctuations and has to be taken as an upper limit only. In fact, the variations of the gas-amplification factor due to local field inhomogeneities far from the pillars are negligible. The fraction of charge induced on the resistive traces that reaches the readout electronics depends on the Fourier composition of the signal and on the impedances in the equivalent network. For a given signal frequency, the capacitive couplings to the anode strips are in principle precisely defined and constant from strip to strip. The resistive connections to ground vary from event to event depending on the hit position and their average value may show a few percent variation from trace to trace, which has no effect on the recorded signal. Finally, the readout electronics contributes to the gain variation to a few percent. For all these reasons, and considering that a gain variation in the order of 10% does not significantly worsen the estimation of the cluster position necessary for the space-resolution studies, no offline gain equalization will be applied.

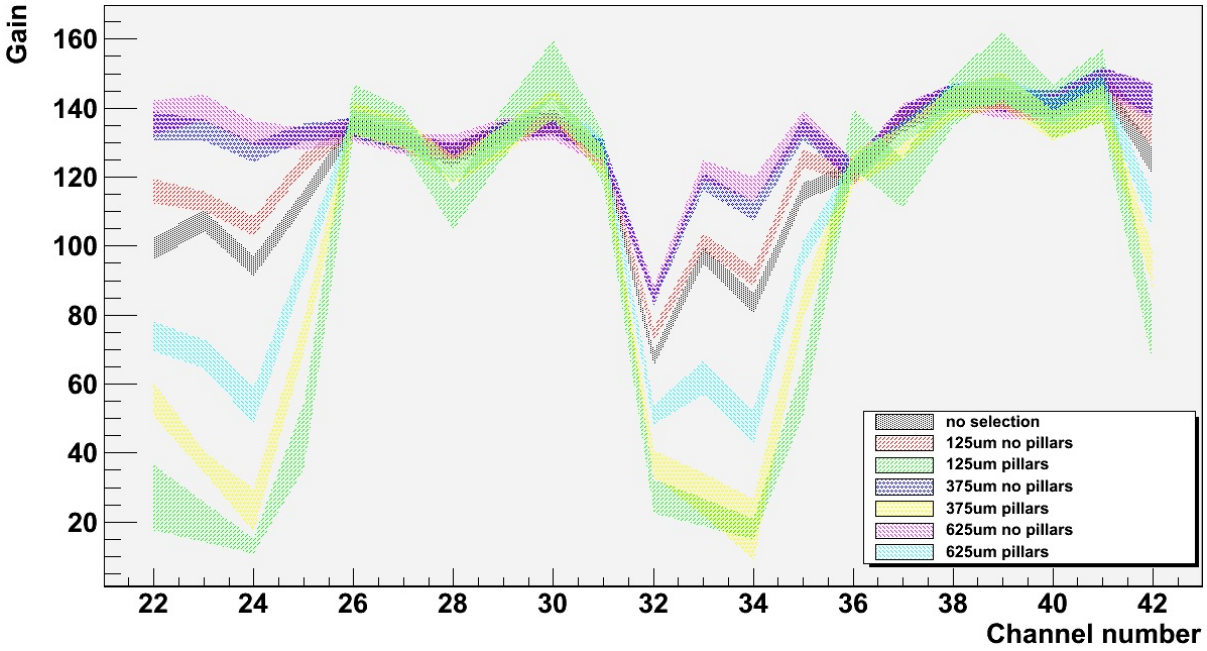

Figure 4.40: Aggregate gain of R12 and the readout electronics at an effective gas gain of 6010. The values, expressed in ADC bins, are shown as a function of the strip channel number. The bands are one-sigma intervals obtained from the hits with a given distance from the nearest row of pillars.

4.4.4.6 Data cleaning and formatting

In Section 4.4.4.2 we presented in some detail the ALTRO-based readout electronics that was used to acquire data from the resistive Micromegas in the first test-beam campaigns. The test-beam data analyzed in this thesis belong to the run period of July 2010 and they all come from such electronics. The performance of the novel Micromegas technology has subsequently been studied in several other beam tests, often in combination with different readout schemes. For example, the APV25 chip has extensively been used on R11, R12, R13 and following chambers and, in more recent times, the VMM chip specifically developed at BNL for the upgrade of the ATLAS Small Wheels has been successfully coupled to Micromegas prototypes. Meaningful data have been acquired with each type of electronics, but not all the chambers have been fully characterized with every chip. To avoid code replication in the data-analysis phase, it is hence worth converting the raw data from each chip to a standard format.

As mentioned in Section 4.4.4.4, the ALTRO raw-data files are handled by the raw-data processor, which takes care of fitting the digitized waveforms with second-order Gamma functions and of merging the extracted information together with that of the three data streams from the tracking telescope. The resulting ROOT file, however, still contains redundant charge and time information. In fact, the raw-data converter saves in the ROOT TTree not only the fit parameters, but also some information on the raw digitized waveforms. Moreover, no selection is made between the high-gain and the low-gain signals produced by the two parallel branches of the shaper amplifiers on the FEE cards. The ALTRO data formatter therefore also has to scan the run file event by event, compare all the available information for each firing channel and pick up the most appropriate values. In this way, the data-analysis codes will deal with a single value of charge and time. In the following, the selection procedure will be explained, with particular focus on the charge information. The estimation of the signal arrival time is not covered in this thesis, but it can be easily plugged into the software framework here developed.

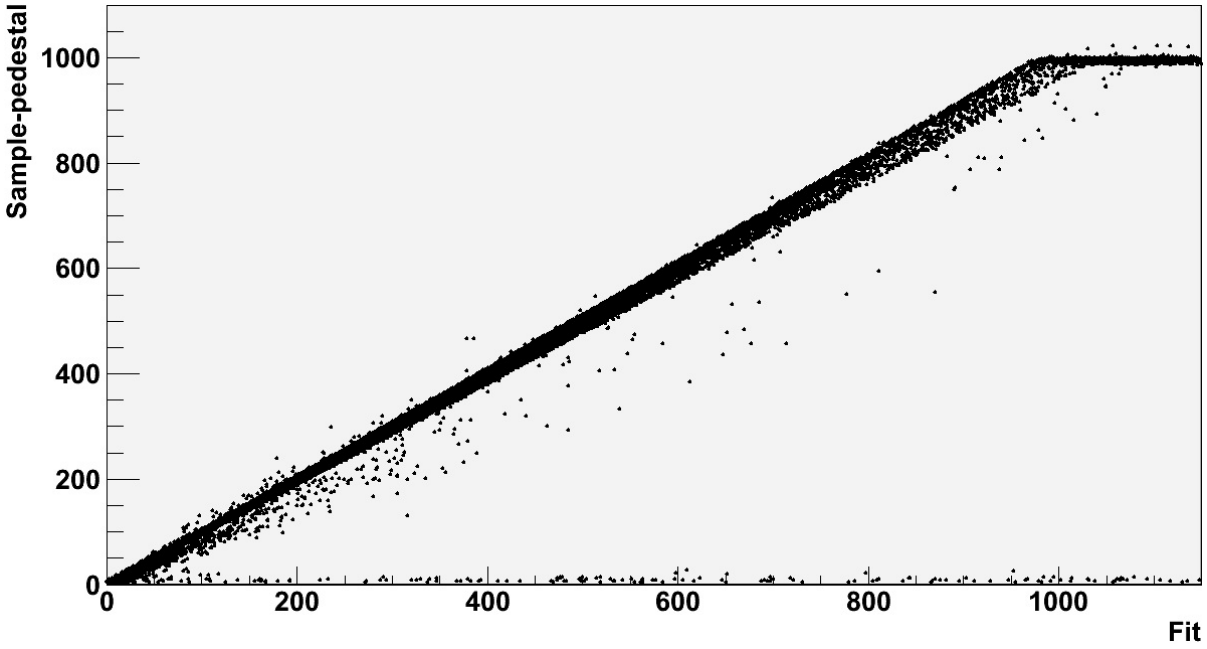

Figure 4.41: Pedestal-subtracted maximum sample vs fit amplitude.

The charge induced on each firing strip is described with four parameters, stored by the raw-data converter in separate branches of the ROOT TTree. The first parameter is the amplitude of the digitized waveform from the high-gain channel, expressed in ADC bins, or in units of 1160 electrons (cf. Section 4.4.4.2). The second and third parameters are the pedestal and the RMS noise, taken from the average and the variance of the pre-trigger samples, respectively. Lastly, the fourth branch is filled with the amplitude of the second-order Gamma function fitted on the digitized waveform. If the signal exceeds a fixed threshold, four additional values are saved, relative to the low-gain channel. When cleaning up the ROOT TTree, the data formatter tries to use in first place the amplitude of the fit to the high-gain channel, which is in principle the most precise estimator of the actual charge. If the parameter does not pass a set of selection cuts, the amplitude of the fit to the low-gain channel is taken instead, properly rescaled according to a lookup table formerly created from the same run data, as explained later in this section. In case not even this value meets the requirements, the choice turns to the pedestal-subtracted maximum sample, from the high-gain channel or from the low-gain channel appropriately rescaled. If none of the above parameters passes the cuts, the strip data are marked as unusable for that event.

Every time the data formatter attempts to use a charge value from a FEE high-gain channel, be it the fit amplitude or the pedestal-subtracted maximum sample, an overflow cut has to be applied. In fact, when the signal amplitude exceeds the ADC range, the resulting digitized waveform will show a flat-top deformation that will bias the charge estimation extracted from both the maximum sample and the second-order Gamma fit. Figure 4.41 shows the pedestal-subtracted maximum sample as a function of the amplitude of the second-order Gamma function fitted on the digitalized waveform, based on the run set R12-85:15-π-2.20-6010 (cf. Table F.6). The two quantities are strongly correlated up to the ADC saturation that, given the 10 bit resolution of the ALTRO digitizers, takes place in channel 1023. The spread of the distribution along the y-axis above the saturation point is due to pedestal fluctuations. For all these reasons, the data formatter validates every value from the FEE high-gain channels by requiring the maximum sample to be less than 1000. Values from the low-gain channels are not subjected to this cut because they have never been observed to saturate the ADC.

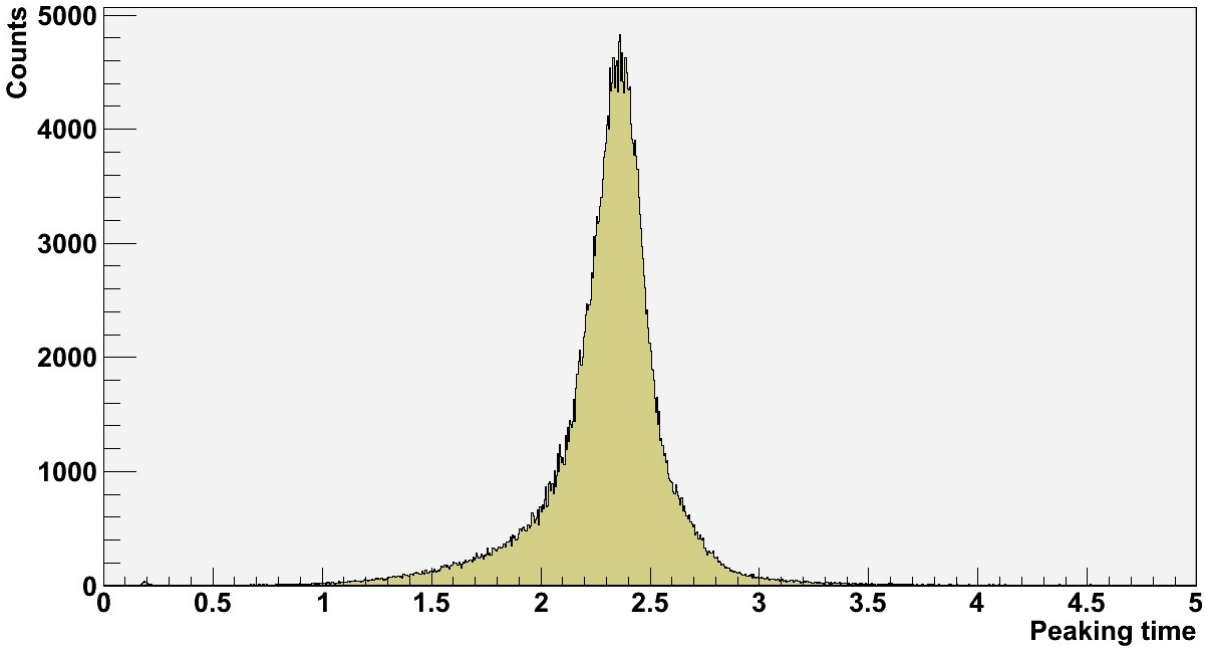

Figure 4.42: Distribution of the peaking time of the second-order Gamma function given in Eq. (4.6). The time values are from fits to the digitized waveforms and they are expressed in ADC clock cycles, with one cycle corresponding to 100 ns.

Another set of selection cuts is applied by the data formatter before saving to the output ROOT TTree any charge information extracted from the second-order Gamma fits to the digitized waveforms, be it from a FEE high-gain or low-gain channel, in order to ensure the goodness of the fits. This selection acts in two ways: firstly the peaking time of the Gamma function is checked against the nominal value and then the fit amplitude is compared to the pedestal-subtracted maximum sample.

As explained in Section 4.4.4.2, the peaking time of the second-order Gamma function at the output of the shaper amplifier is twice the shaping time, or $2\tau_c = 200$ ns. Remembering that the ADC sampling rate is set to 10 MHz, the peaking time is expected to be 2 time bins. Figure 4.42 shows the distribution of the peaking time extracted from the run set R12-85:15-π-2.20-6010 (cf. Table F.6). The histogram peaks between 2 and 2.5 time bins and extends from about 1 to 3.5. The upper and lower cuts are decided by checking a high number of fits on single digitized waveforms. The exercise reveals that in most cases a peaking time below 1.5 or above 4 is symptomatic of either a fit divergence or of a convergence to a wrong local minimum.

The second fitness cut further validates the Gamma fit by comparing its amplitude F to the maximum sample S of the digitized waveform and to the pedestal P. The confrontation can be formulated in four equivalent ways, as shown in Eq. (4.15) to (4.18), where the right sides represent the expected values.

$$F + P - S \simeq 0 \tag{4.15}$$

$$\frac{P}{S - F} \simeq 1 \tag{4.16}$$

$$\frac{S}{F + P} \simeq 1 \tag{4.17}$$

$$\frac{F}{S - P} \simeq 1 \tag{4.18}$$

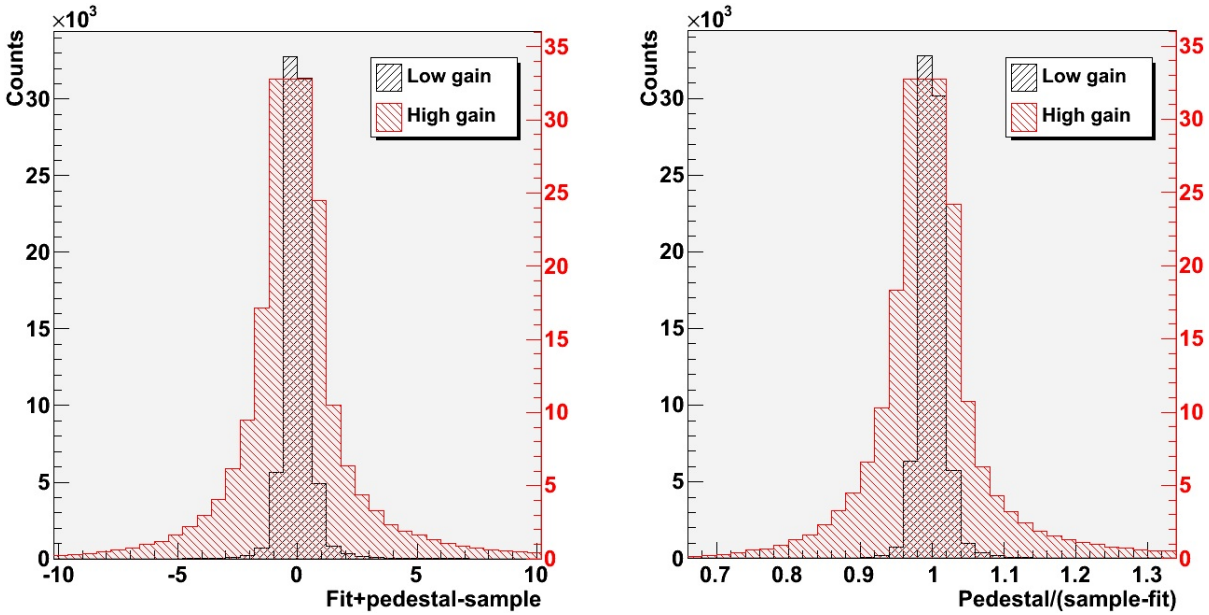

Figure 4.43: Distribution of Eq. (4.15) (left) and (4.16) (right).

It is therefore necessary to establish which formulation is the best to assess the quality of the fit. The searched expression has to enable a good discrimination of bad fits and has to work for all signal amplitudes. The possibility to apply the same cut on signals from both the high-gain and the low-gain branches of the shaper amplifiers is a plus, as it simplifies the parameter adjustment. The left frame of Fig. 4.43 shows the distribution of Eq. (4.15), while the right frame displays the distribution of Eq. (4.16). The histograms are based on the run set R12-85:15-π-2.20-6010 (cf. Table F.6), where each entry is validated both by requiring the maximum sample on the high-gain branch to be lower than 1000 and by requesting the peaking time of the fit to be included between 1.5 and 4. Equation (4.15) is the least suitable of the four, as it is strongly correlated to the amplitude of the signal. Despite taking the ratio of two homogeneous quantities and hence giving rise to a dimensionless value, Eq. (4.16) is not better because it still combines in the wrong way the two variables that are most strongly correlated to the signal amplitude. In fact, an expression that wants to produce results independent on the signal amplitude has to contain the ratio between F and S, appropriately adjusted with the baseline. Equation (4.17) and (4.18), whose distributions are shown respectively in the left and right frame of Fig. 4.44, do a much better job. The latter one is preferred since the distribution for the high-gain and the low-gain branches of the shaper amplifiers are very similar to each other in all the analyzed runs, thus speeding up the tuning of the cut thresholds. The cut window is set to 0.75–1.25 for both branches.

When the data formatter fills the output ROOT TTree with a charge value from the low-gain branch of a shaper amplifier, be it the amplitude of the second-order Gamma fit or the pedestal-subtracted maximum sample of the digitized waveform, it has to rescale the variable with the ratio of the electronics gains in the two branches. As pointed out in Section 4.4.4.2, this ratio is designed to be 16:1, with the purpose of extending the dynamic range of the ADCs by 4 bits. It is anyway interesting to extract the actual value from the data and compare it to the nominal one. Figure 4.45 shows the distribution of the electronics-gain ratio, based on the run set R12-85:15-π-2.20-6010 (cf. Table F.6). The histogram is built by taking, for every event and for every firing strip, the ratio of the charge values extracted from the second-order Gamma fits on the digitized waveforms from the high-gain and the low-gain branches of the shaper amplifier. The fits are validated by requiring the peaking time to be included between

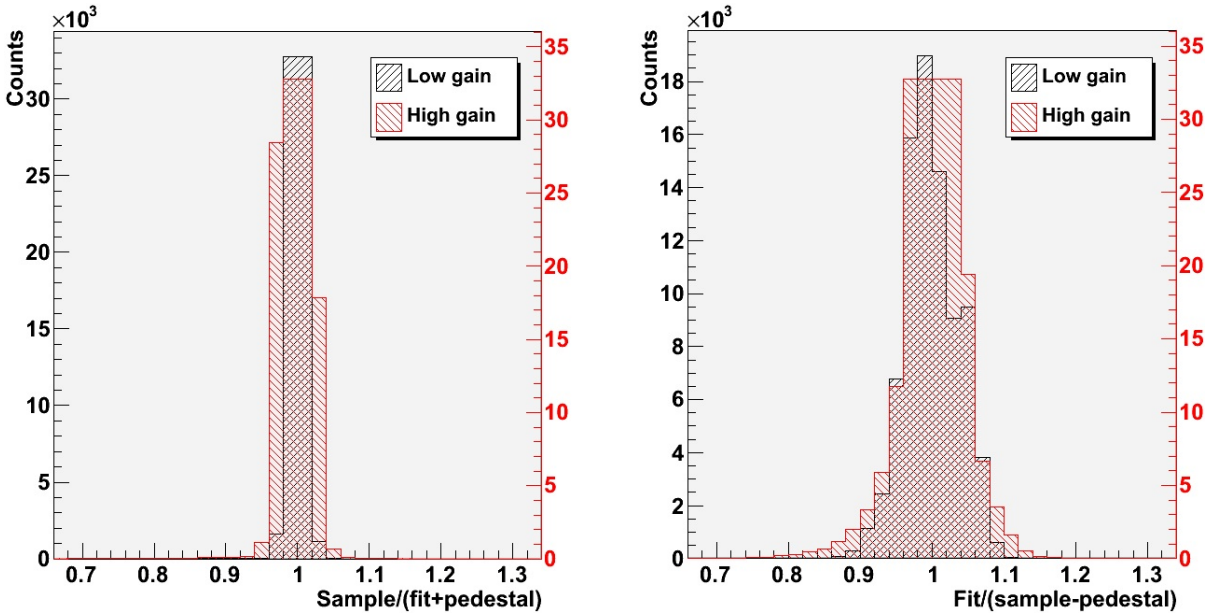

Figure 4.44: Distribution of Eq. (4.17) (left) and (4.18) (right).

1.5 and 4 and by requesting Eq. (4.18) to be in the range from 0.75 to 1.25. The maximum sample from the high-gain branch is also subjected to the overflow cut, with a threshold of 1000. If any of these conditions is not satisfied, the strip is excluded for one event. No charge values from the pedestal-subtracted maximum sample are used to fill the histogram. The resulting distribution is compatible with the expectations, with the Gaussian fit returning a central value of 16.117 ± 0.002.

The above analysis can easily be extended to a channel-by-channel study by distributing the overall statistics into as many histograms as the number of instrumented strips. The data validation is based on the same selection cuts previously applied to produce Fig. 4.45. Figure 4.46 displays the central value extracted from the Gaussian fit to each histogram, together with the corresponding one-sigma interval, as a function of the channel number. Two run sets are considered. The run set R12-85:15-π-2.20-2490 is represented in dashed black, while the run set R12-85:15-π-2.20-6010 (cf. Table F.6) is represented in solid red. As expected, the two sets show the same pattern. The outlier in channel 36 of the run set acquired at lower gas gain has to be attributed to a failure of the Gaussian fit, rather than an actual anomaly in the setup.

The graphs are saved to disk as text files containing gain-ratio maps, which can subsequently be loaded and exploited by other pieces of software. The data formatter thus acquires the capability of rescaling charge values from the low-gain branch of the shaper amplifiers with the gain ratio specific to the single strip. Outliers caused by fit failures, as in the case seen above, are manually removed from the map. In case the channel of interest is not present in the gain-ratio map, the global value from Fig. 4.45 is used instead.

The implemented data formatter successfully cleans the ROOT files produced by the ALTRO raw-data processor and converts them into standard format. On average, more than 90% of the times the charge value stored in the output ROOT TTree is extracted from the amplitude of the second-order Gamma fit to the digitized waveform from the high-gain branch of the shaper amplifier. In a few percent of the cases, the fit amplitude from the low-gain branch or the pedestal-subtracted maximum sample from the high-gain branch are used instead. Finally, the probabilities of picking the maximum sample from the low-gain branch or of marking the strip as unusable are both negligible.

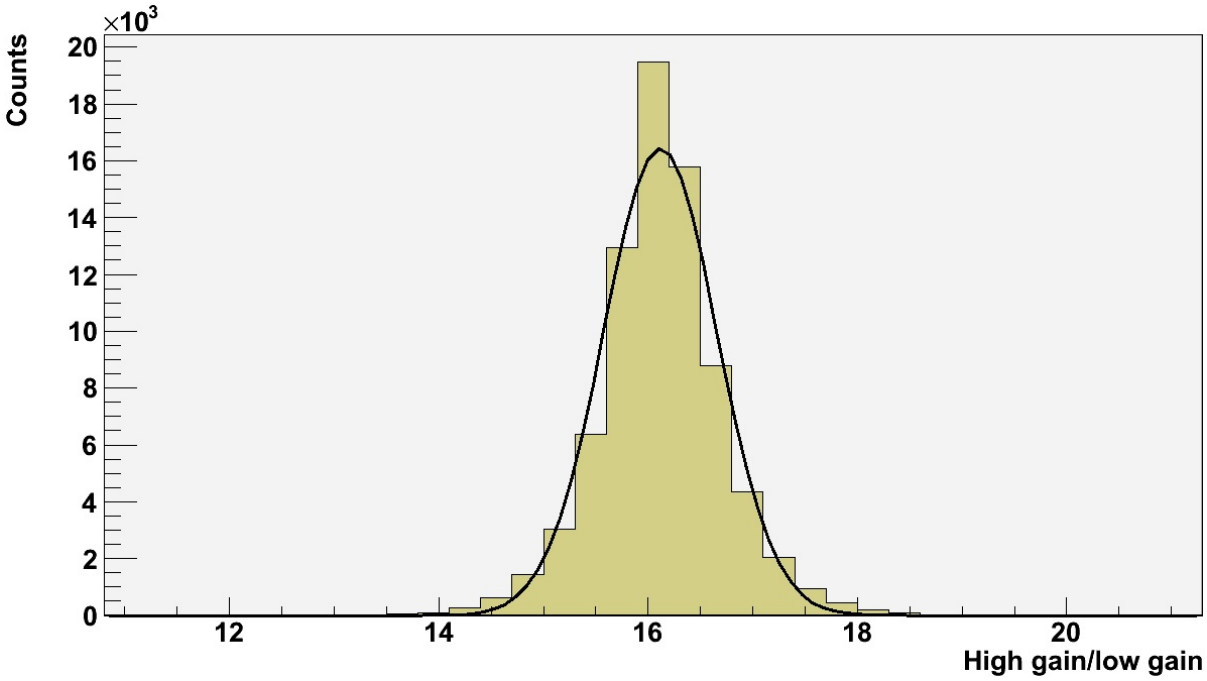

Figure 4.45: Distribution of the electronics-gain ratio.

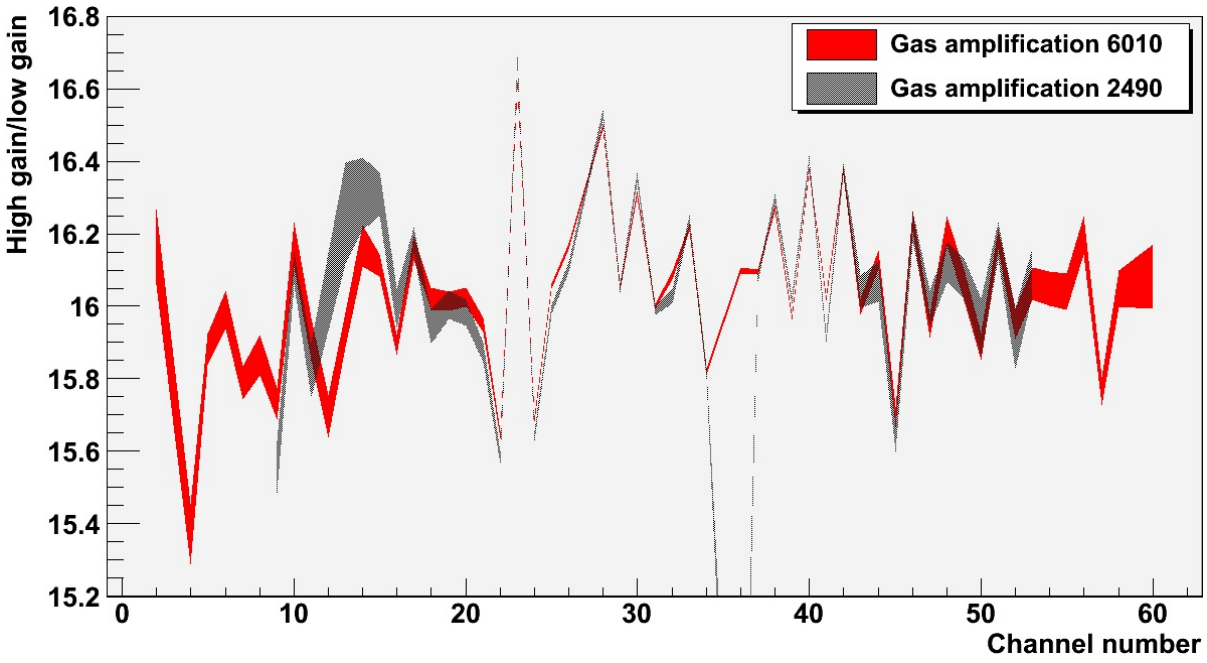

Figure 4.46: Electronics-gain ratio vs channel number.

4.4.4.7 Charge clustering

A key step in evaluating the detection efficiency of the resistive Micromegas and in estimating their space resolution from test-beam data is the identification of the charge clusters in the readout elements. In order to meet the requirements for use in the ATLAS new Small Wheels, the transverse diffusion of charges in the gas and the granularity of the anode strips of the Micromegas chambers are in fact tuned so that the ionization charge released by a particle traversing the drift gap is typically spread over several readout strips even in case of 0° incidence angle. Any reconstruction of the particle properties is therefore based on the correct recognition of the charge clusters.

Given a statistical data set, a cluster is generically defined as a subset of objects that are, in some sense or another, more similar to each other than to those in another group [77]. Clustering is hence the task of recognizing clusters in a data set. More extensively, a cluster is a subset of objects that share a common property. This latter definition is more flexible, as it also allows for soft or fuzzy clustering, where objects may belong to more than one cluster.

In our specific case, a charge cluster is a group of readout elements on which a detectable signal is induced by the same particle traversing the drift gap. The goal is that of coding a software module that, given a ROOT data file in standard format (cf. Section 4.4.4.6), identifies the charge clusters and computes their parameters. For the purpose of efficiency and space-resolution studies, the clustering software is only requested to work for particles traversing the chamber with 0° incidence angle. In this case, the parameters of interest are the cluster extension in channel number, the coordinate of the impact point, the total induced charge and the average arrival time of the signal. As a design choice, the charge and time information stored in the ROOT TTree for each firing strip is kept and the cluster parameters are added in separate branches.

The task is somewhat complicated by the presence of overlapping clusters and dead channels. In the following, these issues will be addressed and analyzed individually.

Overlapping clusters happen when one or more neighboring anode elements receives a non-negligible charge contribution from different particles traversing the drift gap. In turn, this can arise from a double-track event at high beam intensities, it can be the consequence of a cosmic interaction taking place synchronously to a data acquisition, or it can follow the emission of a delta ray by a particle in the beam, just to mention a few possible scenarios. Depending on the nature of the underlying physical phenomena and on their relative topology, it can be more or less difficult to recognize the charge clusters from the distribution of charge induced on the readout structures. While it may be quite straightforward to identify and correctly treat a double-hit event in which the two charge clusters are almost completely resolved, the implementation of a general algorithm that covers all cases is not possible. A hard-clustering approach is hence followed and no attempt is made to distinguish possibly overlapping clusters within a group of neighboring firing strips. An explorative analysis of the test-beam data reveals that a few percent of the events feature overlapping clusters of some kind, which have to be properly handled in order not to bias the subsequent efficiency and space-resolution studies. In later data-analysis phases, double-track occurrences will be excluded by using only events with a single track reconstructed in the silicon beam telescope, which has a much finer granularity. All other sources, such as cosmic interactions and delta-ray productions, which give rise to wide overlapping clusters, will be ruled out by cutting on the cluster size.

Dead channels are readout channels that stopped working normally and became unable to provide a signal correlated to physics events, resulting either constantly silent or recording only baseline noise. The origin of the anomalous behaviour can be manifold and it is most commonly of hardware nature, ranging from a damage or degradation of the detector itself to a mis-plugged connector, to a broken electronics channel. The condition is usually permanent, until a manual intervention is performed to

fix the faulty piece of hardware. For this reason, in a running experiment where the detectors and the front-end electronics are only accessible during shutdown periods, dead channels are typically handled with dead-channel maps. These are lookup tables containing the position of the faulty channels that can thus be easily identified in the data-analysis phase. In the present case, such an approach is however not suitable for two reasons. Firstly, the configuration of the Micromegas chambers and of the readout electronics is often changed during the beam test, with the purpose of probing the behaviour of the detectors under different experimental conditions. As a consequence, the position of the dead channels varies from run to run, thus making the compilation of dead-channel maps a time-consuming task. Additionally, the presence of partially-dead channels is noticed in some runs. These are channels that appear to be dead only for part of the run and otherwise work normally, most probably because of a bad contact in a mis-plugged connector. Both issues are tackled with a clustering algorithm that dynamically identifies and corrects for dead channels on a event-by-event basis.

In summary, a further analysis of the data acquired either from the resistive or from the non-resistive Micromegas chamber in the beam test of interest necessitates of a clustering algorithm that, although not required to recognize overlapping clusters, has to actively identify dead channels and merge groups of firing strips belonging to the same charge cluster. The choice therefore goes to hierarchical algorithms, which seek to build a hierarchy of clusters from a given set of elements. More specifically, the searched algorithm has to be of agglomerative type. This implies a bottom-up approach, where clusters are compared and combined in pairs as one moves up the hierarchy, with merges usually determined in a greedy manner. Agglomerative hierarchical algorithms normally start with each observation in its own singleton. However, the clustering process can be considerably sped up by introducing a custom step-zero in which fundamental clusters are built from neighboring firing channels. The algorithm then iteratively attempts to unify pairs of fundamental clusters into superclusters, until all the fundamental clusters in the event have been scanned. Only at this point the properties of the resulting superclusters are computed, such as the coordinate of the impact point, the total induced charge and the average arrival time of the signal.

The decision on whether two clusters should be merged into a supercluster is based on two criteria. The first is of metric nature and it parametrizes the fact that anode elements reached by the charge originating from the same particle are close to each other. Since the probability of neighboring dead channels is negligible, cluster combination is attempted only when there is a single silent strip between the two considered clusters. The second criterion implements the observation that, for particles traversing the drift gap with 0° incidence angle, the spatial distribution of the detected charge is approximatively Gaussian. The distribution of charge induced on the channels belonging to the candidate supercluster is hence fitted with a Gaussian function and cuts are applied on the reduced χ^2, as well as on the extracted fit parameters. Since such a fit is statistically meaningful only for four or more data points, the handling of superclusters with less than four firing strips is controlled by Boolean constants located in the configuration file of the software module.

The exploitation of the reduced χ^2 to validate the merging of clusters presupposes a careful error assignment. More specifically, it is necessary to estimate the uncertainty on the charge Q_i extracted from the second-order Gamma fit over the i^{th} digitized waveform, with respect to the true value of charge induced on the readout channel. Because Q_i refers to a well-defined particle, there are neither variations of the ionization charge nor fluctuations of the amplification factor to be taken into account. Instead, four factors should be considered. The largest uncertainty, $\sigma_{\text{Gamma}}(Q_i)$, is introduced when estimating the actual charge from the digitized waveform and it is therefore related to the precision of the second-order Gamma fit. Other contributions are the RMS noise, $\sigma_{\text{noise}}(Q_i)$, extracted from the pre-trigger samplings of the baseline and the discretization error, σ_{ADC}, introduced by the analog-to-digital converters. Finally, since the space distribution of the detected charge is only in first approximation

Gaussian, but has larger tails, a constant term σ_{tails} has to be added. Considering these sources as statistically independent, the total uncertainty $\sigma_{\text{total}}(Q_i)$ is expressed by:

$$\sigma_{\text{total}}(Q_i) = \sqrt{\sigma^2_{\text{Gamma}}(Q_i) + \sigma^2_{\text{noise}}(Q_i) + \sigma^2_{\text{ADC}} + \sigma^2_{\text{tails}}} \tag{4.19}$$

The RMS noise for each event and each firing strip is originally computed by the raw-data converter and stored in the ROOT TTree, from where it can be promptly retrieved. The ADC discretization error is constant and depends on the resolution of the analog-to-digital converters. Remembering that an ADC bin corresponds to 1160 electrons for the high-gain branch of the shaper amplifiers, σ_{ADC} amounts to about 335 electrons and it is hence negligible. σ_{tails} is tuned by manually scanning through the data and gauging the deviation of the tails of the spatial distribution of the detected charge from a Gaussian shape, which is evaluated to be 5 ADC channels. Finally, the fit precision is expected to be proportional to the charge itself, or $\sigma_{\text{Gamma}}(Q_i) = kQ_i$. The proportionality coefficient k is extracted from Fig. 4.47, which shows the difference between the amplitude of the second-order Gamma fit and the pedestal-subtracted maximum sample of the digitized waveform as a function of the charge, represented once more by the pedestal-subtracted maximum sample. The plot is based on the Micromegas run 4935, which belongs to the run set R12-85:15-π-2.20-6010 (cf. Table F.6). The graph is filled with the data recorded by each firing strip in each event. Preference is given to the signals from the high-gain branch of the shaper amplifiers, if the maximum sample of the digitized waveform is below the overflow cut of 1000 ADC bins. Otherwise, the information from the low-gain branch is used, rescaled with the appropriate factor retrieved from the gain-ratio map produced in Section 4.4.4.6. Additional data validation is performed by requiring the peaking time of the second-order Gamma fit to be included between 1.5 and 4 and by requesting Eq. (4.18) to be in the range from 0.75 to 1.25. The figure has features that are remnant of the way in which the raw data are handled. For example, the cut at very low charge values is a consequence of the 5-channel threshold applied to the digitized waveforms, while the vertical bands spaced by 16 units are rescaled signals from the low-gain branch of the shaper amplifiers. Overall, the graph confirms that the amplitude of the second-order Gamma fit is scattered with a spread proportional to the charge. The proportionality coefficient is the same for all the analyzed runs and evaluates to 4%. Putting all together, Eq. (4.19) is rewritten as:

$$\sigma_{\text{total}}(Q_i) = \sqrt{1.6 \times 10^{-3} Q_i^2 + \sigma^2_{\text{noise}}(Q_i) + 25} \tag{4.20}$$

The clustering algorithm therefore uses Eq. (4.20) to assign an uncertainty to the charge reconstructed on each firing strip of the candidate supercluster and fits the resulting histogram with a Gaussian function. Although the reduced χ^2 alone already provides a powerful tool to discern fundamental clusters belonging to the same charge cluster, additional cuts are applied to the other parameters extracted from the Gaussian fit in order to handle a few borderline situations. Specifically, the centre of the Gaussian is required to be in the portion of active area equipped with readout electronics, that is between channel 1 and 64. The width of the Gaussian is required to cover less than 10 strips and its amplitude to be smaller than 1.16×10^7 electrons. These cuts are tuned to deal with a wide range of charge configurations and have proven to produce the correct result in all the observed cases.

Figure 4.48 shows two sample events. The data points represent the charge reconstructed on each firing strip and the error bars are the uncertainties computed with Eq. (4.20). The left frame shows event 43 of the Micromegas run 4857, which belongs to the run set R12-85:15-π-2.20-2490, while the right frame shows event 773 of the Micromegas run 4935, which is part of the run set R12-85:15-π-2.20-6010 (cf. Table F.6). Although the two runs are acquired only a few hours one after the other with no intervention on the setup performed in between, they show dead channels in different positions.

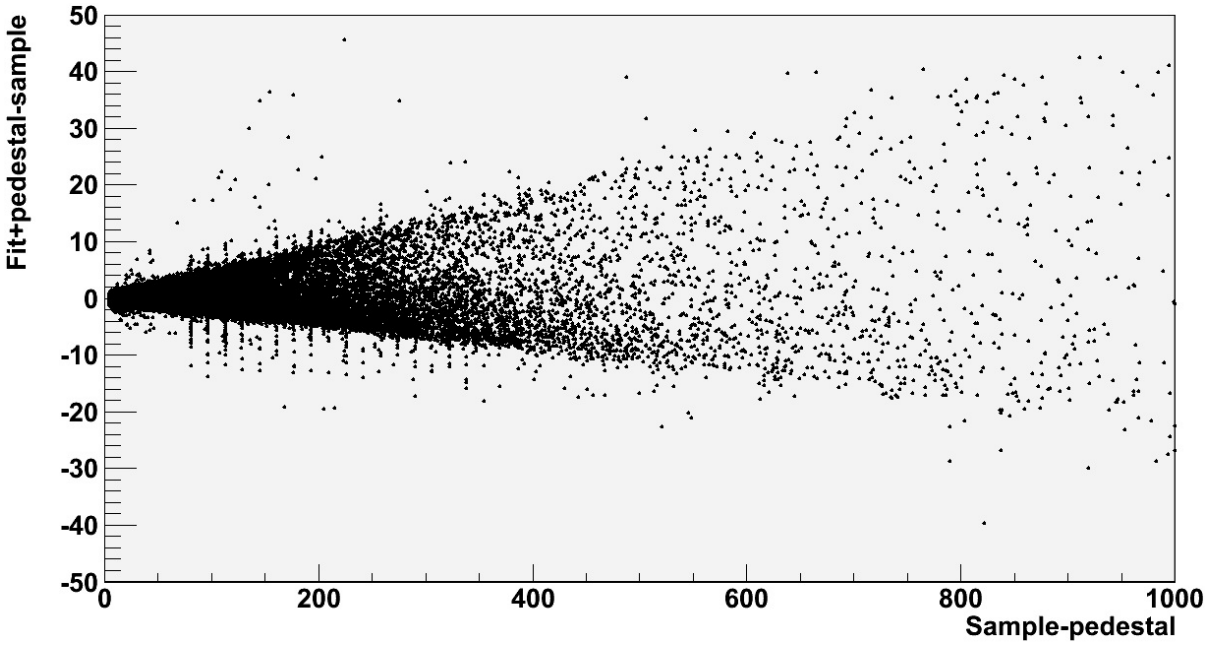

Figure 4.47: Distribution of the error on the amplitude of the second-order Gamma function given in Eq. (4.6). The amplitude values are from fits to the digitized waveforms. The difference between the fit amplitude and the pedestal-subtracted maximum sample, taken as a reference, is shown as a function of the detected charge. Both axes are in ADC bins.

In this case the clustering algorithm demonstrates its flexibility, dynamically recognizing fundamental clusters belonging to the same charge cluster and merging them into a single supercluster with no need for dead-channel maps.

Once the superclusters are formed, the program computes and stores in the ROOT TTree the cluster parameters, such as the coordinate of the impact point, the total induced charge and the average arrival time of the signal. In case the supercluster includes one or more dead channels, the charge from the Gaussian fit is used instead, thus allowing the missing information to be recovered.

4.4.4.8 Impact-point estimation

The estimation of the particle's impact point from the distribution of the charge in a reconstructed cluster is one of the most delicate steps of the data-analysis process. Even in the simplest case of tracks crossing the detector with 0° incidence angle, the procedure is not straightforward. The most common approach involves the computation of the centre of gravity, x_g, defined as the position of the average strip in the cluster, weighted with the charge induced on each channel, as in Eq. (4.21). Here x_i is the coordinate of the i^{th} strip, Q_i the corresponding measured charge and the sum extends over all the firing channels in the cluster.

$$x_g = \frac{\sum_i x_i Q_i}{\sum_i Q_i} \tag{4.21}$$

Although the centre of gravity may seem a reasonable estimator, its blind application leads to a biased evaluation of the impact point. Figure 4.49 shows the distribution of the centre of gravity in the Micromegas run 4935, which belongs to the run set R12-85:15-π-2.20-6010 (cf. Table F.6). Despite the histogram not including singleton clusters, the distribution strongly peaks around the central point of each strip.

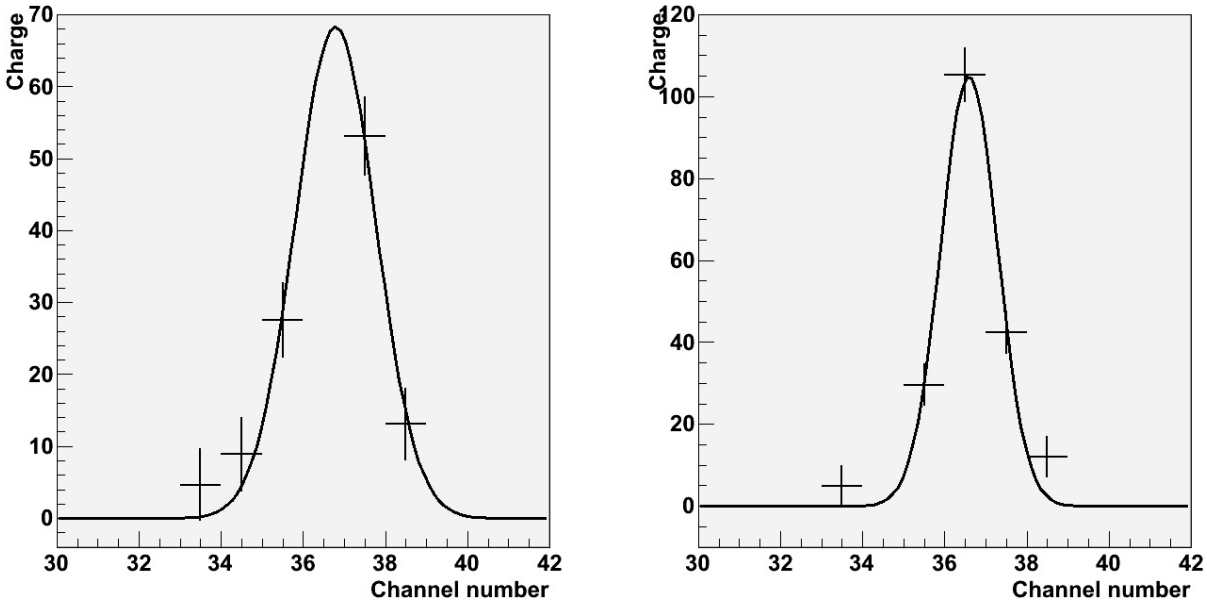

Figure 4.48: Sample events in which a charge cluster is split into two fundamental clusters by a dead channel. The data points represent the reconstructed charge and the associated uncertainty, computed with Eq. (4.20). The solid line is the Gaussian fit. In both cases, the clustering algorithm recognizes the charge cluster and merges the fundamental clusters into a supercluster.

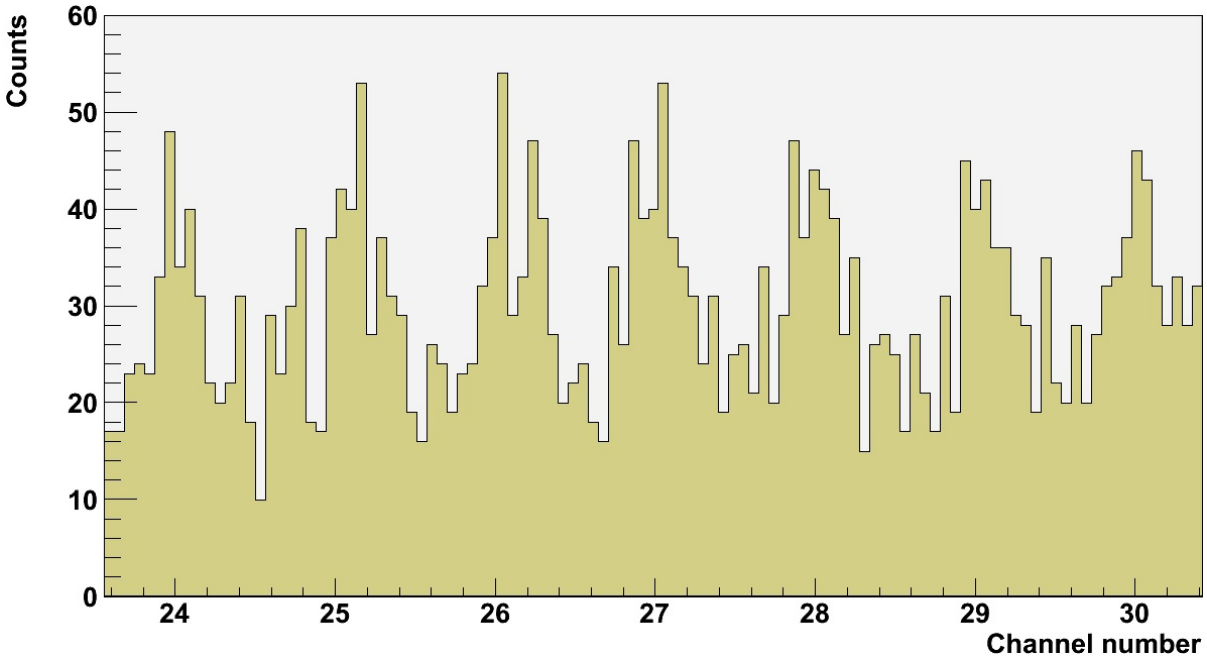

Figure 4.49: Hit position from centre of gravity.

In order to understand the reason why the centre of gravity fails to provide the correct estimate for the impact point, let's consider the one-dimensional analog distribution, $q(x)$, of the charge within a cluster, which is a function of the continuous variable x. The impact point ξ is defined as:

$$\xi = \frac{\int xq(x)\,\mathrm{d}x}{\int q(x)\,\mathrm{d}x} \tag{4.22}$$

Because of the finite segmentation of the detector readout, we do not have access to the analog distribution $q(x)$, but only to its discrete reduction. For simplicity, let's consider a chamber with anode elements perfectly decoupled from each other and an electronics chain with no cross-talk effects. Let's neglect any noise contributions and suppose that exact charge information can be extracted from the digitized waveforms. Even in such an ideal situation, the best we can do is to measure the charges Q_i induced on the strips, which typically represent integrations of $q(x)$ over one readout pitch. The segmentation of the readout therefore introduces a systematic error, usually referred to as discretization error, that spoils the centre of gravity of any simple relation with the impact point. This is clearly expressed by Eq. (4.23), where $\chi_i(x)$ represents the characteristic function of the i^{th} strip.

$$x_g = \frac{\sum_i x_i \int q(x)\chi_i(x)\,\mathrm{d}x}{\int q(x)\,\mathrm{d}x} \neq \xi \tag{4.23}$$

As demonstrated in [78], there exist charge distributions that are free from discretization errors and for which the centre of gravity coincides with the impact point. Examples are all the $q(x)$ that can be expressed as convolutions of an arbitrary function with a characteristic function of the width of a strip. In the same article it is also shown that some types of cross-talk spreads are able to eliminate the discretization error on charge distributions of any shape. In the general case, and also for the data analyzed in the present thesis, the estimation of the impact point requires more effort.

Let's consider Eq. (4.24), which defines the variable η_N. Here, s_i is the number of the i^{th} readout channel in the cluster and $s_{\max}$ the number of the channel on which the maximum charge is measured. N is a fixed parameter that is required to be equal to or greater than 2 and indicates the number of strips used in the computation. For odd values of N, the channels are taken symmetrically around $s_{\max}$, while for even values of N, the strips are taken around the two channels detecting the maximum charges.

$$\eta_N = \frac{\sum_{i=1}^{N}(s_i - s_{\max})\,Q_i}{\sum_{i=1}^{N} Q_i} \tag{4.24}$$

η_N is a periodic version of the centre of gravity, computed over a fixed number of channels and normalized with the strip pitch. The periodicity makes it applicable to all the channels in the same way, while the normalization makes it independent from the strip pitch. For non-negative charge distributions with a single maximum, $|\eta_N| < (N-1)/4$ for odd values of N, $|\eta_N| < (N-2)/4$ for even values of N other than 2 and $|\eta_2| < 1/2$. Finally, considering only the central channels of the cluster, one can optimize the signal-to-noise ratio by excluding the tails of the charge distribution, where the noise is more important. The η_2 variable has the best signal-to-noise figure, but it presents an appreciable discontinuity in the origin. Based on the average cluster size in the acquired data, N is set to 3 in all the following analysis.

Figure 4.50 shows the distribution of η_3 in clusters with more than one firing strip, for the example run considered above. The shape is that of a typical η_3 frequency histogram for symmetric charge distributions, featuring a central peak and a symmetry axis in the origin. The two regions of low probability at the edges of the allowed range are also characteristic and arise from the fact that, when η_3 approaches

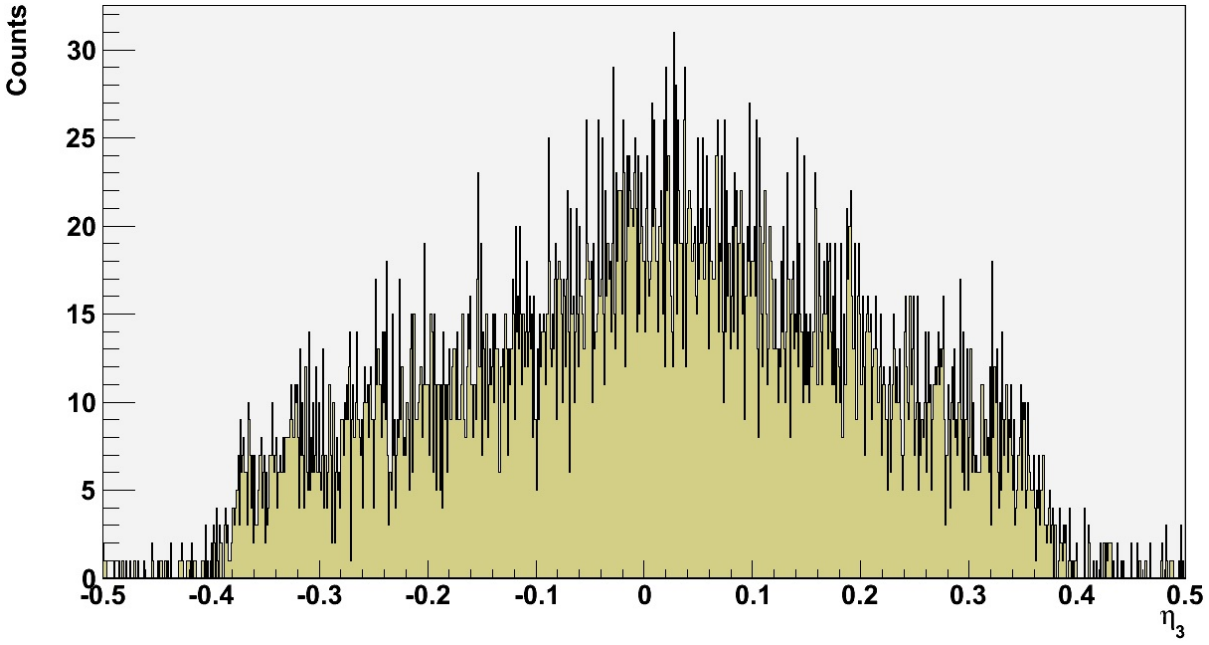

Figure 4.50: Experimental distribution of η_3.

the lower bound, the charge of the rightmost channel tends to increase the centre of gravity, whilst when η_3 approaches the upper limit, the contribution of the leftmost strip pulls down the centre of gravity.

For a generic probability density function $\psi(\xi)$ of the impact point, the probability density function $\varphi(\eta_N)$ of the periodic centre of gravity is:

$$\varphi(\eta_N) = \psi(\xi)\frac{\mathrm{d}\xi}{\mathrm{d}\eta_N} \tag{4.25}$$

If the detector is uniformly irradiated, $\psi(\xi)$ is constant over every channel and equal to the reciprocal of the strip pitch, p. In such a case, Eq. (4.25) can be solved as a differential equation, leading to Eq. (4.26). $f(p, s_{\max}, N)$ is an offset that takes into account the detector geometry and the form of the charge distribution. Possible discontinuities of $\eta_N(\xi)$ are of no concern, as they just imply the existence of values with zero probability in $\varphi(\eta_N)$.

$$\xi = f(p, s_{\max}, N) + p\int_{\eta_{N\min}}^{\eta_N} \varphi\left(\eta'_N\right)\mathrm{d}\eta'_N \tag{4.26}$$

In most of the cases $\varphi(\eta_N)$ is not known a priori. For practical purposes, however, the probability density function of the periodic centre of gravity can often be approximated with a frequency histogram $h(\eta_N)$ like the one of Fig. 4.50, obtained by evaluating Eq. (4.24) for all the clusters with more than one firing channel. The integration constant $f(p, s_{\max}, N)$ has no simple analytic expression, but for symmetric charge distributions it is easy to determine. For a periodic centre of gravity with $N = 3$, the integration constant is $p(s_{\max} - 1/2)$. Putting all together and normalizing $h(\eta_3)$ with the number of entries, Eq. (4.26) becomes:

$$\xi_3 = p\left[s_{\max} - \frac{1}{2} + \frac{\int_{-1/2}^{\eta_3} h\left(\eta'_3\right)\mathrm{d}\eta'_3}{\int_{-1/2}^{1/2} h\left(\eta'_3\right)\mathrm{d}\eta'_3}\right] \tag{4.27}$$

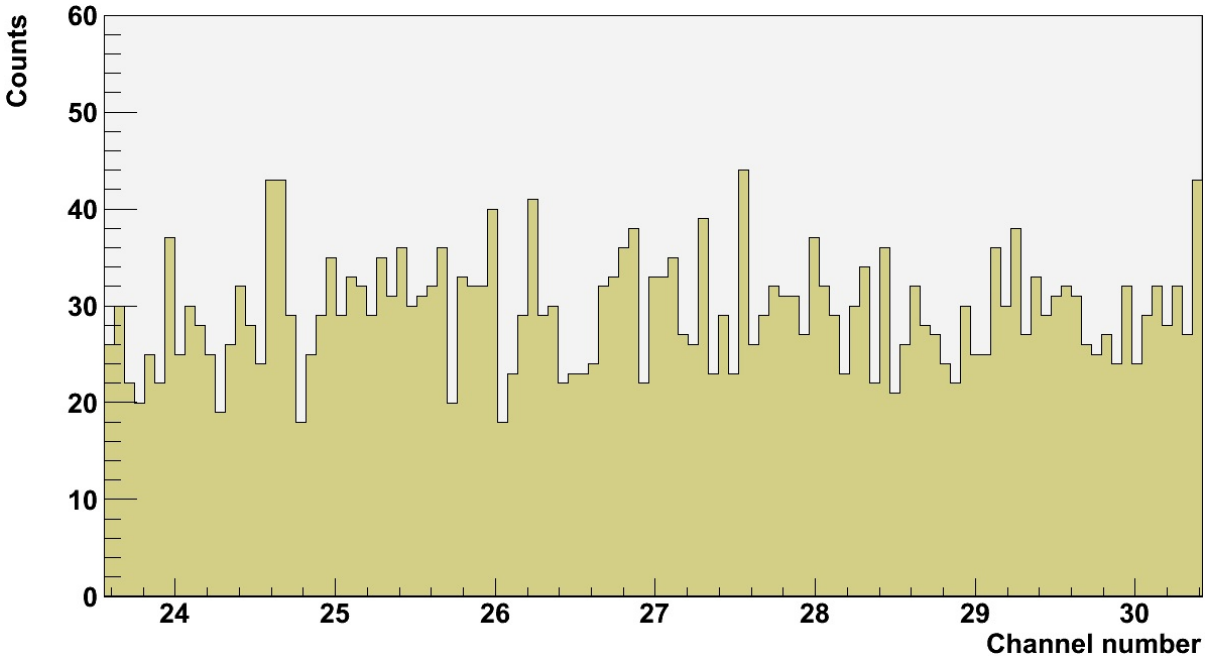

Figure 4.51: Hit position after η correction.

The clustering algorithm discussed in Section 4.4.4.7 indeed takes advantage of Eq. (4.27) to reconstruct the impact point of clusters with multiple firing channels. While building the clusters, the software also fills the frequency histogram for η_3. Once all the events have been processed, the program jumps back to the first event and makes use of the histogram to estimate the impact point of each cluster. Figure 4.51 shows that the resulting distribution of ξ_3 is uniform.

4.4.4.9 Detector-rotation compensation

When the experimental apparatus is set up for the beam test, the edges of all the detectors are carefully aligned to the axes of the coordinate system, in order to have the readout elements oriented in the direction of the reference axes. Perfect matching is not possible due to the tolerances in the support mechanics and to the finite precision of the alignment tools, but small deviations are easy to correct offline, as explained in the following.

Figure 4.52 shows the distribution of the x spatial residuals of the Micromegas as a function of y. The residuals are computed as the difference between the impact point, estimated with the procedure described in Section 4.4.4.8, and the horizontal coordinate of the track reconstructed in the beam telescope, extrapolated to the Micromegas plane. Since the chambers under study have the anode segmented along x only, the y-information is taken from the track reconstructed in the beam telescope. The data are from the BAT run 4199 and the Micromegas run 4935, which belong to the run set R12-85:15-π-2.20-6010 (cf. Table F.6). The graph is based on events with a single track in the vertical direction, in order to give an unambiguous assignment of the y-coordinate. A single reconstructed track in the horizontal direction is also required to reject possibly overlapping clusters in the Micromegas (cf. Section 4.4.4.7). Delta rays are excluded by rejecting clusters covering 10 strips or more.

The graph clearly highlights that the Micromegas has a rotation around the beam axis. The angle is about 12 mrad counterclockwise, when looking at the chamber with the beam. As it appears by projecting the scatter plot along the vertical axis of the graph, the rotation makes the residual distribution

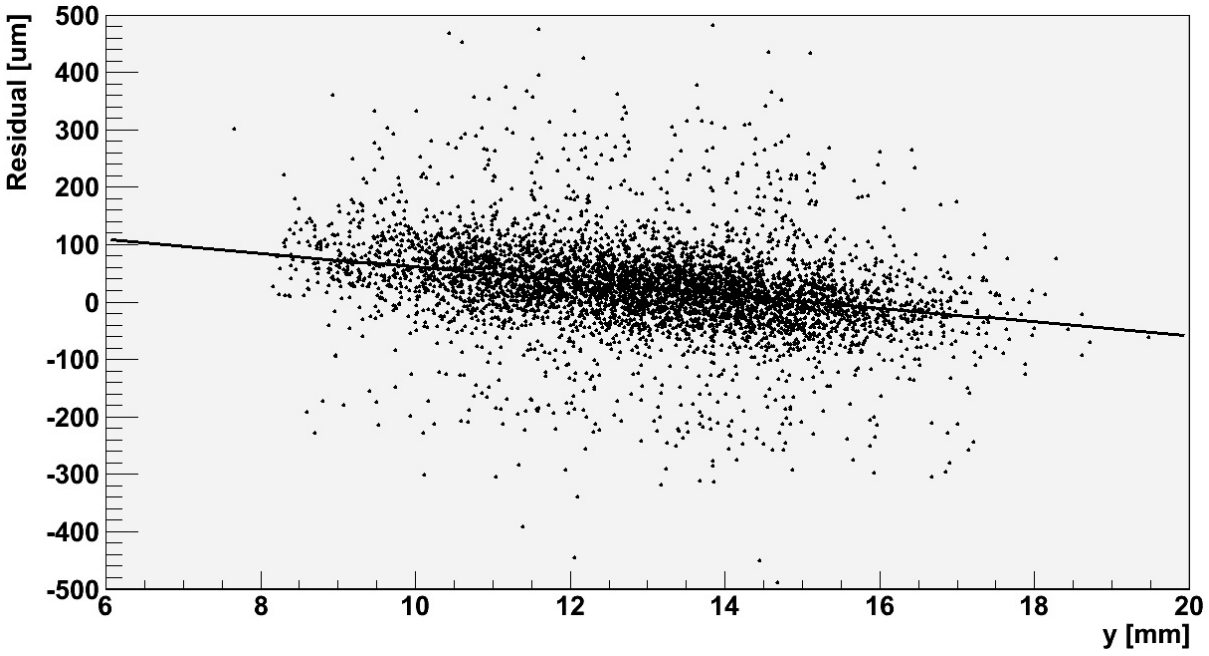

Figure 4.52: x spatial residual vs y hit position.

deviate from the expected Gaussian shape, giving rise to a flat-top that biases the estimation of the spatial resolution towards larger values. The effect therefore has to be removed before proceeding further in the data analysis.

The most effective way to compensate the rotation is to perform a simple linear regression on the data of Fig. 4.52. The angular coefficient times the y-coordinate gives the correction to be applied to the x spatial residual, while the intercept of the regression line provides the alignment constant of the Micromegas with respect to the beam tracker.

4.4.4.10 Efficiency

As stated in Section 4.2, one of the requirements for the chambers of the ATLAS new Small Wheels is a detection efficiency of more than 98% per plane for minimum ionizing particles. Figure 4.53 summarizes the efficiencies extracted from all the analyzed test-beam runs, as a function of the effective gain. Every point on the chart represents a set of runs acquired under like experimental conditions, whose data are merged to reduce the statistical uncertainties. The number of events for a single point ranges from about 10^4 to 5×10^4. In order to be able to correct for the Micromegas rotation around the beam axis, only events with a single reconstructed track in the vertical plane of the beam telescope are considered. The presence of a single track in the horizontal direction is also requested to reject possibly overlapping clusters, and the closest charge cluster in the Micromegas is found, if present. Tracks with a matching cluster covering 10 strips or more are excluded from the analysis in order to reject delta rays created in the Micromegas, which may give either false positives or false negatives. Tracks whose x-coordinate extrapolated to the Micromegas plane lies outside the region of active area equipped with readout electronics are also excluded, to prevent false negatives. The number of tracks passing these cuts is labeled as n. A track is then marked as detected if its extrapolated horizontal position is close enough to the estimated impact point of the matching cluster in the Micromegas, computed according to the algorithm introduced in Section 4.4.4.8 and corrected with the procedure presented in Section

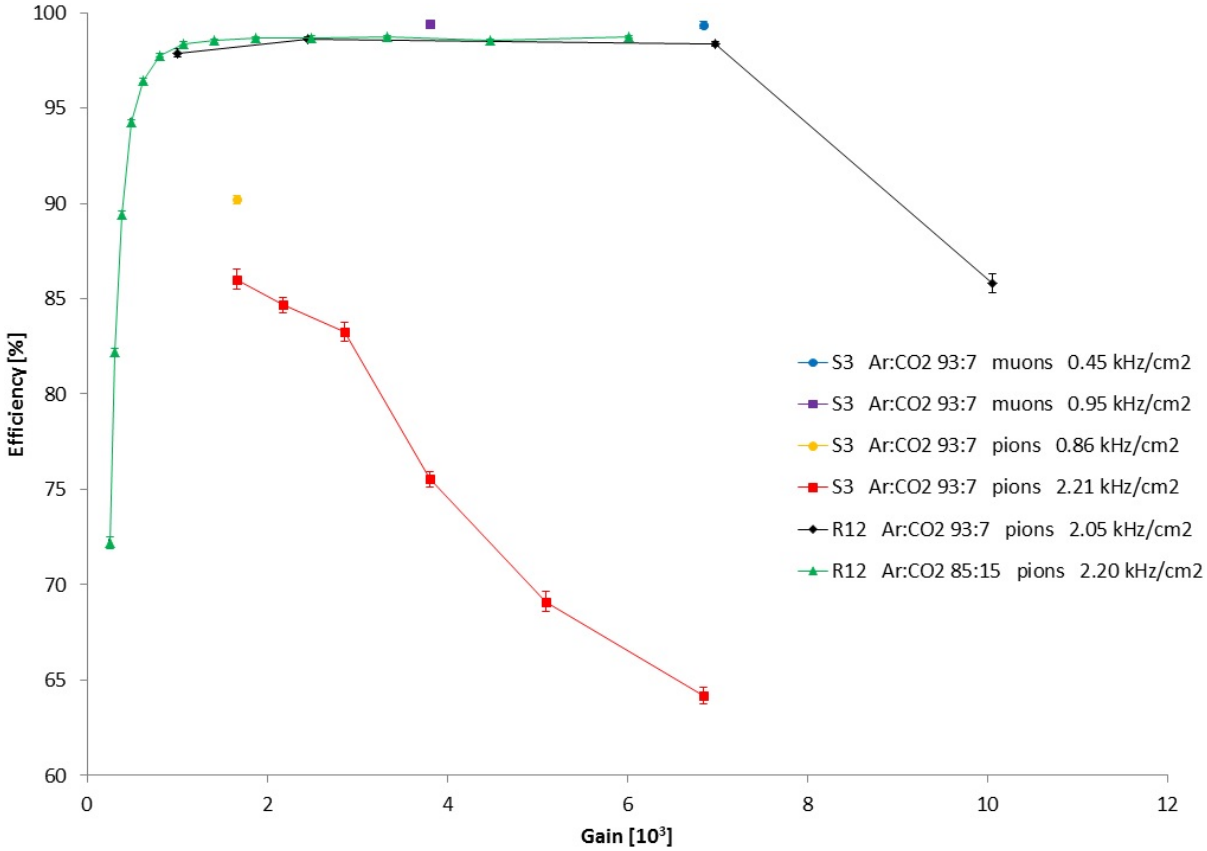

Figure 4.53: Detection efficiency vs gain.

4.4.4.9. The threshold distance is fixed to 1 mm based on the average cluster size, and the outcome of the selection has proven not to change significantly for cut radii ranging from 0.75 to 2 mm. Letting k be the number of positives, the efficiency is estimated as $\varepsilon = k/n$ and the corresponding error is evaluated assuming a binomial hypothesis.

Standard Micromegas are known to reach detection efficiencies close to 100% for minimum ionizing leptons. This is confirmed by the analysis made on the data sets S3-93:7-μ-0.45 (cf. Table F.1) and S3-93:7-μ-0.95 (cf. Table F.2). The extracted efficiency is higher than 99% for both data sets, as shown in Fig. 4.53.

Moving from a lepton to a hadron beam, standard Micromegas do not behave equally well, as highlighted in Fig. 4.53 by the curves obtained from the data sets S3-93:7-π-0.86 (cf. Table F.3) and S3-93:7-π-2.21 (cf. Table F.4). Pions with energy of 120 GeV mainly undergo electromagnetic interactions as they traverse the detector and therefore they behave in great part like minimum ionizing muons. The small but non-zero hadronic cross section of pions, however, carries a finite probability of producing highly ionizing particles. If the density of the charge deposited by these particles is high enough to exceed Raether's limit in the amplification region, the consequent streamer creates a short between the steel mesh and the unprotected copper anode strips. This causes a sudden dump of part of the stored energy to ground and results in a drop of the mesh voltage for a short lapse of time. Hence the fall of the detection efficiency. Such interpretation is supported by the fact that in Fig. 4.53 the efficiency decreases both at higher particle fluxes and at higher gas gains. The interpretation is also confirmed by Fig. 4.54, which shows the x- and y-position of the tracks, reconstructed in the beam telescope and extrapolated

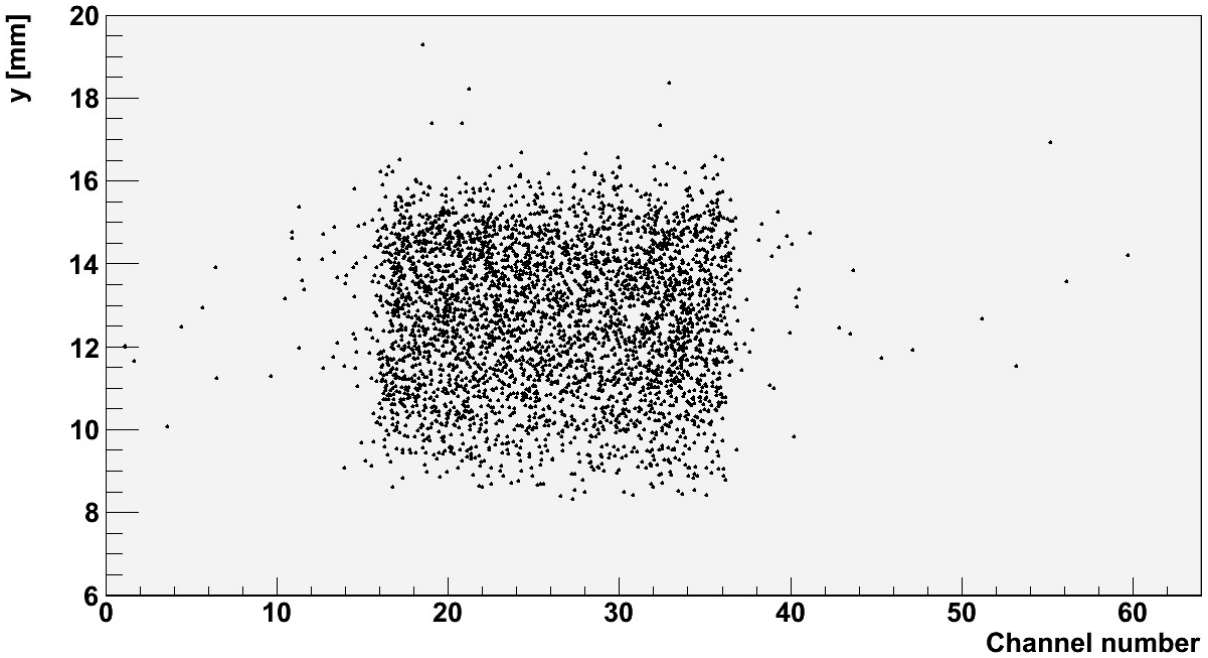

Figure 4.54: Inefficiencies in the run set S3-93:7-π-2.21-6840 (cf. Table F.4). The scatter plot shows the x-y position of the tracks, reconstructed in the beam telescope and extrapolated to the Micromegas plane, with no matching event in S3.

to the Micromegas plane, with no matching event in S3. The figure, based on the run set S3-93:7-π-2.21-6840 (cf. Table F.4), shows that the undetected hits are uniformly scattered over the trigger area, because the drop of the potential applied to the amplification mesh equally affects all the active area.

High efficiency is restored thanks to resistive Micromegas. The discharge probability in these detectors is the same as in standard Micromegas, but the charges reaching the anode plane are not immediately evacuated due to the impedance of the resistive elements. Because of the limited current flowing to ground, the resistive traces involved in the spark rapidly charge up, generating a local decrease of the amplification field that effectively quenches the streamer before it can cause a significant drop of the mesh voltage. Moreover, the segmentation of the resistive layer allows the area affected by the discharge to be contained. The analysis performed on the data sets R12-93:7-π-2.05 (cf. Table F.5) and R12-85:15-π-2.20 (cf. Table F.6) demonstrates the superior performance of the resistive Micromegas in a pion beam, as it can be seen from Fig. 4.53. In both data sets, efficiencies of more than 98% are secured over a broad gas-gain window and up to effective charge-amplification factors of about 10^4. Table 4.2 lists the run sets with efficiency above 98% and hence compatible with the requirements for the ATLAS new Small Wheels. The remaining inefficiencies are compatible with the expected amount of dead area arising from the pillars that support the mesh. Figure 4.55, which is based on the run set R12-85:15-π-2.20-6010 (cf. Table F.6), shows that the undetected tracks indeed cluster around structures whose diameter and pitch match the ones of the pillars holding the amplification mesh.

4.4.4.11 Space resolution

The test-beam data can also be exploited to assess the space resolution of the resistive Micromegas and draw a comparison with the one of non-resistive detectors. The software tools detailed in Section 4.4.4.7 through 4.4.4.9 play here a fundamental role to provide a precise reconstruction of the impact point.

Table 4.2: Test-beam run sets with efficiency above 98% in a hadron beam.

Run set	Efficiency [%]
R12-93:7-π-2.05-2450	98.64 ± 0.10
R12-93:7-π-2.05-6980	98.38 ± 0.14
R12-85:15-π-2.20-1070	98.38 ± 0.08
R12-85:15-π-2.20-1410	98.52 ± 0.07
R12-85:15-π-2.20-1870	98.65 ± 0.07
R12-85:15-π-2.20-2490	98.69 ± 0.07
R12-85:15-π-2.20-3340	98.74 ± 0.07
R12-85:15-π-2.20-4470	98.53 ± 0.07
R12-85:15-π-2.20-6010	98.75 ± 0.07

The space-resolution study is performed following the same procedure employed in the previous section to evaluate the detection efficiency. Runs acquired under like experimental conditions are merged in order to reduce the statistical uncertainties, gathering about 10^4 to 5×10^4 events for each run set. Events with multiple reconstructed tracks in either the horizontal or the vertical plane (or both) of the beam telescope are excluded from the analysis. In the former case, requiring a single track prevents the possibility of overlapping charge clusters in the Micromegas, while in the latter case it enables the compensation of the chamber rotation around the beam axis. The track is extrapolated to the z-coordinate of the Micromegas under study and the distance to each charge cluster is computed. More specifically, the space residual is calculated as the difference between the impact point on the Micromegas, estimated with the algorithm introduced in Section 4.4.4.8 and corrected with the procedure explained in Section 4.4.4.9, and the horizontal coordinate of the extrapolated track reconstructed in the beam telescope. The charge cluster with the lowest space residual is identified and validated by requesting its size to be smaller than 10 channels, so to reject delta rays created in the Micromegas and cosmic-ray interactions, which may bias the results.

The space residuals follow a Gaussian probability distribution centred around zero, as shown in Fig. 4.56 for the run set R12-85:15-π-2.20-6010 (cf. Table F.6). Figure 4.56 also displays a Gaussian fit superimposed on the central part of the histogram. The fit is based only on those residuals whose absolute value is lower than 100 µm, so to exclude the non-Gaussian tails. The extracted width is $\widetilde{\sigma_{\mu\mathrm{M}}} = 45.0 \pm 0.3\,\mu\mathrm{m}$. However, this value does not correspond to the space resolution $\sigma_{\mu\mathrm{M}}$ of the Micromegas, because the variable plotted in the histogram is the sum of several contributions. The first is indeed the intrinsic space resolution of the Micromegas, which is the quantity we want to assess. The most important amongst the other terms are the precision of the reconstructed track in the beam telescope, in first place, and the multiple Coulomb scattering in the three BAT stations and in air, which contribute to a lesser extent. These six quantities are represented by as many independent random variables, all of them following Gaussian probability distributions with zero average value, but different widths. Since the considered space residual is the sum of such variables, its probability distribution is the convolution of the single probability distributions. The result is a Gaussian centred around zero and with a variance equal to the sum of the variances of the single probability distributions. In order to estimate the intrinsic space resolution of the Micromegas, it is therefore necessary to model the other phenomena and determine their contribution.

Multiple Coulomb scattering is described in Section 1.3. The contributions of the three silicon layers of the tracking telescope are obtained by multiplying the width θ_{RMS} of the projected angular distribution, computed with Eq. (1.7), by the lever arm between the corresponding BAT module and the

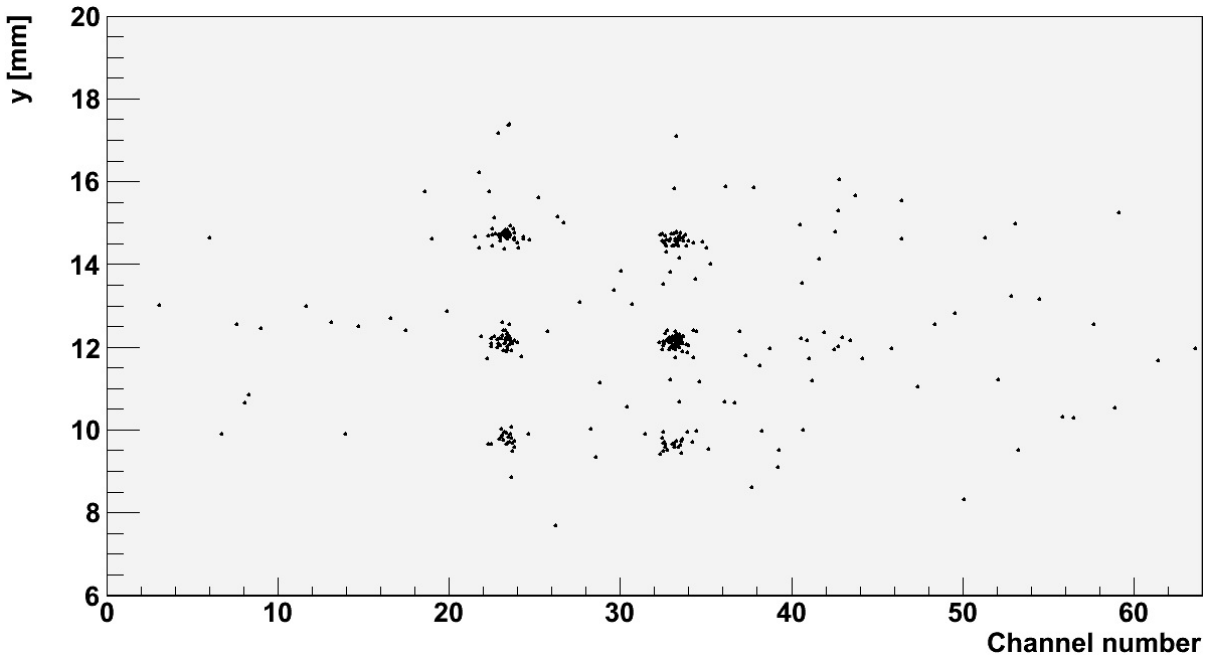

Figure 4.55: Inefficiencies in the run set R12-85:15-π-2.20-6010 (cf. Table F.6). The scatter plot shows the x-y position of the tracks, reconstructed in the beam telescope and extrapolated to the Micromegas plane, with no matching event in R12.

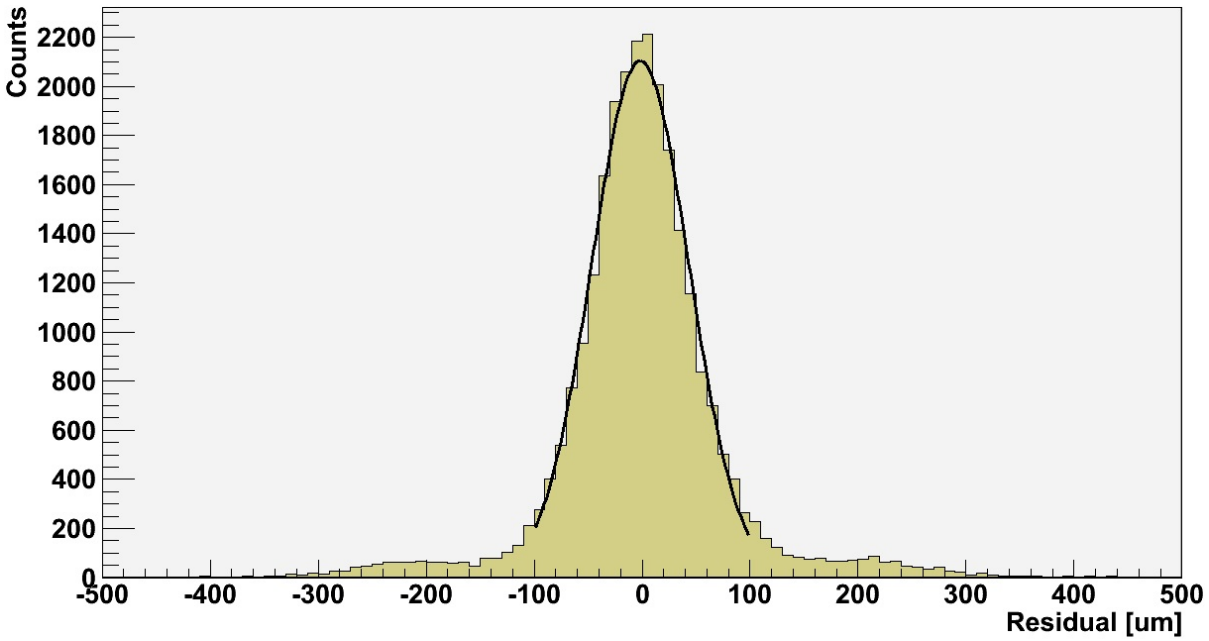

Figure 4.56: Distribution of space residuals for R12.

Table 4.3: Multiple-scattering contributions to the space residuals of R12 and BAT3.

Detector	σ_{Si1} [µm]	σ_{Si3} [µm]	σ_{Si6} [µm]	σ_{air} [µm]
R12	4.6 ± 0.5	8.4 ± 0.9	8.7 ± 1.0	6.8 ± 0.8
BAT3	3.9 ± 0.4		0.22 ± 0.02	2.1 ± 0.2

Micromegas. In the case of air, Eq. (1.8) is used instead. The thickness of the scatterers is 0.3 mm for each silicon layer and 1.726 m for air, while the radiation length, X_0, is 93.7 mm and 303.9 m respectively, as from [1]. The results are summarized in the middle row of Table 4.3. The errors are set to 11% because of the precision of Eq. (1.7) and (1.8).

The evaluation of the uncertainty, σ_{track}, on the hit position from the track reconstructed in the beam telescope and extrapolated to the Micromegas plane requires the knowledge of the space resolution, σ_{BAT}, of the three silicon detectors in the BAT. The estimation of the latter quantity is performed exploiting test-beam data and adopting an approach similar to the one used above to extract $\widetilde{\sigma_{\mu\mathrm{M}}}$. The analysis is done on a run-by-run basis, accepting only events with a single charge cluster in the horizontal direction of each station of the beam telescope. For every BAT module, the space residual between the position of the eta-corrected centre of gravity and the x-coordinate of the extrapolated (or interpolated) track reconstructed with the other two stations is calculated and used to fill a histogram.

Figure 4.57 shows the distribution of space residuals for the three detectors in the beam telescope for the BAT run 4267, which belongs to the run set S3-93:7-π-2.21-6840 (cf. Table F.4). The expressions of the three residuals have the same form, with the only difference lying in a scaling factor involving the distance between the two modules chosen for track reconstruction. As a consequence, all of the three histograms in Fig. 4.57 have the same shape, and their average value and width scale with the proportionality factor. The small differences that can be spotted from one histogram to the other are binning artifacts. In analogy to what has been observed in Fig. 4.56 for the Micromegas residuals, the BAT space residuals follow Gaussian probability distributions. A Gaussian fit is superimposed on each histogram and the extracted parameters are overlaid. The slight deviation of the average values from zero arises from the alignment of the stations, and is of no concern. In order to extract the space resolution of the detectors in the beam telescope one has to consider that, like in the case of the Micromegas residuals, the BAT space residuals are the sum of different contributions, the main ones being the space resolution, the track-reconstruction precision and the multiple Coulomb scattering. In BAT1 the track-reconstruction uncertainty is by far the dominant term, due to the proximity of BAT3 and BAT6 and to the large extrapolation distance. In the other two modules the extrapolation (or interpolation) error is much lower, and of similar magnitude. The specific layout of the beam telescope has been selected to grant the best possible precision of the reconstructed hit position on the Micromegas plane. The vicinity of BAT3 and BAT6 in fact imposes a tight bound on the track reconstructed using all the three stations. The drawback of this configuration appears when attempting to assess the space resolution of the BAT detectors. The reduced distance between BAT3 and BAT6 results in a track-reconstruction uncertainty for these two modules that is as large as their space resolution. For all these reasons, the space resolution σ_{BAT} of the silicon detectors, assumed to be the same for all the three stations, is given by:

$$\sigma_{\mathrm{BAT}} = \sqrt{\frac{\widetilde{\sigma_{\mathrm{BAT}}}^2 - \sigma_{\mathrm{Si1}}^2 - \sigma_{\mathrm{Si6}}^2 - \sigma_{\mathrm{air}}^2}{2}} \tag{4.28}$$

Here, $\widetilde{\sigma_{\mathrm{BAT}}} = 21.74 \pm 0.05\,\mu\mathrm{m}$ is the weighted mean of the widths extracted from Gaussian fits to the distributions of space residuals of BAT3 for 19 different runs. The employed BAT runs are the ones

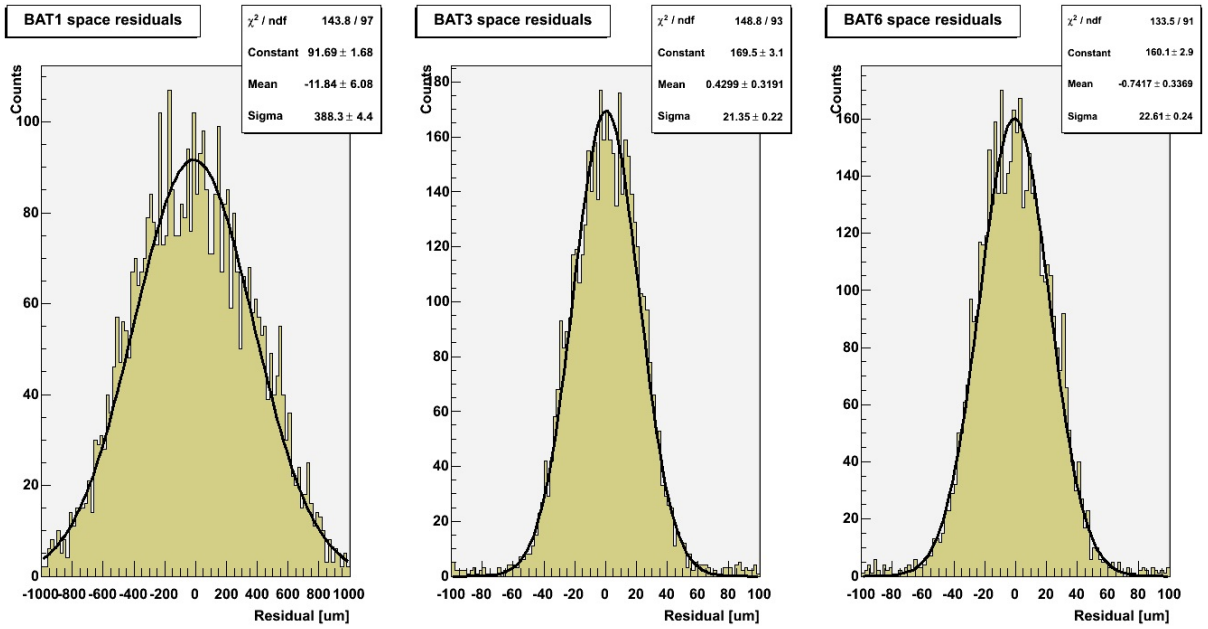

Figure 4.57: Distribution of space residuals for the tracking telescope.

listed in Table F.3, F.4 and F.5, and the BAT run 4441. The other three terms in Eq. (4.28) are the contributions of the multiple Coulomb scattering, whose numerical values based on Eq. (1.7) and (1.8) are summarized in the last row of Table 4.3. The computation leads to $\sigma_{\mathrm{BAT}} = 15.05 \pm 0.07\,\mu\mathrm{m}$. This is the effective space resolution of each silicon station and it is larger than the intrinsic space resolution of the detectors, which is better than 6.3 µm, as from [72]. In fact, σ_{BAT} includes a term arising from the rotation of the three BAT modules around the beam axis, which has to be taken into account in the evaluation of σ_{track}.

The software module that reconstructs the particle trajectories in the tracking telescope uses independent simple linear regressions of the type $x_{\mu\mathrm{M}} = A + Bz_{\mu\mathrm{M}}$ to calculate the hit position on the Micromegas plane along x and y. The error σ_{track} on the extrapolated point is:

$$\sigma_{\mathrm{track}} = \sqrt{\sigma_A^2 + z_{\mu\mathrm{M}}^2\sigma_B^2 + 2z_{\mu\mathrm{M}}\mathrm{cov}_{AB}} \tag{4.29}$$

σ_A, σ_B and the covariance term are all simple functions of the z-coordinates of the three silicon detectors and of their space resolution σ_{BAT}. Equation (4.29) can therefore be computed analytically, leading to $\sigma_{\mathrm{track}} = 34.58 \pm 0.16\,\mu\mathrm{m}$.

The intrinsic space resolution $\sigma_{\mu\mathrm{M}}$ of the Micromegas is then obtained by subtracting the uncertainty σ_{track} on the reconstructed extrapolated track and the contributions of the multiple Coulomb scattering in the various materials from the width $\widetilde{\sigma_{\mu\mathrm{M}}}$ of the Gaussian fit on the Micromegas residuals:

$$\sigma_{\mu\mathrm{M}} = \sqrt{\widetilde{\sigma_{\mu\mathrm{M}}}^2 - \sigma_{\mathrm{track}}^2 - \sigma_{\mathrm{Si1}}^2 - \sigma_{\mathrm{Si3}}^2 - \sigma_{\mathrm{Si6}}^2 - \sigma_{\mathrm{air}}^2} \tag{4.30}$$

Figure 4.58 summarizes the space resolution of S3 and R12 for all the analyzed test-beam runs, as a function of the effective gain. The resistive Micromegas exhibits a much better performance with respect to the non-resistive detector, reaching $\sigma_{\mu\mathrm{M}} = 24.9 \pm 0.8\,\mu\mathrm{m}$ in the run set R12-85:15-π-2.20-6010 (cf. Table F.6).

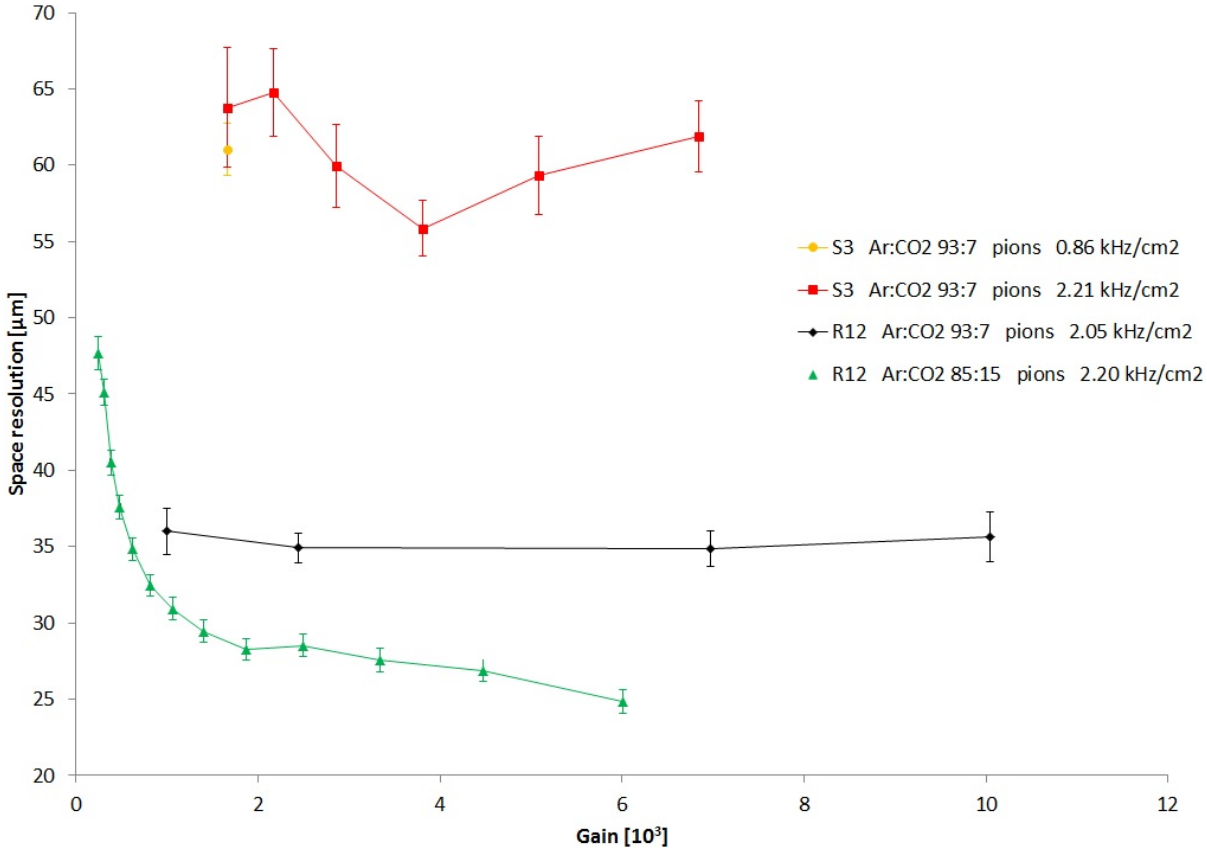

Figure 4.58: Space resolution vs gain.

In order to explain the observed behaviour it is useful to study the size of the charge clusters in the Micromegas. Figure 4.59 displays the average cluster size for all the analyzed test-beam runs, as a function of the effective gain. Runs acquired under like experimental conditions are merged together and events are validated with the same procedure previously used for the space-resolution study, so to enable a direct comparison with Fig. 4.58.

For a given detector and gas mixture, the cluster size increases with the gain. A higher charge amplification in fact results in a larger average number of anode elements on which a signal is induced that exceeds the threshold for data storage. Moreover, the cluster size grows only sub-linearly with the gain and it is expected to level out. In the direction perpendicular to the electric field, the electron cloud from a point-like charge deposition has a Gaussian charge-density distribution, as from Eq. (1.27). The spread is dominated by the transverse diffusion in the conversion region, the amplification gap adding a negligible contribution because of its small thickness. In a non-resistive detector, the number of firing channels hence approaches a value that depends on the transverse diffusion in the drift region, on the thickness of the conversion gap and on the readout pitch.

In a resistive Micromegas, the cluster size is systematically larger than in a non-resistive detector. For example, S3 is here operated in Ar:CO_2 93:7 with a drift field of 0.75 kV/cm. According to the Magboltz simulation reported in Fig. B.3, the corresponding transverse diffusion is 400 µm/cm. The ionization charge liberated at the top of the 0.4 cm thick conversion region therefore reaches the anode with a Gaussian spread whose sigma is about 160 µm. When R12 is operated in the same gas mixture, the electric field is maintained at 0.4 kV/cm, which leads to a transverse diffusion of 320 µm/cm. Again,

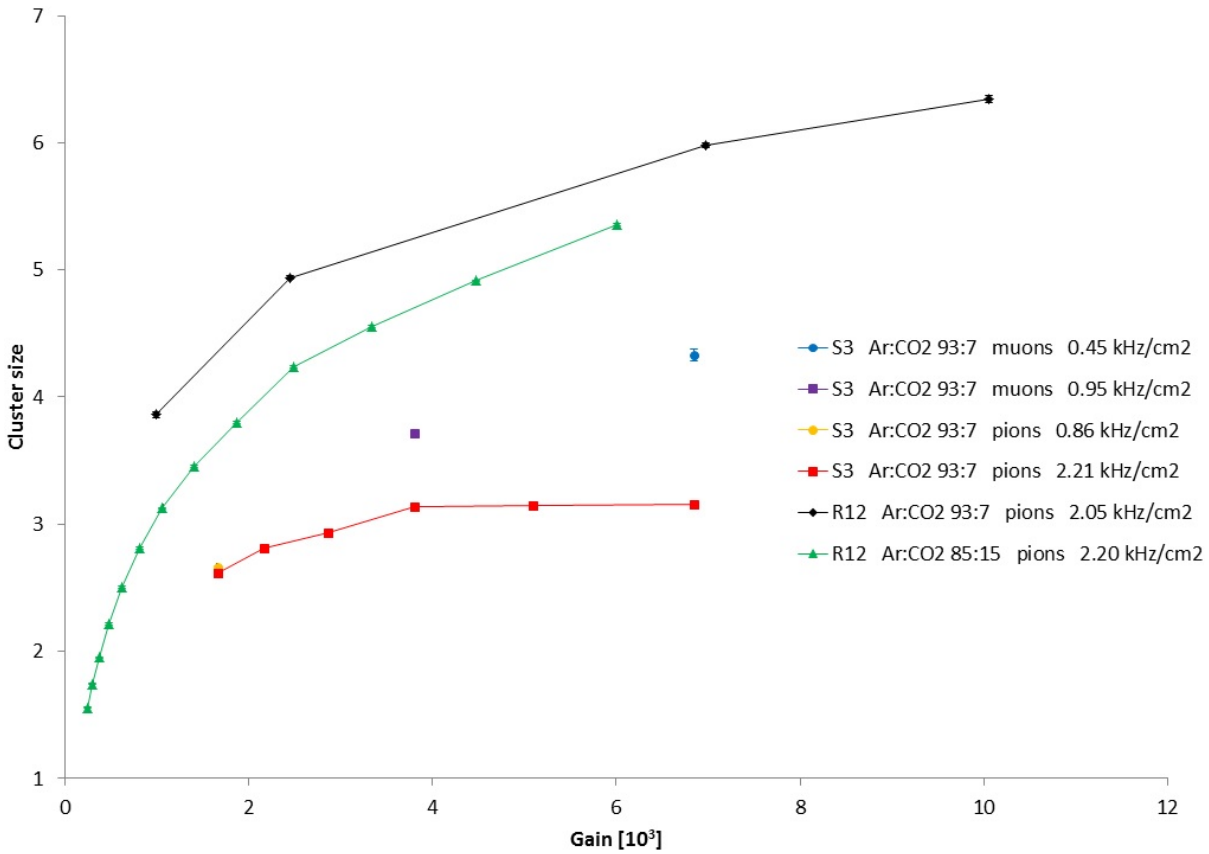

Figure 4.59: Average cluster size vs gain.

the ionization charge produced in the proximity of the cathode reaches the amplification mesh, located at a distance of 0.5 cm, with a Gaussian spread of about 160 µm. Although the specific distribution of charge density will not be the same, one can expect the spread of the electron cloud to be very similar in the two configurations. In spite of this, R12 exhibits a cluster size systematically larger than S3. The observation is explained by taking into account the various capacitive couplings between the resistive traces facing the amplification gap and the readout strips. In fact, although most of the signal on a resistive trace is transferred to the metallic strip right below it, the insulating layer gives rise to non-negligible capacitive couplings to the farther readout strips. The net effect is that of spreading the charge in the direction perpendicular to the strips, hence enlarging the cluster size. Finally, the cluster-size curve for R12 in Ar:CO_2 85:15 is understood to lie below the one for the same chamber in Ar:CO_2 93:7 because of the lower transverse diffusion. The drift field is here kept at 0.6 kV/cm that, according to Fig. B.2, leads to a transverse diffusion of 210 µm/cm.

It is interesting to notice how the average cluster size of S3 decreases when switching from a muon to a pion beam. The reason is the same that provokes the fall of detection efficiency seen in Fig. 4.53. In a non-resistive detector like S3, sparks create a short circuit between the amplification mesh and the grounded anode, with a consequent drop of the mesh potential. The power supply requires some time to recharge the mesh and while doing so the gas gain over all the active area of the Micromegas is negatively affected. Hence, the reduced average cluster size in a pion beam, where the discharge probability is elevated due to hadron-induced reactions that create highly ionizing particles. In the absence of sparks, the cluster-size curve for S3 in a pion beam would overlap the data points of the

muon runs. Instead, it soon stabilizes on a lower value because of the effect of discharges, whose probability grows as the gas gain does. While the amplification mesh is recharging, the chances are high to get clusters with only one firing channel. In such a case, the centre of gravity and the eta algorithm described in Section 4.4.4.8 are of no help for the estimation of the impact point. Moreover, smaller signal amplitudes imply a lower signal-to-noise ratio. Hence the poor space resolution observed in Fig. 4.58. In a similar fashion, this explains the worse space resolution of R12 at effective gas gains below one thousand, even though in this case the limited detection efficiency, the high probability of singleton clusters and the low signal-to-noise ratio are consequences of the insufficient bias voltage rather than of sparks. Otherwise, the resistive Micromegas exhibits a very good space resolution. Discharges do take place, and with the same probability as in a non-resistive detector, but they just change the potential of a few resistive elements, with little or no variation of the mesh voltage. Therefore the amplification field diminishes only locally, in correspondence to the traces reached by the streamer, while the rest of the active area remains unaffected.

4.5 Conclusions

During the second long LHC shutdown, currently scheduled for 2018, the ATLAS experiment will install a new pair of Small Wheels, replacing the present ones. The upgrade is meant to overcome the limited rate capability of the MDTs ($\simeq$ 150 Hz/cm^2) and of the CSCs ($\simeq$ 1 kHz/cm^2) that currently compose the innermost station of the end-cap tracking system, in order to cope with the increased particle fluxes ($\lesssim$ 16 kHz/cm^2) expected in the HL-LHC era. The intervention is also intended to substantially enhance the level-1 trigger by suppressing fake high-p_T ($\geq$ 20 GeV) muons, thanks to Small Wheels capable of providing a direction vector for the detected tracks. Additional requirements for the new chambers include a detection efficiency for minimum ionizing particles of more than 98% per plane, trigger capability, good resistance to radiation and good aging properties.

All these requisites can be satisfied with Micromegas. In 2007, the MAMMA collaboration was born with the aim of developing tracking chambers for the new Small Wheels based on the Micromegas technology. The main bottleneck is identified in the elevated discharge probability in the ATLAS environment. The research work presented in this chapter investigates different techniques to make Micromegas spark-tolerant and enable their employment in the new Small Wheels.

A possible approach is that of limiting the onset of streamers by extending the dynamic range of ionization charge in which the detector can be operated with a low discharge probability, to include the interactions of highly ionizing particles. Specifically, this is done by distributing the total gas gain necessary to achieve the requested MIP detection efficiency over more than one amplification stage, thus spreading the charge and lowering its density in the multiplication region. The idea was probed with a 10×10 cm^2 test chamber, in which a preamplification GEM can optionally be fitted in between the Micromegas mesh and the drift electrode. A reduction of the discharge probability of more than an order of magnitude is secured at a total effective gain of 10^3, with the spark suppression becoming more efficient at higher gains.

This is not sufficient to guarantee safe operation in the ATLAS environment. Moreover, the approach has other weaknesses that become apparent when moving to large areas. The preamplification GEM has to be stretched and glued to its frame, and spacing elements have to be included in the gas volume to support the foil. Stretch-free and/or spacer-free GEMs may be exploited instead, but such technologies are still in a early stage of development. The increased mechanical complexity has a negative impact on the manpower cost and the assembly time that cannot be neglected in the construction phase. Finally, additional services have to be accounted for when considering integration into the ATLAS experiment.

If a single-amplification-stage configuration has to be used, the discharge probability will be higher. However, the detector can still be safely operated if a method is found to mitigate the undesired effects of streamers, and especially the dead time. With resistive Micromegas, one does not seek to lower the discharge probability, which is the same as in a non-resistive chamber. The Micromegas layout is instead modified in order to limit the current flowing to ground in case of a spark, with the purpose of quenching the streamer. This is accomplished by decoupling the readout strips from the gas volume with a thin insulating sheet, on top of which resistive traces are printed, matching the readout pattern and grounded through a high-value resistor. Sparks only result in a transient decrease of the potential of a few resistive traces, with a consequent local reduction of the amplification field, while limiting or altogether averting voltage drops on the amplification mesh. The employment of high-value grounding resistors ensures high DC impedance to ground for efficient streamer quenching and at the same time enables the use of a low surface resistance over the active area for high-rate capability. Dead time is drastically reduced and the detection efficiency remains above 98% over a broad gain window ranging up to effective amplification factors of about 10^4. Furthermore, the space resolution is significantly improved with respect to non-resistive chambers, reaching $24.9 \pm 0.8\,\mu m$ in Ar:CO_2 85:15 with a strip pitch of $250\,\mu m$.

Following the research work presented in this thesis, the R&D activity of the MAMMA collaboration has progressed further and several other resistive detectors have been made. To date, the largest chamber has an active area of about $2.2 \times 1\,m^2$. In 2012, the resistive Micromegas technology has been selected for the realization of the primary tracking detectors of the ATLAS new Small Wheels, complemented by sTGCs as the primary trigger chambers.

APPENDIX A

Drift velocity

Drift velocity of electrons as a function of the electric-field strength for the gas mixtures used in this thesis. The data are from Magboltz version 7.07, while the plots are rendered with Garfield version 7.43.

The mobility of an electron depends on its kinetic energy and therefore on the applied electric field. The electron mobility exhibits maxima and minima due to the Ramsauer-Townsend effect, a quantum-mechanical interference phenomenon that comes into play when the electron wavelength, $\lambda = h/p$, approaches molecular dimensions. This is reflected in the drift velocity of electrons which, as opposed to that of positive and negative ions, does not increase linearly with the field. In a mixture of argon and carbon dioxide, the drift velocity decreases for higher concentrations of the noble gas.

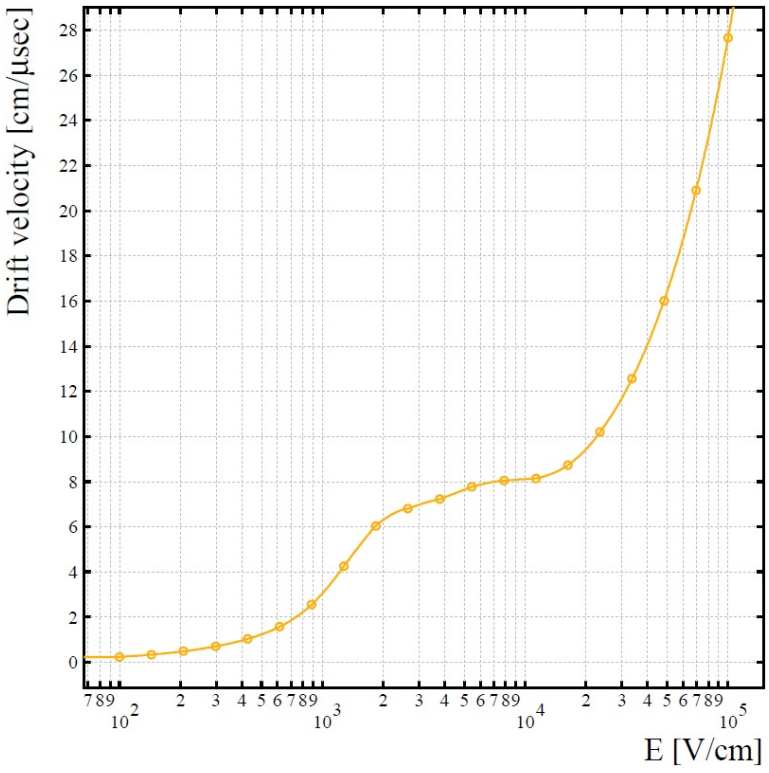

Figure A.1: Drift velocity of electrons in Ar:CO_2 70:30.

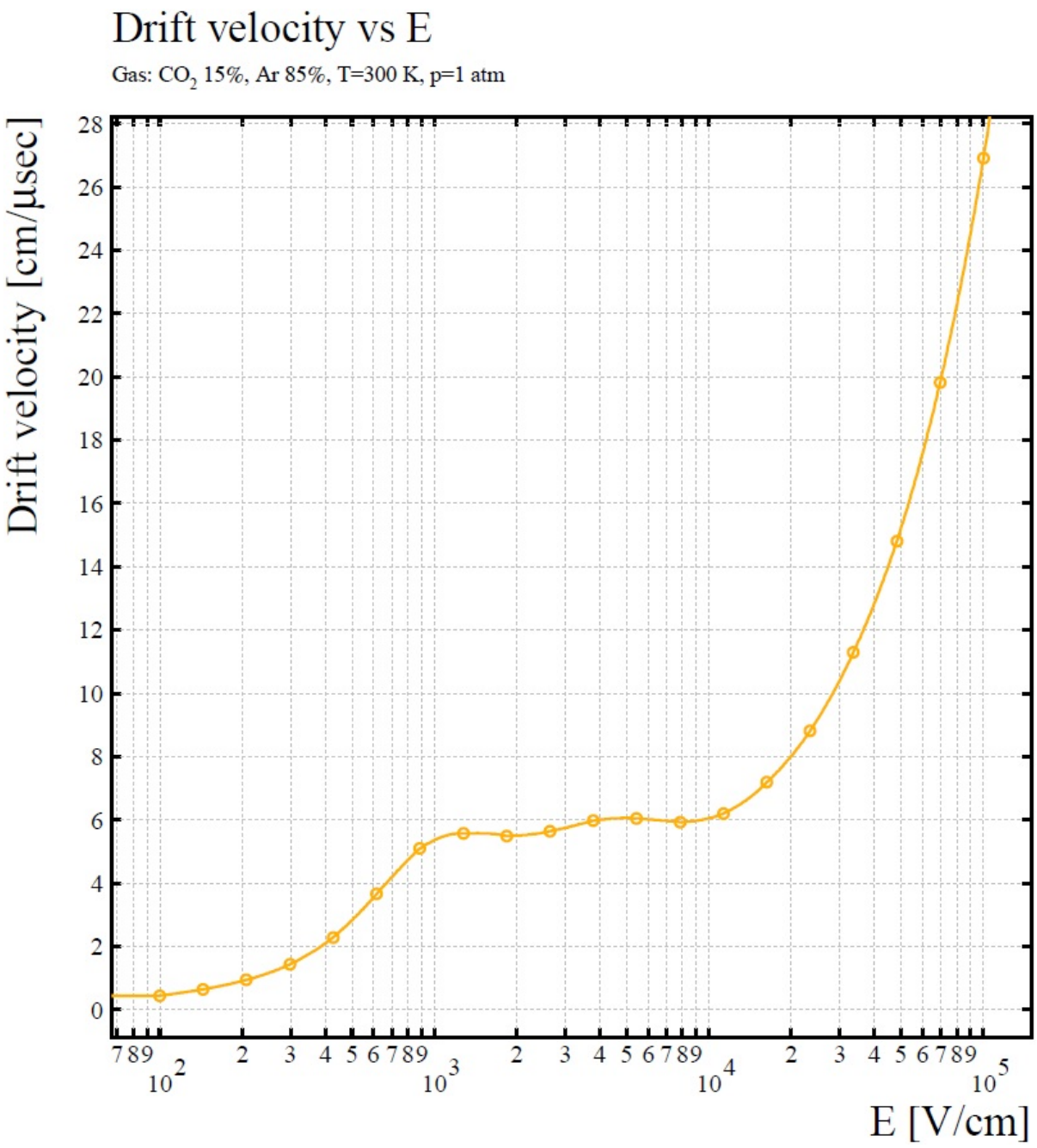

Figure A.2: Drift velocity of electrons in Ar:CO_2 85:15.

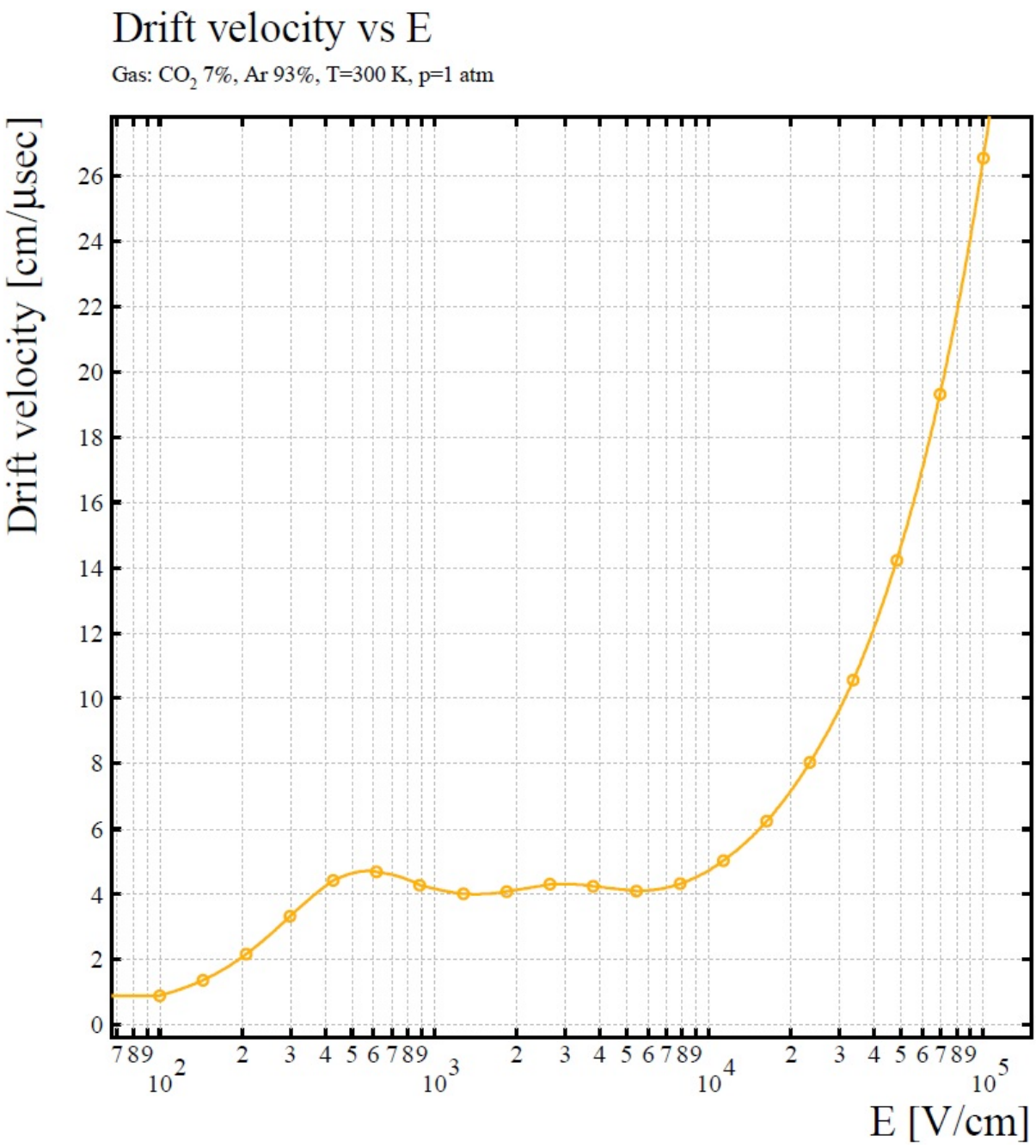

Figure A.3: Drift velocity of electrons in Ar:CO_2 93:7.

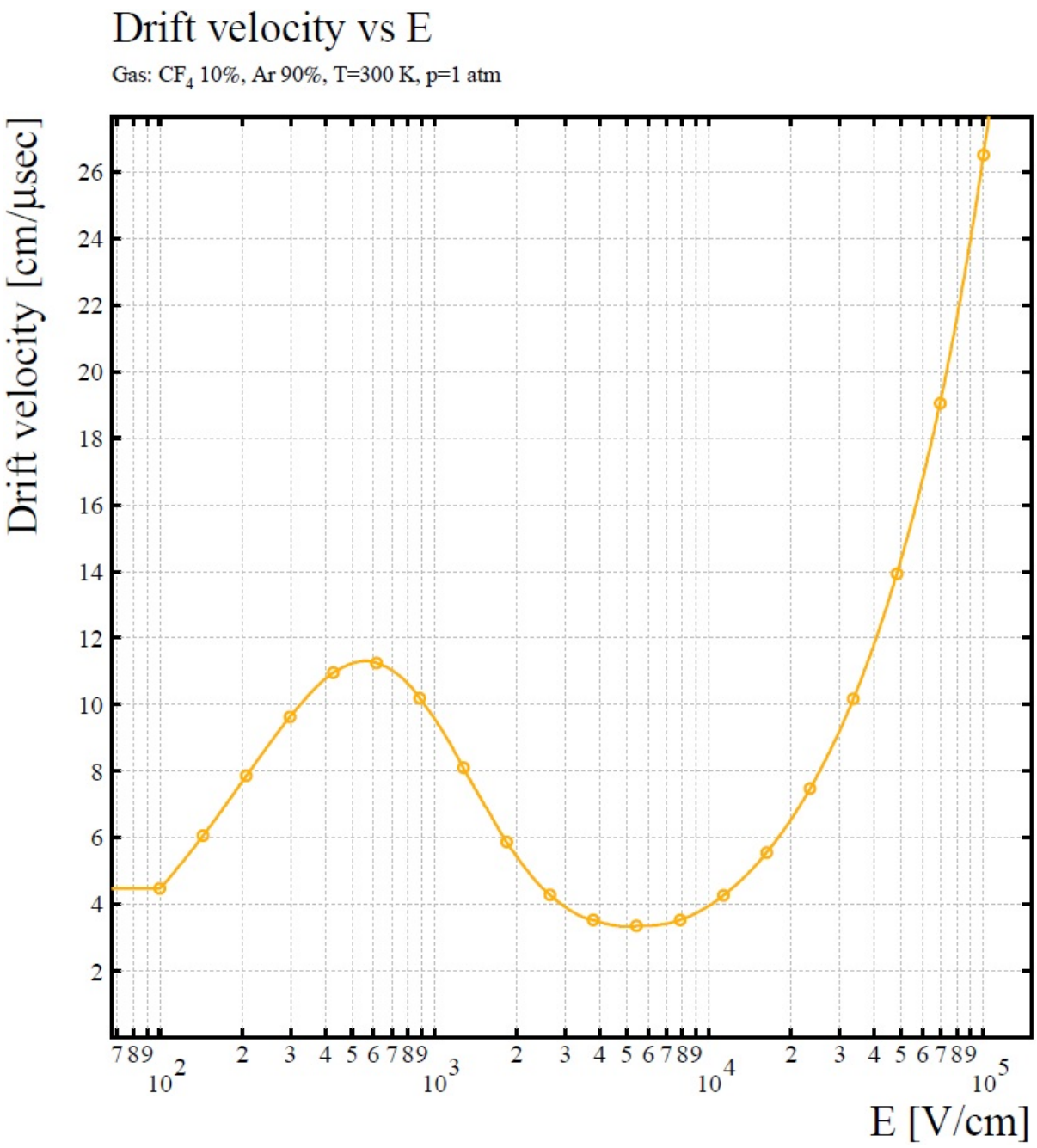

Figure A.4: Drift velocity of electrons in Ar:CF_4 90:10.

APPENDIX **B**

Longitudinal and transverse diffusion

Longitudinal diffusion (in yellow) and transverse diffusion (in green) of electrons as a function of the electric-field strength for the gas mixtures used in this thesis. The data are from Magboltz version 7.07, while the plots are rendered with Garfield version 7.43.

In a mixture of argon and carbon dioxide, both the longitudinal and the transverse diffusion increase for higher concentrations of the noble gas. CF_4 has a low longitudinal-diffusion coefficient and therefore it is usually employed when a good time resolution is required.

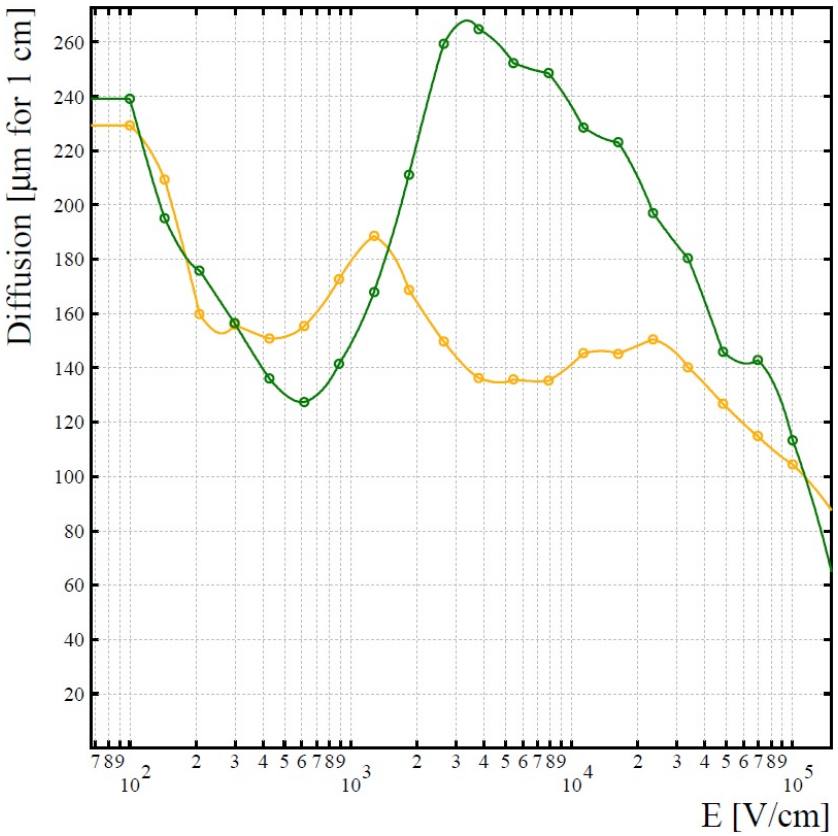

Figure B.1: Longitudinal and transverse diffusion of electrons in Ar:CO_2 70:30.

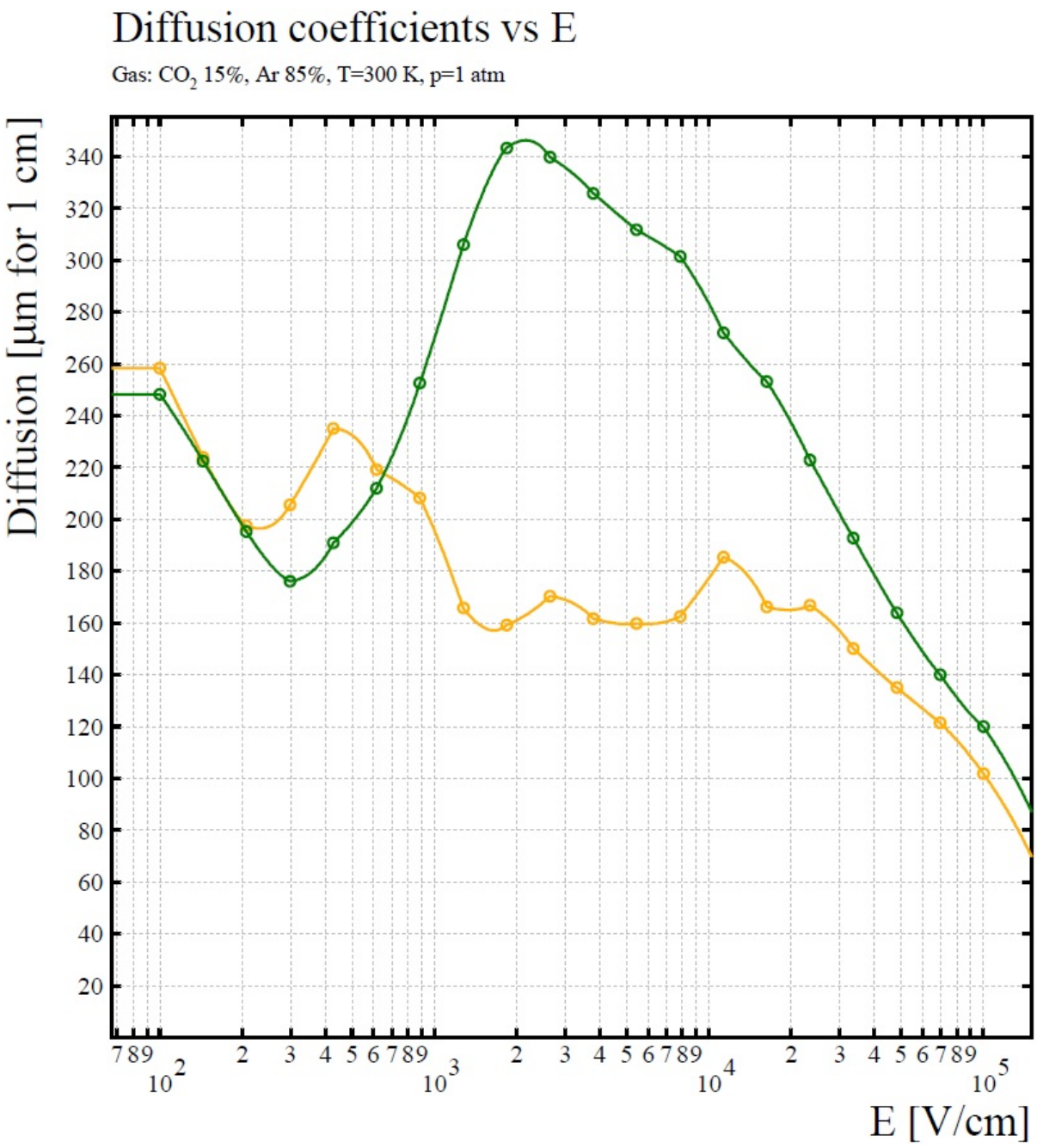

Figure B.2: Longitudinal and transverse diffusion of electrons in Ar:CO_2 85:15.

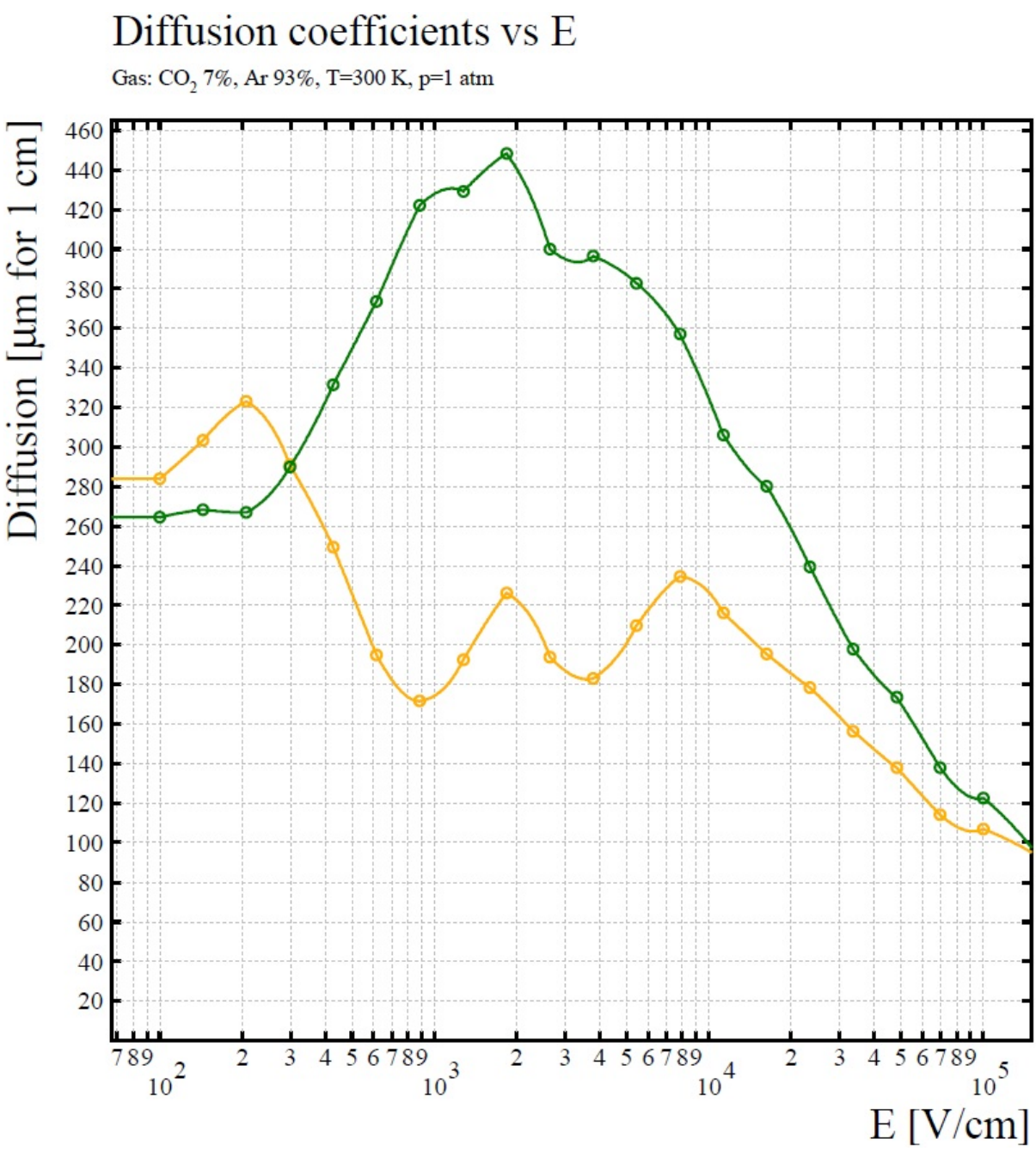

Figure B.3: Longitudinal and transverse diffusion of electrons in Ar:CO_2 93:7.

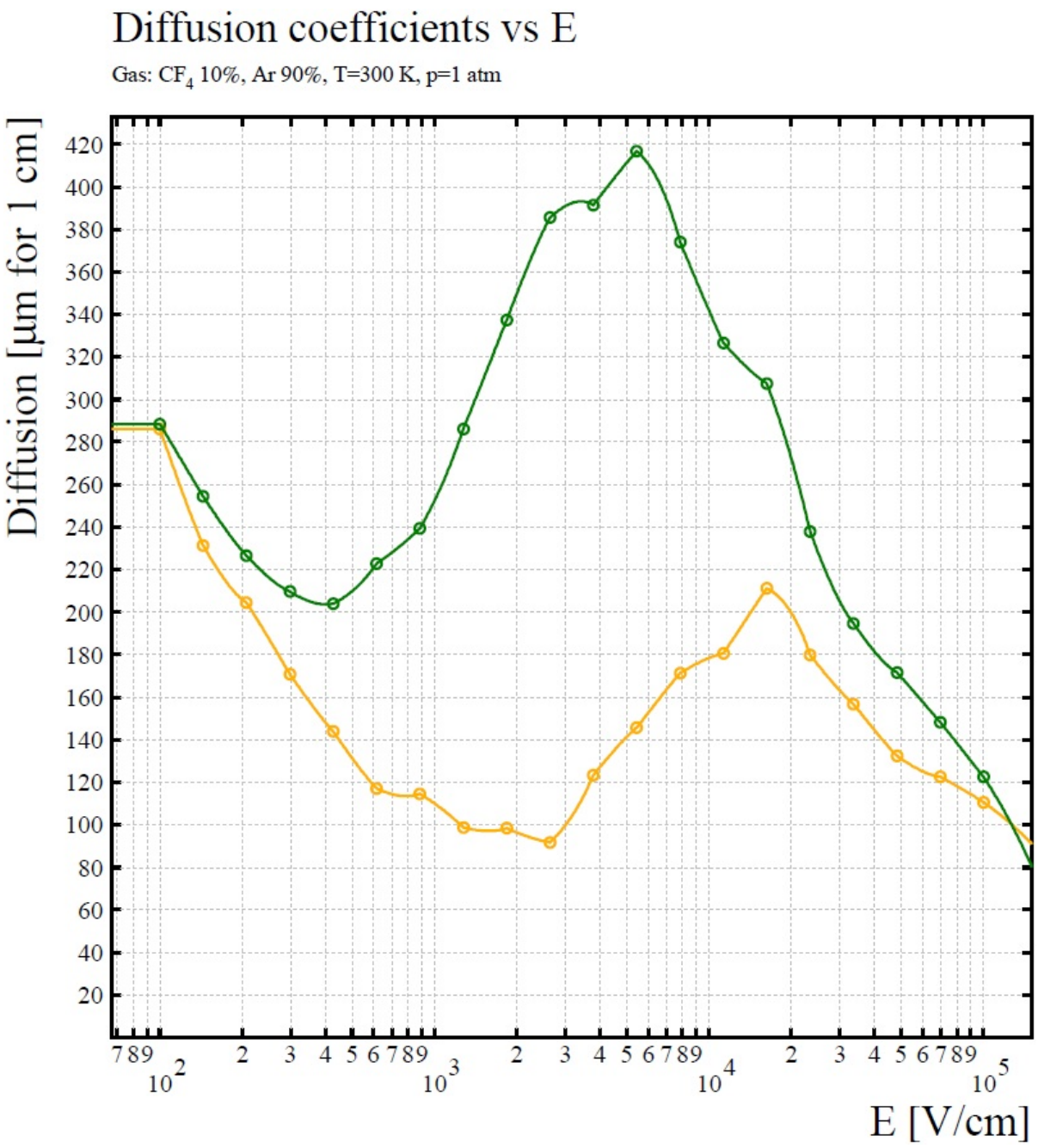

Figure B.4: Longitudinal and transverse diffusion of electrons in Ar:CF_4 90:10.

APPENDIX C

First Townsend and attachment coefficient

First Townsend coefficient (in yellow) and attachment coefficient (in green) as a function of the electric-field strength for the gas mixtures used in this thesis. The data are from Magboltz version 7.07, while the plots are rendered with Garfield version 7.43.

In a mixture of argon and carbon dioxide, the first Townsend coefficient increases for higher concentrations of the noble gas.

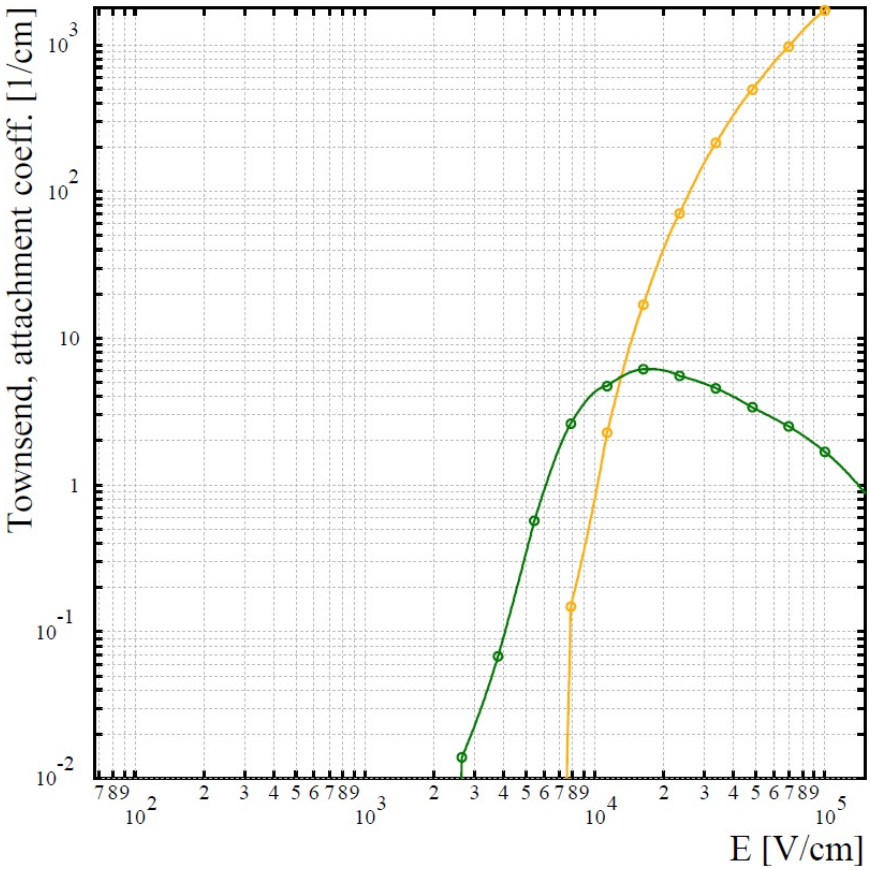

Figure C.1: First Townsend and attachment coefficient in Ar:CO_2 70:30.

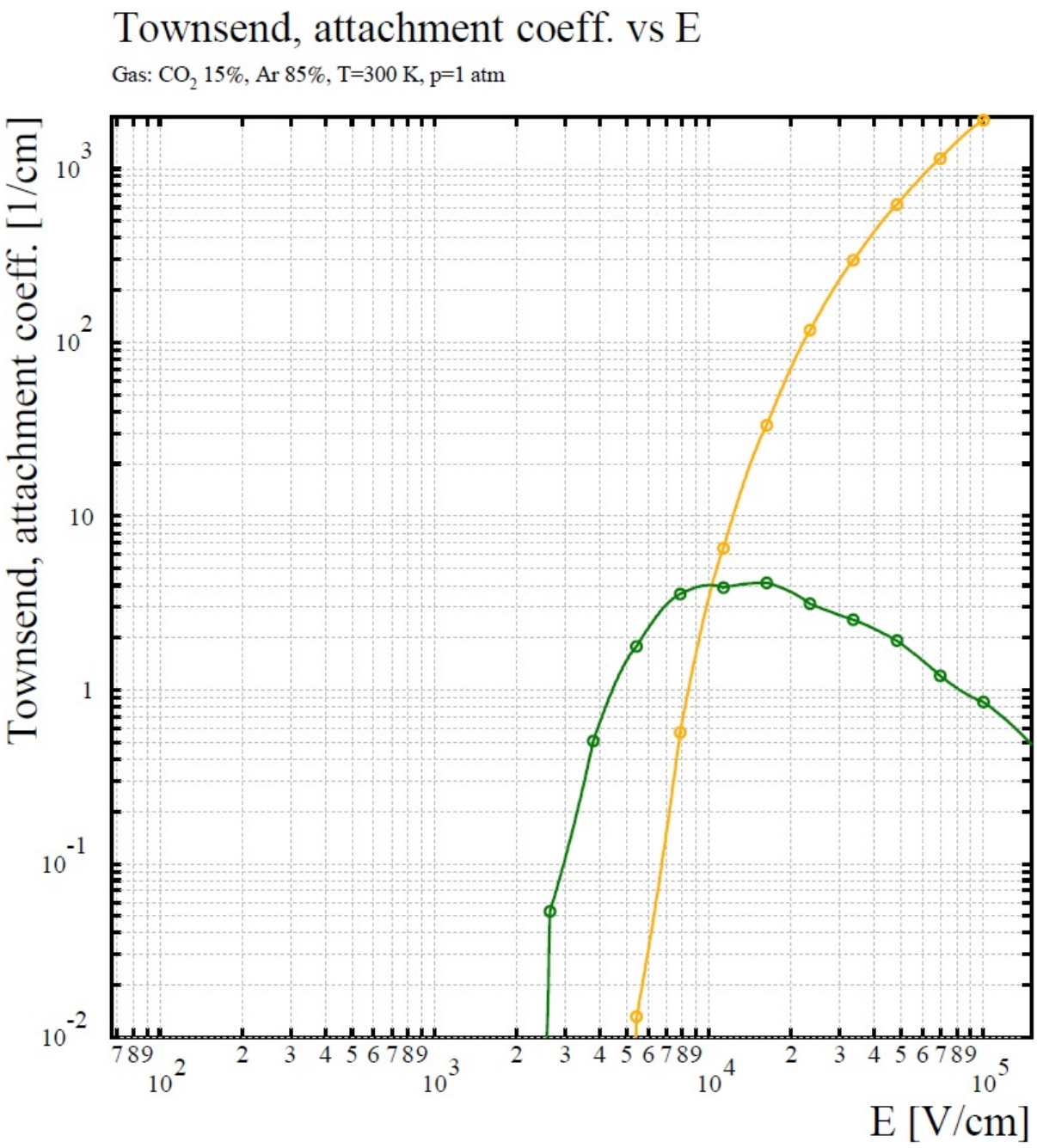

Figure C.2: First Townsend and attachment coefficient in Ar:CO_2 85:15.

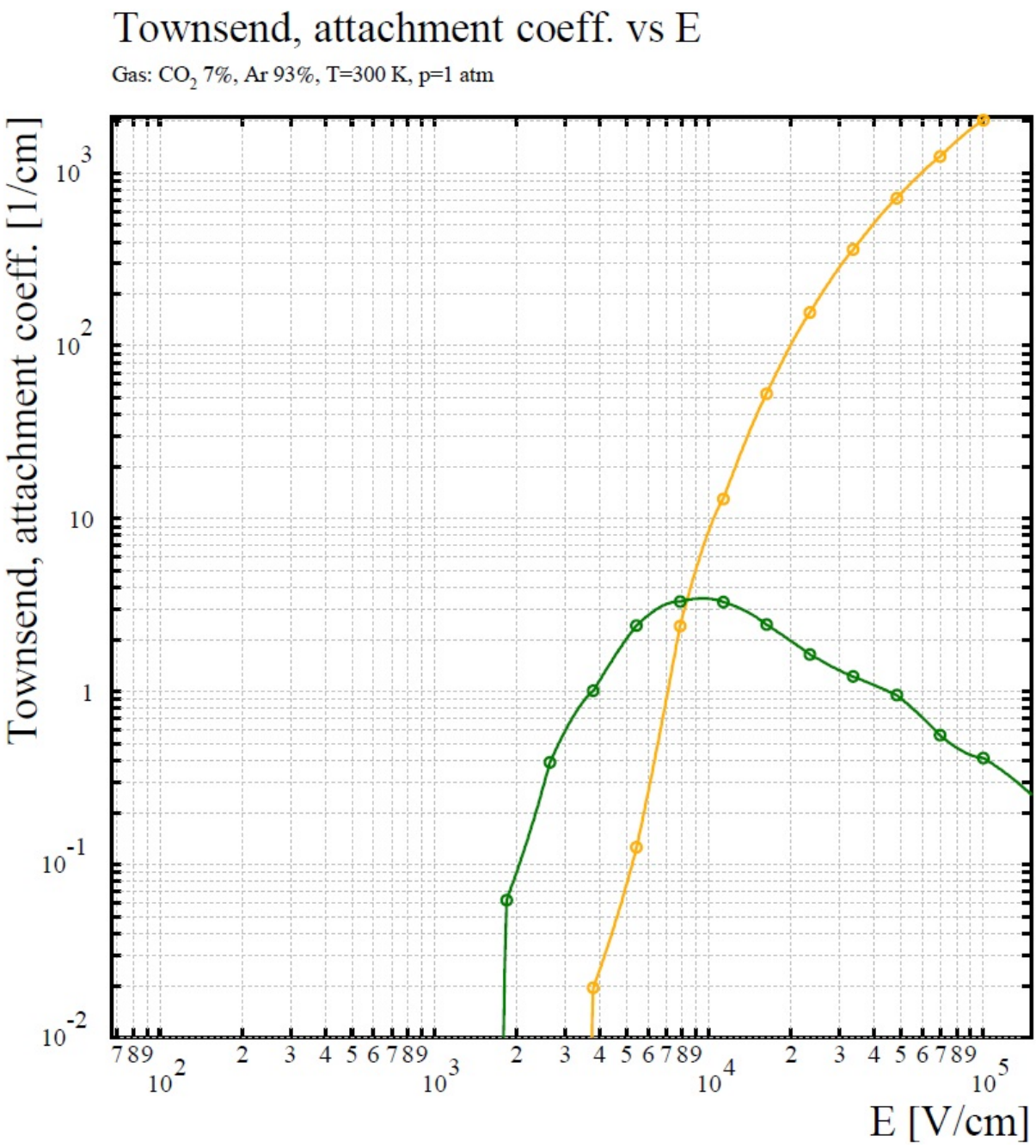

Figure C.3: First Townsend and attachment coefficient in Ar:CO_2 93:7.

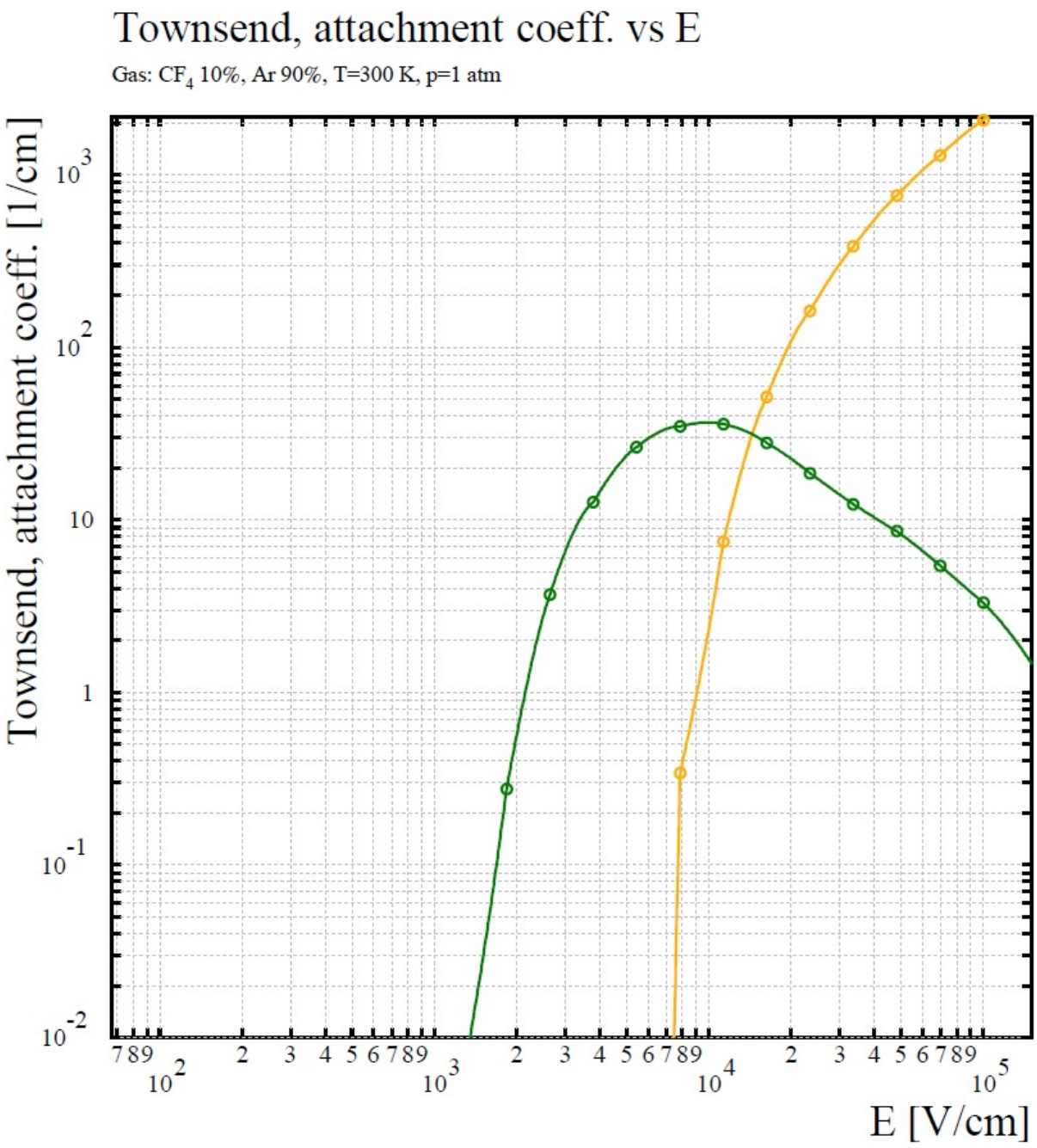

Figure C.4: First Townsend and attachment coefficient in Ar:CF_4 90:10.

APPENDIX D

Electron energy

Energy distribution of electrons in Ar:CO_2 70:30 for electric-field strengths from 1 to 100 kV/cm in 10 logarithmically spaced steps. The data are from Magboltz version 7.07, while the plots are rendered with Garfield version 7.43.

The distributions are used in this thesis to select the maximum kinetic energy that electrons are allowed to reach in the microscopic-tracking Monte Carlo algorithm described in Section 3.3.3.

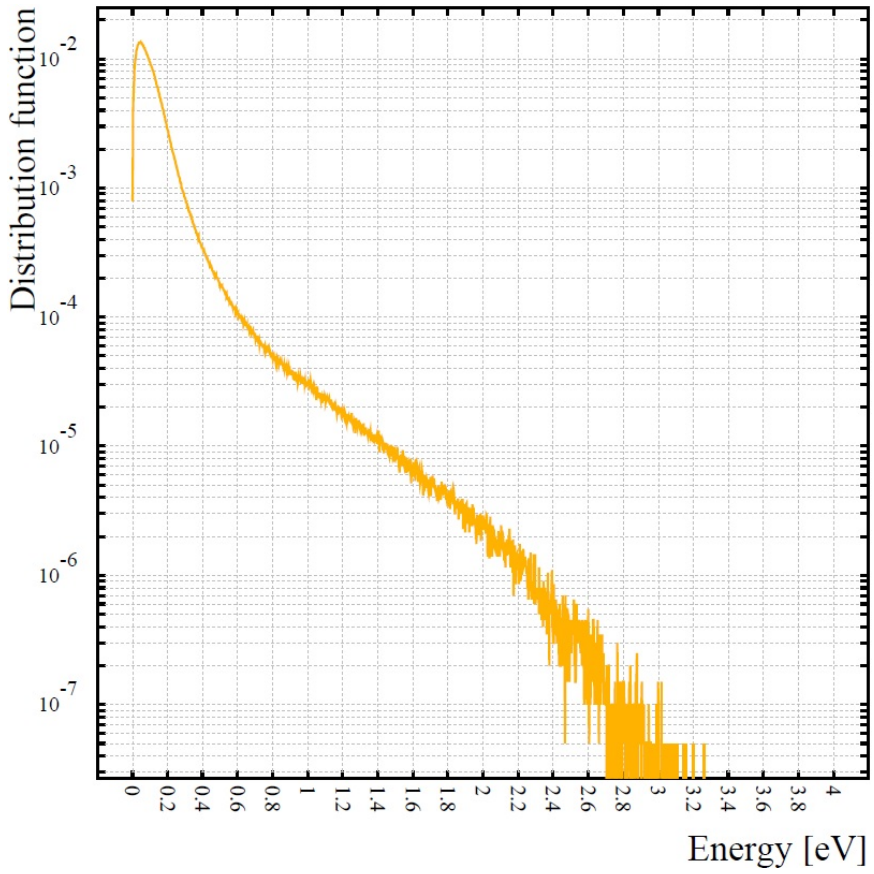

Figure D.1: Energy distribution of electrons in Ar:CO_2 70:30 at 10^3 V/cm.

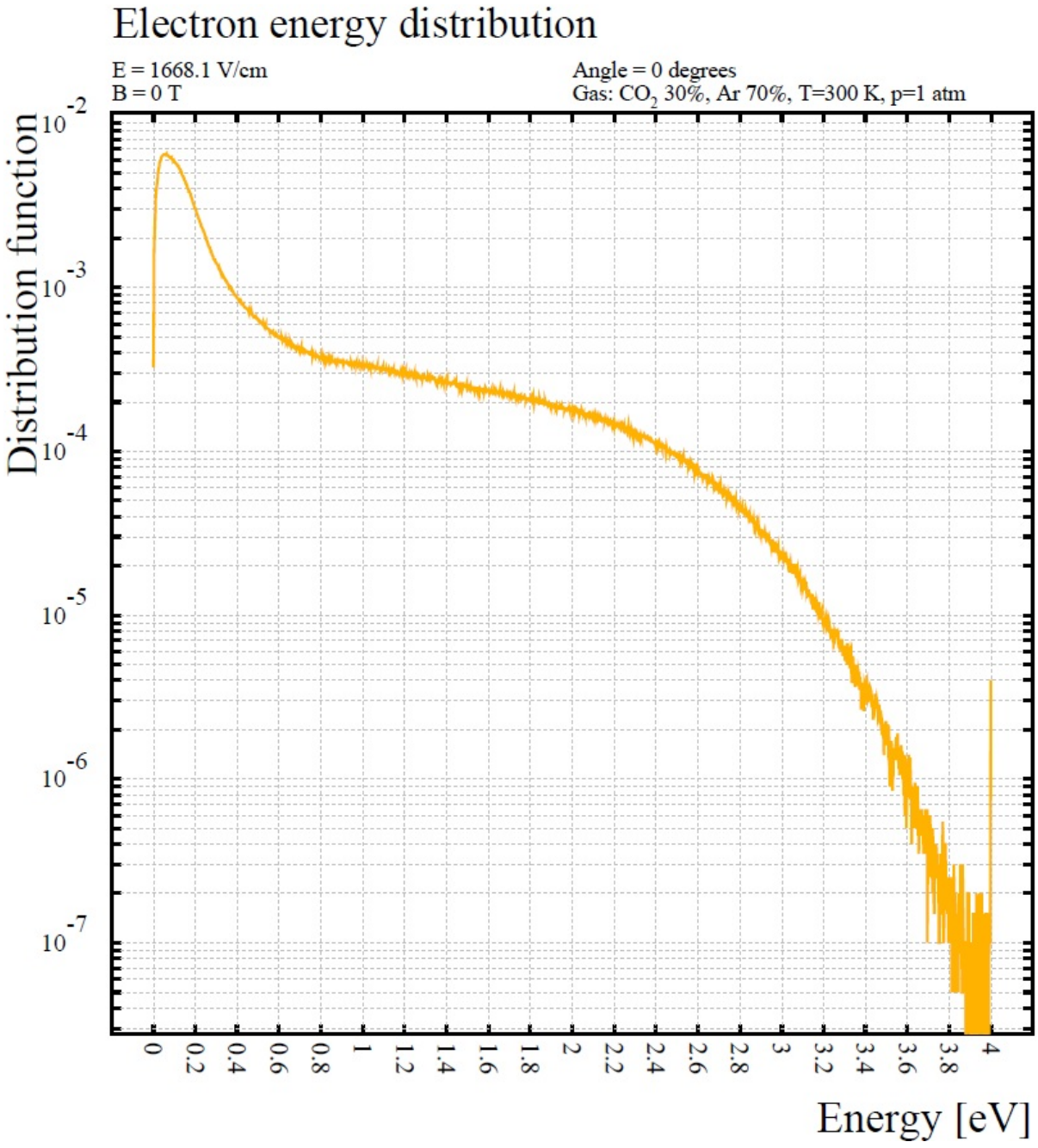

Figure D.2: Energy distribution of electrons in Ar:CO_2 70:30 at 1.67×10^3 V/cm.

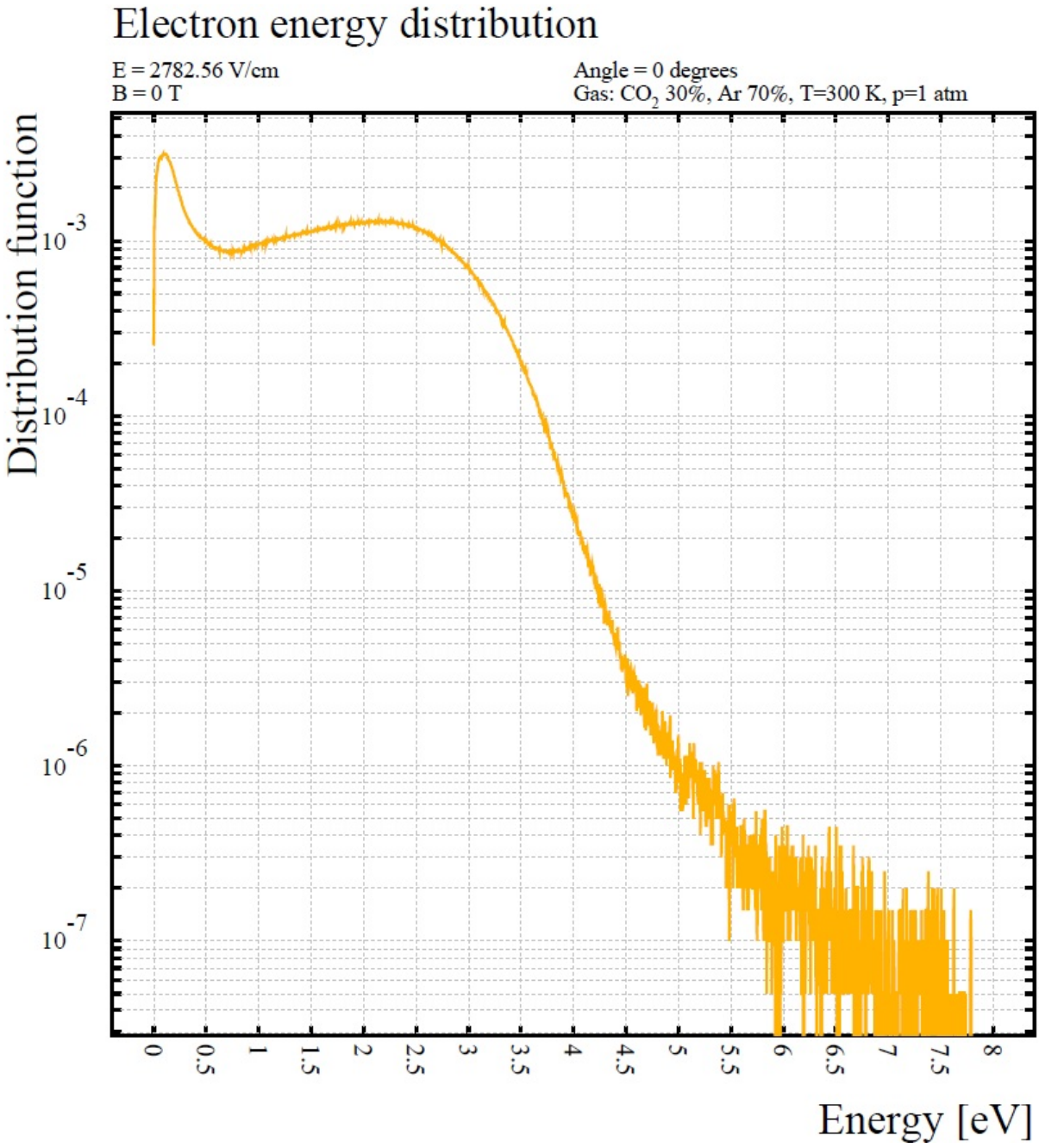

Figure D.3: Energy distribution of electrons in Ar:CO_2 70:30 at 2.78×10^3 V/cm.

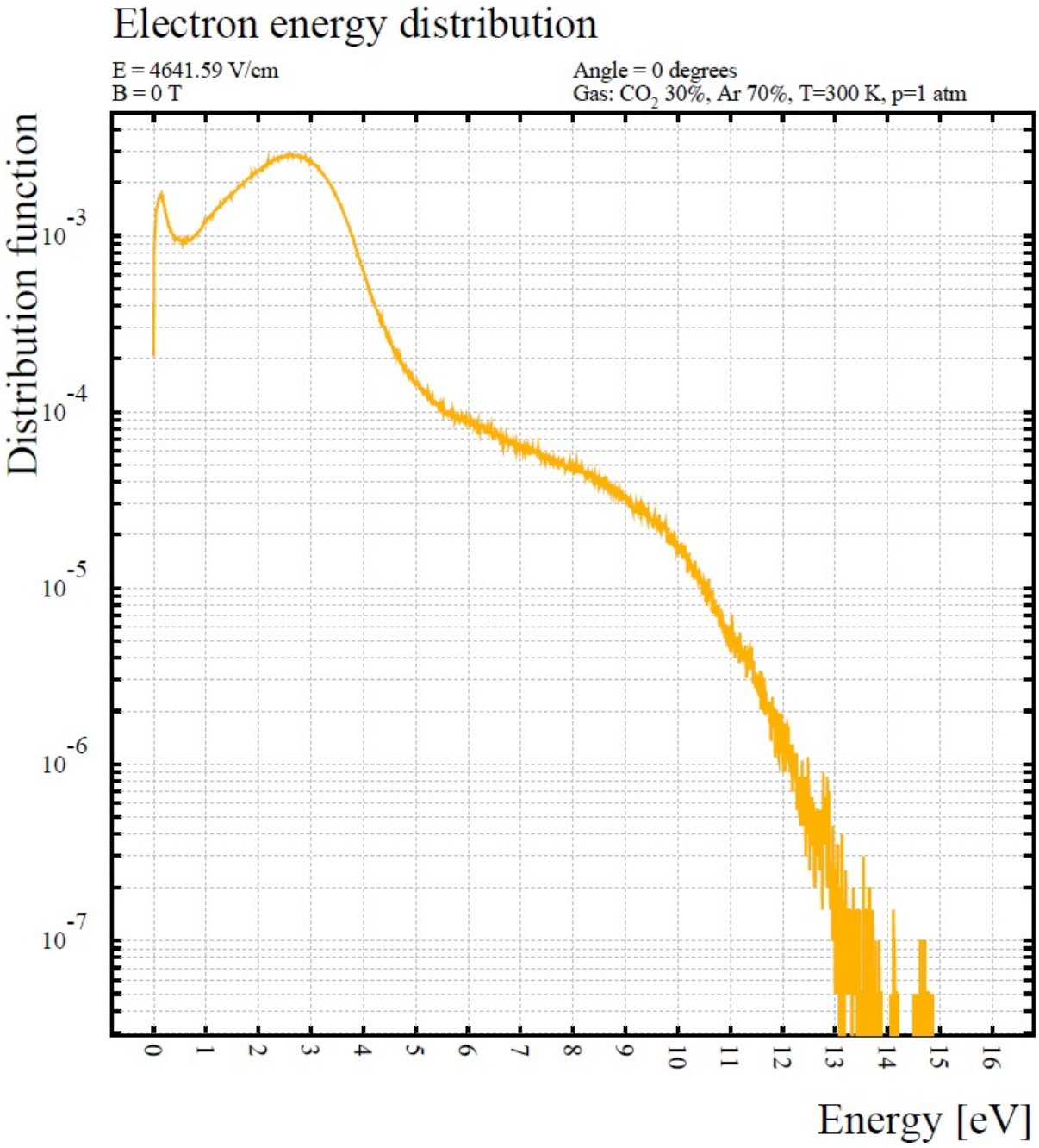

Figure D.4: Energy distribution of electrons in Ar:CO_2 70:30 at 4.64×10^3 V/cm.

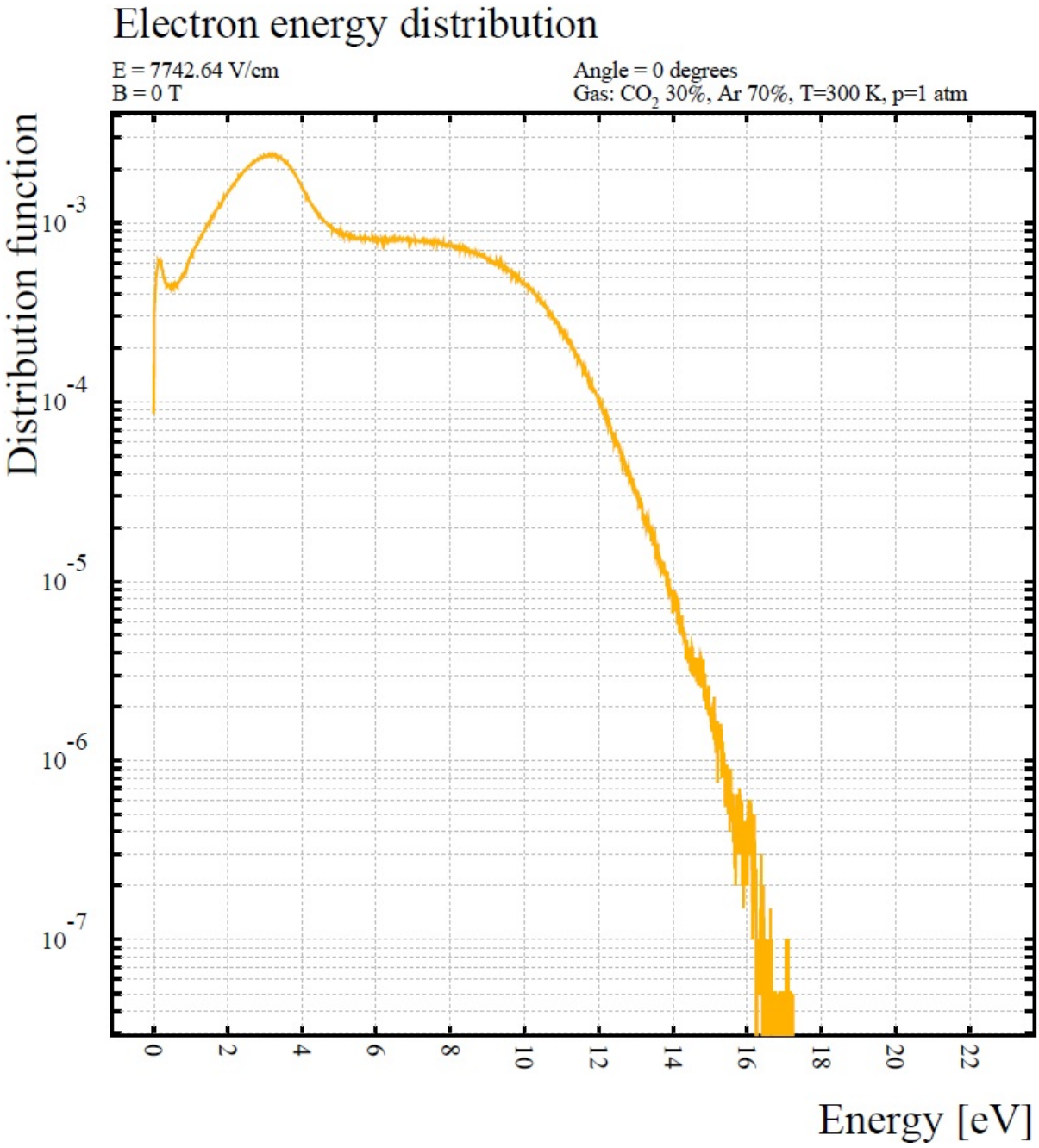

Figure D.5: Energy distribution of electrons in Ar:CO_2 70:30 at 7.74×10^3 V/cm.

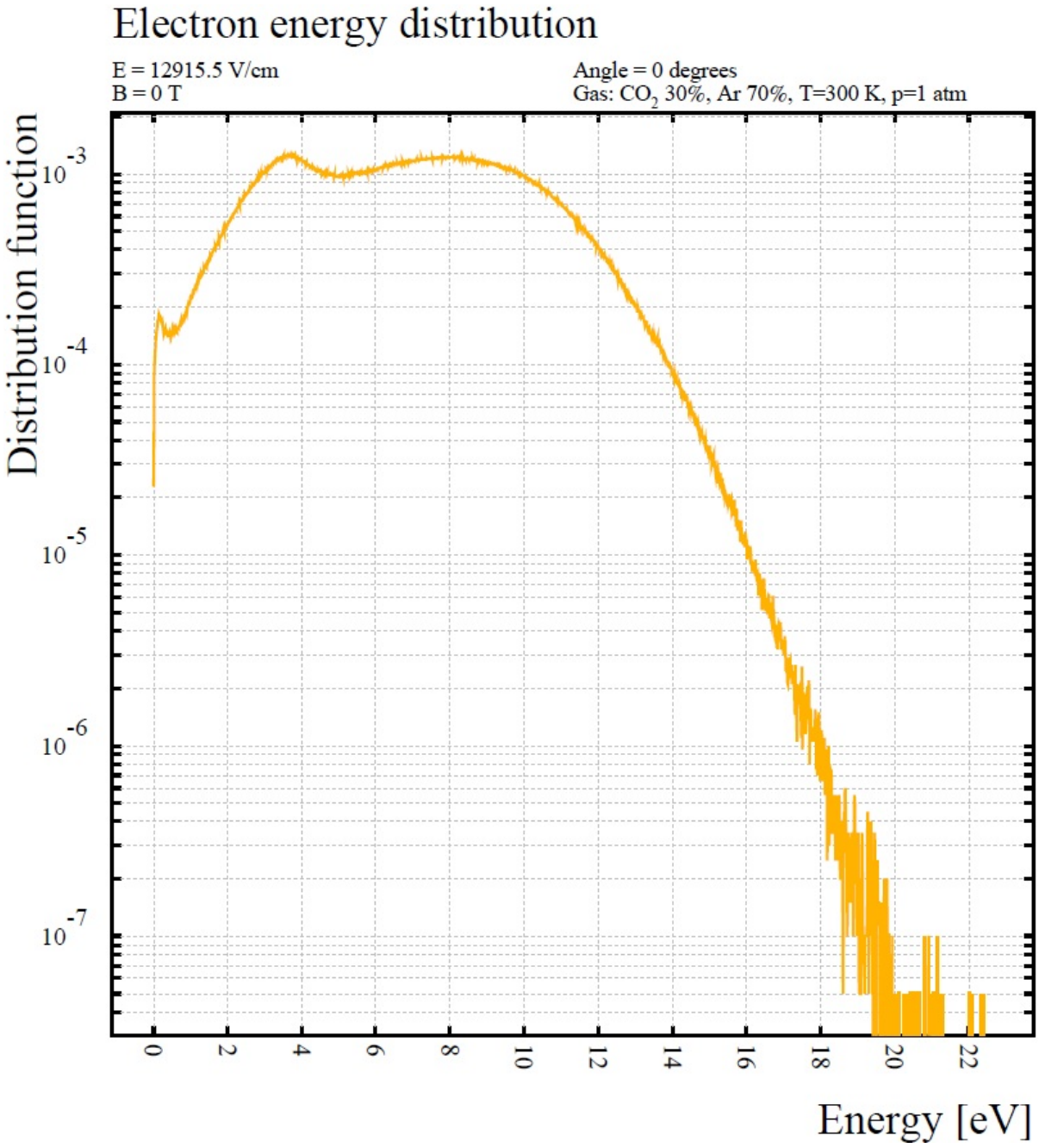

Figure D.6: Energy distribution of electrons in Ar:CO_2 70:30 at 1.29×10^4 V/cm.

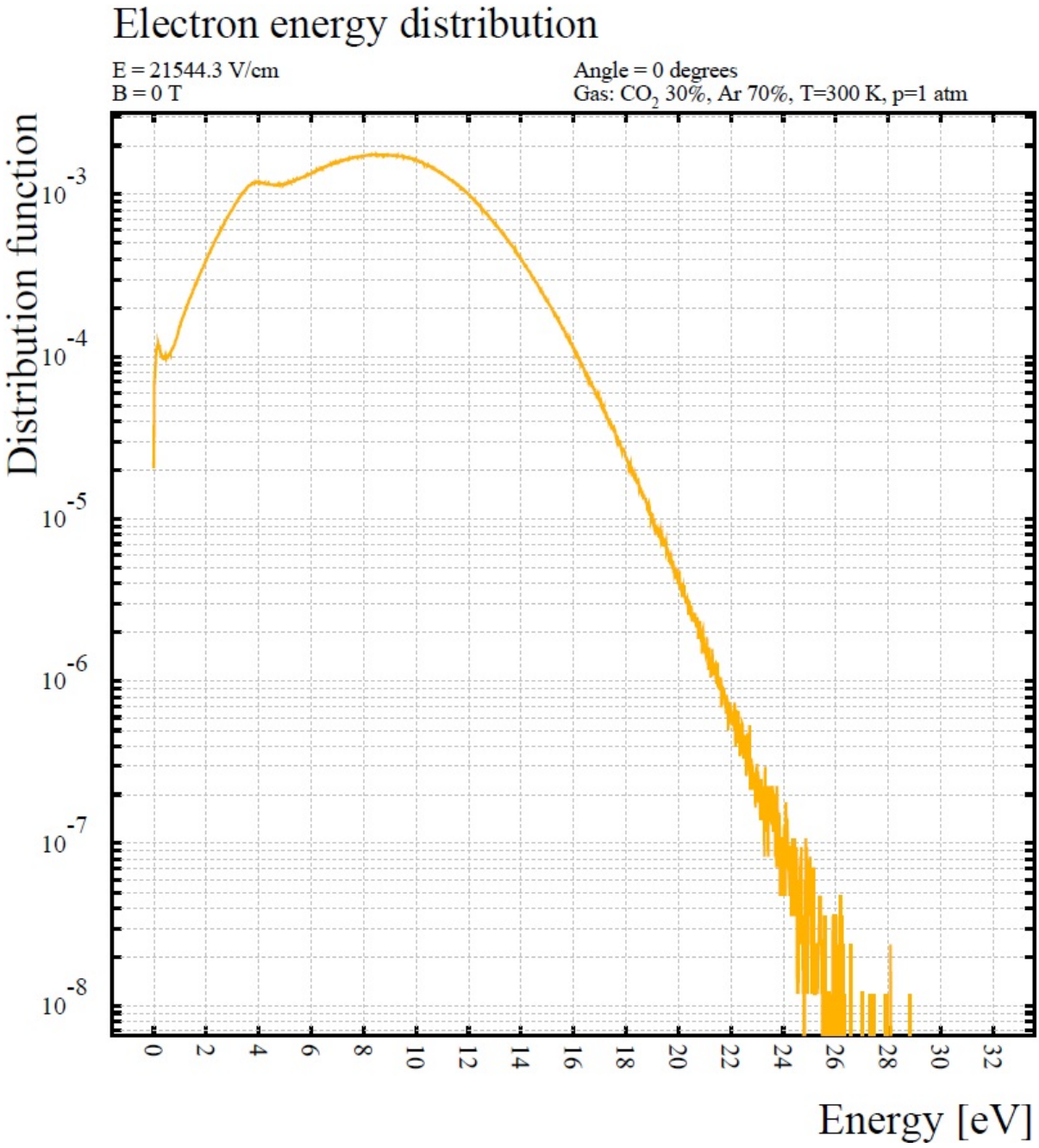

Figure D.7: Energy distribution of electrons in Ar:CO_2 70:30 at 2.15×10^4 V/cm.

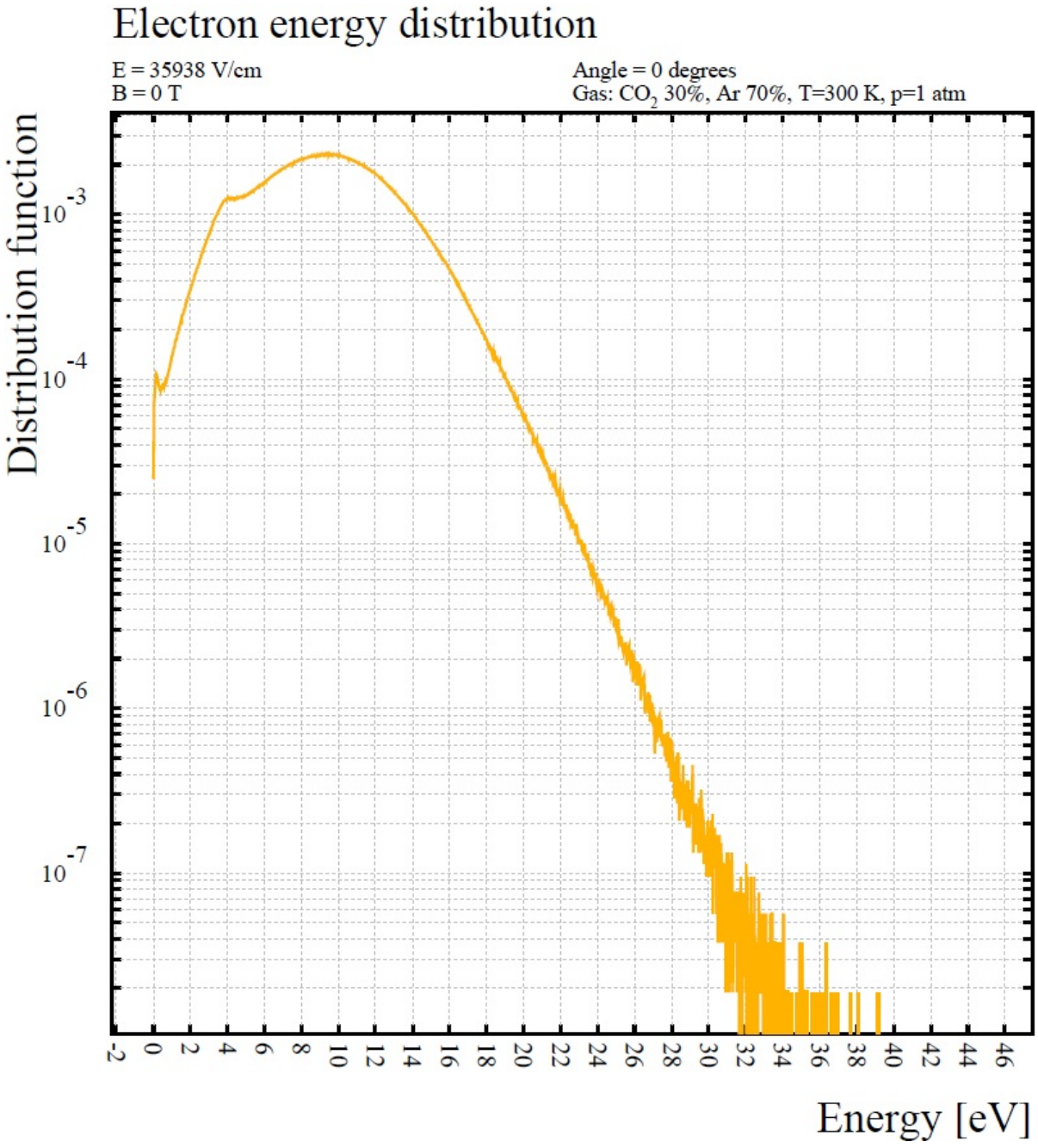

Figure D.8: Energy distribution of electrons in Ar:CO_2 70:30 at 3.59×10^4 V/cm.

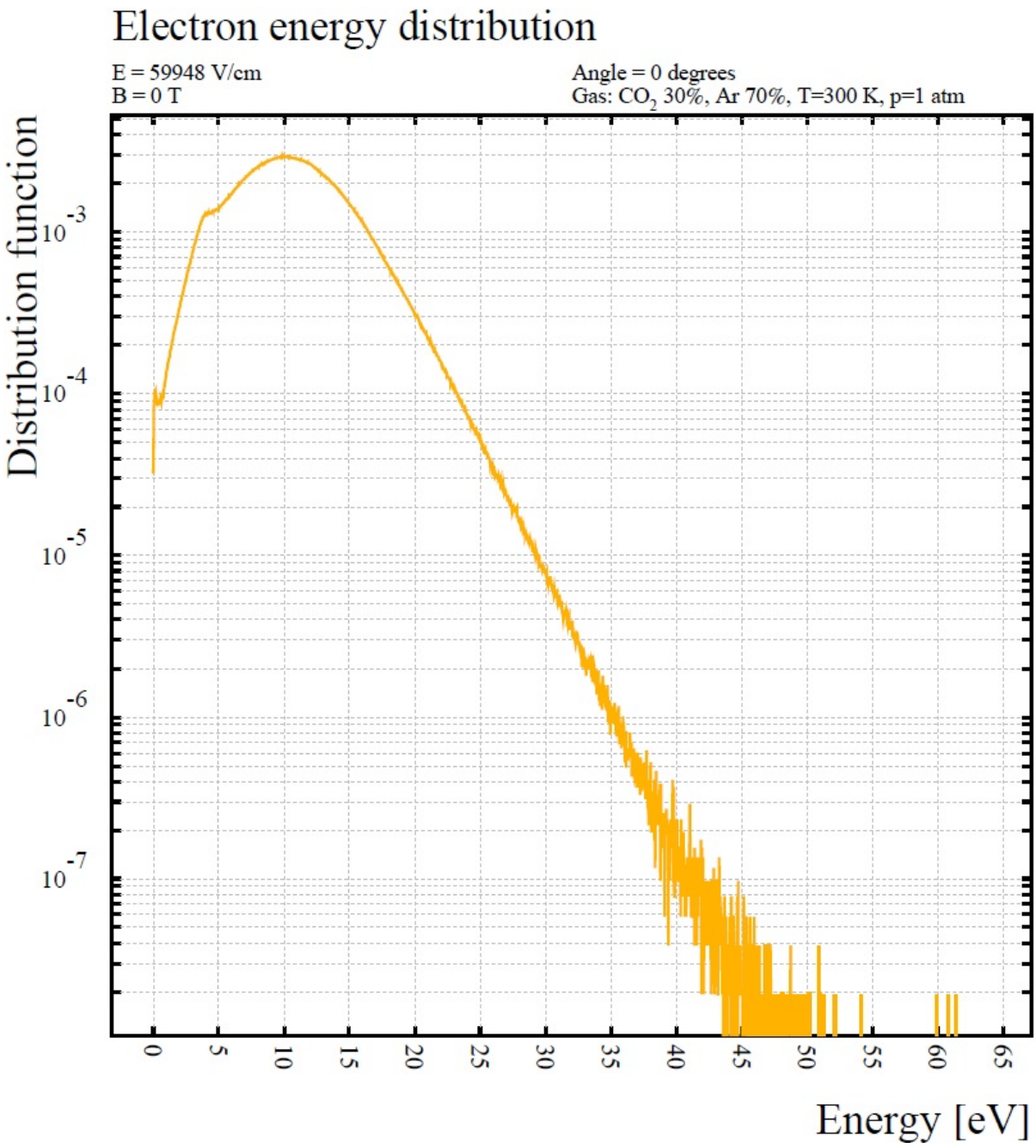

Figure D.9: Energy distribution of electrons in Ar:CO_2 70:30 at 5.99×10^4 V/cm.

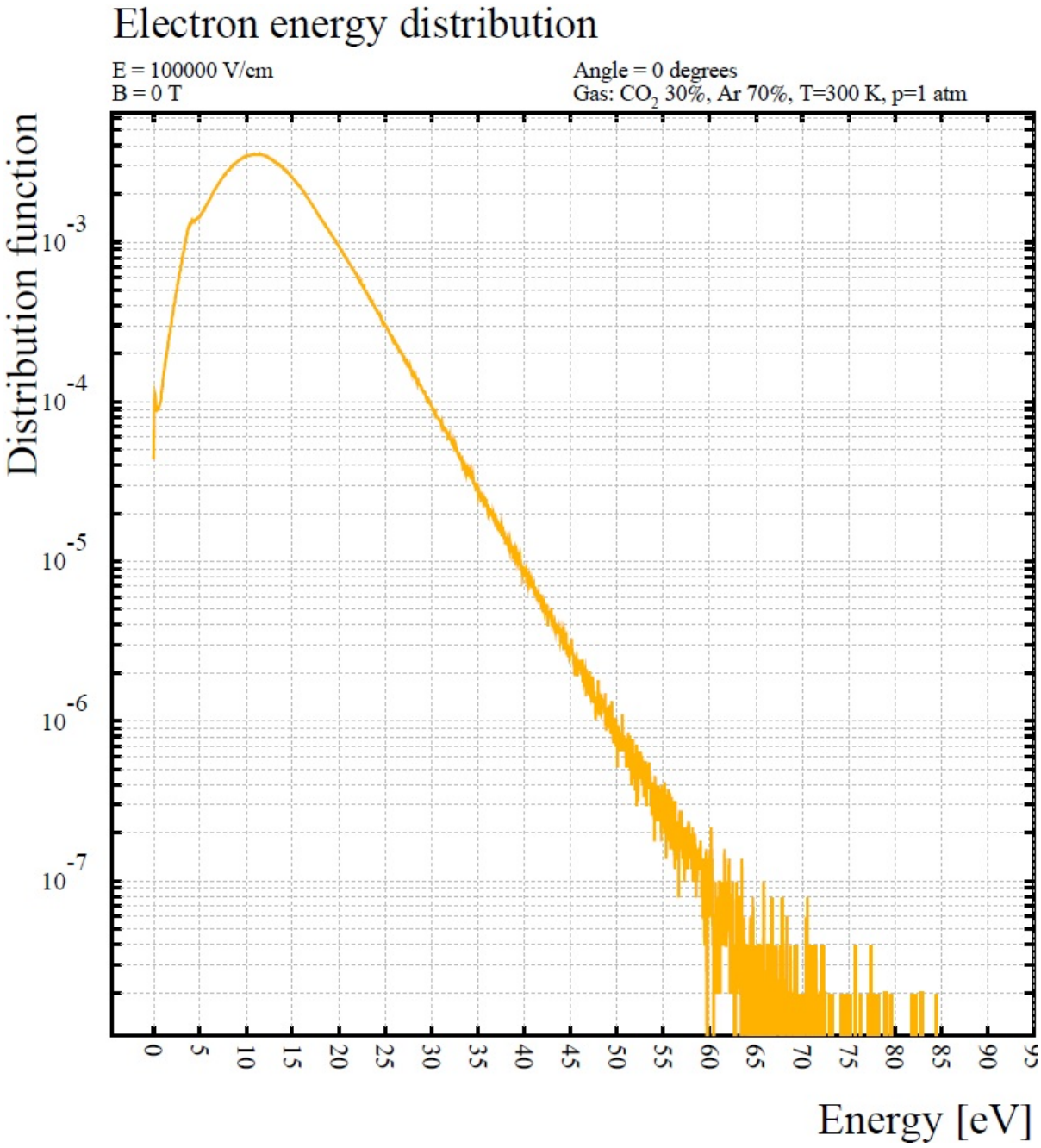

Figure D.10: Energy distribution of electrons in Ar:CO_2 70:30 at 10^5 V/cm.

APPENDIX E

Field simulation

Left frame: equipotential lines (in green) and field lines (in yellow) on the axial plane of a single-mask conical GEM for different hole geometries. Right frame: corresponding electric-field strength along the axis. The polyimide thickness is 50 µm, the copper thickness is 5 µm, the gas mixture is Ar:CO_2 70:30, the drift and induction fields are 3 kV/cm and the difference of potential across the GEM is 400 V. The field map is generated with ANSYS version 13.0, the gas data are from Magboltz version 7.07, while the plots are rendered with Garfield version 7.43.

The sharp discontinuities in the right frame of Fig. E.4, E.5, E.6, E.7 and E.9 are artifacts generated by the finite-element-method package used to compute the electric field on the discretized problem domain. For a critical analysis of the results presented in this appendix, see Section 3.3.4.

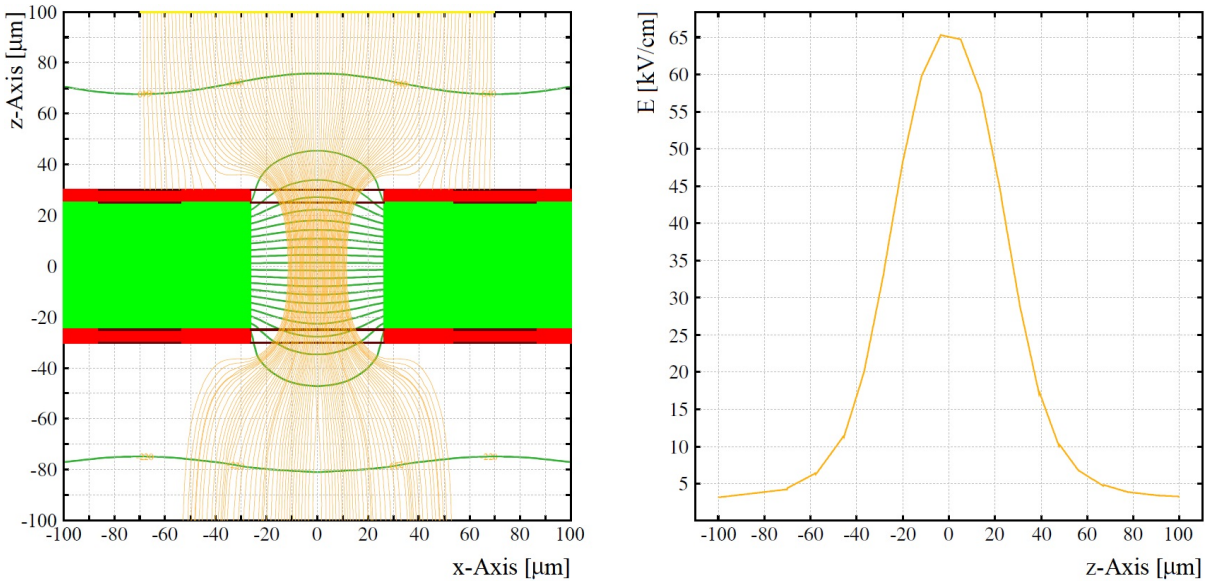

Figure E.1: Electric field in a single-mask conical GEM with ∅ = 55 : 55 µm.

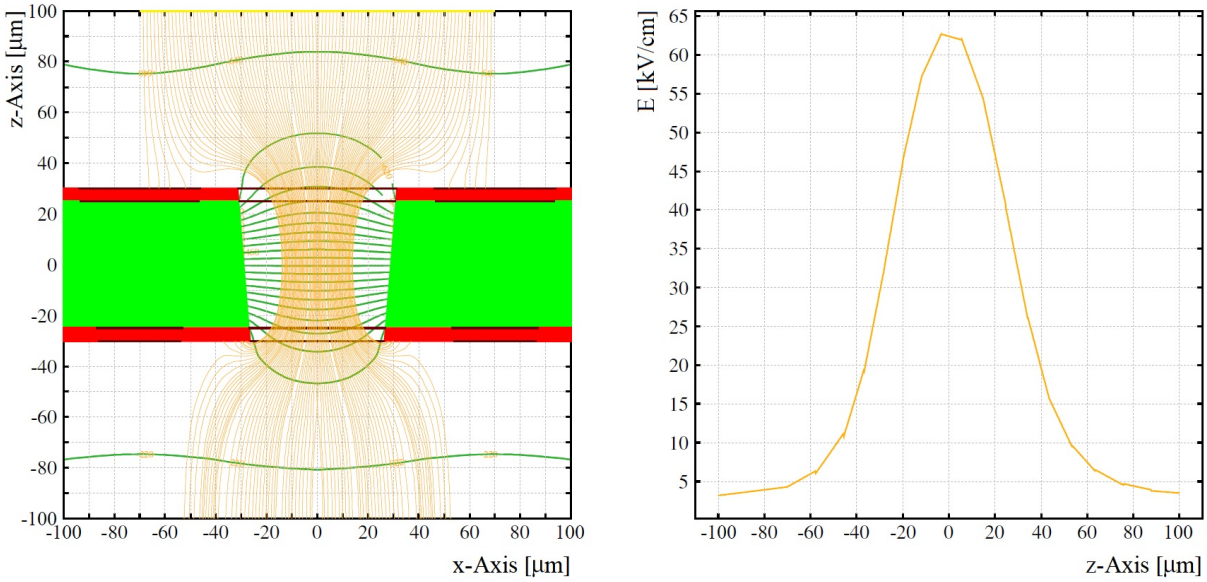

Figure E.2: Electric field in a single-mask conical GEM with ∅ = 65 : 55 µm.

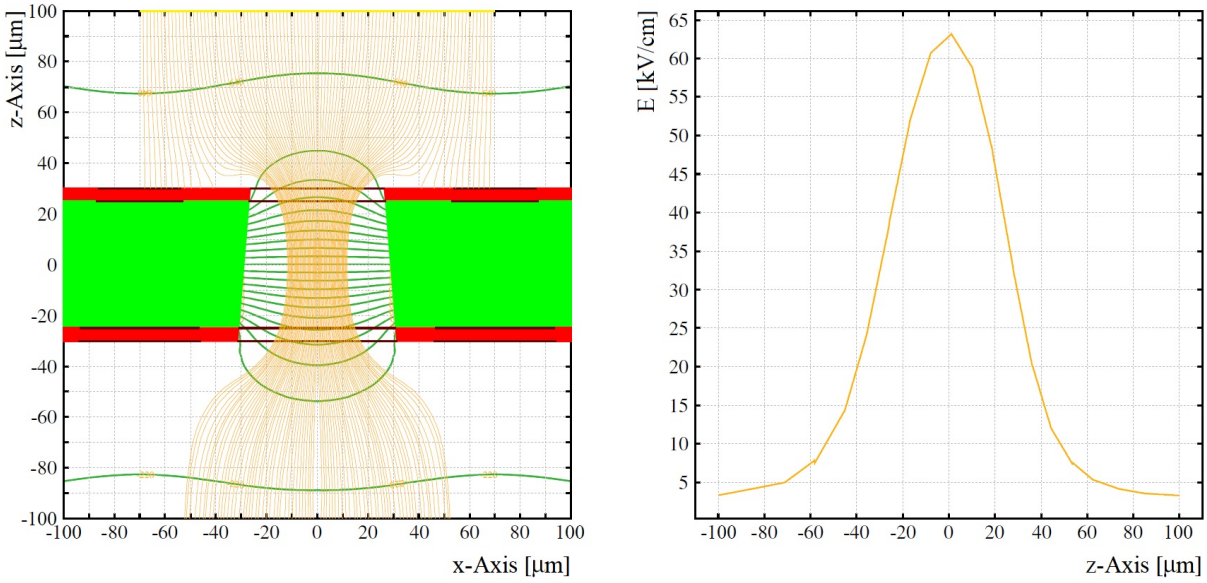

Figure E.3: Electric field in a single-mask conical GEM with ∅ = 55 : 65 µm.

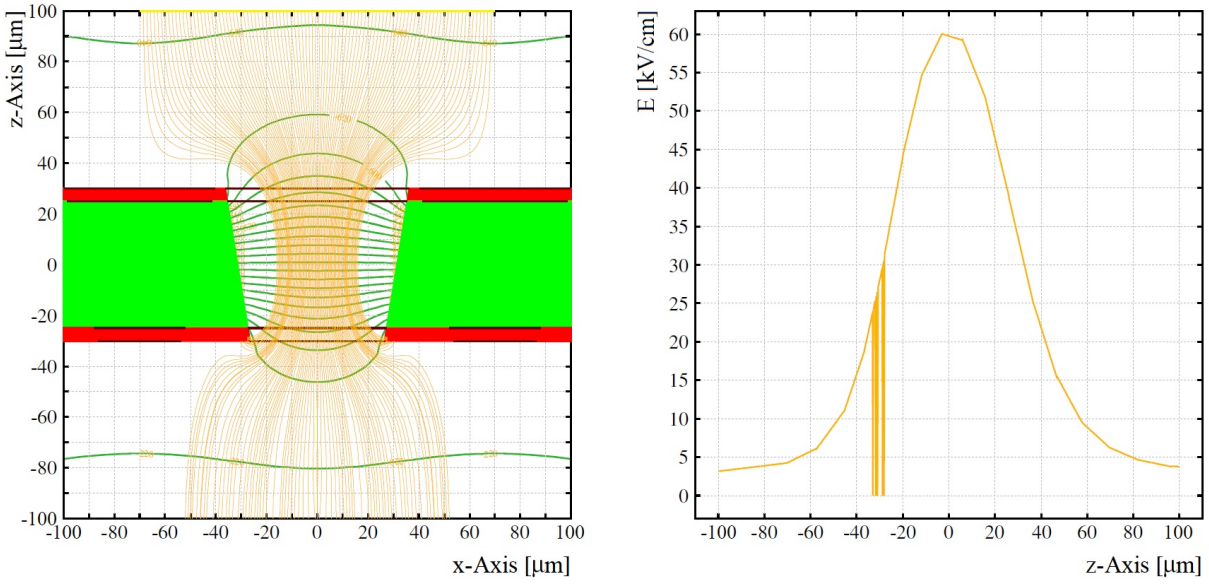

Figure E.4: Electric field in a single-mask conical GEM with ∅ = 75 : 55 µm.

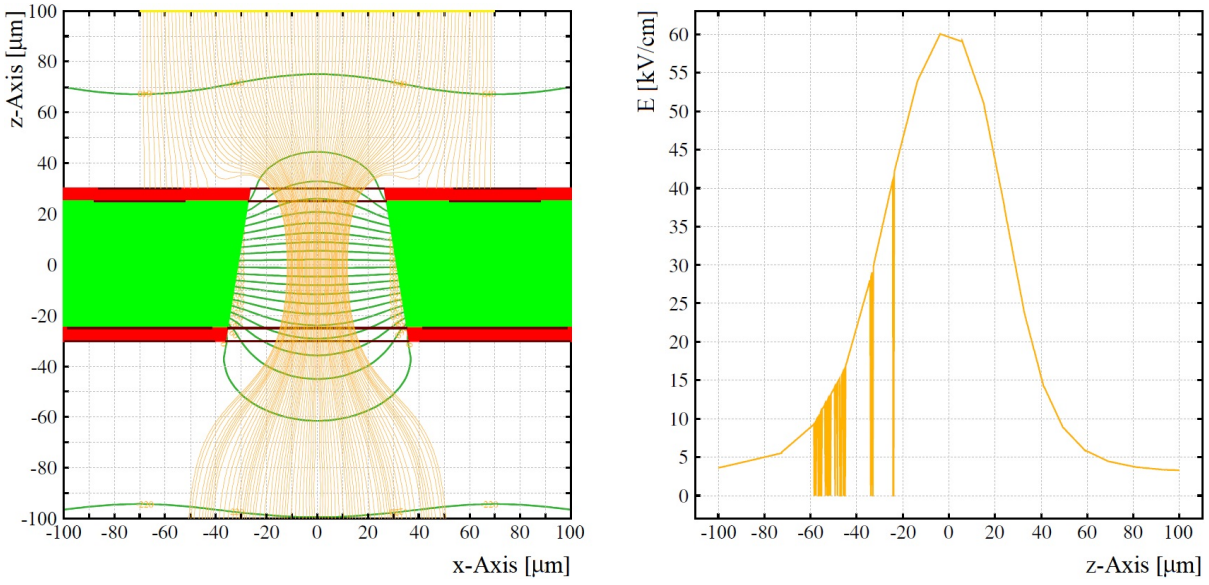

Figure E.5: Electric field in a single-mask conical GEM with ∅ = 55 : 75 µm.

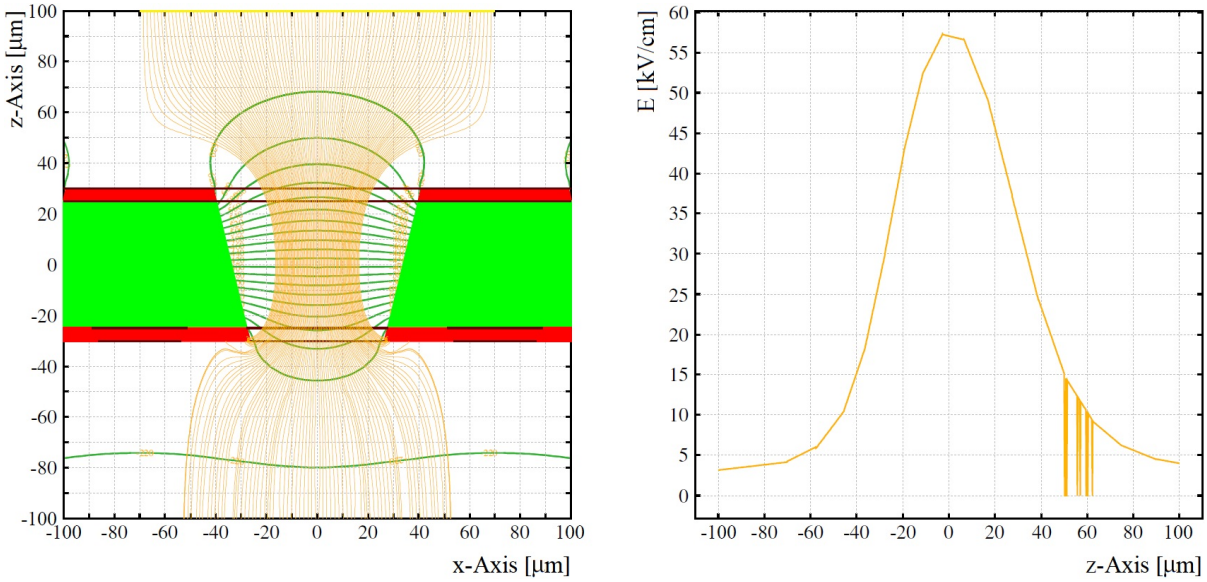

Figure E.6: Electric field in a single-mask conical GEM with ∅ = 85 : 55 µm.

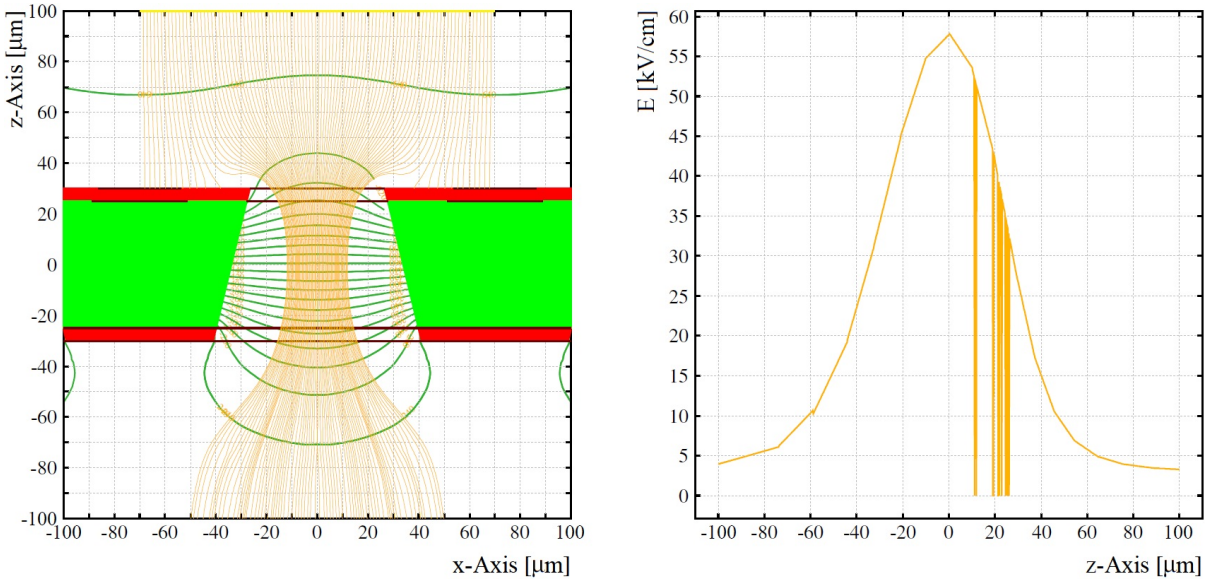

Figure E.7: Electric field in a single-mask conical GEM with ∅ = 55 : 85 µm.

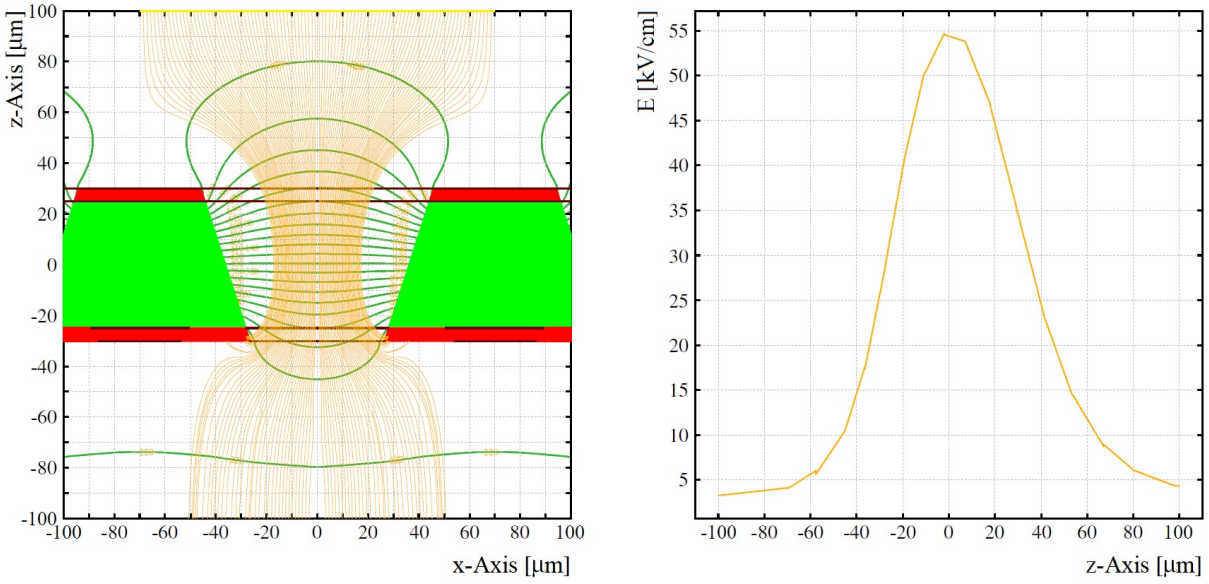

Figure E.8: Electric field in a single-mask conical GEM with ∅ = 95 : 55 µm.

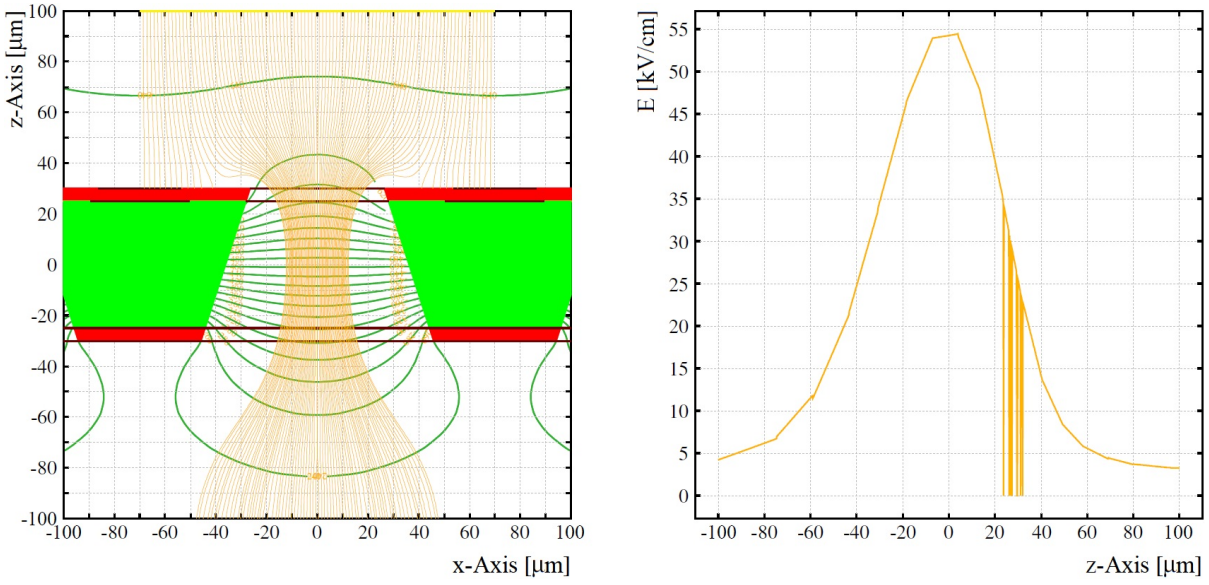

Figure E.9: Electric field in a single-mask conical GEM with ∅ = 55 : 95 µm.

APPENDIX F

List of test-beam data runs

This appendix lists the test-beam data runs used in the analysis described in Section 4.4.4 and in its subsections. The runs are grouped into six tables, corresponding to the data sets of Fig. 4.53, 4.58 and 4.59. Within each data set, the Micromegas chamber, the gas mixture, the beam type and the particle flux are fixed, while the gas gain of the Micromegas changes from a run set to another. The naming conventions for the data sets and the run sets are explained in Section 4.4.4.3.

Table F.1: List of test-beam runs in the data set S3-93:7-μ-0.45. The drift field of the Micromegas is 0.75 kV/cm and the difference of potential across the amplification gap is 540 V, for an effective gas gain of 6840.

Run set	BAT run	Micromegas run
S3-93:7-μ-0.45-6840	4298	4998

Table F.2: List of test-beam runs in the data set S3-93:7-μ-0.95. The drift field of the Micromegas is 0.75 kV/cm and the difference of potential across the amplification gap is 520 V, for an effective gas gain of 3810.

Run set	BAT run	Micromegas run
S3-93:7-μ-0.95-3810	4295	4996

Table F.3: List of test-beam runs in the data set S3-93:7-π-0.86. The drift field of the Micromegas is 0.75 kV/cm and the difference of potential across the amplification gap is 490 V, for an effective gas gain of 1660.

Run set	BAT run	Micromegas run
S3-93:7-π-0.86-1660	4232	4978
	4233	4979
	4234	4980

Table F.4: List of test-beam runs in the data set S3-93:7-π-2.21. The drift field of the Micromegas is 0.75 kV/cm and the difference of potential across the amplification gap ranges from 490 to 540 V, for effective gas gains from 1660 to 6840.

Run set	BAT run	Micromegas run
S3-93:7-π-2.21-1660	4257	4984
S3-93:7-π-2.21-2170	4258	4985
	4259	4986
S3-93:7-π-2.21-2860	4261	4988
S3-93:7-π-2.21-3810	4262	4989
	4263	4990
S3-93:7-π-2.21-5090	4264	4991
	4265	4992
S3-93:7-π-2.21-6840	4266	4993
	4267	4994

Table F.5: List of test-beam runs in the data set R12-93:7-π-2.05. The drift field of the Micromegas is 0.4 kV/cm and the difference of potential across the amplification gap ranges from 500 to 570 V, for effective gas gains from 1000 to 10 000.

Run set	BAT run	Micromegas run
R12-93:7-π-2.05-1000	3694	4409
R12-93:7-π-2.05-2450	3696	4411
	3697	4412
R12-93:7-π-2.05-6980	3701	4416
R12-93:7-π-2.05-10 000	3699	4414

Table F.6: List of test-beam runs in the data set R12-85:15-π-2.20. The drift field of the Micromegas is 0.6 kV/cm and the difference of potential across the amplification gap ranges from 480 to 600 V, for effective gas gains from 249 to 6040.

Run set	BAT run	Micromegas run
R12-85:15-π-2.20-249	4134	4869
	4135	4870
	4136	4871
	4137	4872
	4138	4873
R12-85:15-π-2.20-305	4139	4874
	4140	4875
	4141	4876
	4142	4877
	4143	4878
R12-85:15-π-2.20-382	4144	4879
	4145	4881
	4146	4882
	4147	4883
	4148	4884

Table F.6: Continued.

Run set	BAT run	Micromegas run
R12-85:15-π-2.20-485	4149	4885
	4150	4886
	4151	4887
	4152	4888
	4153	4889
R12-85:15-π-2.20-624	4154	4890
	4155	4891
	4156	4892
	4157	4893
	4158	4894
R12-85:15-π-2.20-812	4159	4895
	4160	4896
	4161	4897
	4162	4898
	4163	4899
R12-85:15-π-2.20-1070	4166	4901
	4167	4902
	4170	4905
	4171	4906
	4172	4907
R12-85:15-π-2.20-1410	4173	4908
	4174	4909
	4175	4910
	4176	4911
	4177	4912
	4178	4913
R12-85:15-π-2.20-1870	4179	4914
	4180	4915
	4181	4916
	4183	4918
	4184	4919
R12-85:15-π-2.20-2490	4124	4857
	4125	4858
	4129	4861
	4132	4867
	4133	4868
R12-85:15-π-2.20-3340	4186	4921
	4187	4922
	4188	4923
	4189	4924
	4192	4928

Table F.6: Continued.

Run set	BAT run	Micromegas run
R12-85:15-π-2.20-4470	4193	4929
	4194	4930
	4195	4931
	4196	4932
	4197	4933
	4198	4934
R12-85:15-π-2.20-6010	4199	4935
	4200	4936
	4201	4937
	4202	4938
	4203	4939

Summary

Micropattern gas detectors (MPGDs) are a class of devices introduced in the late 80's with the purpose of overcoming some of the limitations of multiwire proportional chambers, and especially to achieve a higher rate capability. The principle of operation of MPGDs is similar to that of previous proportional chambers: ionization charge is liberated in the gas and multiplied in a region of high electric field. However, MPGDs rely on microscopic structures to generate the amplification field, with typical distances between the electrodes in the sub-millimetre range. The fast ion collection reduces the space-charge effects and boosts the rate capability. Other benefits of MPGDs include good energy, space and time resolution, ion-feedback suppression and good radiation hardness and aging properties.

The gas electron multiplier (GEM) is a micropattern electron-amplification structure made from a metal-clad insulating polymer foil some tens of micron thick, pierced with a regular and dense matrix of holes. The most widespread method to pattern the base material makes use of techniques that are common in the printed circuit board industry, such as photolithography and chemical wet etching. GEMs manufactured with the traditional double-mask process have maximum linear dimensions of about 30 cm, because of the difficulty in the manual alignment of the two photolithographic masks. Given the growing demand for large-area GEMs, mainly triggered by the needs of the high-energy-physics community, in 2007 the single-mask technology was introduced, which is scalable up to square metre size. The first generation of single-mask GEMs presented some flaws, such as lower gas gains for a given bias voltage and longer stabilization times with respect to double-mask foils. The research work described here enabled the novel technique to be enhanced.

The long stabilization time is tracked down to the presence of a wide clearance on the upper electrode around the edge of the holes in the polyimide. In the single-mask process, the base material is patterned on one side only and then etched layer after layer, from top to bottom, until through-holes are formed. The rim arises because of the isotropic behaviour of the metal-etching chemistry, that attacks the upper electrode of the GEM while holes are opened in the lower layer. Mechanical protection of the top face by means of gold or tin plating gives unsatisfactory results. The difficulty to ensure perfect tightness at the junction between metal and polyimide leads to etching of the electrode under the shielding and to the formation of dents that degrade the hole shape. Electroetching of the bottom layer also proves to be inadequate, as it gives rise to irregular hole contours and leaves spikes that make the GEMs more likely to discharge. Finally, a solution is found in the electrochemical active corrosion protection, where the upper face is protected with the application of a negative voltage.

The low gas gain, on the other hand, is due to the suboptimal geometry of the holes in the polyimide. The electrostatic properties of the GEM as a function of the hole shape are studied with numerical simulations. The results of the study, together with the measurements performed on the first electrochemically protected specimens, suggest to abandon the conical geometry in favour of a biconical shape that resembles the one of double-mask GEMs. The final performance is compatible with the one of traditional foils in terms of leakage current, robustness against sparks and gas gain. Outgassing, aging

and radiation hardness are also expected to be as good. The optimized single-mask GEMs are currently at the base of various experiments and upgrade projects.

During the second long shutdown of the Large Hadron Collider (LHC), the ATLAS experiment will replace the present Small Wheels, which constitute the innermost layer of the end-cap muon system. With the prospected increase of luminosity in the HL-LHC era, the occupancy of the gas detectors that make up the current Small Wheels will in fact become unbearably high. Hence the need for new chambers. In addition, the new Small Wheels are expected to provide a direction vector for the detected tracks, with the purpose of suppressing fake high-p_T ($\geq 20\,\text{GeV}$) muons and thus enhancing the level-1 trigger. The new chambers must have a detection efficiency for minimum ionizing particles (MIPs) of more than 98% per plane, trigger capability, good resistance to radiation and good aging properties. The micro-mesh gaseous structure (Micromegas) technology has been chosen for the tracking chambers. There are two main challenges: the large area coverage and the elevated discharge probability in the ATLAS environment. Here I describe my contribution to the realization of spark-tolerant Micromegas.

A first approach aims at reducing the discharge probability to an acceptable level by lowering the charge density in the amplification region. In turn, this is done by splitting the gas gain necessary for efficient MIP detection over multiple stages. The idea is probed with a $10 \times 10\,\text{cm}^2$ test chamber, in which a preamplification GEM can optionally be fitted in between the Micromegas mesh and the drift electrode. The Micromegas is characterized in both standalone configuration and in combination with the GEM. The effective gas gain is measured with soft X-rays, while the spark rate is estimated using alpha particles. With optimal field tuning, a reduction of the discharge probability between one and two orders of magnitudes is obtained in the preamplified detector. Since this is not sufficient to guarantee safe operation in the ATLAS environment, and because of the mechanical complications introduced by the preamplification stage when moving to large areas, this approach is abandoned.

A second option is that of using single-stage resistive Micromegas. In this case, no attempt is made to reduce the discharge probability, which remains the same as in a standard Micromegas. The purpose is instead that of mitigating the undesired effects of streamers, and in particular the dead time. Resistive Micromegas are manufactured by clothing the readout strips with an insulating layer, topped with resistive traces matching the readout pattern and grounded through high-value resistors. In case of a spark, the grounding resistors limit the discharge current and hence effectively quench the streamer before it can cause significant drops of the mesh voltage. I performed in-depth data analysis of test-beam data acquired with a resistive Micromegas and compared its performance to that of a standard chamber. I developed the analysis framework and studied the gain homogeneity, the detection efficiency and the space resolution. Efficiencies above 98% are achieved over a broad gas-gain window ranging up to about 10^4, even in hadronic beams where standard Micromegas suffer from severe spark-induced dead time. The space resolution is also improved and reaches $24.9 \pm 0.8\,\mu\text{m}$ in Ar:CO_2 85:15 with a strip pitch of $250\,\mu\text{m}$.

Bibliography

[1] Particle Data Group, *Atomic and Nuclear Properties of Materials*, 2011, URL: http://pdg.lbl.gov/2011/AtomicNuclearProperties/.

[2] K. Nakamura and Particle Data Group, "Review of Particle Physics", *Journal of Physics G: Nuclear and Particle Physics* 37.7A (2010) 075021, URL: http://stacks.iop.org/0954-3899/37/i=7A/a=075021.

[3] Y. Tsai, "Pair production and bremsstrahlung of charged leptons", *Reviews of Modern Physics* 46 (4 Oct. 1974) 815–851, DOI: 10.1103/RevModPhys.46.815, URL: http://link.aps.org/doi/10.1103/RevModPhys.46.815.

[4] Y. Tsai, "Erratum: Pair production and bremsstrahlung of charged leptons", *Reviews of Modern Physics* 49 (2 Apr. 1977) 421–423, DOI: 10.1103/RevModPhys.49.421, URL: http://link.aps.org/doi/10.1103/RevModPhys.49.421.

[5] H. Davies, H. A. Bethe and L. C. Maximon, "Theory of Bremsstrahlung and Pair Production. II. Integral Cross Section for Pair Production", *Physical Review* 93 (4 Feb. 1954) 788–795, DOI: 10.1103/PhysRev.93.788, URL: http://link.aps.org/doi/10.1103/PhysRev.93.788.

[6] W. T. Scott, "The Theory of Small-Angle Multiple Scattering of Fast Charged Particles", *Reviews of Modern Physics* 35 (2 Apr. 1963) 231–313, DOI: 10.1103/RevModPhys.35.231, URL: http://link.aps.org/doi/10.1103/RevModPhys.35.231.

[7] V. L. Highland, "Some practical remarks on multiple scattering", *Nuclear Instruments and Methods* 129.2 (1975) 497–499, ISSN: 0029-554X, DOI: 10.1016/0029-554X(75)90743-0, URL: http://www.sciencedirect.com/science/article/pii/0029554X75907430.

[8] V. L. Highland, "Erratum: Some practical remarks on multiple scattering", *Nuclear Instruments and Methods* 161.1 (1979) 171, ISSN: 0029-554X, DOI: 10.1016/0029-554X(79)90379-3, URL: http://www.sciencedirect.com/science/article/pii/0029554X79903793.

[9] G. R. Lynch and O. I. Dahl, "Approximations to multiple Coulomb scattering", *Nuclear Instruments and Methods in Physics Research Section B: Beam Interactions with Materials and Atoms* 58.1 (1991) 6–10, ISSN: 0168-583X, DOI: 10.1016/0168-583X(91)95671-Y, URL: http://www.sciencedirect.com/science/article/pii/0168583X9195671Y.

[10] C. M. Davisson, "Interaction of γ-RADIATION with Matter", *Alpha-, Beta- and Gamma-ray Spectroscopy*, ed. by K. Siegbahn, 1965 37.

[11] National Institute of Standards and Technology, *Photon Cross Sections in Matter*, 2011, URL: http://physics.nist.gov/PhysRefData/Xcom/html/xcom1.html.

[12] O. Klein and T. Nishina, "Über die Streuung von Strahlung durch freie Elektronen nach der neuen relativistischen Quantendynamik von Dirac", *Zeitschrift für Physik A Hadrons and Nuclei* 52 (11 1929) 853–868, ISSN: 0939-7922, URL: http://dx.doi.org/10.1007/BF01366453.

[13] A. Sharma, "Properties of some gas mixtures used in tracking detectors", *SLAC ICFA Instrumentation Bulletin* 16.3 (July 1998), URL: http://www.slac.stanford.edu/pubs/icfa/summer98/paper3/paper3a.html.

[14] H. Raether, *Electron avalanches and breakdown in gases*, Butterworths advanced physics series: Monographs on ionization and electrical discharges in gases, Butterworths, 1964.

[15] Y. Ivaniouchenkov et al., "Breakdown limit studies in high-rate gaseous detectors", *Nuclear Instruments and Methods in Physics Research Section A: Accelerators, Spectrometers, Detectors and Associated Equipment* 422.1–3 (1999) 300–304, ISSN: 0168-9002, DOI: 10.1016/S0168-9002(98)00962-0, URL: http://www.sciencedirect.com/science/article/pii/S0168900298009620.

[16] S. Ramo, "Currents Induced by Electron Motion", *Proceedings of the IRE* 27.9 (Sept. 1939) 584–585, ISSN: 0096-8390, DOI: 10.1109/JRPROC.1939.228757.

[17] A. Oed, "Position-sensitive detector with microstrip anode for electron multiplication with gases", *Nuclear Instruments and Methods in Physics Research Section A: Accelerators, Spectrometers, Detectors and Associated Equipment* 263.2–3 (1988) 351–359, ISSN: 0168-9002, DOI: 10.1016/0168-9002(88)90970-9, URL: http://www.sciencedirect.com/science/article/pii/0168900288909709.

[18] T. Tanimori et al., "Development of an imaging microstrip gas chamber with a 5 cm × 5 cm area based on multi-chip module technology", *Nuclear Instruments and Methods in Physics Research Section A: Accelerators, Spectrometers, Detectors and Associated Equipment* 381.2–3 (1996) 280–288, ISSN: 0168-9002, DOI: 10.1016/S0168-9002(96)00833-9, URL: http://www.sciencedirect.com/science/article/pii/S0168900296008339.

[19] A. Oed, "Properties of micro-strip gas chambers (MSGC) and recent developments", *Nuclear Instruments and Methods in Physics Research Section A: Accelerators, Spectrometers, Detectors and Associated Equipment* 367.1–3 (1995) 34–40, ISSN: 0168-9002, DOI: 10.1016/0168-9002(95)00657-5, URL: http://www.sciencedirect.com/science/article/pii/0168900295006575.

[20] F. Sauli, "GEM: A new concept for electron amplification in gas detectors", *Nuclear Instruments and Methods in Physics Research Section A: Accelerators, Spectrometers, Detectors and Associated Equipment* 386.2–3 (1997) 531–534, ISSN: 0168-9002, DOI: 10.1016/S0168-9002(96)01172-2, URL: http://www.sciencedirect.com/science/article/pii/S0168900296011722.

[21] The TOTEM Collaboration, "The TOTEM Experiment at the CERN Large Hadron Collider", *Journal of Instrumentation* 3.08 (2008) S08007, URL: http://stacks.iop.org/1748-0221/3/i=08/a=S08007.

[22] S. Bachmann et al., "Discharge studies and prevention in the gas electron multiplier (GEM)", *Nuclear Instruments and Methods in Physics Research Section A: Accelerators, Spectrometers, Detectors and Associated Equipment* 479.2–3 (2002) 294–308, ISSN: 0168-9002, DOI: 10.1016/S0168-9002(01)00931-7, URL: http://www.sciencedirect.com/science/article/pii/S0168900201009317.

[23] C. Altunbas et al., "Construction, test and commissioning of the triple-gem tracking detector for compass", *Nuclear Instruments and Methods in Physics Research Section A: Accelerators, Spectrometers, Detectors and Associated Equipment* 490.1–2 (2002) 177–203, ISSN: 0168-9002, DOI: 10.1016/S0168-9002(02)00910-5, URL: http://www.sciencedirect.com/science/article/pii/S0168900202009105.

[24] T. Zeuner, "The MSGC-GEM Inner Tracker for HERA-B", *Nuclear Instruments and Methods in Physics Research Section A: Accelerators, Spectrometers, Detectors and Associated Equipment* 446.1–2 (2000) 324–330, ISSN: 0168-9002, DOI: 10.1016/S0168-9002(00)00042-5, URL: http://www.sciencedirect.com/science/article/pii/S0168900200000425.

[25] M. Alfonsi et al., "High-rate particle triggering with triple-GEM detector", *Nuclear Instruments and Methods in Physics Research Section A: Accelerators, Spectrometers, Detectors and Associated Equipment* 518.1–2 (2004) 106–112, ISSN: 0168-9002, DOI: 10.1016/j.nima.2003.10.035, URL: http://www.sciencedirect.com/science/article/pii/S0168900203027463.

[26] The NA61 Collaboration, *NA61 Gas Electron Multipliers*, 2006, URL: https://na61.web.cern.ch/na61/xc/index.html?0=detector/GEM-detector.

[27] A. Balla et al., "Design and construction of a cylindrical GEM detector as Inner Tracker in KLOE-2", *Nuclear Science Symposium and Medical Imaging Conference (NSS/MIC), 2011 IEEE*, Oct. 2011 1002–1005, DOI: 10.1109/NSSMIC.2011.6154309.

[28] S. Duarte Pinto et al., "Making spherical GEMs", *Journal of Instrumentation* 4.12 (2009) P12006, URL: http://stacks.iop.org/1748-0221/4/i=12/a=P12006.

[29] S. Duarte Pinto et al., "Spherical gems for parallax-free detectors", *Nuclear Science Symposium Conference Record (NSS/MIC), 2009 IEEE*, Nov. 2009 225–230, DOI: 10.1109/NSSMIC.2009.5401786.

[30] S. Duarte Pinto et al., "First results of spherical GEMS", *Nuclear Science Symposium Conference Record (NSS/MIC), 2010 IEEE*, Nov. 2010 1877–1880, DOI: 10.1109/NSSMIC.2010.5874100.

[31] V. da Silva et al., "An innovative "ChemicalVia" process for the production of high density interconnect printed circuit boards", *Circuit World* 30 (4 2004) 27–33, ISSN: 0305-6120, DOI: 10.1108/03056120410539885.

[32] Y. Giomataris et al., "MICROMEGAS: a high-granularity position-sensitive gaseous detector for high particle-flux environments", *Nuclear Instruments and Methods in Physics Research Section A: Accelerators, Spectrometers, Detectors and Associated Equipment* 376.1 (1996) 29–35, ISSN: 0168-9002,

DOI: 10.1016/0168-9002(96)00175-1,
URL: http://www.sciencedirect.com/science/article/pii/0168900296001751.

[33] Y. Bilevych et al., "Spark protection layers for CMOS pixel anode chips in MPGDs", *Nuclear Instruments and Methods in Physics Research Section A: Accelerators, Spectrometers, Detectors and Associated Equipment* 629.1 (2011) 66–73, ISSN: 0168-9002, DOI: 10.1016/j.nima.2010.11.116, URL: http://www.sciencedirect.com/science/article/pii/S016890021002663X.

[34] IPHE Lausanne, *LHCb Inner Tracker Micromegas*, 1999, URL: http://lphe.epfl.ch/lhcb/micromegas/.

[35] A. Delbart et al., "New developments of Micromegas detector", *Nuclear Instruments and Methods in Physics Research Section A: Accelerators, Spectrometers, Detectors and Associated Equipment* 461.1–3 (2001) 84–87, ISSN: 0168-9002, DOI: 10.1016/S0168-9002(00)01175-X, URL: http://www.sciencedirect.com/science/article/pii/S016890020001175X.

[36] Y. Giomataris, "Development and prospects of the new gaseous detector "Micromegas"", *Nuclear Instruments and Methods in Physics Research Section A: Accelerators, Spectrometers, Detectors and Associated Equipment* 419.2–3 (1998) 239–250, ISSN: 0168-9002, DOI: 10.1016/S0168-9002(98)00865-1, URL: http://www.sciencedirect.com/science/article/pii/S0168900298008651.

[37] J. Derré et al., "Spatial resolution in Micromegas detectors", *Nuclear Instruments and Methods in Physics Research Section A: Accelerators, Spectrometers, Detectors and Associated Equipment* 459.3 (2001) 523–531, ISSN: 0168-9002, DOI: 10.1016/S0168-9002(00)01051-2, URL: http://www.sciencedirect.com/science/article/pii/S0168900200010512.

[38] Y. Giomataris et al., "Micromegas in a bulk", *Nuclear Instruments and Methods in Physics Research Section A: Accelerators, Spectrometers, Detectors and Associated Equipment* 560.2 (2006) 405–408, ISSN: 0168-9002, DOI: 10.1016/j.nima.2005.12.222, URL: http://www.sciencedirect.com/science/article/pii/S0168900205026501.

[39] D. Thers et al., "Micromegas as a large microstrip detector for the COMPASS experiment", *Nuclear Instruments and Methods in Physics Research Section A: Accelerators, Spectrometers, Detectors and Associated Equipment* 469.2 (2001) 133–146, ISSN: 0168-9002, DOI: 10.1016/S0168-9002(01)00769-0, URL: http://www.sciencedirect.com/science/article/pii/S0168900201007690.

[40] A. Magnon et al., "Tracking with $40 \times 40\,\mathrm{cm}^2$ MICROMEGAS detectors in the high energy, high luminosity COMPASS experiment", *Nuclear Instruments and Methods in Physics Research Section A: Accelerators, Spectrometers, Detectors and Associated Equipment* 478.1–2 (2002) 210–214, ISSN: 0168-9002, DOI: 10.1016/S0168-9002(01)01759-4, URL: http://www.sciencedirect.com/science/article/pii/S0168900201017594.

[41] F. Kunn et al.,
"The gaseous microstrip detector micromegas for the COMPASS experiment at CERN",
Nuclear Physics A 721.0 (2003) C1087–C1090, ISSN: 0375-9474,
DOI: 10.1016/S0375-9474(03)01291-0,
URL: http://www.sciencedirect.com/science/article/pii/S0375947403012910.

[42] S. Andriamonje et al., "A Low Background Micromegas Detector for Axion Searches",
Nuclear Instruments and Methods in Physics Research Section A: Accelerators, Spectrometers, Detectors and Associated Equipment 535.1–2 (2004) 309–313, ISSN: 0168-9002,
DOI: 10.1016/j.nima.2004.07.231,
URL: http://www.sciencedirect.com/science/article/pii/S0168900204016675.

[43] P. Abbon et al., "The Micromegas detector of the CAST experiment",
New Journal of Physics 9.6 (2007) 170,
URL: http://stacks.iop.org/1367-2630/9/i=6/a=170.

[44] J. G. Lacarra,
Probing eV-mass scale axions with a Micromegas detector in the CAST experiment, 2011,
URL: http://arxiv.org/abs/1102.1406v2.

[45] P. Colas et al., "First test of a Micromegas TPC in a magnetic field",
Nuclear Instruments and Methods in Physics Research Section A: Accelerators, Spectrometers, Detectors and Associated Equipment 535.1–2 (2004) 181–185, ISSN: 0168-9002,
DOI: 10.1016/j.nima.2004.07.123,
URL: http://www.sciencedirect.com/science/article/pii/S0168900204015980.

[46] B. Peyaud, "KABES: a novel beam spectrometer for NA48",
Nuclear Instruments and Methods in Physics Research Section A: Accelerators, Spectrometers, Detectors and Associated Equipment 535.1–2 (2004) 247–252, ISSN: 0168-9002,
DOI: 10.1016/j.nima.2004.07.275,
URL: http://www.sciencedirect.com/science/article/pii/S016890020401647X.

[47] S. Andriamonje et al., "Experimental studies of a Micromegas neutron detector",
Nuclear Instruments and Methods in Physics Research Section A: Accelerators, Spectrometers, Detectors and Associated Equipment 481.1–3 (2002) 120–129, ISSN: 0168-9002,
DOI: 10.1016/S0168-9002(01)01246-3,
URL: http://www.sciencedirect.com/science/article/pii/S0168900201012463.

[48] M. Huff, "MEMS fabrication", *Sensor Review* 22 (1 2002) 18–33, ISSN: 0260-2288,
DOI: 10.1108/02602280210697087.

[49] S. Duarte Pinto,
"Gas Electron Multipliers: Development of large area GEMs and spherical GEMs",
PhD thesis: Bonn U., 2011.

[50] ANSYS Inc., *ANSYS website*, 2012, URL: http://www.ansys.com/.

[51] S. F. Biagi, *Magboltz website*, 2012, URL: http://magboltz.web.cern.ch/magboltz/.

[52] R. Veenhof, *Garfield interface to Magboltz*, 2012,
URL: http://garfield.web.cern.ch/garfield/help/garfield_31.html#Ref0340.

[53] S. F. Biagi, "Monte Carlo simulation of electron drift and diffusion in counting gases under the influence of electric and magnetic fields",
Nuclear Instruments and Methods in Physics Research Section A: Accelerators, Spectrometers, Detectors and Associated Equipment 421.1–2 (1999) 234–240, ISSN: 0168-9002,
DOI: 10.1016/S0168-9002(98)01233-9,
URL: http://www.sciencedirect.com/science/article/pii/S0168900298012339.

[54] R. Veenhof, *Garfield website*, 2012, URL: http://garfield.web.cern.ch/garfield/.

[55] D. Abbaneo et al.,
"Construction of the first full-size GEM-based prototype for the CMS high-η muon system",
Nuclear Science Symposium Conference Record (NSS/MIC), 2010 IEEE, Nov. 2010 1909–1913,
DOI: 10.1109/NSSMIC.2010.5874107.

[56] D. Abbaneo et al., "Test beam results of the GE1/1 prototype for a future upgrade of the CMS high-η muon system",
Nuclear Science Symposium and Medical Imaging Conference (NSS/MIC), 2011 IEEE,
Oct. 2011 1806–1810, DOI: 10.1109/NSSMIC.2011.6154688.

[57] D. Abbaneo et al., "An overview of the design, construction and performance of large area triple-GEM prototypes for future upgrades of the CMS forward muon system",
Journal of Instrumentation 7.05 (2012) C05008,
URL: http://stacks.iop.org/1748-0221/7/i=05/a=C05008.

[58] A. Sharma, *A GEM Detector System for an Upgrade of the CMS Muon Endcaps*, 2012,
URL: https://twiki.cern.ch/twiki/pub/MPGD/CmsGEMCollaboration/GEM_technical_proposal.pdf.

[59] M. Alfonsi et al., "Activity of CERN and LNF groups on large area GEM detectors",
Nuclear Instruments and Methods in Physics Research Section A: Accelerators, Spectrometers, Detectors and Associated Equipment 617.1–3 (2010) 151–154, ISSN: 0168-9002,
DOI: 10.1016/j.nima.2009.06.063,
URL: http://www.sciencedirect.com/science/article/pii/S0168900209013278.

[60] J. Yu et al., "Development of GEM based digital hadron calorimeter",
Nuclear Science Symposium Conference Record, 2008. NSS '8. IEEE, Oct. 2008 1544–1548,
DOI: 10.1109/NSSMIC.2008.4774703.

[61] M. Hohlmann et al., "GEANT4 Simulation of a Cosmic Ray Muon Tomography System With Micro-Pattern Gas Detectors for the Detection of High-Z Materials",
IEEE Transactions on Nuclear Science 56.3 (June 2009) 1356–1363, ISSN: 0018-9499,
DOI: 10.1109/TNS.2009.2016197.

[62] D. Attié, "TPC review", *Nuclear Instruments and Methods in Physics Research Section A: Accelerators, Spectrometers, Detectors and Associated Equipment* 598.1 (2009) 89–93,
ISSN: 0168-9002, DOI: 10.1016/j.nima.2008.08.114,
URL: http://www.sciencedirect.com/science/article/pii/S0168900208011996.

[63] The ATLAS Collaboration, "The ATLAS Experiment at the CERN Large Hadron Collider",
Journal of Instrumentation 3.08 (2008) S08003,
URL: http://stacks.iop.org/1748-0221/3/i=08/a=S08003.

[64] R. Bouclier et al., "Update on Discharge studies in MSGCs", tech. rep. CMS-NOTE-1997-020, CERN, Apr. 1997.

[65] R. de Oliveira, J. Wotschack and V. Polychronakos, *MAMMA: spark-protected Micromegas*, 2010, URL: https://indico.cern.ch/getFile.py/access?contribId=30&sessionId=3&resId=1&materialId=slides&confId=89325.

[66] T. Alexopoulos et al., "A spark-resistant bulk-micromegas chamber for high-rate applications", *Nuclear Instruments and Methods in Physics Research Section A: Accelerators, Spectrometers, Detectors and Associated Equipment* 640.1 (2011) 110–118, ISSN: 0168-9002, DOI: 10.1016/j.nima.2011.03.025, URL: http://www.sciencedirect.com/science/article/pii/S0168900211005869.

[67] R. de Oliveira, J. Wotschack and V. Polychronakos, *Qualitative simplified model of a Bulk Micromegas detector*, 2010, URL: https://indico.cern.ch/getFile.py/access?contribId=67&sessionId=5&resId=1&materialId=slides&confId=89325.

[68] P. Fonte et al., "A spark-protected high-rate detector", *Nuclear Instruments and Methods in Physics Research Section A: Accelerators, Spectrometers, Detectors and Associated Equipment* 431.1–2 (1999) 154–159, ISSN: 0168-9002, DOI: 10.1016/S0168-9002(99)00221-1, URL: http://www.sciencedirect.com/science/article/pii/S0168900299002211.

[69] M. S. Dixit et al., "Position sensing from charge dispersion in micro-pattern gas detectors with a resistive anode", *Nuclear Instruments and Methods in Physics Research Section A: Accelerators, Spectrometers, Detectors and Associated Equipment* 518.3 (2004) 721–727, ISSN: 0168-9002, DOI: 10.1016/j.nima.2003.09.051, URL: http://www.sciencedirect.com/science/article/pii/S0168900203026822.

[70] Y. Giomataris, "High rate applications of micromegas and prospects", *eConf* C0604032 (2006) 0023, arXiv:physics/0610153 [physics].

[71] R. de Oliveira et al., "First Tests of MICROMEGAS and GEM-Like Detectors Made of a Resistive Mesh", *IEEE Transactions on Nuclear Science* 57.6 (2010) 3744–3752, ISSN: 0018-9499, DOI: 10.1109/TNS.2010.2073483.

[72] J. Treis et al., "A modular PC based silicon microstrip beam telescope with high speed data acquisition", *Nuclear Instruments and Methods in Physics Research Section A: Accelerators, Spectrometers, Detectors and Associated Equipment* 490.1–2 (2002) 112–123, ISSN: 0168-9002, DOI: 10.1016/S0168-9002(02)00913-0, URL: http://www.sciencedirect.com/science/article/pii/S0168900202009130.

[73] H. Muller et al., "Configurable electronics with low noise and 14-bit dynamic range for photodiode-based photon detectors", *Nuclear Instruments and Methods in Physics Research Section A: Accelerators, Spectrometers, Detectors and Associated Equipment* 565.2 (2006) 768–783, ISSN: 0168-9002, DOI: 10.1016/j.nima.2006.05.246, URL: http://www.sciencedirect.com/science/article/pii/S0168900206009909.

[74] R. E. Bosch et al.,
"The ALTRO chip: a 16-channel A/D converter and digital processor for gas detectors",
IEEE Transactions on Nuclear Science 50.6 (Dec. 2003) 2460–2469, ISSN: 0018-9499,
DOI: 10.1109/TNS.2003.820629.

[75] R. Brun et al., *ROOT TTree*, 2012, URL: http://root.cern.ch/root/html/TTree.html.

[76] L. Landau, "On the energy loss of fast particles by ionization",
Journal of Physics (USSR) 8 (1944) 201–205.

[77] Wikipedia, *Cluster analysis*, 2012,
URL: http://en.wikipedia.org/wiki/Cluster_analysis.

[78] G. Landi, "Properties of the center of gravity as an algorithm for position measurements",
Nuclear Instruments and Methods in Physics Research Section A: Accelerators, Spectrometers, Detectors and Associated Equipment 485.3 (2002) 698–719, ISSN: 0168-9002,
DOI: 10.1016/S0168-9002(01)02071-X,
URL: http://www.sciencedirect.com/science/article/pii/S016890020102071X.

List of Figures

List of Tables